Unification and Development of Quantum Field Theory Methods in Many-Particle Physics

Christopher J. N. Coveney
Merton College
University of Oxford

A thesis submitted for the degree of
Doctor of Philosophy
Theoretical Condensed Matter Physics

Trinity Term, 2026

Abstract

The quantum theory of many-particle systems is deeply connected to the mathematical formalism and techniques of quantum field theory, which are crucial in order describe the emergent phenomena that arise in condensed matter physics. The main goal of this thesis is to provide a unified description of quantum field theory methods in the context of many-particle physics in order to extend and develop these techniques to better understand the different quantum properties of matter. This both furthers the conceptual understanding of quantum many-body correlation and also allows for the development of novel theoretical techniques that combine the different formalisms employed in condensed matter theory, quantum chemistry and nuclear physics.

To achieve this aim, the thesis is composed of two parts. Part I deals with many-body fermion-fermion interactions and is physically motivated by the non-relativistic electronic structure problem. Here, we introduce the Keldysh contour formulation of quantum field theory to provide a unified presentation of quantum systems both in and out-of-equilibrium. Then, we extend the conventional quantum theory of many-particle systems, based on hermitian quantum mechanics, to describe systems governed by non-hermitan Hamiltonians. This allows us to present a natural unification of two major pillars in the *ab initio* quantum theory of many-particle systems: coupled-cluster theory and the Green's function formalism. This unification is further demonstrated through the emergence of the coupled-cluster amplitude equations from the Green's function formalism. In particular, this analysis has direct bearing on the development of novel theoretical approaches to the electronic structure and nuclear many-body problems. Our findings are also relevant to the study of general non-hermitian as well as open quantum systems.

Part II focuses on the quantum field theory of electron-nuclear interactions in infinite solids. Here, we use the Keldysh contour representation presented in Part I to understand excited state dynamics that include electron-electron and electron-lattice interactions in materials. We also derive the analytic continuation of the Green's function for systems

that have continuous eigenspectra. This analysis demonstrates the relationship between the Green's function formalism and scattering theory, making the role of the continuum and causality conditions explicitly clear in the context of the pole condition of the Dyson equation. Using the analytic continuation of the propagator, we provide an in-depth analysis of electron-phonon and exciton-phonon scattering channels, with a particular focus on phonon-driven exciton dissociation scattering. Our theoretical analysis then firmly demonstrates the connection between the extension of the Bethe-Salpeter equation approach to include electron-phonon interactions and effective field theories based on composite exciton-phonon coupling. We subsequently combine the techniques presented in Part I, based on the Dyson supermatrix formulation, with the analysis presented in Part II to calculate, from first principles, the effects of including electron-phonon interactions on the excited states of heterogeneous semiconductors.

Finally, we provide a summary of the fundamental contributions presented in this thesis and the potential further research directions to be pursued.

Acknowledgments

This thesis is dedicated to my mother and father. I will never be able to find the words to express how grateful I am to you both for the countless sacrifices you have made to provide for our family. I owe everything to you.

To my mother, I am eternally grateful to have you in my life and to be your son. You are the strongest person I know and the one I admire the most. You have taught me the importance of the soul, how emotion and family are what define our humanity and make life worth living. The power of compassion and empathy. How to passionately stand up for what you believe to be right. Everything I have learned from you is more real than any interpretation of quantum theory.

To my father, you always said the best grade to aim for was maximum attainment with minimal effort. You have taught me how to think independently, to not be bothered by what the crowd are doing. I admire the way you have always encouraged me to be original and to never bow down mindlessly to authority. I deeply appreciate the way that you are always unapologetically yourself. Your humour is second to none as well as your insanely diverse range of interests. I will always remember all the time you spent taking me and my friends across the UK to my football matches. Through you, I have come to understand the true meaning of intelligence and originality. You are ridiculous and I love you.

To my sister, I adore you. You have the biggest heart of us all and I will always be there in your corner fighting for you.

My time in Oxford has consisted of some hilarious memories as well as some profoundly sad moments. I feel incredibly lucky to have been supervised by Professor David Tew and Professor Marina Filip. During the first year of my DPhil, my uncle passed away. I cannot thank either of you enough for your compassion and understanding to allow me time off to be with my family in Lebanon during that period.

I first interacted with Professor David Tew during the second year of my undergraduate degree at Oxford. The year before starting my Part II project, we discussed potential

research directions that would be interesting to explore. He floated the idea that it would be exciting to pursue the field-theoretic Green's function formalism and its relationship to the traditional wavefunction-based approaches of quantum chemistry. This undoubtedly changed the entire trajectory of my academic life. In fact, it was also his idea that I be co-supervised by him and Professor Marina Filip.

Professor David Tew, you are an inspiration to me. Your approach to research along with the depth of your ideas and insight is truly profound. I feel that your kindness and consideration towards your students is something very special. Your belief in me and my ideas, as well as the advice you have shared with me over the years, has had a foundational impact on myself both professionally and personally. Without your encouragement and support, I would never have been able to publish my solo author paper that constitutes Chapter 4 of this thesis. I hope that we will continue to remain in contact for many years to come.

It has been an incredible pleasure and an exciting experience to have been also co-supervised by Professor Marina Filip. Working with you on exciton-phonon interactions in infinite solids truly made me into a proper condensed matter theorist. I learned so much both professionally and personally from you through the way you supported my independence and exploration of new theoretical techniques. Without working with you, I would not have gained such a broad education in physics. Your encouragement that I present my work at the March Meetings of the American Physical Society (APS) was also instrumental in broadening my perspective on academia. Thank you for your kindness and relentless dedication to help finding ways to support my work and future in academia.

I must also thank Merton College, Oxford for supporting my work through their Graduate Prize Scholarship as well as providing funding for me to present my research at several difference conferences throughout my DPhil.

Professor Antonios Alvertis was crucial in helping me get to grips with electron-phonon physics. Working with you genuinely changed my outlook on physics and academia and it has been a great pleasure to collaborate with you on such a diverse range of projects. You taught me how to properly structure and write my first academic paper and I greatly appreciate your belief in my ability to do analytic work. We have also

had some hilarious moments having to deal and respond to criticism of our work and I am glad that I had your support throughout.

During my second year I was able to present some of my research at the APS 2024 March Meeting in Minneapolis. It was at this conference that I was first introduced to Stephen Gant. I could not have asked for a better friend and collaborator to work with. Our collaborative work has certainly strongly influenced the second part of this thesis and I am very grateful to you for supporting my ideas. We had some ridiculous nights in Minneapolis and also when you came to Oxford. I don't think I have laughed so hard and continuously like that. I will always remember that night out in London (for good and bad reasons) that ended with us and my friends eating Jollof rice that was cooked inside the floor of some random garage. Also, you hosted me like a brother when I visited UC Berkeley which I am super grateful for.

I must also thank Professor Jeffrey Neaton at UC Berkeley for his support, kindness and help throughout my DPhil. You are loved by everyone that has had the privilege of interacting with you. I learned a lot from the way you carry yourself and your clarity of mind when approaching research. I am also grateful to you for letting me visit your group at UC Berkeley as well as providing me access to the Lawrence Berkeley National Lab and the Molecular Foundry. In particular, I will never forget the view from the Foundry followed by the lift you gave me back to campus. You put on great barbecues, are an even better host and also a fellow West Ham fan. I am sure we will watch a game together sometime soon.

Dr Jonah Haber, you are an incredibly deep thinker and I have found it massively helpful to discuss theoretical concepts with you over the course of my DPhil. I really admire the way you approach problems as well as the breadth and depth of your knowledge of condensed matter physics. Also, thanks for putting up with a number of late night pub selfies of Stephen and I declaring the exciton-polaron show to be on the road.

During the third year of my DPhil, I was able to visit the European Theoretical Spectroscopy Facility (ETSF) at École Polytechnique de Paris. I am greatly indepted to Professor Lucia Reining for enabling me to visit despite the grave challenges posed by French bureaucracy. It was through discussions with you that I was first properly introduced to the Keldysh contour formalism and I think it is clear that this has left a lasting impression on the presentation of the work in this thesis. You are an inspirational

human being and I feel incredibly lucky to have had the opportunity to work with you. The sharpness of your intellect and your ability to cut straight through to the essence of an idea was incredible to witness. I also hope that we continue to stay in touch.

I must also thank and acknowledge the other members of the ETSF. In particular Professor Vitaly Gorelov, Professor Matteo Gatti and Professor Francesco Sottile were incredible to interact with and really made the office a great atmosphere to be around. Ilayda Ashgar was super helpful in helping me access the department at the beginning of my stay as French bureaucracy challenged my sanity. I am very grateful to Sarbajit Dutta, Marc Aichner and Carlos Rodriguez Perez who provided me with much needed comedic relief during my time in Paris.

Finally (on the academic front), I would also like to acknowledge Professor Carlo Barbieri and Dr Francesco Marino. Your work is of the highest standard and its presentation is always meticulously well crafted. Towards the end of my DPhil I have very much enjoyed our discussions on the connections between coupled-cluster theory and the Green's function formalism. I hope that we will remain in touch and hopefully continue our joint collaboration.

Frankly this thesis would not have been possible without the support of my family and friends: Antonio Nehme, Samin Inan, Kareem Hussain, Samuel Telling, Joseph Menzies, William Telling and David Lampietti (Ardvard 'Edge Lord' Vitten). I love each and every one of you. In particular, I must acknowledge a ridiculous night when Samin Inan came to visit me in Oxford during the second year of my DPhil. That night will live long in my memory. We'll burn that bridge when we get to it. A mention must also go to Orestis Tzirtzilakis who was huge in helping me get through a difficult time when I returned from Paris to Oxford. There are too many ridiculous stories to recount and I have already probably written too much here. Nights with Ardvard at The Bank of Friendship have also facilitated the rapid and efficient completion of this thesis.

During the second year of my DPhil, one of my closest childhood friends, Conrad Marsden Jeeves, tragically passed away. This thesis is also dedicated to the memory of him and my uncle, Akram Nehme.

There is one final person I must acknowledge that has had a crucial impact on my intellectual and personal development. Estez–Batal: Alex Nehme. I admire your strength

of character and the way you carry yourself in every social situation. You are the most reliable guy I know. Hopefully I won't find you taht l'jizr. Our adventures together have formed some of the greatest memories I have. And yes, I did manage to finish this thesis, despite your best efforts...

To my family in Lebanon; I keep you all in my heart each day. Ana bhebkon kelkon.

Christopher James Nehme Coveney

List of Publications

This thesis contains results that contributed to the following publications that arose from the research carried out during my DPhil (October 2022 to March 2026).

Publications:

- **C. J. N. Coveney** and D. P. Tew, *A regularized second-order correlation method from Green's function theory*, Journal of Chemical Theory and Computation **19**, 3915, (2023) [1].
- A. M. Alvertis, J. B. Haber, Z. Li, **C. J. N. Coveney**, S. G. Louie, M. R. Filip and J. B. Neaton, *Phonon screening and dissociation of excitons at finite temperatures from first principles*, Proceedings of the National Academy of Sciences **121**, e2403434121, (2024) [2].
- **C. J. N. Coveney**, J. B. Haber, A. M. Alvertis, J. B. Neaton and M. R. Filip, *Rearrangement collision theory of phonon-driven exciton dissociation*, Physical Review B **110**, 054307, (2024) [3].
- **C. J. N. Coveney** and D. P. Tew, *Diagrammatic theory of the irreducible coupled-cluster self-energy*, Physical Review B **112**, 045104, (2025) [4].
- **C. J. N. Coveney**, *Uncovering relationships between the electronic self-energy and coupled-cluster doubles theory*, Journal of Physical Chemistry A Special Issue: 'Forty Years of Response Function Theory' **129**, 8689, (2025) [5].
- S. E. Gant, A. M. Alvertis, **C. J. N. Coveney**, J. B. Haber, M. R. Filip and J. B. Neaton, *Ultrafast spontaneous exciton dissociation via phonon emission in $BiVO_4$*, Physical Review Research **8**, 013105, (2026) [6].

- **C. J. N. Coveney** and D. P. Tew, *Non-hermitian Green's function theory with N-body interactions: The coupled-cluster similarity transformation*, Physical Review Research **8**, 013322, (2026) [7].

- N. Tubman, **C. J. N. Coveney**, C.-E. Hsu, A. Montoya-Castillo, M. R. Filip, J. B. Neaton, Z. Li, V. Vlcek and A. M. Alvertis, *Theory of ab initio downfolding with arbitrary range electron-phonon coupling*, Physical Review B **113**, 245144, (2026) [8].

In addition, the following works are either currently in review or about to be submitted for review:

- **C. J. N. Coveney**, N. Tubman, C.-E. Hsu, A. Montoya-Castillo, M. R. Filip, J. B. Neaton, Z. Li, V. Vlcek and A. M. Alvertis, *Phonon-mediated electron attraction in $SrTiO_3$ via the generalized Fröhlich and deformation potential mechanisms*, In Review, (2026) [9].

- **C. J. N. Coveney**, S. E. Gant, J. B. Haber, A. M. Alvertis, J. B. Neaton and M. R. Filip, *Non-perturbative solutions of the finite temperature Dyson equation in periodic systems via an ab initio supermatrix formulation: Application to the lattice screening of excitons*, To be Submitted, (2026) [10].

- **C. J. N. Coveney**, S. E. Gant, J. B. Haber, A. M. Alvertis, J. B. Neaton and M. R. Filip, *Non-perturbative finite temperature exciton-phonon scattering in heterogeneous semiconductors*, To be Submitted, (2026) [11].

Chapter 3 contains results that contributed to the publication of Refs [4, 7]. Chapter 4 contains results that contributed to the publications of Refs [1, 5]. Chapters 5 and 6 contain results that contributed to the publication of Refs [2, 3, 6] as well as Refs [10, 11] which are about to be submitted for review.

Contents

1 Introduction

The quantum theory of many-particle systems is central to the study of a vast array of physical phenomena [12–17]. In particular, all forms of quantum matter can be described in terms of a many-body Hamiltonian. Since the advent of quantum field theory [12], the philosophical and mathematical formalism has found widespread application across condensed matter, nuclear and high energy physics. The development of quantum field theory methods in the context of many-particle physics originated from the identification that low-energy effective field theories emerge from the thermodynamic limit of a macroscopically large number of interacting particles. Inspired by the successes of these methods in describing the ground and excited state properties of solids and nuclei, quantum field theory methods are being increasingly more employed in quantum chemistry. This thesis focuses on the unification and development of these methods in the study of a wide range of physical phenomena from the behaviour of electrons in quantum chemistry, many-body nuclear-nuclear interactions to electron-phonon interactions in semiconductors and insulators as well as systems governed by non-hermitian Hamiltonians. In the following, we provide an overview of the fundamental non-relativistic many-body problem of interacting electrons and nuclei which provides the physical motivation for the theoretical advancements presented in this thesis. We conclude this Chapter by providing an outline of the structure of the thesis.

1.1 The many-body problem of electrons and nuclei

Of central importance in the study of condensed matter and quantum chemistry is the non-relativistic coupled electron-nuclear Hamiltonian (written in atomic units)

$$H = -\frac{1}{2}\sum_i \nabla_i^2 - \sum_\kappa \frac{\nabla_\kappa^2}{2M_\kappa} - \sum_{i,\kappa} \frac{Z_\kappa}{|\mathbf{r}_i - \mathbf{R}_\kappa|} + \frac{1}{2}\sum_{i\neq j} \frac{1}{|\mathbf{r}_i - \mathbf{r}_j|} + \frac{1}{2}\sum_{\kappa\neq\kappa'} \frac{Z_\kappa Z_{\kappa'}}{|\mathbf{R}_\kappa - \mathbf{R}_{\kappa'}|} \ , \tag{1.1.0.1}$$

where $\{\mathbf{r}_i\}$ and $\{\mathbf{R}_\kappa\}$ refer to the electron and nuclear coordinates, respectively. The set of nuclear masses and charges is given by $\{M_\kappa\}$ and $\{Z_\kappa\}$. Finding the many-body eigenstates of Eq. 1.1.0.1 is extremely complicated due to the correlated motion of the nuclei, electrons as well as their coupled electron-nuclear motion.

To make the problem more tractable, it is common to introduce the Born-Oppenheimer approximation which is obtained from the limit: $M_\kappa \to \infty$ [18]. This removes the contribution of the nuclear kinetic energy and therefore results in the 'clamped-ion' picture whereby the nuclei are fixed in place. As a result the electronic energy becomes a parametric function of the 'clamped-ion' nuclear positions. In many cases, this constitutes a good approximation as the nuclei masses are much larger than the mass of the electron. When this approximation is made, we obtain the electronic structure Hamiltonian:

$$H_{\text{el}} = \sum_i h(\mathbf{r}_i) + \frac{1}{2}\sum_{i\neq j} v(\mathbf{r}_i, \mathbf{r}_j) \tag{1.1.0.2}$$

where we have defined the one-body and two-body terms as

$$h(\mathbf{r}_i) = -\frac{1}{2}\nabla_i^2 + \phi(\mathbf{r}_i) \tag{1.1.0.3a}$$

$$\phi(\mathbf{r}_i) = -\sum_\kappa \frac{Z_\kappa}{|\mathbf{r}_i - \mathbf{R}_\kappa|} \tag{1.1.0.3b}$$

$$v(\mathbf{r}_i, \mathbf{r}_j) = \frac{1}{|\mathbf{r}_i - \mathbf{r}_j|} \ . \tag{1.1.0.3c}$$

Within the Born-Oppenheimer approximation, the internuclear repulsion simply contributes an additive constant to the electronic Hamiltonian and therefore is not included in Eq. 1.1.0.2. The electronic structure problem is then defined by the eigenvalue problem

$$H_{\text{el}}\Psi_\nu(\mathbf{x}_1, \mathbf{x}_2, \cdots, \mathbf{x}_N; \{\mathbf{R}_\kappa\}) = E_\nu^N(\{\mathbf{R}_\kappa\})\Psi_\nu(\mathbf{x}_1, \mathbf{x}_2, \cdots, \mathbf{x}_N; \{\mathbf{R}_\kappa\}) \ , \tag{1.1.0.4}$$

where $\mathbf{x} \equiv (\mathbf{r}, \sigma)$ is the space-spin coordinate of an electron, ν indexes the many-body eigenstates and we have explicitly denoted the parametric dependence of the electronic

wavefunction and energy on the positions of the 'clamped-ions'. However, even within the Born-Oppenheimer approximation the eigenvalue problem of Eq. 1.1.0.4 remains highly computationally intractable due to the correlated motion of the electrons. Therefore, we are required to resort to more sophisticated theoretical techniques for its effective solution.

1.2 Structure of the thesis

This thesis is composed of two parts. Part I is centered around the electronic structure problem given by the Hamiltonian of Eq. 1.1.0.2 obtained from the Born-Oppenheimer approximation. In Chapter 2, we introduce and develop the formalism of quantum field theory for systems of many interacting fermions, with Eq. 1.1.0.2 providing the main motivation for this analysis. This leads us to introduce the Keldysh contour formulation of quantum field theory which provides a unified description of systems in and out-of-equilibrium. We introduce the single-particle Green's function and self-energy, focusing on their formally exact analytic and algebraic structures for systems governed by hermitian many-body Hamiltonians. We provide an overview of the exact and perturbative Dyson equations, with their relationship to Hedin's equations. We then introduce and extend the Dyson supermatrix formulation to describe many-body systems at finite temperatures. Finally, we derive and summarize several formally exact properties of the two-particle Green's function and Bethe-Salpeter equation used to describe correlated two-particle states.

In Chapter 3, we extend the conventional hermitian Green's function formalism to account for N-body non-hermitian interactions. This analysis is motivated in order to provide a unified description of quantum many-body correlation by combination of field theoretic correlation functions and canonical transformations. One of the most useful canonical transformations introduced in the context of the nuclear many-body and electronic structure problems is the coupled-cluster similarity transformation, which is the 'gold standard' method used to perform highly accurate quantum-chemical and nuclear calculations of ground state correlation effects. However, coupled-cluster theory generates a non-hermitian N-body Hamiltonian that is isospectral to the original physical Hamiltonian of interest. As a result of the complexity of the non-hermitian N-body Hamiltonian generated by this transformation, a complete and unified description of the relationship between the conventional hermitian Green's function formalism and

coupled-cluster theory has remained uncovered. The formalism presented in this Chapter achieves this unified description, furthering the conceptual understanding of many-body correlation in the context of condensed matter, nuclear physics and quantum chemistry, while also allowing for the description of fundamentally non-hermitian many-body quantum systems, open quantum systems and more.

In Chapter 4, we focus on how specific approximations of coupled-cluster theory can be generated directly from the conventional hermitian Green's function formalism. This analysis complements that of Chapters 2 and 3, providing, for the first time, the derivation of the *complete* coupled-cluster doubles amplitude equations starting from the hermitian Green's function formalism. In addition, the relationship to the equation-of-motion coupled-cluster theory is also outlined. We demonstrate the exact analytic results obtained by exact solution of the Hubbard dimer. We believe that this contribution will lead to the development of novel electronic structure and nuclear physics methods.

In Part II of this thesis, we focus on going beyond the Born-Oppenheimer approximation by including the effects of interactions between the electronic and lattice degrees of freedom in infinite solids. In particular, we focus on the inclusion of electron-phonon interactions to understand the dynamics of the excited electronic states of semiconductors and insulators.

In Chapter 5, we provide an in-depth analysis of the structure of the Green's function for systems that possess a continuous spectrum. In this case, the Green's function develops a branch cut discontinuity on the real axis. We specifically derive the exact analytic continuation for the Green's function across the branch cut in order to understand the pole condition of the Dyson equation and its relationship to scattering theory and causality. We then introduce the quantum field theory of the electron-nuclear interaction to derive the phonon contribution to the screened interaction and electronic self-energy that appear in the Hedin-Baym equations. Using this analysis, we extend the Bethe-Salpeter equation to account for electron-phonon interactions providing a complete overview of the origin of these contributions as well as their relationship to scattering channels such as phonon-driven exciton dissociation. Finally, we provide an overview of the effective field theory based on the linear coupling of excitons to a bath of phonons.

In Chapter 6, we derive the Dyson supermatrix formulation to account for the lattice screening of exciton states at finite temperatures using the analysis derived in Chapter 5.

In the process, we provide a rigorous connection between the Bethe-Salpeter equation and the effective field theory based on the linear exciton-phonon coupling. We then apply our formalism to compute non-perturbative temperature-dependent phonon-driven exciton dissociation rates and energy renormalizations for heterogeneous semiconductors in a computationally efficient and physically transparent manner using the Block Lanczos algorithm. As a proof of concept, we predict ultrafast exciton dissociation at room temperature for CdS, GaN and $BiVO_4$, opening up the computation of this quantity for a broad range of materials.

In Chapter 7, we present the conclusions of this thesis and provide an outlook for ongoing and future work to be done towards the unification and development of quantum field theory methods to understand systems of many interacting particles. Finally, the four appendices cover more detailed step by step derivations relevant to the results presented in the main body of the thesis.

Part I

Electron–Electron Interactions

"They consider relativistic quantum field theory and electrodynamics to be quite perfect theories and it is not necessary to be anxious about the situation. I should say that I do not like that at all, because according to such 'perfect' theory we have to neglect, without any reason, infinities that appear in the equations. It is just mathematical nonsense."

— Paul Dirac

2

Quantum Field Theory Methods for Many-Fermions

Contents

2.1 Second quantization

The non-relativistic electronic structure Hamiltonian given in Eq. 1.1.0.2 can be written

in terms of the electron field operators as [12]

$$H_{\text{el}} = \int d\mathbf{x}\psi^\dagger(\mathbf{x})h(\mathbf{r})\psi(\mathbf{x}) + \frac{1}{2}\int d\mathbf{x}d\mathbf{x}'\psi^\dagger(\mathbf{x})\psi^\dagger(\mathbf{x}')v(\mathbf{r},\mathbf{r}')\psi(\mathbf{x}')\psi(\mathbf{x}) \ , \tag{2.1.0.1}$$

where $\psi^\dagger(\mathbf{x})/\psi(\mathbf{x})$ act to create/annihilate electrons at space-spin location $\mathbf{x}$. The field operators operate on the Fock space which allows for the description of many-body quantum systems that vary in particle number [12, 16]. The integrals here are defined as $\int d\mathbf{x} \equiv \sum_\sigma \int d\mathbf{r}$, where the summation runs over the spin degrees of freedom. The field operators are defined in the Schrödinger picture and obey the canonical anti-commutation relations:

$$\{\psi(\mathbf{x}), \psi^\dagger(\mathbf{x}')\} = \delta(\mathbf{x}-\mathbf{x}') \ \ ; \ \ \{\psi(\mathbf{x}), \psi(\mathbf{x}')\} = \{\psi^\dagger(\mathbf{x}), \psi^\dagger(\mathbf{x}')\} = 0 \ . \tag{2.1.0.2}$$

This commutator algebra, along with the fact that states are created from a unique vacuum state ($\psi(\mathbf{x})\left|\text{vac}\right\rangle = 0$; $\psi^\dagger(\mathbf{x})\left|\text{vac}\right\rangle = \left|\mathbf{x}\right\rangle \ \forall\, \mathbf{x}$), recovers the correct Fermi-Dirac statistics required to describe systems of many-fermions [12]. By transformation to a general single-particle spin-orbital basis[1]

$$\psi^\dagger(\mathbf{x}) = \sum_p \phi_p^*(\mathbf{r})a_p^\dagger \ , \tag{2.1.0.3}$$

where $\phi_p^*(\mathbf{r}) = \langle\phi_p|\mathbf{r}\rangle$, with p representing a combined index that also includes the spin degrees of freedom, we can re-write the Hamiltonian as [12, 13, 15–17]

$$H_{\text{el}} = \sum_{pq} h_{pq}a_p^\dagger a_q + \frac{1}{2}\sum_{pq,rs} v_{pq,rs}a_p^\dagger a_q^\dagger a_s a_r \ . \tag{2.1.0.4}$$

Here, we have defined the one-body and two-body matrix elements as

$$h_{pq} = \int d\mathbf{r}\phi_p^*(\mathbf{r})h(\mathbf{r})\phi_q(\mathbf{r}) \tag{2.1.0.5a}$$

$$v_{pq,rs} = \int d\mathbf{r}d\mathbf{r}'\phi_p^*(\mathbf{r})\phi_q^*(\mathbf{r}')v(\mathbf{r},\mathbf{r}')\phi_s(\mathbf{r}')\phi_r(\mathbf{r}) \ . \tag{2.1.0.5b}$$

As Eq. 2.1.0.3 represents a canonical transformation, the rotated electron field operators also obey the anti-commutator algebra

$$\{a_p, a_q^\dagger\} = \delta_{pq} \ \ ; \ \ \{a_p, a_q\} = \{a_p^\dagger, a_q^\dagger\} = 0 \ . \tag{2.1.0.6}$$

Finally, it is useful to write the Hamiltonian in the fully anti-symmetrized form [19]

$$H_{\text{el}} = \sum_{pq} h_{pq}a_p^\dagger a_q + \frac{1}{4}\sum_{pq,rs} \bar{v}_{pq,rs}a_p^\dagger a_q^\dagger a_s a_r \ , \tag{2.1.0.7}$$

[1] Throughout Part I of this thesis, indices and wavevectors $i\mathbf{k}_i, j\mathbf{k}_j, \cdots$ denote occupied (valence band) spin-orbitals and $a\mathbf{k}_a, b\mathbf{k}_b, \cdots$ will denote virtuals (conduction band). Unless otherwise stated, a mixture of latin and greek indices $p\mathbf{k}_p, \alpha\mathbf{k}_\alpha, \cdots$, will be used to denote general single-particle states. The wavevector dependence will be omitted for notational clarity.

where $\bar{v}_{pq,rs} = v_{pq,rs} - v_{pq,sr}$ is the anti-symmetrized electron-electron repulsion integral. In the quantum chemistry literature, it is common to also denote the anti-symmetrized electron-electron repulsion integral by $\langle pq||rs\rangle \equiv \bar{v}_{pq,rs}$. As will be demonstrated in Chapter 3, introduction of the anti-symmetrized Hamiltonian allows for the direct inclusion of fermion exchange symmetry. In general, we can extend the results obtained here for the two-body electronic structure Hamiltonian to write the expression for an arbitrary N-body operator on the Fock space as

$$\begin{aligned} O = &\sum_{pq} o_{pq} a_p^\dagger a_q + \frac{1}{(2!)^2} \sum_{pq,rs} \bar{o}_{pq,rs} a_p^\dagger a_q^\dagger a_s a_r + \frac{1}{(3!)^2} \sum_{pqr,stu} \bar{o}_{pqr,stu} a_p^\dagger a_q^\dagger a_r^\dagger a_u a_t a_s \\ &+ \cdots + \frac{1}{(N!)^2} \sum_{\substack{pqrs\cdots \\ utwv\cdots}} \bar{o}_{pqrs\cdots,utwv\cdots} a_p^\dagger a_q^\dagger a_r^\dagger a_s^\dagger \cdots a_v a_w a_t a_u \ . \end{aligned} \tag{2.1.0.8}$$

In this equation all matrix elements are fully anti-symmetrized with respect to fermionic exchange. For example, the anti-symmetrized three-body integral contains six integrals [20]:

$$\bar{o}_{pqr,stu} = o_{pqr,stu} - o_{pqr,uts} - o_{pqr,sut} - o_{pqr,tsu} + o_{pqr,tus} + o_{pqr,ust} \ , \tag{2.1.0.9}$$

where the three-body matrix element is defined as

$$o_{pqr,stu} = \int d\mathbf{r} d\mathbf{r}' d\mathbf{r}'' \phi_p^*(\mathbf{r}) \phi_q^*(\mathbf{r}') \phi_r^*(\mathbf{r}'') O(\mathbf{r}, \mathbf{r}', \mathbf{r}'') \phi_u(\mathbf{r}'') \phi_t(\mathbf{r}') \phi_s(\mathbf{r}) \ . \tag{2.1.0.10}$$

From this analysis, it is clear how these relationships can be generalized to generate an anti-symmetrized N-body matrix element.

2.2 Generalized Keldysh contour

The quantum theory of many-particle systems is centered around the analysis of Green's functions. Green's functions are dynamical correlation functions that contain information about the way a quantum field changes with time. Therefore, it is crucial to understand and provide an overview of the role of time-dependence in quantum mechanics. This analysis is also necessary in order to provide a complete description of the forthcoming non-hermitian theory, to be presented in Chapter 3, where the time-dependence of states and operators must be carefully addressed. In order to provide a unified description of quantum systems at zero and finite temperature, the analysis presented here is centered around the Keldysh contour [21, 22].

2.2.1 Zero-temperature formalism

Suppose that we have a system governed by a time-dependent hermitian Hamiltonian, $H(t)$. The Schrödinger equation is therefore

$$i\frac{\partial}{\partial t}\left|\Psi_S(t)\right\rangle = H(t)\left|\Psi_S(t)\right\rangle \ . \tag{2.2.1.1}$$

Given an initial state $|\Psi(t_0)\rangle$, we can write the formal solution as [13–15, 17]

$$\left|\Psi_S(t)\right\rangle = U(t,t_0)\left|\Psi_S(t_0)\right\rangle \ , \tag{2.2.1.2}$$

where $U(t,t_0)$ is the time-evolution operator defined as

$$U(t,t_0) = \mathcal{T}\left\{e^{-i\int_{t_0}^{t} dtH(t)}\right\} \ . \tag{2.2.1.3}$$

Here, we introduce the time-ordering operator $\mathcal{T}$, which acts to place operators with later time arguments to the left. Therefore, within the time-ordering operator, the Hamiltonians at different times can be treated as commuting operators. It is important to note that Eq. 2.2.1.3 is valid for both forward- ($t > t_0$) or backward- ($t < t_0$) time evolution. By using the group property of the time-evolution operator [13, 14, 17], we can define the backward time-evolution operator as

$$U(t,t_0) = \bar{\mathcal{T}}\left\{e^{i\int_{t}^{t_0} dtH(t)}\right\} \ , \tag{2.2.1.4}$$

where we have introduced the anti-time-ordering operator $\bar{\mathcal{T}}$, which acts to place operators with earlier time arguments to the left. The appearance of the time-ordering operators in Eqs 2.2.1.3 and 2.2.1.4 can be used to reveal the underlying Keldysh contour construction.

In the Schrödinger picture, all operators are time-independent and the time-dependence enters via the state vector, $|\Psi_S(t)\rangle$. Alternatively, the Heisenberg picture works with time-dependent operators and stationary state vectors. The Heisenberg formulation corresponds more intuitively to the classical picture where observables such as position and momentum vary with time. The state-vector in the Heisenberg representation is time-independent and is given by $|\Psi_H\rangle = |\Psi_S(t_0)\rangle$. Heisenberg operators are related to Schrödinger operators via [13–15]

$$\begin{aligned} O_H(t) &= U(t_0,t)O_S(t)U(t,t_0) \\ &= \bar{\mathcal{T}}\left\{e^{-i\int_{t}^{t_0} dtH(t)}\right\} O_S(t) \mathcal{T}\left\{e^{-i\int_{t_0}^{t} dtH(t)}\right\} \ , \end{aligned} \tag{2.2.1.5}$$

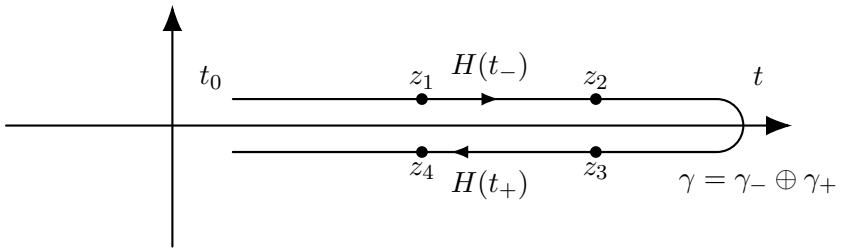

Figure 2.1: Keldysh contour construction [21, 22].

where we have introduced the notation $O_S(t)$ to indicate any explicit time-dependence of the operator. By introducing the notation in Eq. 2.2.1.5, we can rewrite this expression by using the Keldysh contour depicted in Figure 2.1 [16, 17, 21, 22]. The contour is explicitly time-directed, consisting of a forward branch (γ_-) from t_0 to t and a backward branch (γ_+) from t to t_0. With respect to the contour, time arguments on the backward branch are always 'later' than those on the forward branch. A generic time-argument associated with the contour is denoted by z, while a time argument on the forward (backward) branch is denoted as $t_-(t_+)$. The contour is completed by specifying the time-dependence of the set of operators on each branch. For the purposes of this thesis, we define operators such that they are identical on either branch of the contour: $O_S(t_-) = O_S(t_+) = O_S(t)$. However, it should be noted that this is a choice that can be modified depending on the physical problem of interest. If an operator is time-independent then $O_S(t_\pm) = O_S$. However, we keep the time-dependence of all operators in order to correctly specify their position along the contour. Importantly, on both branches of the contour the Hamiltonian is given by $H(t)$.

The Keldysh contour is also defined alongside the contour time-ordering operator, $\mathcal{T}_\gamma$. The contour time-ordering operator is defined such that it moves operators with 'later' contour time arguments to the left. Therefore, for time-arguments on the forward branch $\mathcal{T}_\gamma \equiv \mathcal{T}$, whereas on the backward branch $\mathcal{T}_\gamma \equiv \bar{\mathcal{T}}$. For strings of operators containing time arguments on either side of the branch, the contour time-ordering operator simply gives the product of the operators with their time arguments on the backward branch to the left of those with their time arguments on the forward branch. Using the contour, we can re-write the expectation value of an operator at zero temperature as [17]

$$\langle O(t)\rangle_0 = \langle \Psi(t_0)|\mathcal{T}_\gamma \left\{ e^{-i\int_\gamma dz H(z)} O_S(t) \right\} |\Psi(t_0)\rangle \ . \tag{2.2.1.6}$$

By using the group property of the time-evolution operator, we can extend the length of the contour to infinity as $U(t,t_0) = U(t,\infty)U(\infty,t_0)$. Using the Keldysh contour, we

introduce the contour ordered Keldysh representation as [17]

$$O_{\mathrm{K}}(z) = U(z_0, z) O_S(z) U(z, z_0) \ , \tag{2.2.1.7}$$

where we have defined the contour time-evolution operator as

$$U(z, z_0) = \mathcal{T}_\gamma \left\{ e^{-i \int_{z_0}^{z} d\bar{z} H(\bar{z})} \right\} \ , \tag{2.2.1.8}$$

with z 'later' than z_0. Eq. 2.2.1.7 is equivalent to the Heisenberg picture when $z = t_\pm$ and $z_0 = t_{0\pm}$. This gives rise to the contour equation-of-motion

$$i \frac{d}{dz} O_{\mathrm{K}}(z) = [O_K(z), H_K(z)] \ , \tag{2.2.1.9}$$

where we have assumed the operator $O_S(z)$ has no explicit time-dependence.

2.2.2 Time-dependent ensemble averages

The time-dependent ensemble average of a quantum system of many interacting particles is defined as

$$O_{\mathrm{ens}}(t) = \mathrm{Tr} \left\{ \rho_{\mathrm{eq}} O(t) \right\} \ , \tag{2.2.2.1}$$

where the trace is taken over the Fock space. Here, ρ_{eq} is the equilibrium density matrix corresponding to the Grand Canonical Ensemble (GCE) and defined as

$$\rho_{\mathrm{eq}} = \frac{e^{-\beta H^{\mathrm{M}}}}{Z} \ , \tag{2.2.2.2}$$

where $H^{\mathrm{M}} = H - \mu N$, with μ being the chemical potential, and $Z = \mathrm{Tr} \left\{ e^{-\beta H^{\mathrm{M}}} \right\}$ is the partition function, with $\beta = \frac{1}{k_B T}$ being the inverse temperature. The GCE describes an open system at constant volume in thermal equilibrium with a reservoir, thereby allowing for both fluctuations in energy and particle number. It is important to note that the thermal average given in Eq. 2.2.2.1 is defined with respect to a time-independent density matrix that has already reached an equilibrium state. Therefore, any attempts to extend this equation to define a general time-dependent ensemble average for a system that is explicitly out-of-equilibrium will be seriously constrained in its applicability. This is because Eq. 2.2.2.1 does not account for energy dissipation and so it cannot describe the long-time dynamics of the system as it re-approaches an equilibrium state. However, for systems at equilibrium at finite temperature, Eq. 2.2.2.1 provides a formally exact description of their dynamical properties.

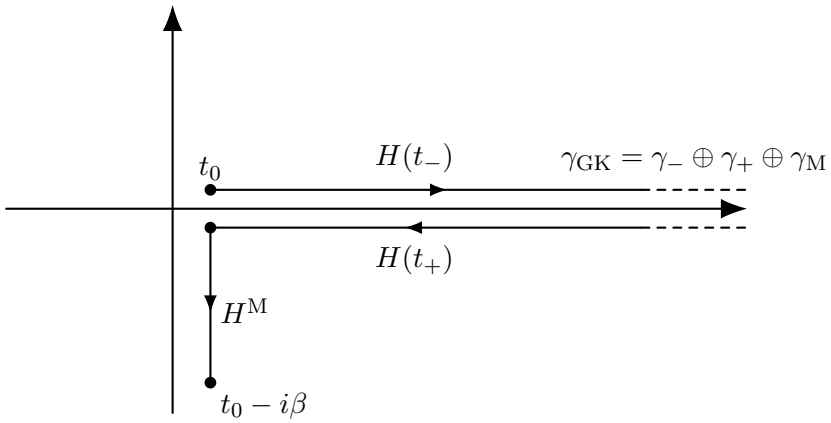

Figure 2.2: Generalized Keldysh contour construction [17].

Using Eq. 2.2.1.6, we can re-write the time-dependent ensemble average in the suggestive form

$$\begin{aligned} O_{\rm ens}(z) &= \frac{\mathrm{Tr}\left\{e^{-\beta H^{\rm M}}\mathcal{T}_\gamma\left\{e^{-i\int_\gamma d\bar{z}\ H(\bar{z})}O(z)\right\}\right\}}{\mathrm{Tr}\left\{e^{-\beta H^{\rm M}}\right\}} \\ &= \frac{\mathrm{Tr}\left\{\mathcal{T}_{\gamma_{\rm GK}}\left\{e^{-i\int_{\gamma_{\rm GK}} d\bar{z}\ H(\bar{z})}O(z)\right\}\right\}}{\mathrm{Tr}\left\{\mathcal{T}_{\gamma_{\rm GK}}\left\{e^{-i\int_{\gamma_{\rm GK}} d\bar{z}\ H(\bar{z})}\right\}\right\}} \ . \end{aligned} \tag{2.2.2.3}$$

In the final equality, we have introduced the generalized Keldysh contour (depicted in Figure 2.2) to re-write the equilibrium density matrix in terms of time-evolution over the Matsubara contour and used the fact that integration over the Keldysh contour γ gives the identity.

The generalized Kelydsh contour consists of three connected and explicitly ordered branches. The first two are the forward (γ_-) and backward (γ_+) real-time branches previous outlined in Subsection 2.2.1. The third branch is commonly referred to as the Matsubara contour ($\gamma_{\rm M}$) and extends from t_0 to $t_0 - i\beta$ [13, 14, 16, 17]. In Figure 2.2, the Matsubara contour is depicted as a vertical strip. However, the Matsubara contour can be represented by any contour in the complex plane provided that the difference between the end points is exactly $-i\beta$. On the Matsubara contour, the Hamiltonian is time-independent and defined as $H^{\rm M}$. Clearly, the time-evolution along the Matsubara contour is non-unitary.

Extension of the Keldysh contour to the imaginary Matsubara axis gives rise to the generalized Keldysh picture defined as

$$O_{\rm GK}(z) = U(z_0, z)O_S(z)U(z, z_0) \ , \tag{2.2.2.4}$$

for $z, z_0 \in \gamma_{\mathrm{GK}}$, where

$$U(z, z_0) = \mathcal{T}_{\mathrm{GK}} \left\{ e^{-i \int_{z_0}^{z} d\bar{z} H(\bar{z})} \right\} , \tag{2.2.2.5}$$

provided that z is 'later' than z_0 with respect to the contour. Using this expression, we can write the time-dependent ensemble average as

$$O_{\mathrm{ens}}(z) = \frac{\mathrm{Tr}\left\{U(z_f, z_0) O_{\mathrm{GK}}(z)\right\}}{\mathrm{Tr}\left\{U(z_f, z_0)\right\}} \tag{2.2.2.6}$$

where $U(z_f, z_0) = \mathcal{T}_{\mathrm{GK}} \left\{ e^{-i \int_{\gamma_{\mathrm{GK}}} d\bar{z} H(\bar{z})} \right\} = e^{-\beta H^{\mathrm{M}}}$ is the time-evolution operator that runs from the initial and final points of the contour. For the purposes of this thesis we define operators on the Matsubara contour to be time-independent: $O(z \in \gamma_{\mathrm{M}}) = O$. By inspection of Figure 2.2, it can be seen that $z_0 = t_0$ and $z_f = t_0 - i\beta$ are the initial and final time arguments of the generalized Keldysh contour.

2.2.3 The Gell-Mann and Low theorem and Interaction picture

At equilibrium, the dynamics of the system is governed by a time-independent Hamiltonian. Therefore, on the Keldysh contour the Hamiltonian is given by $H(t_\pm) = H$. For the rest of this thesis, we will be working at equilibrium and therefore within the equilibrium Keldysh formalism [23]. The time-independence of the Hamiltonian at equilibrium allows us to introduce the Gell-Mann and Low (GML) theorem for the ground state of a quantum field theory [24]. In general, at equilibrium, the Hamiltonian of the system can be decomposed into the sum of a reference operator, H_0, and an interaction term, H_1. The GML theorem introduces the adiabatic 'switching on' of the interaction through the time-dependent Hamiltonian:

$$H_\eta(t) = H_0 + e^{-\eta|t-t_0|} H_1 , \tag{2.2.3.1}$$

where η is a positive infinitesimal. With the introduction of this Hamiltonian we see that, at large earlier and later times, the Hamiltonian tends to H_0. At $t = t_0$, the Hamiltonian is exactly the full Hamiltonian of the interacting system. Finally, taking the limit as $\eta \to 0$ at the end of the calculation corresponds to adiabatically switching on the interaction [13].

To understand the Gell-Mann and Low theorem requires us to introduce the Interaction picture of quantum mechanics. This is done by application of the time-dependent unitary

transformation on the Schrödinger state vector to define the Interaction state vector: $|\Psi_I(t)\rangle = e^{iH_0 t}\,|\Psi_S(t)\rangle$. This gives rise to the Interaction picture Schrödinger equation

$$i\frac{\partial}{\partial t}\,|\Psi_I(t)\rangle = H_1(t)\,|\Psi_I(t)\rangle \ , \tag{2.2.3.2}$$

where $H_1(t) = e^{iH_0 t}H_1 e^{-iH_0 t}$ is the explicitly time-dependent interaction Hamiltonian defined in the Interaction picture. By comparison with Eqs 2.2.1.1 and 2.2.1.3, we see that the general solution is given by

$$|\Psi_I(t)\rangle = \mathcal{T}\left\{e^{-i\int_{t_0}^{t} d\bar{t}H_1(\bar{t})}\right\}|\Psi_I(t_0)\rangle \ , \tag{2.2.3.3}$$

remembering that the state vectors and operators are defined in the Interaction picture. Therefore, the Interaction picture corresponds to an explicitly time-dependent formulation of quantum mechanics even if the Hamiltonian in the Schrödinger representation is time-independent. This means that the Interaction picture can be immediately associated with the Keldysh contour construction presented in Subsection 2.2.1. Using the relationship between the Schrödinger and Interaction state vectors, we find that the Heisenberg state vector is given by

$$|\Psi_H\rangle = e^{-iH_0 t_0}U_I(t_0, t')\,|\Psi_I(t')\rangle \ . \tag{2.2.3.4}$$

As the initial time t_0 is arbitrary, we can set $t_0 = 0$ for simplicity. By introduction of the adiabatic 'switching on' Hamiltonian in Eq. 2.2.3.1, we find that

$$|\Psi_H\rangle = U_I^{\eta}(0, t')\,|\Psi_I(t')\rangle \ , \tag{2.2.3.5}$$

where $U_I^{\eta}(0, t')$ is given by replacing $H_1(\bar{t})$ in Eq. 2.2.3.3 by $e^{-\eta|\bar{t}|}H_1(\bar{t})$. Letting the time limit t' approach $-\infty$, while taking the physical limit as $\eta \to 0$ of Eq. 2.2.3.5 leads immediately to the GML theorem on the ground state of a quantum field theory [25]. The GML theorem states that if the quantity

$$\lim_{\eta\to 0}\frac{U_\eta(0,-\infty)\,|\Phi_0\rangle}{\langle\Phi_0|U_\eta(0,-\infty)|\Phi_0\rangle} \equiv \frac{|\Psi_0\rangle}{\langle\Phi_0|\Psi_0\rangle} \tag{2.2.3.6}$$

converges to all orders in perturbation theory, then it is an eigenstate of the full Hamiltonian such that

$$H\frac{|\Psi_0\rangle}{\langle\Phi_0|\Psi_0\rangle} = E\frac{|\Psi_0\rangle}{\langle\Phi_0|\Psi_0\rangle} \ , \tag{2.2.3.7}$$

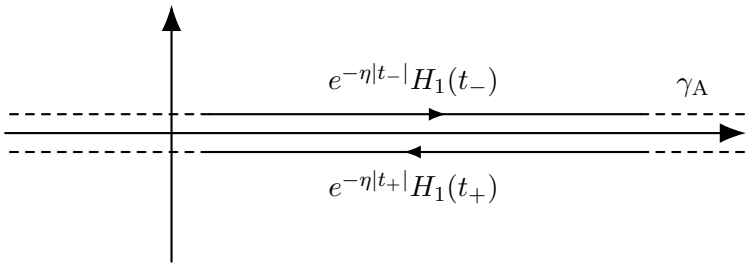

Figure 2.3: Zero temperature adiabatic Keldysh contour from the Gell-Mann and Low theorem.

where $|\Phi_0\rangle$ is an eigenstate of the reference operator, $H_0 |\Phi_0\rangle = E^{(0)} |\Phi_0\rangle$. In this way an eigenstate of the full Hamiltonian is generated adiabatically from $|\Phi_0\rangle$ as the interaction is switched on. If $|\Phi_0\rangle$ is the ground state of the reference Hamiltonian, then the eigenstate generated from this procedure is usually the true ground state. However, this is not always the case. Importantly, the limits of the numerator and denominator as $\eta \to 0$ in Eq. 2.2.3.6 do not exist separately. The theorem only asserts that if the limit of their ratio exists, then the eigenstate is well defined and is an eigenstate of the full Hamiltonian [24]. It can also be shown that the state can also be obtained from evolving 'backward' in time from $+\infty$ to the initial time. Using these results, along with the Keldysh contour construction, we depict the zero temperature adiabatic Keldysh contour in Figure 2.3. This can be used to construct contour-ordered perturbative expressions for expectation values of time-ordered strings of operators as

$$R(z_1, z_2) = \langle \Phi_0 | \mathcal{T}_{\gamma_{\mathrm{A}}} \left\{ e^{-i \int_{\gamma_{\mathrm{A}}} dz H(z)} O_I(z_1) O_I(z_2) \right\} |\Phi_0\rangle \ , \tag{2.2.3.8}$$

where the Hamiltonian on the contour is depicted in Figure 2.3.

It is important to note that the GML theorem can be used to construct perturbative expansions for time-ordered operators without reference to the Keldysh contour [13–15]. However, in this Chapter we choose to present the contour formulation in order to unify the zero temperature and finite temperature formalisms. This will be especially useful for the theoretical analysis to be presented on electron- and exciton-phonon interactions in Chapter 5. Furthermore, the Keldysh representation (Eq. 2.2.1.7) implicitly encodes both time-ordered and anti-time-ordered components. Focusing on the time-ordered component of Eq. 2.2.3.8 evaluated on the forward branch of the contour: $R^{\mathrm{T}}(t_1, t_2) = R(z_1 = t_{1,-}, z_2 = t_{2,-})$, we recover the conventional expression

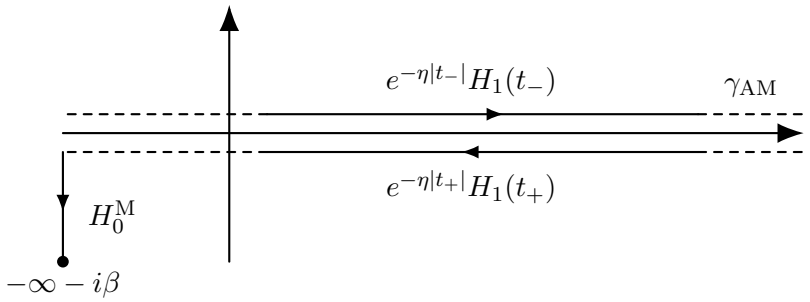

Figure 2.4: Finite temperature adiabatic Keldysh contour construction.

$$\begin{aligned} R^{\rm T}(t_1,t_2) &= \langle\Phi_0|\bar{\mathcal{T}}\left\{e^{-i\int_{\infty}^{-\infty}dte^{-\eta|t|}H_1(t)}\right\}\mathcal{T}\left\{e^{-i\int_{-\infty}^{\infty}dte^{-\eta|t|}H_1(t)}O_I(t_1)O_I(t_2)\right\}|\Phi_0\rangle \\ &= \frac{\langle\Phi_0|\mathcal{T}\left\{e^{-i\int_{-\infty}^{\infty}dte^{-\eta|t|}H_1(t)}O_I(t_1)O_I(t_2)\right\}|\Phi_0\rangle}{\langle\Phi_0|\mathcal{T}\left\{e^{-i\int_{-\infty}^{\infty}dte^{-\eta|t|}H_1(t)}\right\}|\Phi_0\rangle} \,. \end{aligned} \tag{2.2.3.9}$$

In these expressions we have dropped the implicit limit as $\eta \to 0$ for notational clarity. Therefore, at zero temperature, we can choose to work either with the conventional formulation or on the Keldysh contour which includes both time-orderings and time-directions.

We can also use the adiabatic 'switching on' procedure and GML theorem for systems at finite temperature. This is because the GML theorem can be applied to every eigenstate of the full Hamiltonian and so we can generate the fully interacting GCE density matrix from eigenstates of the reference equilibrium density matrix: $\rho_0^{\rm eq} = \frac{e^{-\beta H_0^{\rm M}}}{{\rm Tr}\left\{e^{-\beta H_0^{\rm M}}\right\}}$ [13, 14, 17]. Therefore, at equilibrium, we can write the time-dependent ensemble expectation value over a time-ordered string of operators as

$$R(z_1,z_2) = \frac{{\rm Tr}\left\{\mathcal{T}_{\gamma_{\rm AM}}\left\{e^{-i\int_{\gamma_{\rm AM}}d\bar{z}\ H(\bar{z})}O_I(z_1)O_I(z_2)\right\}\right\}}{{\rm Tr}\left\{\mathcal{T}_{\gamma_{\rm AM}}\left\{e^{-i\int_{\gamma_{\rm AM}}d\bar{z}\ H(\bar{z})}\right\}\right\}} \,, \tag{2.2.3.10}$$

where the finite temperature adiabatic Keldysh contour is depicted in Figure 2.4. Here, we define the Interaction picture on the Matsubara contour as $O_I(z \in \gamma_{\rm M}) = e^{H_0^{\rm M}\tau}O_S e^{-H_0^{\rm M}\tau}$ to capture the time-evolution of the non-interacting equilbirium density matrix.

In the rest of this thesis, we will simply refer to the Keldysh contour construction as γ. This is because the specific contour required will depend on the formulation as demonstrated in this Section. However, the structure of correlation functions remains identical and is independent of the specific contour chosen. Therefore, we can write expressions for

correlation functions on an arbitrary Keldysh contour construction, obtaining specific cases through choice of the contour.

2.3 Single-particle Green's function

The single-particle Keldysh Green's function is defined as the contour-ordered string of time-dependent operators in the Keldysh representation:

$$iG_{pq}(z_1, z_2) = \left\langle \mathcal{T}_\gamma \left\{ a_p(z_1) a_q^\dagger(z_2) \right\} \right\rangle . \tag{2.3.0.1}$$

In Eq. 2.3.0.1, we have purposefully not specified the expectation value: $\langle \mathcal{T}_\gamma \{\cdots\} \rangle$. This is to demonstrate that the structure of the equations for the single-particle Green's function at zero and finite temperatures is formally identical. The zero temperature formulation simply takes the expectation value to be defined over the exact ground state wavefunction, while the finite temperature formulation gives the Green's function as an ensemble average over the GCE. In addition, the Keldysh contour, γ, has also not been specified as the contour can vary depending on whether the system is at zero or finite temperatures as well as in or out-of-equilibrium as demonstrated in Section 2.2.

The Keldysh Green's function contains the following causal structure

$$G_{pq}(z, z') = \theta(z, z') G_{pq}^{>}(z, z') + \theta(z', z) G_{pq}^{<}(z, z') \tag{2.3.0.2}$$

where $\theta(z, z')$ is the contour-ordered Heaviside step function. It is defined such that the result is one if z is 'later' than z' on the contour but zero otherwise. The power of the Keldysh formalism arises when specifying which branches of the contour the time arguments of the propagator lie on. For the work presented in this thesis, the most important components that can be directly obtained from the contour are given by

$$G_{pq}^{\mathrm{T}}(t, t') = G_{pq}(z = t_-, z' = t'_-) \tag{2.3.0.3a}$$

$$G_{pq}^{\bar{\mathrm{T}}}(t, t') = G_{pq}(z = t_+, z' = t'_+) \tag{2.3.0.3b}$$

$$G_{pq}^{<}(t, t') = G_{pq}(z = t_-, z' = t'_+) \tag{2.3.0.3c}$$

$$G_{pq}^{>}(t, t') = G_{pq}(z = t_+, z' = t'_-) \tag{2.3.0.3d}$$

$$\mathcal{G}_{pq}^{\mathrm{M}}(\tau, \tau') = G_{pq}(z = t_0 - i\tau, z' = t_0 - i\tau') \ . \tag{2.3.0.3e}$$

These are the real time-ordered (G^{T}), real anti-time-ordered ($G^{\bar{\mathrm{T}}}$), lesser ($G^{<}$), greater ($G^{>}$) and Matsubara ($\mathcal{G}^{\mathrm{M}}$) components, respectively. At zero temperature, we are restricted to the first four. There are also two other important Green's functions that are particularly relevant to the study of quantum systems at finite temperatures and systems that are out-of-equilibrium. These are the retarded and advanced components:

$$G^{\mathrm{R}}_{pq}(t,t') = \theta(t-t')\left(G^{>}_{pq}(t,t') - G^{<}_{pq}(t,t')\right) \tag{2.3.0.4a}$$

$$G^{\mathrm{A}}_{pq}(t,t') = -\theta(t'-t)\left(G^{>}_{pq}(t,t') - G^{<}_{pq}(t,t')\right) \ . \tag{2.3.0.4b}$$

In general, the retarded, advanced, lesser and greater components are related to each other by

$$G^{>}_{pq}(t,t') - G^{<}_{pq}(t,t') = G^{\mathrm{R}}_{pq}(t,t') - G^{\mathrm{A}}_{pq}(t,t') \ . \tag{2.3.0.5}$$

To make the structure contained in the Keldysh contour Green's function more explicit, we can collect all the components contained in Eq. 2.3.0.1 to form the Keldysh branch time-matrix representation

$$\hat{\mathbf{G}}^{\mathrm{K}} = \begin{pmatrix} G^{\mathrm{T}}_{pq}(t,t') & G^{<}_{pq}(t,t') & G^{\rceil}_{pq}(t,\tau') \\ G^{>}_{pq}(t,t') & G^{\mathrm{T}}_{pq}(t,t') & G^{\rceil}_{pq}(t,\tau') \\ G^{\lfloor}_{pq}(\tau,t) & G^{\lfloor}_{pq}(\tau,t) & \mathcal{G}^{\mathrm{M}}_{pq}(\tau,\tau') \end{pmatrix} \ , \tag{2.3.0.6}$$

where we have defined the 'left' and 'right' Keldysh components as $G^{\rceil}_{pq}(t,\tau') = G_{pq}(z = t_{\pm}, z' = t_0 - i\tau')$ and $G^{\lfloor}_{pq}(\tau,t') = G_{pq}(z = t_0 - i\tau, z' = t'_{\pm})$, respectively [17].

2.3.1 Exact Dyson equation on the Keldysh contour

In this Section, we derive the exact equation-of-motion for the single-particle Green's function on the Keldysh contour. For simplicity, we assume that the Hamiltonian on each branch of the contour is a two-body operator. However, the formalism can be generalized to account for higher-body interaction Hamiltonians. Using the definition of the single-particle Green's function given in Eq. 2.3.0.1, the equation-of-motion of the single-particle Green's function operator is [17]

$$\sum_{r}\left(i\frac{\partial}{\partial z_1}\delta_{pr} - h_{pr}(z_1)\right)G_{rq}(z_1,z_2) = \delta(z_1,z_2)\delta_{pq} + \frac{1}{2}\sum_{rst}\int_{\gamma} dz_3 \bar{v}_{pr,st}(z_1,z_3)G^{4\mathrm{pt}}_{st,rq}(z_1,z_3;z_3^{+},z_2), \tag{2.3.1.1}$$

where z_3^+ is the time argument evaluated on the same branch of the contour as z_3 but at an infinitesimally later time: $z_3^+ = \lim_{\eta\to 0^+} z_3 + \eta$. Here, we have also defined the four-point Green's function on the contour as

$$iG^{\text{4pt}}_{pq,rs}(z_1, z_2; z_3, z_4) = \left\langle \mathcal{T}_\gamma \left\{ a_q(z_2) a_p(z_1) a_r^\dagger(z_3) a_s^\dagger(z_4) \right\} \right\rangle \ . \tag{2.3.1.2}$$

Importantly, we have chosen to explicitly indicate the time-dependence of the Hamiltonian and defined the two-body interaction as $v_{pr,st}(z_1, z_2) = v_{pr,st}(z_1)\delta(z_1, z_2)$. The integral over the contour, γ, is general but specifically depends on whether the system is at zero or finite temperatures or out-of-equilibrium.

As can be seen, the equation-of-motion for the single-particle Green's function is coupled to the higher-body four-point Green's function. However, we can formally close this equation by introduction of the exact *irreducible self-energy*:

$$\Sigma_{pq}(z_1, z_2) = \frac{1}{2} \sum_{rstu} \int_\gamma dz_3 dz_4 \bar{v}_{pr,st}(z_1, z_3) G^{\text{4pt}}_{st,ru}(z_1, z_3; z_3^+, z_4) G^{-1}_{uq}(z_4, z_2) \ . \tag{2.3.1.3}$$

This gives

$$\sum_r \left(i\frac{d}{dz_1}\delta_{pr} - h_{pr}(z_1) \right) G_{rq}(z_1, z_2) = \delta(z_1, z_2)\delta_{pq} + \sum_r \int_\gamma dz_3 \Sigma_{pr}(z_1, z_3) G_{rq}(z_3, z_2) \ . \tag{2.3.1.4}$$

By defining the functional inverse of the non-interacting Green's function on the contour as $[G_0]^{-1}_{pq}(z_1, z_2) = \sum_r \left(i\frac{d}{dz_1}\delta_{pr} - h_{pr}(z_1) \right) \delta(z_1, z_2)$, we arrive at the contour Dyson equation

$$\mathbf{G}(z_1, z_2) = \mathbf{G}_0(z_1, z_2) + \sum_{rs} \int_\gamma dz_3 dz_4 \ \mathbf{G}_0(z_1, z_3) \mathbf{\Sigma}(z_3, z_4) \mathbf{G}(z_4, z_2) \ . \tag{2.3.1.5}$$

Here, we have introduced matrix notation for the Green's function, $\mathbf{G}(z_1, z_2)$, and self-energy, $\mathbf{\Sigma}(z_1, z_2)$, for notational simplicity. The Dyson equation is a first-order differential equation and therefore a well-defined solution can only be obtained if specific boundary conditions are satisfied. In particular, at finite temperature, the fermionic Green's function must satisfy the Kubo-Martin-Schwinger (KMS) boundary conditions [26, 27]:

$$\mathbf{G}(z_i, z_2) = -\mathbf{G}(z_f, z_2) \tag{2.3.1.6a}$$

$$\mathbf{G}(z_1, z_i) = -\mathbf{G}(z_1, z_f) \ . \tag{2.3.1.6b}$$

The KMS boundary conditions require the Matsubara contour to be attached to the forward and backward real time branches of the Keldysh contour in order that a unique solution

can be obtained from the Dyson equation. At finite temperatures the KMS boundary conditions result in the fermionic Green's function being anti-periodic in imaginary time.

Eq. 2.3.1.5 is the exact Dyson equation defined on the Keldysh contour. However, in order to obtain Dyson equations for the Green's function components defined in Eqs 2.3.0.3, we must project the time arguments onto the different contour branches. From the branch matrix structure given in Eq 2.3.0.6, it is clear that the time-convolutions over the contour will result in the mixing of different time-projected components of the propagator. For simplicity, we work at equilibrium where the mixing between the Matsubara and real components vanishes. Therefore, we can discard convolutions that mix the Matsubara and real-time components [17, 28, 29].

At equilibrium, by evaluating both the external Green's function time-arguments on the forward branch of the contour ($z = t_-, z' = t'_-$), we arrive at the zero temperature Dyson equation for the time-ordered single-particle Green's function as

$$\mathbf{G}^{\mathrm{T}}(t_1, t_2) = \mathbf{G}_0^{\mathrm{T}}(t_1, t_2) + \sum_{rs} \int_{\gamma_A} dz_3 dz_4 \; \mathbf{G}_0(t_{-,1}, z_3)\mathbf{\Sigma}(z_3, z_4)\mathbf{G}(z_4, t_{-,2}) \; . \tag{2.3.1.7}$$

In order to convert the contour time convolution integrals from the contour to the projected Green's function components requires the introduction of the Langreth rules given in Appendix A.1. Using these rules, we find that the time-ordered Green's function equation-of-motion is

$$\begin{aligned} \mathbf{G}^{\mathrm{T}}(t_1, t_2) = \mathbf{G}_0^{\mathrm{T}}(t_1, t_2) + [\mathbf{G}_0^{\mathrm{T}} * \mathbf{\Sigma}^{\mathrm{T}} * \mathbf{G}^{\mathrm{T}}](t_1, t_2) - [\mathbf{G}_0^{\mathrm{T}} * \mathbf{\Sigma}^{<} * \mathbf{G}^{>}](t_1, t_2) \\ - [\mathbf{G}_0^{<} * (\mathbf{\Sigma} * \mathbf{G})^{>}](t_1, t_2), \end{aligned} \tag{2.3.1.8}$$

where we have introduced the notation $[A{*}B{*}C](t, t') = \int_{-\infty}^{\infty} dt_1 dt_2 A(t, t_1)B(t_1, t_2)C(t_2, t')$. The structure of Eq. 2.3.1.8 is extremely revealing. It shows that, in general, the Dyson equation for the real-time-ordered Green's function is *not* closed. This is because the real-time-ordered component is explictly coupled to the greater and lesser propagators. By Fourier transformation to the frequency domain, we have

$$\begin{aligned} \mathbf{G}^{\mathrm{T}}(\omega) = \mathbf{G}_0^{\mathrm{T}}(\omega) + \mathbf{G}_0^{\mathrm{T}}(\omega)\mathbf{\Sigma}^{\mathrm{T}}(\omega)\mathbf{G}^{\mathrm{T}}(\omega) - \mathbf{G}_0^{\mathrm{T}}(\omega)\mathbf{\Sigma}^{<}(\omega)\mathbf{G}^{>}(\omega) \\ - \mathbf{G}_0^{<}(\omega)\left(\mathbf{\Sigma}(\omega)\mathbf{G}(\omega)\right)^{>} \; . \end{aligned} \tag{2.3.1.9}$$

In contrast, using the Langreth rules, we see that the Dyson equations for the retarded/advanced components are closed regardless of whether the system is in or out-of-equilibrium. The Fourier transform of these Dyson equations is given by

$$\mathbf{G}^{\mathrm{R/A}}(\omega) = \mathbf{G}_0^{\mathrm{R/A}}(\omega) + \mathbf{G}_0^{\mathrm{R/A}}(\omega)\mathbf{\Sigma}^{\mathrm{R/A}}(\omega)\mathbf{G}^{\mathrm{R/A}}(\omega) \; . \tag{2.3.1.10}$$

By evaluating both the external time-arguments of the Green's function on Matsubara contour we find that the Matsubara component also obeys a closed Dyson equation. Using the KMS boundary conditions (Eqs 2.3.1.6), it can be shown that, at equilibrium, the Matsubara component is anti-periodic with a period given by the inverse temperature, β. This follows from the relation: $\mathcal{G}^{\mathrm{M}}(0) = -\mathcal{G}^{\mathrm{M}}(\beta)$. Therefore, the Matsubara component can be expanded as a Fourier series with respect to the discrete Matsubara frequencies, $i\omega_n = \frac{(2n+1)i\pi}{\beta}$. This gives rise to the closed Matsubara Dyson equation [13–17]:

$$\mathcal{G}^{\mathrm{M}}(i\omega_n) = \mathcal{G}_0^{\mathrm{M}}(i\omega_n) + \mathcal{G}_0^{\mathrm{M}}(i\omega_n)\Sigma^{\mathrm{M}}(i\omega_n)\mathcal{G}^{\mathrm{M}}(i\omega_n) \ . \tag{2.3.1.11}$$

As we will demonstrate in subsection 2.3.3, the fact that the retarded, advanced and Matsubara components all form closed Dyson equations on the contour is the origin for the analytic continuation connection between the Matsubara and retarded/advanced Green's functions. This is also why analytic continuation cannot be used to directly obtain the time-ordered Green's function from the Matsubara component.

However, at equilibrium and at *zero temperature* the time-ordered Dyson equation closes as $\mathbf{G}^{>}(\omega)\mathbf{\Sigma}^{<}(\omega) = \mathbf{G}^{<}(\omega)\mathbf{\Sigma}^{>}(\omega) = 0$ [29]. This can be seen directly from the analytical structure of the Green's function and self-energy at zero temperature and is a result of the detailed balance condition [29]. As a result, we can write the zero temperature Dyson equation, at equilibrium, for the time-ordered Green's function as

$$\mathbf{G}^{\mathrm{T}}(\omega) = \mathbf{G}_0^{\mathrm{T}}(\omega) + \mathbf{G}_0^{\mathrm{T}}(\omega)\mathbf{\Sigma}^{\mathrm{T}}(\omega)\mathbf{G}^{\mathrm{T}}(\omega) \ . \tag{2.3.1.12}$$

Therefore, at equilibrium and at zero temperature, the integrals over the backward branch, γ_+, of the Keldysh contour vanish and so the contour integrations can simply be restricted to the forward, real-time-ordered branch. This remarkable result connects directly with the conventional zero temperature Gell-Mann and Low formulation presented in Subsection 2.2.3 and Refs [13–15].

The fact that, at finite temperatures, the time-ordered Dyson equation is not closed means that we will focus our analysis on the Matsubara and retarded components. However, at equilibrium and zero temperature, for simplicity we will focus on the time-ordered Green's function.

2.3.2 Lehmann representation at zero temperature

At equilibrium and at zero temperature, the single-particle Green's function depends only on the time difference. Using Eq. 2.3.0.3a, the real time-ordered Green's function is given by

$$G^{\mathrm{T}}_{pq}(t,t') = \theta(t-t')G^{>}_{pq}(t,t') + \theta(t'-t)G^{<}_{pq}(t,t') \ , \tag{2.3.2.1}$$

where the greater and lesser components are defined as

$$G^{>}_{pq}(t,t') = -i \left\langle \Psi_0 | a_p e^{-iH(t-t')} a^\dagger_q | \Psi_0 \right\rangle e^{iE^N_0(t'-t)} \tag{2.3.2.2a}$$

$$G^{<}_{pq}(t,t') = i \left\langle \Psi_0 | a^\dagger_q e^{-iH(t'-t)} a_p | \Psi_0 \right\rangle e^{iE^N_0(t-t')} \ . \tag{2.3.2.2b}$$

Resolving the complete set of $(N \pm 1)$-particle eigenstates of the Hamiltonian in Eqs 2.3.2.2 and taking the Fourier transform of Eq. 2.3.2.1 yields the Lehmann representation of the time-ordered Green's function:

$$G^{\mathrm{T}}_{pq}(\omega) = \lim_{\eta \to 0^+} \left(\sum_\mu \frac{(Y^\mu_p)^* Y^\mu_q}{\omega - \varepsilon^{N+1}_\mu + i\eta} + \sum_\nu \frac{X^\nu_p (X^\nu_q)^*}{\omega - \varepsilon^{N-1}_\nu - i\eta} \right) \ , \tag{2.3.2.3}$$

where $Y^{\mu *}_p = \langle \Psi_0 | a_p | \Psi^{N+1}_\mu \rangle$ and $X^\nu_p = \langle \Psi^{N-1}_\nu | a_p | \Psi_0 \rangle$. The poles of the zero temperature propagator are given by $\varepsilon^{N+1}_\mu = E^{N+1}_\mu - E^N_0$ and $\varepsilon^{N-1}_\nu = E^N_0 - E^{N-1}_\nu$ and correspond to the exact removal and addition energies of the system, respectively. The appearance of the infinitesimal η in the denominators of Eq. 2.3.2.3 is necessary in order to converge the Fourier transform. In the rest of this thesis, the implicit limit as $\eta \to 0$ will be dropped for notational clarity. As can be seen, the poles of the time-ordered Green's function lie above and below the real frequency axis. The retarded/advanced propagators are found by simply placing all the poles of the time-ordered Green's function below/above the real axis. The Fourier transform of the greater and lesser components give

$$G^{>}_{pq}(\omega) = -2\pi i \sum_\mu (Y^\mu_p)^* Y^\mu_q \delta(\omega - \varepsilon^{N+1}_\mu) \tag{2.3.2.4a}$$

$$G^{<}_{pq}(\omega) = 2\pi i \sum_\nu X^\nu_p (X^\nu_q)^* \delta(\omega - \varepsilon^{N-1}_\nu) \ . \tag{2.3.2.4b}$$

Finally, the Lehmann representation of the non-interacting Green's function is given by

$$G^{0,\mathrm{T}}_{pq}(\omega) = \delta_{pq} \left(\frac{\bar{n}_p}{\omega - \epsilon_p + i\eta} + \frac{n_p}{\omega - \epsilon_p - i\eta} \right) \ , \tag{2.3.2.5}$$

where $\bar{n}_p = 1 - n_p$ and $n_p = 1$ if p corresponds to a state that is occupied in the reference determinant $|\Phi_0\rangle$, and zero otherwise. The non-interacting retarded/advanced propagator is simply

$$G_{pq}^{0,\mathrm{R/A}}(\omega) = \frac{\delta_{pq}}{\omega - \epsilon_p \pm i\eta} \ . \tag{2.3.2.6}$$

2.3.3 Lehmann representation at finite temperature

At equilibrium and at finite temperature, the Green's function also admits a Lehmann representation. Using Eq. 2.3.0.3e, we find the Matsubara component as

$$\mathcal{G}_{pq}^{\mathrm{M}}(\tau, \tau') = \theta(\tau - \tau') G_{pq}^{>}(\tau, \tau') + \theta(\tau' - \tau) G_{pq}^{<}(\tau, \tau'), \tag{2.3.3.1}$$

where the imaginary-time greater and lesser components are defined as

$$G_{pq}^{>}(\tau, \tau') = -i \sum_n \rho_n \langle \Psi_n | a_p e^{-(H^{\mathrm{M}} - E_n^{\mathrm{M}})(\tau - \tau')} a_q^\dagger | \Psi_n \rangle \tag{2.3.3.2a}$$

$$G_{pq}^{<}(\tau, \tau') = +i \sum_n \rho_n \langle \Psi_n | a_q^\dagger e^{-(H^{\mathrm{M}} - E_n^{\mathrm{M}})(\tau' - \tau)} a_p | \Psi_n \rangle \ , \tag{2.3.3.2b}$$

with $\rho_n = \frac{e^{-\beta E_n^{\mathrm{M}}}}{Z}$ and $E_n^{\mathrm{M}} = E_n - \mu N_n$. As $[H^{\mathrm{M}}, H] = 0$, we can choose the eigenstates of H^{M} such that they are also eigenstates of H with eigenvalue, E_n. From the KMS boundary conditions (Eq. 2.3.1.6), we know that the Matsubara component is anti-periodic and therefore can be represented as a Fourier series over the Matsubara frequencies. Therefore, resolving the identity of eigenstates of H^M and taking the Fourier component, we can write the Matsubara component as [13, 16, 17]

$$\mathcal{G}_{pq}^{\mathrm{M}}(i\omega_m) = \sum_{nl} \frac{\langle \Psi_n | a_p | \Psi_l \rangle \langle \Psi_l | a_q^\dagger | \Psi_n \rangle}{i\omega_m + \mu - (E_l - E_n)} \Big(\rho_n + \rho_l \Big) \ . \tag{2.3.3.3}$$

Importantly, the only non-zero terms in this summation are for the states where $N_l - N_n = 1$. However, in contrast to the zero temperature formulation, the Green's function at finite temperature is defined as an ensemble average and so the Lehmann representation does not cleanly split into an addition and removal part. The poles, $E_l - E_n$, instead correspond to removal and addition energies of the system defined within the GCE as $N_l - N_n = 1$. It is important to note that the poles are temperature-independent and that the temperature-dependence of the propagator is contained entirely in its residues.

Similarly, we can obtain the Lehmann representation of the retarded/advanced Green's function as [13–16]

$$G_{pq}^{\mathrm{R/A}}(\omega) = \sum_{nl} \frac{\langle \Psi_n | a_p | \Psi_l \rangle \langle \Psi_l | a_q^\dagger | \Psi_n \rangle}{\omega + \mu - (E_l - E_n) \pm i\eta} \Big(\rho_n + \rho_l \Big) \ . \tag{2.3.3.4}$$

Here, we clearly see the relationship between the Matsubara (Eq. 2.3.3.3) and retarded/advanced components at finite temperatures. It is straightforward to see that analytically continuing $i\omega_m \to \omega + i\eta$ for the Matsubara component gives the retarded component. Therefore, we can introduce a general Green's function $G(s)$, where $s \in \mathbb{C}$ is now a complex frequency argument, that is analytic everywhere except on the real axis and at the Matsubara frequencies. From the general Green's function, we can obtain the different Matsubara/retarded/advanced components from the relations:

$$G_{pq}(s) = \left\{ \begin{array}{ll} G_{pq}(i\omega_m) & = \mathcal{G}_{pq}^{\mathrm{M}}(i\omega_m) \\ G_{pq}(\omega + i\eta) & = G_{pq}^{\mathrm{R}}(\omega) \\ G_{pq}(\omega - i\eta) & = G_{pq}^{\mathrm{A}}(\omega) \end{array} \right\} \ . \tag{2.3.3.5}$$

This analytic continuation between the Matsubara and retarded/advanced components is a direct reflection of that fact that both components obey closed Dyson equations (see Eqs 2.3.1.10 and 2.3.1.11). As a result, no similar direct relationship can be established for the time-ordered Green's function at finite temperature as it does not obey a closed Dyson equation. Using these relationships, we can write the analytically continued finite temperature Dyson equation as

$$\mathbf{G}(s) = \mathbf{G}_0(s) + \mathbf{G}_0(s)\mathbf{\Sigma}(s)\mathbf{G}(s) \tag{2.3.3.6}$$

where the analytically continued self-energy is defined as:

$$\Sigma_{pq}(s) = \left\{ \begin{array}{ll} \Sigma_{pq}(i\omega_m) & = \Sigma_{pq}^{\mathrm{M}}(i\omega_m) \\ \Sigma_{pq}(\omega + i\eta) & = \Sigma_{pq}^{\mathrm{R}}(\omega) \\ \Sigma_{pq}(\omega - i\eta) & = \Sigma_{pq}^{\mathrm{A}}(\omega) \end{array} \right\} \ . \tag{2.3.3.7}$$

At finite temperatures, Eq. 2.3.3.6 is the unified Dyson equation we will work with in this thesis. It is also useful to write the Lehmann representation of the analytically continued Green's function as:

$$G_{pq}(s,T) = \sum_{nl} \frac{\mathcal{X}_p^{nl}(T)\mathcal{X}_q^{nl*}(T)}{s - \omega_{nl}} \ , \tag{2.3.3.8}$$

where $\mathcal{X}_p^{nl}(T) = \langle \Psi_n | a_p | \Psi_l \rangle \sqrt{\rho_n + \rho_l}$, and $\omega_{nl} = E_l - E_n - \mu$. This makes the temperature-dependence of the propagator explicit and will be useful in the Dyson supermatrix

formulation in Section 2.6. The exact spectral representation of the finite temperature single-particle Green's function given in given in Eq. 2.3.3.8 is not commonly stated in the literature.

Finally, the non-interacting Green's function at finite temperature is given by

$$G^0_{pq}(s,T) = \frac{\delta_{pq}}{s-\xi_p} \tag{2.3.3.9}$$

where $\xi_p = \epsilon_p - \mu$. It is interesting to note that this propagator is temperature-independent, whereas the non-interacting 'lesser' and 'greater' components are explicitly temperature dependent [14, 17]:

$$G^{0,<}_{pq}(s,T) = \delta_{pq} 2\pi i f(\xi_p)\delta(s-\xi_p) \tag{2.3.3.10a}$$

$$G^{0,>}_{pq}(s,T) = -\delta_{pq} 2\pi i (1-f(\xi_p))\delta(s-\xi_p)\ . \tag{2.3.3.10b}$$

Here, the temperature-dependence enters through the Fermi-Dirac distribution: $f(\omega) = (e^{\beta\omega}+1)^{-1}$.

2.3.4 Relationship to physical observables

In general, knowledge of the single-particle Green's function gives access to the expectation value of any one-body operator, the exact addition and removal spectrum as well as the spectral function. For the case where the interaction Hamiltonian is a two-body operator, the Green's function also gives the exact ground state energy.

One-body observables:

We can immediately identify the one-particle reduced density matrix from the single-particle Green's function using Eq. 2.3.0.3c to give

$$\Gamma_{pq}(t) = -iG^<_{qp}(t,t) = \mathrm{Tr}\left\{\rho_{\mathrm{eq}} a^\dagger_p(t) a_q(t)\right\}\ . \tag{2.3.4.1}$$

At finite temperature and at equilibrium, this relationship gives

$$\Gamma_{pq} = -iG^<_{qp}(t,t) = -i\mathcal{G}^{\mathrm{M}}_{qp}(\tau,\tau^+) = \mathrm{Tr}\left\{\rho_{\mathrm{eq}} a^\dagger_p a_q\right\}\ . \tag{2.3.4.2}$$

Therefore, we can define the expectation value of any one-body observable in terms of the single-particle Green's function as

$$\langle O(z)\rangle = -i\sum_{pq} o_{pq}(z) G^<_{qp}(z,z)\ . \tag{2.3.4.3}$$

Spectral function:

At equilibrium, the single-particle Green's function gives the spectral function from the identity

$$\begin{aligned}\mathcal{A}_{pp}(\omega) &= \frac{i}{2\pi}\left[G^{\mathrm{R}}_{pp}(\omega) - G^{\mathrm{A}}_{pp}(\omega)\right] = \frac{i}{2\pi}\left[G^{>}_{pp}(\omega) - G^{<}_{pp}(\omega)\right] \\ &= -\frac{1}{\pi}\mathrm{Im}G^{\mathrm{R}}_{pp}(\omega) \geq 0 \ .\end{aligned} \tag{2.3.4.4}$$

It is important to note that the spectral function is guaranteed to be positive semi-definite [17]. Using the exact definitions derived in subsections 2.3.2 and 2.3.3, we can re-write the exact spectral function at zero and finite temperatures as

$$\mathcal{A}_{pp}(\omega) = \begin{cases} \left(\sum_\mu |Y^\mu_p|^2\delta(\omega - \varepsilon^{N+1}_\mu) + \sum_\nu |X^\nu_p|^2\delta(\omega - \varepsilon^{N-1}_\nu)\right) & (T=0) \\ \sum_{nl} |\mathcal{X}^{nl}_p|^2\delta(\omega - \omega_{nl}) & (T\neq 0) \end{cases} . \tag{2.3.4.5}$$

Using the definitions in Eq. 2.3.4.5, it is straightforward to show that the spectral function is normalized to one:

$$\int_{-\infty}^{\infty} d\omega \mathcal{A}_{pp}(\omega) = 1 \ . \tag{2.3.4.6}$$

Ground state energy:

Using the contour equation-of-motion for the Green's function (Eq. 2.3.1.1), for a two-body interaction Hamiltonian, we can obtain the exact ground state energy as

$$E(z_1) = -\frac{i}{2}\sum_{pr}\left(i\frac{\partial}{\partial z_1}\delta_{pr} + h_{pr}(z_1)\right)G^{<}_{rp}(z_1, z_1) \tag{2.3.4.7}$$

Using the definition of the irreducible self-energy, we can re-write this equation as

$$E(z_1) = -i\sum_{pq} h_{pq}(z_1)G^{<}_{qp}(z_1, z_1) + \frac{1}{2i}\sum_{pr}\int_\gamma \Sigma_{pr}(z_1, z_3)G(z_3, z_1^+) \ . \tag{2.3.4.8}$$

At equilibrium, we can use this equation to write the Galitskii-Migdal formula for the ground state energy

$$E = \begin{cases} -i\sum_{pq} h_{pq}G^{<}_{qp}(t,t) + \frac{1}{2}\lim_{\eta\to 0}\sum_{pr}\int_{-\infty}^{\infty}\frac{d\omega}{2\pi i}e^{i\eta\omega}\Sigma^{\mathrm{T}}_{pr}(\omega)G^{\mathrm{T}}_{rp}(\omega) & (T=0) \\ -i\sum_{pq} h_{pq}G^{<}_{qp}(t,t) + \frac{1}{2i}\lim_{\eta\to 0}\sum_{pr}\sum_{i\omega_n} e^{\eta i\omega_n}\Sigma^{\mathrm{M}}_{pr}(i\omega_n)\mathcal{G}^{\mathrm{M}}_{rp}(i\omega_n) & (T\neq 0) \end{cases} , \tag{2.3.4.9}$$

which is time-independent. However, for systems governed by interaction Hamiltonians that contain higher-body interactions, the exact ground state energy cannot be obtained from the single-particle Green's function [20, 30].

2.3.5 Differences between finite and continuous systems

For simplicity, in this subsection we restrict our analysis to systems at equilibrium at zero temperature. However, the general conclusions are also valid for systems at finite temperatures. In finite closed systems such as nuclear, atomic and molecular systems, the single-particle Green's function has a simple structure. It is a meromorphic function that has simple poles at the exact, discrete charged excitation energies of the system [13]. This can be seen by using the Dirac identity: $\lim_{\eta\to 0^+} \frac{1}{\omega \pm i\eta} = \mathcal{PV}(\frac{1}{\omega}) \mp i\pi\delta(\omega)$ [13–17], to find the imaginary part of the Green's function as

$$\begin{aligned} -\frac{1}{\pi}\mathrm{Im}G^{\mathrm{R}}_{pp}(\omega) = &\sum_{\mu} \left| \langle \Psi^{N+1}_{\mu} | a^{\dagger}_{p} | \Psi_0 \rangle \right|^2 \delta(\omega - \varepsilon_{\mu}) \\ &+ \sum_{\nu} \left| \langle \Psi^{N-1}_{\nu} | a_{p} | \Psi_0 \rangle \right|^2 \delta(\omega - \varepsilon_{\nu}) \ . \end{aligned} \tag{2.3.5.1}$$

Clearly, as the summations in Eq. 2.3.5.1 are over discrete eigenstates of the system, the imaginary part of the Green's function is zero when ω is away from the poles. This is because the poles correspond to bound states which have an infinite lifetime and thus the imaginary part effectively represents a Fourier mode decomposition of the discrete excitation energies of the system. This is fundamentally a result of reversible unitary evolution of a finite system that occurs with no energy loss.

For systems in the thermodynamic limit, such as infinite solids, the pole structure of the Green's function fundamentally changes. This is due to the fact that the eigenstates of the Hamiltonian can take a continuous range of energies. As a result, the single-particle Green's function develops a *discontinuity* along the real axis. This can be viewed as the merging of an infinite number of discrete poles to form a continuous energy structure. Therefore, the Green's function is no longer a single valued function. In order to ensure that the Green's function remains single-valued in the complex plane, we introduce a *branch cut* exactly where the range of continuum energy eigenstates occurs. To demonstrate this clearly, we write the expression for the retarded Green's function in terms of its imaginary part:

$$G^{\mathrm{R}}_{pp}(\omega) = \int_{-\infty}^{\infty} d\omega' \frac{\mathcal{A}_{pp}(\omega')}{\omega - \omega' + i\eta} = -\int_{-\infty}^{\infty} \frac{d\omega'}{\pi} \frac{\mathrm{Im}G^{\mathrm{R}}_{pp}(\omega')}{\omega - \omega' + i\eta} \ , \tag{2.3.5.2}$$

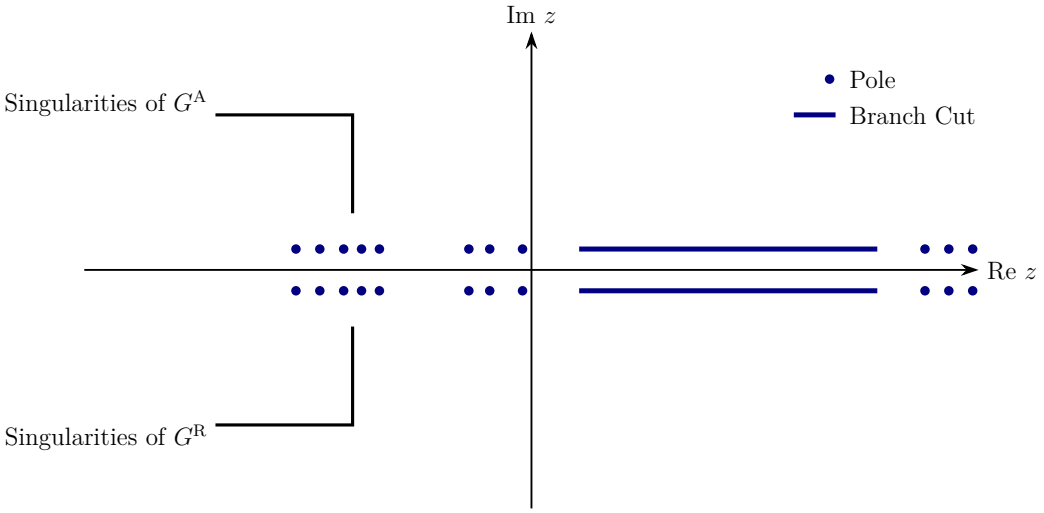

Figure 2.5: Singularity structure in the complex plane showing poles and branch cuts of the Green's function.

where the imaginary part is now given by the integral over the continuous eigenstates of the Hamiltonian:

$$\begin{aligned} -\frac{1}{\pi}\mathrm{Im}G^{\mathrm{R}}_{pp}(\omega) = &\int d\alpha \left| \langle \Psi^{N+1}_{\alpha} | a^{\dagger}_{p} | \Psi_0 \rangle \right|^2 \delta(\omega - \varepsilon_{\alpha}) \\ &+ \int d\beta \left| \langle \Psi^{N-1}_{\beta} | a_{p} | \Psi_0 \rangle \right|^2 \delta(\omega - \varepsilon_{\beta}) \ . \end{aligned} \tag{2.3.5.3}$$

It is important to note that Eq. 2.3.5.2 is a Kramers-Kronig relation that states that the propagator is *completely determined* by the structure of its imaginary part [31, 32]. As Eq. 2.3.5.3 involves an integral over the continuous eigenstates of the Hamiltonian, the imaginary part of the Green's function becomes a finite and smooth function over regions of ω. This is directly because the energy conservation condition enforced by the Dirac delta distributions can be satisfied by infinitely many nearby states, thereby giving rise to irreversible decay and the non-unitary evolution of states. This is fundamentally different from the imaginary part of the propagator obtained for finite closed systems, which is a discontinuous function that vanishes away from the simple poles. In Figure 2.5, we plot the pole structure of the Green's function in the general case where both bound state solutions and continuous branch cuts are present.

To further demonstrate how the continuum gives rise to the branch cut structure of the Green's function, we provide a simple example here of a single flat band model. In this case, the spectral function can be written as $\mathcal{A}(\omega) = \frac{1}{2W}\theta(W - |\omega|)$, where W is the width of the band. In this case, using the Kramers-König relation (Eq. 2.3.5.2)

the general Green's function becomes

$$G(s) = \int_{-\infty}^{\infty} d\omega' \frac{1}{2W} \frac{\theta(W - |\omega'|)}{s - \omega'} = \frac{1}{2W} \log\left(\frac{s + W}{s - W}\right) . \tag{2.3.5.4}$$

It is clear that $G(s)$ has developed a discontinuity on the real axis ($s = \omega$), where the complex logarithm jumps by $2\pi i$. This discontinuity is exactly the spectral function: $\mathcal{A}(\omega) \sim G(\omega + i\eta) - G(\omega - i\eta)$. In order to tame the multivalued complex logarithm, we introduce a logarithmic branch cut for the Green's function along the interval $[-W, W]$. Using Eq. 2.3.3.5, we identify the retarded Green's function as

$$\begin{aligned} G^{\mathrm{R}}(\omega) &= \frac{1}{2W} \log\left(\frac{\omega + W + i\eta}{\omega - W + i\eta}\right) \\ &= \frac{1}{2W} \log\left|\frac{\omega + W}{\omega - W}\right| - i\frac{\pi}{2W}\theta(W - |\omega|) . \end{aligned} \tag{2.3.5.5}$$

It is straightforward to see that this expression exactly recovers the continuous spectral function from $-\frac{1}{\pi}\mathrm{Im}G^{\mathrm{R}}(\omega)$ and demonstrates the emergence of the branch cut structure of the Green's function for continuous systems.

2.4 Diagrammatic expansion of the irreducible self-energy

Using the GML theorem (Eq. 2.2.3.8), the perturbation expansion for the single-particle Green's function can be written as

$$G_{pq}(z_1, z_2) = \frac{\left\langle \mathcal{T}_\gamma \left\{ e^{-i\int_\gamma dz H(z)} a_p(z_1) a_q^\dagger(z_1) \right\} \right\rangle}{\left\langle \mathcal{T}_\gamma \left\{ e^{-i\int_\gamma dz H(z)} \right\} \right\rangle} \tag{2.4.0.1}$$

where all operators are defined in the Interaction picture and on the adiabatic contours depicted in subsection 2.2.3. By utilizing Wick's theorem [33] and Goldstone's linked cluster theorem [34] on the contour, it can be shown that Eq. 2.4.0.1 can be simplified to restricting the perturbative expansion to containing only the 'connected' terms, $\mathcal{C}$ [16, 17]:

$$G_{pq}(z_1, z_2) = \left\langle \mathcal{T}_\gamma \left\{ e^{-i\int_\gamma dz H(z)} a_p(z_1) a_q^\dagger(z_1) \right\} \right\rangle_{\mathcal{C}} . \tag{2.4.0.2}$$

Therefore, Eq. 2.4.0.2 represents an infinite-order Feynman diagrammatic expansion for the propagator in terms of diagrams that are fully connected. The number of diagrams (terms) generated by Eq. 2.4.0.2 at each order can be further reduced by collecting all *one-particle irreducible* (1PI) diagrams in the expansion. 1PI diagrams are diagrams that cannot be

divided into different sub-diagrams by cutting a single propagator line and their complete set defines the perturbative expansion for the irreducible self-energy kernel, $\Sigma_{pq}(z_1, z_2)$. By construction, the set of 1PI used to construct the irreducible self-energy is expressed with respect to the non-interacting Green's function G_0, and corresponding interaction vertices of the Hamiltonian normal-ordered with respect to the reference expectation value associated with G_0. All reducible diagrams are then generated by the geometric Dyson series

$$G_{pq}(z_1, z_2) = G^0_{pq}(z_1, z_2) + \sum_{rs} \int_\gamma dz_3 dz_4 G^0_{pr}(z_1, z_3)\Sigma_{rs}(z_3, z_4)G_{sq}(z_4, z_1) \ . \tag{2.4.0.3}$$

This equation is of the exact same form as Eq. 2.3.1.1 except it has been derived in the context of perturbation theory instead from the exact equation-of-motion. The beauty of the Dyson equation is that it allows us to move away from direct Green's function perturbation theory and instead focus on the reduced set of diagrams that constitute the self-energy [35]. At equilibrium, we can take the Fourier transform of Eq. 2.4.0.3 and obtain perturbative Dyson equations for the Green's function components presented in subsection 2.3.1. Formulation of the diagrammatic expansion of the irreducible self-energy on the Keldysh contour allows us to obtain all components of the self-energy through the Langreth rules.

The set of 1PI diagrams of the self-energy means that it can be expressed as a functional of the non-interacting Green's function, $\Sigma[G_0]$. The definition of the self-energy given in Eq. 2.3.1.3 corresponds to the self-consistent representation whereby the self-energy is expressed as a functional of the exact Green's function, $\Sigma[G]$. In terms of the diagrammatic representation, the self-consistent self-energy expansion restricts it to be composed of diagrams that are 1PI, skeleton and interaction-irreducible [17, 20, 30, 36, 37]. Skeleton diagrams are self-energy diagrams that cannot be separated into two pieces by cutting a single fermion line twice at two different points [17, 20]. Interaction-irreducible diagrams are self-energy diagrams that are constructed from the effective interactions that arise when normal-ordering the Hamiltonian with respect to the exact density matrix [20, 36]. Expressing the self-energy with respect to the exact Green's function considerably reduces the number of diagrams constituting the self-energy expansion and is commonly referred to as *self-consistent renormalization*. This will be explicitly demonstrated in Chapter 3, where we extend the conventional hermitian Green's function formulation to account for non-hermitian interactions.

In the context of the two-body electronic structure problem, Hedin's equations constitute a closed set of equations for the self-consistent expansion for the electronic self-energy functional: $\Sigma[G]$ [38]. Using Schwinger's functional derivative technique [39], which involves the introduction of a fictitious local external potential (ϕ) that couples to the electronic density, Hedin derived a set of five coupled integro-differential equations to determine the electronic Green's function. They are given by (see Appendix C.1):

$$G(1,2) = G_0(1,2) + \int d3d4\ G_0(1,3)\Sigma(3,4)G(4,2) \tag{2.4.0.4a}$$

$$W(1,2) = v(1,2) + \int d3d4\ v(1,3)P(3,4)W(4,2) \tag{2.4.0.4b}$$

$$\Sigma(1,2) = i\int d3d4\ W(1,3)G(1,4)\Gamma(3,2;4) \tag{2.4.0.4c}$$

$$P(1,2) = -i\int d3d4\ G(1,3)G(4,1)\Gamma(3,4;2) \tag{2.4.0.4d}$$

$$\Gamma(1,2;3) = \delta(1,3)\delta(2,3) + \int d4d5d6d7\ \frac{\delta\Sigma(1,2)}{\delta G(5,4)}G(4,6)G(7,5)\Gamma(6,7;3) \tag{2.4.0.4e}$$

where $1 \equiv (\mathbf{x}_1, z_1)$ represents the composite spin-space-time coordinate, W represents the screened electronic interaction induced by the electronic polarization P, and Γ is the interaction vertex, explicitly defined as

$$\Gamma(1,2;3) = -\frac{\delta G^{-1}(1,2)}{\delta u_{\mathrm{cl}}(3)} \tag{2.4.0.5}$$

with $u_{\mathrm{cl}} = \phi + v_H$ is the sum of the total classical potential experienced by the electrons, being composed of the sum of the fictitious local external potential and the induced Hartree potential. Hedin's equations give rise to the famous GW approximation when the vertex is taken to be the identity $\Gamma(1,2;3) \approx \delta(1,3)\delta(2,3)$:

$$\Sigma_{GW}(1,2) = iG(1,2)W(1.2)\ . \tag{2.4.0.6}$$

2.5 Exact algebraic properties of the self-energy

In many-body field theory, the irreducible self-energy has equal importance alongside the single-particle Green's function. Through the Dyson equation, an approximation for the self-energy defines the corresponding approximation for the single-particle Green's function. This is also continued to the two-particle Green's function and so on through the functional-diagrammatic relationships of quantum field theory. The self-energy is a function in Keldysh

space and, at equilibrium, is composed of a static component and a dynamical contribution

$$\Sigma_{pq}(z_1, z_2) = \Sigma^{\infty}_{pq}\delta(z_1, z_2) + \theta(z_1, z_2)\Sigma^{>}_{pq}(z_1, z_2) + \theta(z_2, z_1)\Sigma^{<}_{pq}(z_1, z_2) \ , \tag{2.5.0.1}$$

where Σ^{∞}_{pq} is the static component and $\Sigma^{\lessgtr}$ are the lesser/greater components of the self-energy, respectively. From the exact relationships derived in Section 2.3, at equilibrium, it was demonstrated that the Matsubara and retarded/advanced components of the single-particle Green's function and self-energy can be connected by analytic continuation. This means that we can obtain the Matsubara component from the advanced/retarded component and vice-versa. Therefore, we simply restrict our analysis to either the real-time or the Matsubara sector.

Due to its connection to the single-particle Green's function through the Dyson equation, the self-energy also has a spectral Lehmann representation given by [40, 41]

$$\Sigma_{pq}(s) = \Sigma^{\infty}_{pq} + \int_{-\infty}^{\infty} d\omega' \frac{\Gamma_{pq}(\omega')}{s - \omega'} \ , \tag{2.5.0.2}$$

where we have introduced the scattering function as

$$\begin{aligned} \Gamma_{pq}(\omega) &= \frac{i}{2\pi}\left(\Sigma^{>}_{pq}(\omega) - \Sigma^{<}_{pq}(\omega)\right) = \frac{i}{2\pi}\left(\Sigma^{\mathrm{R}}_{pq}(\omega) - \Sigma^{\mathrm{A}}_{pq}(\omega)\right) \\ &= -\frac{1}{\pi}\mathrm{Im}\Sigma^{\mathrm{R}}_{pq}(\omega) \ . \end{aligned} \tag{2.5.0.3}$$

Eq. 2.5.0.2 is therefore another Kramers-Kronig relation that implies that the dynamical component of the self-energy is determined entirely by the structure of its imaginary part. It is straightforward to demonstrate that $\Gamma_{pq}(\omega) = \Gamma^{*}_{qp}(\omega)$, such that $\Gamma_{pp}(\omega) \geq 0$. The positive semi-definite property of Γ requires the imaginary part of the retarded self-energy to be negative semi-definite

$$\mathrm{Im}\Sigma^{\mathrm{R}}_{pp}(\omega) \leq 0 \ . \tag{2.5.0.4}$$

This condition is necessary in order to maintain the proper causal structure of the theory as well as to ensure the positive semi-definite property of the spectral function $\mathcal{A}$. This can be seen from the exact relationship between the spectral function and the self-energy [17]

$$\begin{aligned} \mathcal{A}_{pp}(\omega) &= \sum_{rs} G^{\mathrm{R}}_{pr}(\omega)\Gamma_{rs}(\omega)G^{\mathrm{A}}_{sp}(\omega) \\ &= -\frac{1}{\pi}\sum_{rs} G^{\mathrm{R}}_{pr}(\omega)\mathrm{Im}\Sigma^{\mathrm{R}}_{rs}(\omega)G^{\mathrm{A}}_{sp}(\omega) \geq 0 \ . \end{aligned} \tag{2.5.0.5}$$

Writing the spectral decomposition for the imaginary part of the self-energy, making the temperature-dependence explicit, we have

$$\Gamma_{pq}(\omega, T) = \sum_{\lambda} (v_p^{\lambda}(T))^* v_q^{\lambda}(T) \delta(\omega - \sigma_{\lambda}) + \sum_{\delta} u_p^{\delta}(T) (u_q^{\delta}(T))^* \delta(\omega - \sigma_{\delta}) \ . \tag{2.5.0.6}$$

Using the Kramers-Kronig relation of Eq. 2.5.0.2, we can immediately write the exact spectral representation of the self-energy as [35, 36, 41, 42]

$$\Sigma_{pq}(s, T) = \Sigma_{pq}^{\infty}(T) + \sum_{\lambda} \frac{(v_p^{\lambda}(T))^* v_q^{\lambda}(T)}{s - \sigma_{\lambda}} + \sum_{\delta} \frac{u_p^{\delta}(T) (u_q^{\delta}(T))^*}{s - \sigma_{\delta}} \ . \tag{2.5.0.7}$$

Here we have provided an explicit representation of the self-energy at finite temperature. In general, the poles ($\sigma_{\lambda}/\sigma_{\delta}$) and amplitudes ($v_p^{\lambda}(T)/u_p^{\delta}(T)$) of the self-energy cannot be directly related to physical quantities [35, 41]. Importantly, the indices λ/δ are composite and are connected to the excited state configurations of the system. Therefore, they span a configuration space outside of the single-particle subspace indexed by $\{p, q, \cdots\}$. By unitary transformation, we can write this expression in the non-diagonal form as [35, 41, 43]

$$\Sigma_{pq}(s, T) = \Sigma_{pq}^{\infty}(T) + \sum_{PP'} M_{pP}^{\dagger}(T) \, (s\mathbb{1} - \mathbf{\Lambda})_{PP'}^{-1} \, M_{P'q}(T) + \sum_{PP'} N_{pP}(T) \, (s\mathbb{1} - \mathbf{\Gamma})_{PP'}^{-1} \, N_{P'q}^{\dagger}(T) \tag{2.5.0.8}$$

where $\mathbf{M}_p(T) = \mathbf{U}\mathbf{v}_p(T)$, $\mathbf{N}_p(T) = \mathbf{V}^{\dagger}\mathbf{u}_p(T)$ and $\mathbf{\Lambda} = \mathbf{U}\sigma\mathbf{U}^{\dagger}$, $\mathbf{\Gamma} = \mathbf{V}^{\dagger}\sigma\mathbf{V}$ define the unitary transformation between the diagonal and non-diagonal representation of the self-energy. In the non-diagonal representation, the indices PP' label multi-particle-hole Intermediate State Configurations (ISCs) [35, 41]. ISCs represent states which mediate between the exact eigenstates of the Hamiltonian and the particle configurations resulting from excitation with respect to the ensemble 'ground' state. In general, the indices PP' are composed of different particle, hole and momenta character and they conserve the associated scattered momenta between the excited configurations. In the case of the electronic self-energy, they are associated with excited state configurations containing $(N \pm 1)$-particles relative to the ground state. The $\mathbf{\Lambda}_{PP'}$ and $\mathbf{\Gamma}_{PP'}$ matrices represent the interactions between the different ISCs. The coupling matrices, $\mathbf{M}/\mathbf{N}$, link the initial and final single-particle states to the ISCs, thereby allowing the dynamical self-energy to be coupled to many-body interactions. From the Lehmann representation of the finite-temperature Green's function (Eq. 2.3.3.8), it can be seen that the coupling matrices are temperature-dependent, whereas the interaction matrices are temperature-independent.

At zero temperature, due to the corresponding Lehmann representation of the Green's function, the self-energy Lehmann representation splits into definite $(N \pm 1)$-particle parts. Therefore, we can restrict the summations in Eq. 2.5.0.8 to be only over forward-time (JJ') and backward-time (AA') ISCs. The forward-time (JJ') indices are associated with excited configurations containing $(N+1)$-particles, while the backward-time (AA') indices correspond to excited configurations containing $(N-1)$-particles. Using this notation, at zero temperature, we have

$$\Sigma_{pq}(s) = \Sigma^{\infty}_{pq} + \sum_{JJ'} U^{\dagger}_{pJ} \left(s\mathbb{1} - (\mathbf{K}^{>} + \mathbf{C}^{>})\right)^{-1}_{JJ'} U_{J'q} + \sum_{AA'} V_{pA} \left(s\mathbb{1} - (\mathbf{K}^{<} + \mathbf{C}^{<})\right)^{-1}_{AA'} V^{\dagger}_{A'q} \ . \tag{2.5.0.9}$$

Here, we have decomposed the interaction matrices to be composed of either entirely forward-time or backward-time interactions: $\mathbf{\Lambda} \to \mathbf{K}^{>} + \mathbf{C}^{>}$ and $\mathbf{\Gamma} \to \mathbf{K}^{<} + \mathbf{C}^{<}$. In general, the $\mathbf{K}^{\lessgtr}$-matrices are block diagonal by definition and the $\mathbf{C}^{\lessgtr}$-matrices contain off-diagonal contributions [41]. Similarly, we restrict the coupling matrices to be composed entirely of 'forward'-time and 'backward'-time contributions: $\mathbf{M} \to \mathbf{U}$ and $\mathbf{N} \to \mathbf{V}$.

2.6 Dyson supermatrix formulation

The Dyson equation at equilibrium (Eq. 2.3.3.6) can be rearranged to give

$$\mathbf{G}^{-1}(s) = \mathbf{G}_0^{-1}(s) - \mathbf{\Sigma}(s) \ . \tag{2.6.0.1}$$

For a system that has bound and metastable states, the poles and residues of the Green's function are found from the condition

$$\det \mathbf{G}^{-1}(s) = \det \left(\mathbf{G}_0^{-1}(s) - \mathbf{\Sigma}(s)\right) = 0 \ . \tag{2.6.0.2}$$

Using the fact that $\mathbf{G}_0^{-1}(s) = s\mathbb{1} - \mathbf{h}$, we can recast this condition in terms of diagonalization of the effective Hamiltonian:

$$\sum_{q} \hat{H}_{pq}(\varepsilon_\gamma) \mathcal{Z}^{\gamma}_{q} = \mathcal{Z}^{\gamma}_{p} \varepsilon_\gamma \ . \tag{2.6.0.3}$$

where $\hat{H}_{pq}(\varepsilon_\gamma) = h_{pq} + \Sigma_{pq}(\varepsilon_\gamma)$. Here, γ is a composite index that spans the poles and residues of the Green's function. In this thesis, Eq. 2.6.0.3 will be referred to as the

quasiparticle equation. When the full set of 1PI diagrams are included in the definition of the self-energy, the eigenvalues of Eq. 2.6.0.3 are the exact poles of the Green's function:

$$\varepsilon_\gamma \equiv \begin{cases} \varepsilon_\mu^{N+1} \cup \varepsilon_\nu^{N-1} & (T=0) \\ \omega_{nl} & (T \neq 0) \end{cases} . \tag{2.6.0.4}$$

Similarly, the residues corresponding to a given pole are given by

$$\mathcal{Z}_p^\gamma \equiv \begin{cases} (Y_p^\mu)^* \cup X_p^\nu & (T=0) \\ \mathcal{X}_p^{nl}(T) & (T \neq 0) \end{cases} . \tag{2.6.0.5}$$

From the eigenvector solutions of Eq. 2.6.0.3, it is often useful to introduce the quasiparticle renormalization factor as

$$Z^\gamma = \left(1 - \frac{\partial \Sigma_{\gamma\gamma}(s)}{\partial s} \bigg|_{s=\varepsilon_\gamma} \right)^{-1} \tag{2.6.0.6}$$

where $\Sigma_{\gamma\gamma}(s)$ is the self-energy rotated into the normalized eigenbasis of Eq. 2.6.0.3. The quasiparticle renormalization factor is constrained to be between zero and one such that the particle number is conserved.

For systems in the thermodynamic limit, in Subsection 2.3.5, we demonstrated that the Green's function also possesses branch cuts on the real axis as the Green's function develops a finite imaginary part at a continuous range of frequencies. In this case, the eigenvalue problem of Eq. 2.6.0.3 is non-hermitian and the eigenvalue solutions can take on complex values. These solutions correspond to 'metastable' states and are defined on the analytically continued second Riemann sheet of the Green's function, $G(s)$. This can also result in the emergence of complex residues. Importantly, these solutions do not correspond to 'exact' excitation energies as they exist on the second Riemann sheet where the Green's function has been analytically continued as a result of the branch cut. However, they still contain valuable physical information corresponding to particle decay rates as they encode the emergence of the branch cut on the real axis. This will be discussed at length in Chapter 5.

By using the Feshbach–Fano partitioning [44–46], (equivalent to the Löwdin partitioning [47] or the Schur complement [48]), we can re-write the frequency-dependent equation (Eq. 2.6.0.3) in terms of a frequency-independent supermatrix:

$$\mathbf{D}(T) = \begin{pmatrix} h_{pq} + \Sigma_{pq}^\infty(T) & M_{pP'}^\dagger(T) & N_{pP'}(T) \\ M_{Pq}(T) & \mathbf{\Lambda}_{PP'} & \mathbf{0} \\ N_{Pq}^\dagger(T) & \mathbf{0} & \mathbf{\Gamma}_{PP'} \end{pmatrix} \tag{2.6.0.7}$$

with eigenvalue solutions given by

$$\mathbf{D}(T)\begin{pmatrix} \mathcal{Z}_p^\gamma \\ W_P^\gamma \\ V_P^\gamma \end{pmatrix} = \varepsilon_\gamma \begin{pmatrix} \mathcal{Z}_p^\gamma \\ W_P^\gamma \\ V_P^\gamma \end{pmatrix} . \tag{2.6.0.8}$$

In this thesis, we refer to this representation as the Dyson supermatrix formulation. Importantly, for finite systems that possess only bound states, the eigenvalues and upper component of the eigenvectors of Eq. 2.6.0.8 are exactly those of the original frequency-dependent problem in Eq. 2.6.0.3. It is important to note that, when the self-energy is exact, the eigenvalues of the supermatrix are temperature-independent whereas the eigenvectors are temperature-dependent. This is because ensemble averages simply result in a temperature-dependent population of the particles among temperature-independent eigenstates of the Hamiltonian. By normalization of the supereigenvector, the quasiparticle renormalization factor is simply given by the overlap of the upper component:

$$Z^\gamma = \sum_p \mathcal{Z}_p^\gamma \mathcal{Z}_p^{\gamma *} . \tag{2.6.0.9}$$

At zero temperature, the Dyson supermatrix is given by

$$\mathbf{D}(T=0) = \begin{pmatrix} h_{pq} + \Sigma_{pq}^\infty & U_{pJ'}^\dagger & V_{pA'} \\ U_{Jq} & (\mathbf{K}_{JJ'}^> + \mathbf{C}_{JJ'}^>) & \mathbf{0} \\ V_{Aq}^\dagger & \mathbf{0} & (\mathbf{K}_{AA'}^< + \mathbf{C}_{AA'}^<) \end{pmatrix}, \tag{2.6.0.10}$$

where the coupling and interaction blocks are restricted to the $(N \pm 1)$-particle sectors, respectively.

From the supereigenvector solutions of the Dyson supermatrix, the exact single-particle Green's function can be constructed by taking the resolvent of the Dyson supermatrix in the single-particle subspace. This is given by

$$\begin{aligned} G_{pq}(s) &= \Big(s\mathbb{1} - \mathbf{D}\Big)^{-1}_{pq} \\ &= \sum_\gamma \frac{\mathcal{Z}_p^\gamma \mathcal{Z}_q^{\gamma *}}{s - \varepsilon_\gamma} = \begin{cases} \sum_\mu \frac{(Y_p^\mu)^* Y_q^\mu}{s - \varepsilon_\mu^{N+1}} + \sum_\nu \frac{X_p^\nu (X_q^\nu)^*}{s - \varepsilon_\nu^{N-1}} & (T=0) \\ \sum_{nl} \frac{\mathcal{X}_p^{nl}(T)\mathcal{X}_q^{nl*}(T)}{s - \omega_{nl}} & (T \neq 0) \end{cases} , \end{aligned} \tag{2.6.0.11}$$

where we have explicitly presented the solutions at both zero and finite temperatures.

The spectral representation of the self-energy and Dyson supermatrix representation can be firmly connected to the Feynman diagrammatic expansion outlined in Section 2.4. To see how this is possible, by writing a Feynman diagram expansion for the self-energy and using the Lippmann-Schwinger equation to expand the resolvents in Eq 2.5.0.8, we can

identify the different intermediate states contained in a diagrammatic expansion. By doing so, we can enforce an approximate Feynman diagrammatic expansion for the self-energy to obey the formal properties of the exact self-energy with a negative semi-definite imaginary part. This approach forms the basis of the zero temperature Algebraic Diagrammatic Construction (ADC) method [35, 36, 41]. The diagrammatic expansion can be performed perturbatively in terms of 1PI diagrams for $\Sigma[G_0]$ [35, 41] or in terms of the self-consistent 1PI skeleton diagram series in $\Sigma[G]$ [36]. The difference between the two will be in the exact form of the intermediate state configurations that are present at each order, with the self-consistent solutions depending on the residues and poles of the self-consistent Green's function. However, it is important to emphasize that our analysis has extended the previously existing zero temperature Dyson supermatrix formulation [41] to provide a unified description of many-body quantum systems at zero and finite temperatures.

The Dyson supermatrix formalism presented here applies to closed quantum systems that obey unitary evolution at equilibrium and finite temperatures. However, for open quantum systems or systems that are intrinsically governed by non-hermitian Hamiltonians, the self-energy and supermatrix formulation are fundamentally non-hermitian, the consequences of which will be discussed in Chapters 3 and 5.

2.7 Two-particle Green's function

As was demonstrated in Section 2.3, the single-particle Green's function is coupled to the four-point Green's function through its equation-of-motion. The four-point Green's function is a two-particle Green's function and contains information on two-particle correlation processes, giving access to neutral and two-particle excitation energies. On the Keldysh contour, the four-point response function is defined as

$$L_{pq,rs}(z_1, z_2; z_3, z_4) = G^{\mathrm{4pt}}_{pq,rs}(z_1, z_2; z_3, z_4) - iG_{pr}(z_1, z_3)G_{qs}(z_2, z_4) \ , \tag{2.7.0.1}$$

where the four-point Green's function was defined in Eq. 2.3.1.2 of subsection 2.3.1. The 'non-interacting' four-point response function is

$$L^0_{pq,rs}(z_1, z_2; z_3, z_4) = -iG_{ps}(z_1, z_4)G_{qr}(z_2, z_3) \tag{2.7.0.2}$$

and corresponds to the propagation of two-independent particles. It is important to note that Eq. 2.7.0.2 contains two *exact* single-particle Green's functions. In the study of

correlated particle-hole excitations, we are interested in the properties of the particle-hole response function at equilibrium at zero and finite temperatures. The particle-hole (ph) response function is obtained from the four-point response function as

$$L^{\rm ph}_{pq,rs}(z_1,z_2) = L_{pq,rs}(z_1,z_2;z_1^+,z_2^+)\ , \tag{2.7.0.3}$$

where z_1^+ and z_2^+ are time arguments evaluated on the same branch of the contour as the z_1 and z_2 arguments but at an infinitesimally later time: $z_1^+ = z_1 + \eta$.

2.7.1 Lehmann representation at zero temperature

At zero temperature, the time-ordered particle-hole response function is given by

$$L^{\rm ph,T}_{pq,rs}(t_1,t_2) = G^{\rm 4pt,T}_{pq,rs}(t_1,t_2;t_1^+,t_2^+) - iG^<_{pr}(t_1,t_1)G^<_{qs}(t_2,t_2)\ . \tag{2.7.1.1}$$

The Lehmann representation of this propagator is obtained by Fourier transformation of this equation using the resolution of the identity of eigenstates of the Hamiltonian:

$$L^{\rm ph,T}_{pq,rs}(\omega) = \sum_{\mathcal{S}\neq 0}\left(\frac{\mathcal{A}^{\mathcal{S}*}_{pr}\mathcal{A}^{\mathcal{S}}_{sq}}{\omega-\Omega_{\mathcal{S}}+i\eta} - \frac{\mathcal{A}^{\mathcal{S}*}_{qs}\mathcal{A}^{\mathcal{S}}_{rp}}{\omega+\Omega_{\mathcal{S}}-i\eta}\right)\ , \tag{2.7.1.2}$$

where $\mathcal{A}^{\mathcal{S}}_{rp} = \langle\Psi^N_{\mathcal{S}}|a^\dagger_r a_p|\Psi_0\rangle$. The poles of the particle-hole response function, $\Omega_{\mathcal{S}} = E^N_{\mathcal{S}} - E^N_0$, are the exact neutral excitation energies of the system. From Eq. 2.7.1.2, we see that the four-point response propagator contains a fundamental coupling between the forward-time and backward-time sectors which is different from that contained in the single-particle Green's function. This can be shown simply by analysis of the component:

$$L^{\rm ph,T}_{aj,ib}(\omega) = \sum_{\mathcal{S}\neq 0}\left(\frac{\mathcal{A}^{\mathcal{S}*}_{ai}\mathcal{A}^{\mathcal{S}}_{bj}}{\omega-\Omega_{\mathcal{S}}+i\eta} - \frac{\mathcal{A}^{\mathcal{S}*}_{jb}\mathcal{A}^{\mathcal{S}}_{ia}}{\omega+\Omega_{\mathcal{S}}-i\eta}\right)\ , \tag{2.7.1.3}$$

which demonstrates that the forward and backward matrix blocks of $L^{\rm ph}$ are explicitly coupled to each other as they share the same pole at $\pm\Omega_{\mathcal{S}}$. This means that the propagator cannot be written in the form of a Dyson equation expansion. We can easily find the spectral representation of the 'non-interacting' four-point response function defined in Eq. 2.7.0.2 by replacing the exact single-particle Green's functions with their reference counterparts: $G \to G_0$. This gives the fully 'non-interacting' particle-hole response function as

$$\begin{aligned} L^{{\rm ph}(G_0),{\rm T}}_{aj,ib}(\omega) &= \int\frac{d\omega'}{2\pi i}G^{0,{\rm T}}_{ab}(\omega+\omega')G^{0,{\rm T}}_{ji}(\omega') \\ &= \frac{\delta_{ab}\delta_{ij}}{\omega-(\epsilon_a-\epsilon_i)+i\eta}\ . \end{aligned} \tag{2.7.1.4}$$

It is important to note that this propagator is block diagonal in the combined space of electron-hole pairs spanned by the composite index $\{ai\}$ and is fully decoupled from its backward-time component.

2.7.2 Lehmann representation at finite temperature

At equilibirum and at finite temperature, the Lehmann representation for the particle-hole response function is given by

$$L^{\mathrm{ph}}_{pq,rs}(s) = \sum_{\substack{n \\ n' \neq n}} \frac{\langle \Psi_n | a_r^\dagger a_p | \Psi_{n'} \rangle \langle \Psi_{n'} | a_s^\dagger a_q | \Psi_n \rangle}{s - (E_{n'} - E_n)} \Big(\rho_n - \rho_{n'} \Big) \tag{2.7.2.1}$$

where the number of particles in each state is equal: $N_{n'} = N_n$. The poles of the finite temperature ph response function occur at all the neutral excitation energies accessible in the ensemble. Using the Langreth rules, we can immediately evaluate the retarded component of the fully 'non-interacting' propagator at finite temperature:

$$\begin{aligned} L^{\mathrm{ph}(G_0),\mathrm{R}}_{pq,rs}(\omega) &= \int \frac{d\omega}{2\pi i} \Big(G^{(0),\mathrm{R}}_{ps}(\omega + \omega') G^{(0),<}_{qr}(\omega') + G^{(0),<}_{ps}(\omega + \omega') G^{(0),\mathrm{A}}_{qr}(\omega') \Big) \\ &= \delta_{ps}\delta_{qr} \frac{f(\xi_q) - f(\xi_p)}{\omega - (\epsilon_p - \epsilon_q) + i\eta} \ . \end{aligned} \tag{2.7.2.2}$$

Therefore, the propagator over the occupied-virtual subspace is given by

$$L^{\mathrm{ph}(G_0),\mathrm{R}}_{aj,ib}(\omega) = \delta_{ab}\delta_{ij} \frac{f(\xi_i) - f(\xi_a)}{\omega - (\epsilon_a - \epsilon_i) + i\eta} \ . \tag{2.7.2.3}$$

We again observe that the non-interacting particle-hole response function has forward-time and backward-time contributions that are completely decoupled. For systems with a large band gap, this expression reduces to Eq. 2.7.1.4 as $f(\xi_i) \approx 1$ and $f(\xi_a) \approx 0$.

2.7.3 The Bethe-Salpeter equation

Through Schwinger's functional derivative technique, it can be shown that the four-point response function is given by

$$\begin{aligned} L_{pq,rs}(z_1, z_2; z_3, z_4) &= -i \frac{\delta G_{pr}(z_1, z_3)}{\delta \phi_{sq}(z_4, z_2)} \\ &= G^{\mathrm{4pt}}_{pq,rs}(z_1, z_2; z_3, z_4) - i G_{pr}(z_1, z_3) G_{qs}(z_2, z_4) \ , \end{aligned} \tag{2.7.3.1}$$

where ϕ is the fictitious external potential that couples to the electronic density via $H_1(z) = \sum_{vw} \int_\gamma d\bar{z} \phi_{vw}(z, \bar{z}) a_v^\dagger(z) a_w(\bar{z})$, where $\phi_{vw}(z, \bar{z}) = \phi_{vw}(z)\delta(z, \bar{z})$. By using the identity

$$-i \frac{\delta G_{pr}(z_1, z_3)}{\delta \phi_{sq}(z_4, z_2)} = i \sum_{vm} \int_\gamma dz dz' G_{pv}(z_1, z) \frac{\delta G^{-1}_{vm}(z, z')}{\delta \phi_{sq}(z_4, z_2)} G_{mr}(z', z_3) \ , \tag{2.7.3.2}$$

and the contour Dyson equation: $G^{-1}_{pq}(z,z') = [G_0^{-1}(z,z')]_{pq} - \phi_{pq}(z,z') - \Sigma_{pq}(z,z')$, we arrive at the famous Bethe-Salpeter equation (BSE) [13, 15, 49]

$$L_{pq,rs}(z_1,z_2;z_3,z_4) = L^0_{pq,rs}(z_1,z_2;z_3,z_4) + \sum_{tuvw}\int_\gamma dzdz'dz''dz''' L^0_{pt,ru}(z_1,z;z_3,z')\Xi_{uv,tw}(z',z'';z,z''')L_{wq,vs}(z''',z_2;z'',z_4) \ . \tag{2.7.3.3}$$

The BSE is the two-particle analog of the Dyson equation for the single-particle Green's function, with the kernel of the Bethe-Salpeter equation Ξ, given by the functional derivative of the self-energy with respect to the single-particle Green's function:

$$\Xi_{pq,rs}(z_1,z_2;z_3,z_4) = i\frac{\delta\Sigma_{pr}(z_1,z_3)}{\delta G_{sq}(z_4,z_2)} \ . \tag{2.7.3.4}$$

The kernel is composed of two-particle irreducible (2PI) diagrams [17]. The BSE is fundamentally different from the corresponding Dyson equation for the single-particle Green's function because it cannot be cast in a closed form equation for the ph/hp response function. Restricting the BSE to that of the ph/hp sector, we have

$$L^{\rm ph}_{pq,rs}(z_1,z_2) = L^{\rm ph(0)}_{pq,rs}(z_1,z_2) + \sum_{tuvw}\int_\gamma dzdz'dz''dz''' L^0_{pt,ru}(z_1,z;z_1^+,z')\Xi_{uv,tw}(z',z'';z,z''')L_{wq,vs}(z''',z_2;z'',z_2^+) \ . \tag{2.7.3.5}$$

It is the presence of the kernel, Ξ, that means we cannot send the time arguments in the propagators to the corresponding ones for the ph/hp propagator [50–55]. Therefore, we do not have a closed equation for the ph/hp response function as Eq. 2.7.3.5 is not a functional of $L^{\rm ph}$. This is because the BSE contains a fundamental coupling between the particle-hole, particle-particle and hole-hole response functions via the kernel.

Despite the fact that the BSE does not form a closed equation for the ph response function, we can still make progress by defining an effective kernel such that the formal structure of the Dyson equation is recovered [53, 54]. At equilibrium, due to time translational invariance, the ph response function is a function of three time-differences [53]. The most useful time-differences are those corresponding to the electron-hole convention: $t_{13} = t_1 - t_3$, $t_{24} = t_2 - t_4$ and $t_{23} = t_2 - t_3$. Using this convention, we can define the three-time Fourier transform as (see Appendix A.4) [53, 54]

$$\mathbf{L}(\nu,\nu',\omega) = \int dt_{13}dt_{24}dt_{23}e^{i\nu t_{13}}e^{i\nu' t_{24}}e^{i\omega t_{23}}\mathbf{L}(t_{13},t_{24},t_{23}) \ , \tag{2.7.3.6}$$

where the propagator has been written in matrix form for notational simplicity. Application of this Fourier transform to the BSE (Eq. 2.7.3.3) gives rise to the effective Dyson equation [53]

$$\mathbf{L}(\omega) = \mathbf{L}_0(\omega) + \mathbf{L}_0(\omega)\mathbf{K}^{\Xi}(\omega)\mathbf{L}(\omega) \ , \tag{2.7.3.7}$$

where the effective kernel is given by

$$\mathbf{K}^{\Xi}(\omega) = \int \frac{d\nu d\nu'}{(2\pi)^2}\mathbf{L}_0^{-1}(\omega)\mathbf{L}_0(\nu,\omega)\mathbf{\Xi}(\nu,\nu',\omega)\mathbf{L}(\nu',\omega)\mathbf{L}^{-1}(\omega) \ . \tag{2.7.3.8}$$

Therefore, we can write the BSE is the suggestive form

$$\mathbf{L}^{-1}(\omega) = \mathbf{L}_0^{-1}(\omega) - \mathbf{K}^{\Xi}(\omega) \tag{2.7.3.9}$$

such that the pole condition for the particle-hole response function becomes

$$\mathrm{det}\mathbf{L}^{-1}(\omega) = \mathrm{det}\left(\mathbf{L}_0^{-1}(\omega) - \mathbf{K}^{\Xi}(\omega)\right) = 0 \ . \tag{2.7.3.10}$$

However, there remain substantially non-trivial dynamical terms left as a result of the 'independent-particle' propagator, $\mathbf{L}_0(\omega)$. These can also be explicitly included by introduction of the frequency-dependent kernel as

$$\mathbf{K}^{\Sigma}(\omega) = \mathbf{L}_{G_0}^{-1}(\omega)\mathbf{L}_{\Sigma}(\omega)\mathbf{L}^{-1}(\omega) \ , \tag{2.7.3.11}$$

where we have separated the self-energy contributions to the 'non-interacting' ph propagator as: $\mathbf{L}_0(\omega) = \mathbf{L}_{G_0}(\omega) + \mathbf{L}_{\Sigma}(\omega)$. This identification allows us to re-write the pole condition as

$$\mathrm{det}\mathbf{L}^{-1}(\omega) = \mathrm{det}\left(\mathbf{L}_{G_0}^{-1}(\omega) - \mathbf{K}(\omega)\right) = 0 \ , \tag{2.7.3.12}$$

where $\mathbf{K}(\omega) = \mathbf{K}^{\Sigma}(\omega) + \mathbf{L}_{G_0}^{-1}(\omega)\mathbf{L}_0(\omega)\mathbf{K}^{\Xi}(\omega)$.

It is important to note that the particle-hole response function can also be obtained directly from the perturbative expansion:

$$iG^{\mathrm{4pt}}_{pq,rs}(z_1,z_2;z_1^+,z_2^+) = \frac{\left\langle \mathcal{T}_\gamma \left\{ e^{-i\int_\gamma dzH(z)} a_r^\dagger(z_1^+)a_p(z_1)a_s^\dagger(z_2^+)a_q(z_2) \right\} \right\rangle}{\left\langle \mathcal{T}_\gamma \left\{ e^{-i\int_\gamma dzH(z)} \right\} \right\rangle} \ , \tag{2.7.3.13}$$

from which one may enumerate the diagrams (terms) in the perturbative expansion to generate approximate schemes for its enumeration. This is the approach taken in the ADC method applied to the polarization propagator [35, 56]. Eq. 2.7.3.13 therefore allows for a clean diagrammatic interpretation of the terms that are generated by the particle-hole restricted BSE (Eq. 2.7.3.5).

2.7.4 Excitons

The pole condition of Eq. 2.7.3.12 gives rise to the following self-consistent eigenvalue problem for the neutral excitation energies [13, 17, 19]

$$\begin{pmatrix} \mathbf{H}(\Omega_{\mathcal{S}}) & \mathbf{C}(\Omega_{\mathcal{S}}) \\ -\mathbf{C}^*(-\Omega_{\mathcal{S}}) & -\mathbf{H}^*(-\Omega_{\mathcal{S}}) \end{pmatrix} \begin{pmatrix} \mathbf{A}_{\mathcal{S}} \\ \mathbf{B}_{\mathcal{S}} \end{pmatrix} = \Omega_{\mathcal{S}} \begin{pmatrix} \mathbf{A}_{\mathcal{S}} \\ \mathbf{B}_{\mathcal{S}} \end{pmatrix} \tag{2.7.4.1}$$

with the resonant and anti-resonant matrices defined as

$$H_{ai,bj}(\omega) = \Delta_{ai,bj} + K_{aj,ib}(\omega) \tag{2.7.4.2a}$$

$$C_{ai,bj}(\omega) = K_{ab,ij}(\omega) \ , \tag{2.7.4.2b}$$

where $\Delta_{ai,bj} = (\epsilon_a - \epsilon_i)\delta_{ij}\delta_{ab}$ are the eigenvalue differences of the reference Hamiltonian. The eigenvector blocks are given by $\mathbf{A}_{\mathcal{S}} \equiv \mathcal{A}^{\mathcal{S}}_{ai}$ and $\mathbf{B}_{\mathcal{S}} \equiv \mathcal{A}^{\mathcal{S}}_{ia}$, respectively. The solutions of Eq. 2.7.4.1 are correlated electron-hole pairs, commonly referred to as excitons. Within the Tamm-Dancoff approximation (TDA), we set the anti-resonant block to zero ($\mathbf{C} = 0$) and solve the effective Dyson equation [19]:

$$\sum_{bj} H_{ai,bj}(\Omega_{\mathcal{S}}) A^{\mathcal{S}}_{bj} = \Omega_{\mathcal{S}} A^{\mathcal{S}}_{ai} \ . \tag{2.7.4.3}$$

This approximation is deemed to be valid when ground state correlations are weak such that the $\mathbf{B}_{\mathcal{S}}$ amplitudes are small compared to the $\mathbf{A}_{\mathcal{S}}$ coefficients and so can be safely neglected [19]. To lowest-order in the electron-electron interaction, the self-energy is typically composed of two diagrams (Hartree plus GW) [57]:

$$\begin{aligned} \Sigma_{pq}(z_1, z_2) = \Sigma^{\mathrm{H}}_{pq}(z_1, z_2) + \Sigma^{GW}_{pq}(z_1, z_2) \\ - i \sum_{rs} v_{pr,qs} G_{sr}(z_1, z_1^+) \delta(z_1, z_2) + i \sum_{rs} W_{pr,sq}(z_1, z_2) G_{sr}(z_1, z_2) \ . \end{aligned} \tag{2.7.4.4}$$

The two diagrams gives rise to the GW-BSE kernel

$$\Xi_{pq,rs}(z_1, z_2; z_3, z_4) \approx v_{pq,rs} - W_{pq,sr}(z_1, z_3)\delta(z_1, z_4)\delta(z_2, z_3) \ , \tag{2.7.4.5}$$

where we have neglected the functional derivative of the screened interaction W, with respect to the Green's function: $i\frac{\delta W}{\delta G}$ [58, 59]. At zero temperature, the GW-BSE kernel gives rise to the expression for the effective kernel as [50, 60]

$$K^{\Xi,\mathrm{T}}_{aj,ib}(\omega) = v_{aj,ib} + \int_{-\infty}^{\infty} \frac{d\omega'}{2\pi i} W^{\mathrm{T}}_{aj,bi}(\omega') \left(L^{G_0,\mathrm{T}}_{bi,ib}(\omega + \omega') + L^{G_0,\mathrm{T}}_{aj,ja}(\omega + \omega') \right) \ , \tag{2.7.4.6}$$

where we have linearized Eq. 2.7.3.8 by setting $\mathbf{L} = \mathbf{L}_0 = \mathbf{L}_{G_0}$. This gives rise to the self-consistent eigenvalue problem

$$\sum_{bj} \left(\Delta^{GW}_{ai,bj} + K^{\Xi}_{aj,ib}(\Omega_{\mathcal{S}}) \right) A^{\mathcal{S}}_{bj} = \Omega_{\mathcal{S}} A^{\mathcal{S}}_{ai} \ , \tag{2.7.4.7}$$

where commonly the independent-particle eigenvalues are taken within the quasiparticle *GW* approximation: $\Delta^{GW}_{ai,bj} = (\epsilon^{GW}_a - \epsilon^{GW}_i)\delta_{ab}\delta_{ij}$, where $\epsilon^{GW}_p = \epsilon_p + \Sigma^{GW}_{pp}(\epsilon_p)$ [57–59]. However, taking a static approximation for the screened interaction $W(\omega = 0)$, we can further simply Eq. 2.7.4.7 as

$$K^{\infty}_{aj,ib} = v_{aj,ib} - W_{aj,bi}(\omega = 0) \ . \tag{2.7.4.8}$$

In this case, the static *GW*-BSE within the TDA becomes

$$\sum_{bj} \left(\Delta^{GW}_{ai,bj} + K^{\infty}_{aj,ib} \right) A^{S}_{bj} = \Omega_S A^{S}_{ai} \ . \tag{2.7.4.9}$$

This approximation is particularly useful for semiconductor crystal systems where the relative energy scales of exciton binding energies ($\Delta^{GW}_{ai,ai} - \Omega_S$) and plasmon frequencies (poles of $W(\omega)$) is large [58, 59]. For finite molecular systems, however, it is important to include the full dynamical effects of the screened interaction as the exciton binding energies are typically of a similar order of magnitude to the plasmon frequencies [59, 61]. In Chapters 5 and 6, we will extend the BSE approach presented here to include the effects of interactions between electrons and the lattice vibrations.

'At the moment physics is again terribly confused. In any case, it is too difficult for me, and I wish I had been a movie comedian or something of the sort and had never heard of physics.'

— Wolfgang Pauli

3

Non-Hermitian Green's Function Theory With N-body Interactions: The Coupled-Cluster Similarity Transformation

---

The work presented in this Chapter has contributed to the publications of Refs [4] and [7].

Contents

3.1 Introduction

In this Chapter, we generalize the conventional formulation of Green's function theory given in Chapter 2, based on hermitian two-body (and recently three-body [20]) interactions, to include up to N-body non-hermitian interactions. We present the diagrammatic theory of the self-energy generated by a non-hermitian N-body interaction, focusing specifically on the coupled-cluster similarity transformed Hamiltonian. The non-hermitian Green's function formalism presented in this Chapter unifies and combines the techniques of coupled-cluster and Green's function theory, thereby furthering the conceptual understanding of ground and excited state many-body correlation in the context of condensed matter, nuclear physics and quantum chemistry. The approach is based on taking the coupled-cluster similarity transformed Hamiltonian as the fundamental interaction Hamiltonian. This change of perspective unveils the derivation of the resulting theory of the self-energy and single-particle Green's function that naturally arise within the context of coupled-cluster theory. We arrive at a formally exact formalism that is related to but distinct from prior work on connecting approximate Green's function and coupled-cluster theories. As we are at zero temperature, the analysis is centered about real-time-ordered propagators.

The Green's function formalism is one of the major pillars in the *ab initio* theory of many interacting particles [13, 14, 17]. Green's function theory is based on the analysis of N-point dynamical correlation functions, with the single-particle Green's function occupying the central position. A significant conceptual and computational advantage of Green's functions is that they provide a simultaneous description of ground and excited state many-body correlation. Knowledge of the single-particle Green's function gives access to the exact addition and removal energies, ground state expectation values of any single-particle observable and, for two-body interactions, the exact ground state energy

of the system. Similarly, knowledge of the N-body Green's function yields ground and excited state properties of N-body observables.

Direct computation of the single-particle Green's function scales exponentially with the number of interacting particles, requiring knowledge of exact eigenstates of the full many-body Hamiltonian containing different numbers of particles. However, the single-particle Green's function can also be constructed from the Dyson equation. The Dyson equation relates a known, reference Green's function to the exact, interacting Green's function through the irreducible self-energy. The irreducible self-energy contains all the many-body interactions a single-particle experiences as it propagates through the system. The self-energy itself depends on the exact Green's function such that the Green's function formalism constitutes a self-consistent theory [38]. The self-energy can be expressed either as a perturbative or self-consistent Feynman diagrammatic expansion. For systems of particles governed by a two-body interaction, theories of the self-energy have been well established and extensively explored in nuclear and condensed matter systems [17, 30, 57–59, 62–65]. Only recently, in the context of nuclear theory, has the Green's function formalism been extended to include three-body interactions [20, 36]. Until this work, the development of the Green's function formalism in the context of non-hermitian N-body interactions has been entirely unexplored. Here, we will focus specifically on the non-hermitian coupled-cluster similarity transformed Hamiltonian but the general approach can also be applied to other non-hermitian Hamiltonians.

The discovery that non-hermitian parity-time ($\mathcal{PT}$) symmetric Hamiltonians can possess real spectra [66] has lead to new active areas of theoretical and experimental physics research [67–71]. There has been increasing interest in exploring non-hermitian Hamiltonians as they can describe experimentally verifiable and novel properties of physical systems [68]. For example, non-hermitian Hamiltonians play a role in the theory of open quantum systems [17, 70, 72], dissipative Lindbladian dynamics [73, 74] as well topological quantum phase transitions [75–78]. Experimental work on probing the spectra and eigenstates of non-hermitian Hamiltonians has also recently emerged in the context of optics and photonics [79, 80], magnetic systems [81], exciton-polaritons [82] as well as ultracold atoms [83, 84]. The continued experimental and theoretical exploration of

non-hermitian many-body quantum systems further motivates the development of a new Green's function formalism capable of describing their spectral properties.

Another central pillar in the *ab initio* theory of many interacting particles is coupled-cluster (CC) theory [85, 86]. Coupled-cluster theory is directly concerned with obtaining ground state properties of a system of many interacting particles. It is based on a size-extensive reformulation of the Configuration Interaction that leads to hierarchical and systematically controllable sets of equations that are, in principle, exact. CC theory is formulated in terms of the non-hermitian similarity transformed Hamiltonian. The CC similarity transformation is determined by the ground state CC amplitude equations. In general, when the CC transformation is not truncated, the similarity transformed Hamiltonian is an N-body non-hermitian operator that possesses different left and right eigenstates. Excited state properties are then usually obtained from Configuration Interaction expansions of the CC similarity transformed Hamiltonian, commonly referred to as equation-of-motion coupled-cluster (EOM-CC) theory.

Previous attempts at combining coupled-cluster and Green's function methods have been largely centered around direct construction of the electronic single-particle Green's function using the eigenstates and eigenvalues resulting from ground state and ionization potential/electron affinity equation-of-motion coupled-cluster theory (IP/EA-EOM-CC) [87–91]. In this thesis we refer to the approach first presented in Refs [87] and [88] as the coupled-cluster representation of the electronic Green's function. The approach outlined in Refs [87, 88] has led to many practical advantages over conventional hermitian many-body Green's function techniques for computing spectral functions and charged excitation energies [91–94]. However, these approaches to combining coupled-cluster with Green's function theory do not connect to a diagrammatic construction of the irreducible coupled-cluster self-energy [4]. As a result, the connections to the coupled-cluster representation of the electronic two-particle Green's function remain largely unexplored.

Recently, there has been increasing interest in understanding and exploring the connections between coupled-cluster and Green's function theories based on the G_0W_0 self-energy [95–99]. It has also been demonstrated that the Random Phase (RPA) and static GW-BSE approximations can be recast as approximate forms of CCD theory where the doubles amplitudes are solved for by keeping only the 'ring' diagrams (rCCD) [95,

100]. In the case of the static GW-BSE approximation, the associated rCCD equations contain screened interaction intermediates as well as bare Coulomb vertices [95]. These established connections have also been useful in the development of analytic nuclear gradients for the static GW-BSE approximation through its connection to *unitary* coupled-cluster theory [97, 101, 102]. This work has been crucial in furthering the conceptual understanding of the nature of the many-body self-energy and Bethe-Salpeter kernel in the context of wavefunction based approaches. However, Green's function theory is centered about *universal* and *exact* relationships between the exact single-particle Green's function, irreducible self-energy functional $\Sigma[G]$, and its higher order functional derivatives [17]. To fully understand the relationship between the functional-diagrammatic framework of Green's function theory and the coupled-cluster similarity transformation, it is necessary to develop new methods in order to construct the self-energy generated by a higher than two-body non-hermitian interaction Hamiltonian.

As stated in Chapter 2, the diagrammatic content of the irreducible self-energy depends on whether it is expanded with respect to the non-interacting or exact Green's function. Expansion of the electronic self-energy with respect to the exact Green's function gives rise to self-consistent renormalization and leads to the GF2 and GW approximations [38, 103–110]. In the case of a two-body interaction, the interaction lines/vertices appearing in irreducible self-energy diagrams are 'bare', exhibiting no dependence on the form of the Green's function itself. While it is true that Hedin's equations introduce the screened interaction $W[G]$, which is also a functional of the single-particle Green's function, this is a choice that is not fundamentally necessary to construct the self-consistent self-energy expansion. However, in the presence of higher-body interactions, the interaction lines/vertices appearing in the self-energy expansion are fundamentally dependent on which Green's function the self-energy is expanded with respect to. For example, if the self-energy is expanded with respect to the non-interacting Green's function, G_0, it is composed of one-particle irreducible diagrams that are constructed from effective interactions that arise when normal-ordering the Hamiltonian with respect to the reference state. However, to construct the self-energy as a functional of the exact Green's function requires effective interactions that arise when normal-ordering the Hamiltonian with respect to the exact ground state. It is a fundamental consequence of the Green's function formalism that

interaction vertices of the self-energy are dressed by the Green's function. However, this consideration has been entirely unexplored in the context of non-hermitian interactions and coupled-cluster theory. This analysis is not only crucial to construct the correct renormalized self-energy functional but also to generate the correct diagrams of the Bethe-Salpeter kernel which arise by taking the functional derivative of the renormalized self-energy with respect to the exact Green's function.

This Chapter is organized as follows. In Section 3.2, we review and extend the biorthogonal quantum theory in order to define the pictures of quantum mechanics in the presence of a non-hermitian Hamiltonian. Here, we define the biorthogonal Schrodinger, Heisenberg and Interaction pictures, extending the Gell-Mann and Low theorem to include non-hermitian interactions. In Section 3.3, we define the single-particle Green's function and Dyson equation for a system governed by an N-body non-hermitian Hamiltonian. We demonstrate the generalization of effective interactions required to construct the non-hermitian irreducible self-energy as a functional of the exact Green's function. In Section 3.4, we provide an overview of coupled-cluster theory and the similarity transformed Hamiltonian. This leads us to introduce a novel normal-ordering of the Hamiltonian required for the self-consistent theory of the coupled-cluster self-energy. In Section 3.5, we discuss the coupled-cluster representation of the electronic Green's function which leads us to our novel approach to the genuine single-particle coupled-cluster Green's function. This change of perspective allows us to define a functional-diagrammatic formalism that unifies the Green's function formalism and coupled-cluster theory. In Section 3.6, we derive the perturbative expansion of the single-particle coupled-cluster Green's function, thereby defining the irreducible coupled-cluster self-energy. In Section 3.7, we derive the diagrammatic perturbation expansion of the irreducible coupled-cluster self-energy, demonstrating its relationship to the conventional electronic self-energy. In Section 3.8, we use the biorthogonal theory developed in Section 3.2 to construct the non-perturbative renormalized coupled-cluster self-energy from the exact equation-of-motion of the single-particle coupled-cluster Green's function. Here, we describe how the perturbative expansion is recovered from the self-consistent renormalization procedure. In Section 3.9, we demonstrate how the exact coupled-cluster ground state energy can be obtained from the coupled-cluster self-energy. In Section 3.10, we use the spectral representation of the

coupled-cluster self-energy to derive the associated coupled-cluster Dyson supermatrix. Here, we also introduce several different approximations for the coupled-cluster self-energy that may be readily implemented. In Section 6.6, we demonstrate the relationship between the coupled-cluster self-energy, IP/EA-EOM-CCSD and the G_0W_0 approximation. This motivates us to introduce CC-G_0W_0 theory that combines aspects of Green's function theory and Hedin's equations with coupled-cluster theory. Finally, in Section 3.12, we derive the relationship between the coupled-cluster self-energy and the Bethe-Salpeter kernel.

3.2 Non-hermitian Quantum Mechanics

Within non-hermitian quantum theory, time evolution of states and operators must be formulated carefully. This is due to the fact that the left and right states can be related to each other by a non-trivial metric and therefore evolve under different Hamiltonians. In this Section, we will review aspects of biorthogonal quantum theory, as well as the biorthogonal Schrödinger and Heisenberg pictures. To the best of our knowledge, for the first time we present the biorthogonal Interaction picture and provide an extension of the GML theorem to include non-hermitian interactions. This analysis is required to define a consistent Green's function theory that generates a diagrammatic theory of the self-energy and Bethe-Salpeter kernel. Finally, the biorthogonal Heisenberg picture is central to the self-consistent Green's function theory presented in Section 3.8.

3.2.1 Biorthogonal basis

Suppose we have a diagonalizable non-hermitian Hamiltonian $\bar{H}$ with eigenstates $\{|\Psi_n\rangle\}$ and eigenvalues $\{E_n\}$ such that

$$\bar{H}\,|\Psi_n\rangle = E_n\,|\Psi_n\rangle \quad \Rightarrow \quad \langle\Psi_n|\,\bar{H}^\dagger = \langle\Psi_n|\,E_n^* \;. \tag{3.2.1.1}$$

The eigenstates of the hermitian adjoint $\bar{H}^\dagger$ are

$$\bar{H}^\dagger\,|\Phi_n\rangle = \mathcal{E}_n\,|\Phi_n\rangle \quad \Rightarrow \quad \langle\Phi_n|\,\bar{H} = \langle\Phi_n|\,\mathcal{E}_n^* \;. \tag{3.2.1.2}$$

The set $\{|\Psi_n\rangle\}$ is complete in the Hilbert space, with $\langle\Phi_n|\Psi_m\rangle = \delta_{nm}$, $E_n = \mathcal{E}_n^*\ \forall\ n$. Completeness of $\{|\Psi_n\rangle\}$ implies the completeness of $\{|\Phi_n\rangle\}$ [111, 112]. The eigenstates

of $\bar{H}$ are generally not orthogonal [111]. The basis set $\{|\Phi_m\rangle\}_{m=1}^N$ is referred to as the biorthonormal basis associated with $\{|\Psi_n\rangle\}_{n=1}^N$ [111–113]. A general state

$$|\Psi\rangle = \sum_{n=1}^{N} C_n |\Psi_n\rangle , \tag{3.2.1.3}$$

has an *associated state* and a dual state

$$|\tilde{\Psi}\rangle := \sum_{n=1}^{N} C_n |\Phi_n\rangle \quad \Rightarrow \quad \langle\tilde{\Psi}| = \sum_{n=1}^{N} C_n^* \langle\Phi_n| \ . \tag{3.2.1.4}$$

The state dual to $|\Psi\rangle$ is given by $\langle\tilde{\Psi}|$ and the associated state is given by its hermitian conjugate: $|\tilde{\Psi}\rangle$. The biorthogonal inner product is defined as

$$\langle\Psi, \Psi\rangle_{bo} = \langle\tilde{\Psi}|\Psi\rangle = \sum_n |C_n|^2 , \tag{3.2.1.5}$$

where $\langle ., . \rangle_{bo}$ denotes the biorthogonal inner product. Under the biorthogonal inner product, the set of states, $\{|\Psi_n\rangle, |\Phi_n\rangle\}_{n=1}^N$ forms a complete biorthogonal system. A generic operator, A, can be represented in the biorthogonal basis as

$$A = \sum_{nm} a_{nm} |\Psi_n\rangle \langle\Phi_m| \ , \tag{3.2.1.6}$$

with $a_{nm} = \langle\Phi_n|A|\Psi_m\rangle$. The expectation value of an observable in a pure state $|\Psi\rangle$ is defined as

$$\langle A\rangle = \frac{\langle\tilde{\Psi}|A|\Psi\rangle}{\langle\tilde{\Psi}|\Psi\rangle} , \tag{3.2.1.7}$$

and if the operator is biorthogonally hermitian with $a_{nm} = a_{mn}^*$, the expectation value of the observable will be real. Non-hermitian quantum mechanics can also be formulated in terms of conventional quantum theory where the Hilbert space is endowed with a nontrivial metric. This is known as pseudo-hermitian quantum theory [111, 114, 115].

3.2.2 Biorthogonal Schrödinger and Heisenberg pictures

The formalism of quantum field theory takes place in the Heisenberg picture [12]. Therefore, we must carefully define the relationship between the Schrödinger and Heisenberg pictures in order to define the correct extension of the Green's function formalism for non-hermitian interactions.

The time-dependent non-hermitian Schrödinger equation is written as

$$i\frac{\partial}{\partial t} |\Psi_S(t)\rangle = \bar{H} |\Psi_S(t)\rangle \tag{3.2.2.1}$$

where $\bar{H}$ is a time-independent, pseudo-hermitian Hamiltonian [115]. The formal solution is given by

$$|\Psi_S(t)\rangle = \bar{U}(t,0)\,|\Psi_S(0)\rangle \ , \tag{3.2.2.2}$$

where $\bar{U}(t,0) = e^{-i\bar{H}t}$. It is important to note that the time-evolution operator $\bar{U}$ is not unitary. The associated states necessarily obey the conjugate equation

$$i\frac{\partial}{\partial t}\,|\tilde{\Psi}_S(t)\rangle = \bar{H}^\dagger\,|\tilde{\Psi}_S(t)\rangle \tag{3.2.2.3}$$

yielding the formal solution

$$|\tilde{\Psi}_S(t)\rangle = \tilde{U}^\dagger(t,0)\,|\tilde{\Psi}_S(0)\rangle\,, \tag{3.2.2.4}$$

where $|\tilde{\Psi}_S(0)\rangle$ is the associated state of $|\Psi_S(0)\rangle$ and $\tilde{U}^\dagger(t,0) = e^{-i\bar{H}^\dagger t}$. This ensures that the norm of the state is preserved under time-evolution as $\langle\tilde{\Psi}_S(t)|\Psi_S(t)\rangle = \langle\tilde{\Psi}_S(0)|\Psi_S(0)\rangle$. Clearly, we see that *associated states* evolve according to a different Hamiltonian ($\bar{H}^\dagger$) [116]. This also has important consequences in the theory of non-hermitian quantum electrodynamics [112].

The Heisenberg states are given by the relationship: $|\Psi_H\rangle = |\Psi_S(0)\rangle$ and $|\tilde{\Psi}_H\rangle = |\tilde{\Psi}_S(0)\rangle$. Therefore, the general relationship between an operator in the Heisenberg and Schrödinger representations under the birothogonal inner product is given by

$$O_H(t) = e^{i\bar{H}t}O_S e^{-i\bar{H}t} \ . \tag{3.2.2.5}$$

It should be noted that the same form has been obtained in the pseudo-hermitian theory with respect to the τ-inner product, where τ is the metric [117]. Now that we have defined the biorthogonal Schrödinger and Heisenberg pictures, we introduce the biorthogonal Interaction picture.

3.2.3 Biorthogonal Interaction picture

Assume that a time-independent diagonalizable non-hermitian Hamiltonian $\bar{H}$ may be expressed as the sum of two non-hermitian terms $\bar{H}_0$ and $\bar{H}_1$ such that $\bar{H} = \bar{H}_0 + \bar{H}_1$. Let us define the Interaction state vector in the Hilbert space as $|\Psi_I(t)\rangle = e^{i\bar{H}_0 t}\,|\Psi_S(t)\rangle$ and

it's associated state as $|\tilde{\Psi}_I(t)\rangle = e^{i\bar{H}_0^\dagger t}|\tilde{\Psi}_S(t)\rangle$. This transformation leads to the following Schrödinger equations for the Interaction state vector

$$i\frac{\partial}{\partial t}|\Psi_I(t)\rangle = \bar{H}_1(t)|\Psi_I(t)\rangle \tag{3.2.3.1a}$$

and its associated state

$$i\frac{\partial}{\partial t}|\tilde{\Psi}_I(t)\rangle = \bar{H}_1^\dagger(t)|\tilde{\Psi}_I(t)\rangle \tag{3.2.3.1b}$$

where $\bar{H}_1(t) = e^{i\bar{H}_0 t}\bar{H}_1 e^{-i\bar{H}_0 t}$ and $\bar{H}_1^\dagger(t)$ is the hermitian adjoint. An arbitrary matrix element in the Schrödinger picture requires a general operator in the biorthogonal Interaction picture to be defined as

$$O_I(t) = e^{i\bar{H}_0 t}O_S e^{-i\bar{H}_0 t}\ . \tag{3.2.3.2}$$

In order to find an expression for the time-evolution operator in the biorthogonal Interaction picture, from Eqs 3.2.3.1a and 3.2.3.1b, we immediately find that

$$\begin{aligned}|\Psi_I(t)\rangle &= \mathcal{T}\left\{e^{-i\int_{t_0}^{t}dt'\bar{H}_1(t')}\right\}|\Psi_I(t_0)\rangle \\ &= \bar{U}(t,t_0)|\Psi_I(t_0)\rangle\end{aligned} \tag{3.2.3.3}$$

and

$$\begin{aligned}|\tilde{\Psi}_I(t)\rangle &= \mathcal{T}\left\{e^{-i\int_{t_0}^{t}dt'\bar{H}_1^\dagger(t')}\right\}|\tilde{\Psi}_I(t_0)\rangle \\ &= \tilde{U}^\dagger(t,t_0)|\tilde{\Psi}_I(t_0)\rangle\ .\end{aligned} \tag{3.2.3.4}$$

These relations ensure that the biorthogonal norm of the interaction state-vector is time-independent. As a result, the general relationship between the birothogonal Interaction and Heisenberg pictures under the biorthogonal inner product is given by

$$|\Psi_H\rangle = \bar{U}(0,t_0)|\Psi_I(t_0)\rangle \tag{3.2.3.5a}$$

$$|\tilde{\Psi}_H\rangle = \tilde{U}^\dagger(0,t_0)|\tilde{\Psi}_I(t_0)\rangle \tag{3.2.3.5b}$$

$$O_H(t) = \bar{U}(0,t)O_I(t)\bar{U}(t,0)\ . \tag{3.2.3.5c}$$

3.2.4 Extension of the Gell-Mann and Low theorem

In order to generate a diagrammatically consistent Green's function formalism for non-hermitian interactions, here we demonstrate that we can extend the GML theorem.

Exact eigenstates of the full non-hermitian Hamiltonian can be generated adiabatically by introducing the time-dependent Hamiltonian

$$\bar{H} = \bar{H}_0 + e^{-\eta|t|}\bar{H}_1 \ , \tag{3.2.4.1}$$

where η is a positive infinitesimal. Here, we have made the implicit assumption that $\bar{H}$ can be partitioned as the sum of two diagonalizable non-hermitian Hamiltonians $\bar{H}_0$ and $\bar{H}_1$. At very large times, the Hamiltonian reduces to $\bar{H}_0$ and at $t = 0$, the Hamiltonian is the full non-hermitian Hamiltonian. The general solution for the interaction and associated states is given by

$$|\Psi_I(t)\rangle = \bar{U}_\eta(t, t_0)\,|\Psi_I(t_0)\rangle \tag{3.2.4.2a}$$

$$|\tilde{\Psi}_I(t)\rangle = \tilde{U}^\dagger_\eta(t, t_0)\,|\tilde{\Psi}_I(t_0)\rangle \tag{3.2.4.2b}$$

where the time-evolution operator now takes the form

$$\bar{U}_\eta(t, t_0) = \mathcal{T}\left\{e^{-i\int_{t_0}^{t} dt' e^{-\eta|t'|}\bar{H}_1(t')}\right\} \ , \tag{3.2.4.3}$$

with the analogous form for $\tilde{U}^\dagger_\eta(t, t_0)$. Using these relationships, we take the time limit $t_0 \to -\infty$ and the physical limit as $\eta \to 0$ by extending the GML theorem (see Appendix B.1) such that if the limits of the quantities

$$\frac{|\Psi_0\rangle}{\langle\tilde{\Phi}_0|\Psi_0\rangle} \equiv \lim_{\eta\to 0^+} \frac{\bar{U}_\eta(0,-\infty)\,|\Phi_0\rangle}{\langle\tilde{\Phi}_0|\bar{U}_\eta(0,-\infty)|\Phi_0\rangle} \tag{3.2.4.4a}$$

and

$$\frac{|\tilde{\Psi}_0\rangle}{\langle\Phi_0|\tilde{\Psi}_0\rangle} \equiv \lim_{\eta\to 0^+} \frac{\tilde{U}^\dagger_\eta(0,-\infty)\,|\tilde{\Phi}_0\rangle}{\langle\Phi_0|\tilde{U}^\dagger_\eta(0,-\infty)|\tilde{\Phi}_0\rangle} \tag{3.2.4.4b}$$

exist, then they are the 'right' and 'left' eigenstates of the full Hamiltonian $\bar{H}$:

$$\bar{H}\frac{|\Psi_0\rangle}{\langle\tilde{\Phi}_0|\Psi_0\rangle} = E\frac{|\Psi_0\rangle}{\langle\tilde{\Phi}_0|\Psi_0\rangle} \quad ; \quad \bar{H}^\dagger\frac{|\tilde{\Psi}_0\rangle}{\langle\Phi_0|\tilde{\Psi}_0\rangle} = E\frac{|\tilde{\Psi}_0\rangle}{\langle\Phi_0|\tilde{\Psi}_0\rangle} \ . \tag{3.2.4.5}$$

Importantly, the limit as $\eta \to 0$ of both the numerators and denominators of Eqs 3.2.4.4a and 3.2.4.4b do not separately exist. The proof can be derived in a similar way to the original proof presented for the Hermitian case but can only be obtained by careful analysis of the role of time-dependence of operators for non-hermitian quantum systems. The

theorem also applies equally to the state obtained from evolving from $t = +\infty$ [13, 24]. Using our definition, the associated state is written as

$$\begin{aligned}\frac{\langle\tilde{\Psi}_0|}{\langle\tilde{\Psi}_0|\Phi_0\rangle^*} &= \lim_{\eta\to 0^+}\frac{\langle\tilde{\Phi}_0|\,\tilde{U}_\eta(0,-\infty)}{\langle\tilde{\Phi}_0|\tilde{U}_\eta(0,-\infty)|\Phi_0\rangle^*} \\ &= \lim_{\eta\to 0^+}\frac{\langle\tilde{\Phi}_0|\,\bar{U}_\eta(-\infty,0)}{\langle\tilde{\Phi}_0|\bar{U}_\eta(-\infty,0)|\Phi_0\rangle^*}\ .\end{aligned} \tag{3.2.4.6}$$

Therefore, the state obtained from the adiabatic procedure is an eigenstate of the full non-hermitian Hamiltonian, which may be obtained from either evolving 'forward' or 'backward' in time.

By making use of our extended GML theorem, we can construct perturbative expressions for time-dependent correlation functions by evolving on the right from $-\infty$ and on the left from $+\infty$ as follows (making use of the linked diagram theorem [13, 85])

$$\begin{aligned}\mathcal{R}^{\mathrm{T}}(t_1,t_2,\cdots,t_n) &= \frac{\langle\tilde{\Psi}_0|\mathcal{T}\left\{O_H(t_1)O_H(t_2)\cdots O_H(t_n)\right\}|\Psi_0\rangle}{\langle\tilde{\Psi}_0|\Psi_0\rangle} \\ &= \lim_{\eta\to 0^+}\langle\tilde{\Phi}_0|\mathcal{T}\left\{\bar{S}_\eta O_I(t_1)O_I(t_2)\cdots O_I(t_n)\right\}|\Phi_0\rangle_{\mathcal{C}}\ ,\end{aligned} \tag{3.2.4.7}$$

where the subscript $\mathcal{C}$ indicates that only connected diagrams contribute to the expansion. Here, $\bar{S}_\eta = \bar{U}_\eta(\infty,-\infty)$ is the non-unitary scattering operator. If we choose the partitioning such that the reference Hamiltonian is hermitian, *i.e.* $H_0 = H_0^\dagger$, the results above hold and we have

$$\mathcal{R}^{\mathrm{T}}(t_1,t_2,\cdots,t_n) = \lim_{\eta\to 0^+}\langle\Phi_0|\mathcal{T}\left\{\bar{S}_\eta O_I(t_1)O_I(t_2)\cdots O_I(t_n)\right\}|\Phi_0\rangle_{\mathcal{C}} \tag{3.2.4.8}$$

where now the left and right states of the hermitian reference are simply related to each other via hermitian conjugation.

As demonstrated in Chapter 2, the Interaction picture automatically implies the Keldysh contour construction. However, for simplicity here we work directly on the real-time-ordered contour to make the connection between the non-hermitian formulation and the conventional Green's function theory as clear as possible as we are working at zero temperature.

3.3 The single-particle Green's function for N-body non-hermitian interactions

In this Section, we define the single-particle Green's function for the case of an N-body non-hermitian interaction Hamiltonian and discuss the construction of the non-hermitian

irreducible self-energy that emerges. This analysis provides the foundation for the analysis of the diagrammatic coupled-cluster self-energy presented in Sections 3.7 and 3.8.

Suppose we have an N-body non-hermitian Hamiltonian

$$\begin{aligned}\bar{H} = &\sum_{pq} \bar{h}_{pq} a_p^\dagger a_q + \frac{1}{(2!)^2} \sum_{pq,rs} \bar{v}_{pq,rs} a_p^\dagger a_q^\dagger a_s a_r + \frac{1}{(3!)^2} \sum_{pqr,stu} \bar{w}_{pqr,stu} a_p^\dagger a_q^\dagger a_r^\dagger a_u a_t a_s \\ &+ \frac{1}{(4!)^2} \sum_{\substack{pqrs \\ tuvz}} \bar{u}_{pqrs,tuvz} a_p^\dagger a_q^\dagger a_r^\dagger a_s^\dagger a_z a_v a_u a_t \\ &+ \frac{1}{(5!)^2} \sum_{\substack{pqrsn \\ tuvzm}} \bar{\kappa}_{pqrsn,tuvzm} a_p^\dagger a_q^\dagger a_r^\dagger a_s^\dagger a_n^\dagger a_m a_z a_v a_u a_t + \cdots\end{aligned} \tag{3.3.0.1}$$

with right and left eigenstates given by $\bar{H} \left| \Psi_0^N \right\rangle = E_0^N \left| \Psi_0^N \right\rangle$ and $\bar{H}^\dagger \left| \tilde{\Psi}_0^N \right\rangle = E_0^N \left| \tilde{\Psi}_0^N \right\rangle$. The biorthogonal single-particle Green's function of the non-hermitian theory is defined as the biorthogonal expectation value

$$i\tilde{G}_{pq}^{\mathrm{T}}(t_1, t_2) = \langle \tilde{\Psi}_0^N | \mathcal{T}\{a_p(t_1) a_q^\dagger(t_2)\} | \Psi_0^N \rangle \tag{3.3.0.2}$$

where the time-dependence of the field-operators is given by $a_p(t_1) = e^{i\bar{H}t_1} a_p e^{-i\bar{H}t_1}$ as defined in the biorthogonal Heisenberg picture. The notation $\tilde{G}$ is used to indicate that the Green's function is defined with respect to the biorthogonal inner product.

By partitioning the non-hermitian Hamiltonian into an arbitrary reference operator $\bar{H}_0$, and an interaction term $\bar{H}_1 = \bar{H} - \bar{H}_0$, we can use the extended GML theorem (Eq. 3.2.4.7) to write the perturbative expansion for the Green's function as

$$i\tilde{G}_{pq}^{\mathrm{T}}(t_1, t_2) = \langle \tilde{\Phi}_0 | \mathcal{T} \left\{ e^{-i \int_{-\infty}^{\infty} dt \ \bar{H}_1(t)} a_p(t_1) a_q^\dagger(t_2) \right\} | \Phi_0 \rangle_c , \tag{3.3.0.3}$$

where the time-dependence of the field operators is now defined in the biorthogonal Interaction picture: $a_p(t_1) = e^{i\bar{H}_0 t} a_p e^{-i\bar{H}_0 t}$. Here, $|\Phi_0\rangle$ and $\langle\tilde{\Phi}_0|$ are the right and left ground eigenstates of the reference operator, $\bar{H}_0$. We have dropped the implicit limit as $\eta \to 0$ in Eq. 3.2.4.7 for notational simplicity. Eq. 3.3.0.3 immediately gives rise to the exact geometric Dyson series

$$\tilde{G}_{pq}^{\mathrm{T}}(\omega) = \tilde{G}_{pq}^{0,\mathrm{T}}(\omega) + \sum_{rs} \tilde{G}_{pr}^{0,\mathrm{T}}(\omega) \tilde{\Sigma}_{rs}^{\mathrm{T}}(\omega) \tilde{G}_{sq}^{\mathrm{T}}(\omega) \ , \tag{3.3.0.4}$$

where $\tilde{G}^0$ is the non-interacting Green's function of the reference. The non-hermitian self-energy can be exactly written as the sum of the static ($\tilde{\Sigma}_{pq}^{\infty}$) and forward-/backward-time ($\tilde{\Sigma}_{pq}^{\mathrm{F}}(\omega)/\tilde{\Sigma}_{pq}^{\mathrm{B}}(\omega)$) dynamical contributions

$$\tilde{\Sigma}_{pq}^{\mathrm{T}}(\omega) = \tilde{\Sigma}_{pq}^{\infty} + \tilde{\Sigma}_{pq}^{\mathrm{F}}(\omega) + \tilde{\Sigma}_{pq}^{\mathrm{B}}(\omega) \ , \tag{3.3.0.5}$$

and is a functional of the exact biorthogonal single-particle Green's function, $\tilde{\Sigma}[\tilde{G}]$. The 1PI, skeleton and interaction-irreducible diagrams that make up the self-energy functional $\tilde{\Sigma}[\tilde{G}]$ are obtained from effective interactions. These interactions arise when normal-ordering $\bar{H}$ with respect to the biorthogonal ground state expectation value. In this case, the one-body term is given by

$$\begin{aligned}\tilde{F}_{pq} &= \bar{h}_{pq} + \sum_{rs} \bar{v}_{pr,qs}\tilde{\gamma}_{rs} + \frac{1}{(2!)^2}\sum_{rs,tu} \bar{w}_{prs,qtu}\tilde{\Gamma}_{rs,tu} + \frac{1}{(3!)^2}\sum_{rst,uvz} \bar{u}_{prst,quvz}\tilde{\Gamma}_{rst,uvz} + \cdots \\ &= \tilde{f}_{pq} + \sum_{rs} \bar{v}_{pr,qs}\Big(\tilde{\gamma}_{rs} - \tilde{\gamma}^{\mathrm{ref}}_{rs}\Big) + \frac{1}{(2!)^2}\sum_{rs,tu} \bar{w}_{prs,qtu}\tilde{\Gamma}_{rs,tu} + \frac{1}{(3!)^2}\sum_{rst,uvz} \bar{u}_{prst,quvz}\tilde{\Gamma}_{rst,uvz} \\ &+ \cdots \\ &= \tilde{f}_{pq} + \tilde{\Sigma}^{\infty}_{pq} \ ,\end{aligned} \tag{3.3.0.6a}$$

where $\tilde{f}_{pq}$ is the non-hermitian Fock operator, the exact one-particle reduced density matrix is defined as $\tilde{\gamma}_{pq} = \langle\tilde{\Psi}^N_0|a^\dagger_p a_q|\Psi^N_0\rangle$ and the reference one-particle reduced density matrix is $\tilde{\gamma}^{\mathrm{ref}}_{pq} = \langle\tilde{\Phi}_0|a^\dagger_p a_q|\Phi_0\rangle$. The two-body effective interaction is obtained as

$$\bar{V}_{pq,rs} = \bar{v}_{pq,rs} + \sum_{tu} \bar{w}_{pqt,rsu}\tilde{\gamma}_{tu} + \frac{1}{(2!)^2}\sum_{tu,vz} \bar{u}_{pqtu,rsvz}\tilde{\Gamma}_{tu,vz} + \cdots \tag{3.3.0.6b}$$

with the three-body effective interaction

$$\bar{W}_{pqr,stu} = \bar{w}_{pqr,stu} + \sum_{vx} \bar{u}_{pqrv,stux}\tilde{\gamma}_{vx} + \frac{1}{(2!)^2}\sum_{vw,lo} \bar{\kappa}_{pqrvw,stulo}\tilde{\Gamma}_{vw,lo} + \cdots \tag{3.3.0.6c}$$

The four-body effective interaction is

$$\bar{U}_{pqrs,tuvo} = \bar{u}_{pqrs,tuvo} + \sum_{yx} \bar{\kappa}_{pqrsy,tuvox}\tilde{\gamma}_{yx} + \cdots \tag{3.3.0.6d}$$

This procedure is continued up to the N-body interaction. The two-particle biorthogonal reduced density matrix is defined as $\tilde{\Gamma}_{pq,rs} = \langle\tilde{\Psi}^N_0|a^\dagger_p a^\dagger_q a_s a_r|\Psi^N_0\rangle$ and so on for the higher-body equivalents.

We immediately find the exact static component of the non-hermitian self-energy $\tilde{\Sigma}^{\infty}[\tilde{G}]$ as the remainder of the one-body effective interaction, $\bar{F} - \tilde{f}$:

$$\begin{aligned}\tilde{\Sigma}^{\infty}_{pq} = &\sum_{rs} \bar{v}_{pr,qs}\Big(\tilde{\gamma}_{rs} - \gamma^{\mathrm{ref}}_{rs}\Big) + \frac{1}{(2!)^2}\sum_{rs,tu} \bar{w}_{prs,qtu}\tilde{\Gamma}_{rs,tu} \\ &+ \frac{1}{(3!)^2}\sum_{rst,uvz} \bar{u}_{prst,quvz}\tilde{\Gamma}_{rst,uvz} + \cdots\end{aligned} \tag{3.3.0.7}$$

To construct the non-hermitian self-energy functional self-consistently, it must be composed of the effective interactions $\bar{V}$, $\bar{W}$, $\bar{U}$ and so on, which are required in order to generate

interaction-irreducible self-energy diagrams. Therefore, it is these effective interactions that appear as vertices in the self-consistent expression of the self-energy functional, $\tilde{\Sigma}[\tilde{G}]$. Importantly, all effective interactions up to the N-body term are explicitly functionals of the single-particle Green's function. The perturbative expansion for the self-energy $\tilde{\Sigma}[\tilde{G}_0]$ is obtained by expanding both the propagators and effective interactions with respect to the reference Green's function, $\tilde{G}_0$. For the remainder of this work we will focus on generating the interaction-irreducible Feynman diagrams resulting from the coupled-cluster similarity transformed Hamiltonian. However, the analysis presented in this work is general and can be applied to any N-body hermitian or non-hermitian interaction Hamiltonian.

3.4 Coupled-cluster theory

Within coupled-cluster theory, the following ansatz is made for the exact ground state wavefunction of a system of N interacting particles

$$|\Psi_0^N\rangle = e^T |\Phi_0\rangle \ , \tag{3.4.0.1}$$

where $|\Phi_0\rangle$ is the reference determinant. The wave operator T, creates all excitations with respect to the reference determinant and is defined as

$$T = \sum_{ia} t_i^a a_a^\dagger a_i + \frac{1}{(2!)^2} \sum_{ijab} t_{ij}^{ab} a_a^\dagger a_b^\dagger a_j a_i + \frac{1}{(3!)^2} \sum_{ijkabc} t_{ijk}^{abc} a_a^\dagger a_b^\dagger a_c^\dagger a_k a_j a_i + \cdots \tag{3.4.0.2}$$

where $\{t_i^a, t_{ij}^{ab}, t_{ijk}^{abc}, \cdots\}$ are the cluster amplitudes. Using the CC ansatz, we write the non-hermitian CC eigenvalue problem for the right and left eigenstates of the similarity transformed Hamiltonian as

$$\bar{H} |\Phi_0\rangle = E_0^{\mathrm{CC}} |\Phi_0\rangle \quad ; \quad \langle\tilde{\Psi}_0| \bar{H} = \langle\tilde{\Psi}_0| E_0^{\mathrm{CC}} \ , \tag{3.4.0.3}$$

where

$$\bar{H} = e^{-T} H e^T \tag{3.4.0.4}$$

is the similarity transformed Hamiltonian and H is the bare Hamiltonian. Here, we see that the reference $|\Phi_0\rangle$ is the right eigenstate of the similarity transformed Hamiltonian. The left eigenstate is given by $\langle\tilde{\Psi}_0| = \langle\Phi_0| (\mathbb{1} + \Lambda)$, where Λ is the de-excitation operator defined as

$$\Lambda = \sum_{ai} \lambda_a^i a_i^\dagger a_a + \frac{1}{(2!)^2} \sum_{abij} \lambda_{ab}^{ij} a_i^\dagger a_j^\dagger a_b a_a + \frac{1}{(3!)^2} \sum_{abcijk} \lambda_{abc}^{ijk} a_i^\dagger a_j^\dagger a_k^\dagger a_c a_b a_a + \cdots \tag{3.4.0.5}$$

with $\{\lambda_a^i, \lambda_{ab}^{ij}, \lambda_{abc}^{ijk}, \cdots\}$ representing the de-excitation amplitudes. The excitation, de-excitation amplitudes and ground state energy are obtained from minimization of the coupled-cluster Lagrangian [86]

$$\mathcal{L}_0^{\mathrm{CC}}(\mathbf{t}, \lambda) = \langle \tilde{\Psi}_0 | \bar{H} | \Phi_0 \rangle = \langle \Phi_0 | \bar{H} | \Phi_0 \rangle + \sum_\mu \lambda_\mu \langle \Phi_\mu | \bar{H} | \Phi_0 \rangle \ , \tag{3.4.0.6}$$

where $|\Phi_\mu\rangle$ represents the manifold of excited Slater determinants given by $|\Phi_i^a\rangle = a_a^\dagger a_i |\Phi_0\rangle$ etc. Minimization of the Lagrangian gives rise to the excitation and de-excitation amplitude equations

$$\frac{\partial \mathcal{L}_0^{\mathrm{CC}}}{\partial \lambda_\mu} = \langle \Phi_\mu | \bar{H} | \Phi_0 \rangle = 0 \tag{3.4.0.7a}$$

$$\frac{\partial \mathcal{L}_0^{\mathrm{CC}}}{\partial t_\mu} = \langle \Phi_0 | \bar{H} \tau_\mu | \Phi_0 \rangle + \sum_\nu \lambda_\nu \langle \Phi_\nu | [\bar{H}, \tau_\mu] | \Phi_0 \rangle = 0 \tag{3.4.0.7b}$$

where τ_μ is the excitation operator associated with the cluster amplitude t_μ. Once the excitation amplitudes are determined, the ground state energy is simply given by

$$E_0^{\mathrm{CC}} = \langle \tilde{\Psi}_0 | \bar{H} | \Phi_0 \rangle = \langle \Phi_0 | \bar{H} | \Phi_0 \rangle \ . \tag{3.4.0.8}$$

When T is not truncated, the ground state energy obtained from this procedure is formally exact. Importantly, the reference state $|\Phi_0\rangle$ can be constructed such that the singles amplitudes, t_i^a, are zero by construction. This approach is referred to as Brueckner formulation of coupled-cluster (BCC) theory and implies that the reference state has maximum overlap with the exact ground state. BCC theory uses spin-orbitals that are determined by unitary rotation using the singles amplitude equations [118–120].

In terms of the cluster amplitudes and general spin-orbitals, the coupled-cluster ground state energy corresponding to the electronic structure Hamiltonian is given by

$$E_0^{\mathrm{CC}} = E_0^{\mathrm{ref}} + \frac{1}{4} \sum_{ijab} \langle ij || ab \rangle \left(t_{ij}^{ab} + 2 t_i^a t_j^b \right) + \sum_{ia} f_{ia} t_i^a, \tag{3.4.0.9}$$

where E_0^{ref} is the energy of the reference and $\langle pq || rs \rangle = v_{pq,rs} - v_{pq,sr}$ is the anti-symmetrized Coulomb interaction.

The similarity transformed Hamiltonian $\bar{H}$ possesses the same spectrum as the electronic structure Hamiltonian, H. As $\bar{H}$ is non-hermitian but contains a *real* spectrum, it is necessarily pseudo-hermitian (see Appendix B.5). This fact is not commonly expressed in the literature on coupled-cluster theory. Additionally, $\bar{H}$ is not $\mathcal{PT}$-symmetric, in

contrast to most of the Hamiltonians studied in the literature on non-hermitian quantum systems [67, 69–71, 78, 115, 116, 121].

In ionization potential/electron affinity equation-of-motion coupled-cluster (IP/EA-EOM-CC) theory, the charged excitation energies are obtained by diagonalization of the similarity transformed Hamiltonian expressed in the basis of all Slater determinants containing $(N \pm 1)$-electrons. This is exactly equivalent to a Configuration Interaction expansion of $\bar{H}$. Focusing on the removal energies, the IP-EOM-CC eigenvalue problem can be written as [4, 85]

$$[\bar{H}, R_\nu^{\mathrm{IP}}] \left|\Phi_0\right\rangle = -\varepsilon_\nu^{N-1} R_\nu^{\mathrm{IP}} \left|\Phi_0\right\rangle, \tag{3.4.0.10}$$

where $R_\nu^{\mathrm{IP}} \left|\Phi_0\right\rangle$ is the right $(N-1)$-particle eigenstate of $\bar{H}$, $\left|\Psi_\nu^{N-1}\right\rangle$. In IP-EOM-CC theory, the operator creates all determinants consisting of $(N-1)$ electrons:

$$R_\nu^{\mathrm{IP}} = \sum_i r_i(\nu) a_i + \sum_{i<j,a} r_{ij}^a(\nu) a_a^\dagger a_j a_i + \cdots \tag{3.4.0.11}$$

The IP-EOM-CC eigenvalue problem is written in matrix form in terms of the non-Hermitian supermatrix:

$$\bar{\mathbf{H}}^{\text{IP-EOM-CC}} = -\begin{pmatrix} \langle\Phi_i|\bar{H}_N|\Phi_j\rangle & \langle\Phi_i|\bar{H}_N|\Phi_{kl}^a\rangle & \cdots \\ \langle\Phi_{mn}^b|\bar{H}_N|\Phi_j\rangle & \langle\Phi_{mn}^b|\bar{H}_N|\Phi_{kl}^a\rangle & \cdots \\ \vdots & \vdots & \ddots \end{pmatrix}, \tag{3.4.0.12}$$

where $\bar{H}_N = \bar{H} - E_0^{\mathrm{CC}}$, with $\left|\Phi_i\right\rangle = a_i \left|\Phi_0\right\rangle$, $\left|\Phi_{ij}^a\right\rangle = a_a^\dagger a_j a_i \left|\Phi_0\right\rangle$, and so on. An analogous supermatrix for the EA-EOM-CC eigenvalue problem can also be constructed. In IP/EA-EOM-CC theory, the ionization potential and electron affinity sectors are automatically decoupled as the formalism is based on Configuration Interaction expansions of $\bar{H}$. This approach to obtaining charged excitation spectra can be made to be formally exact, but is distinct from the diagrammatic Green's function formalism which does not decouple the ionization potential and electron affinity sectors.

3.4.1 The similarity transformed Hamiltonian

The analysis of the effective interactions generated by the CC similarity transformed Hamiltonian will be crucial when constructing the perturbative and renormalized expansions of the coupled-cluster self-energy and Bethe-Salpeter kernel in Sections 3.7, 3.8 and 3.12.

The full similarity transformed Hamiltonian is an N-body operator written as

$$\begin{aligned}\bar{H} &= \bar{h} + \bar{V} + \bar{W} + \cdots \\ &= \sum_{pq} \bar{h}_{pq} a_p^\dagger a_q + \frac{1}{(2!)^2} \sum_{pq,rs} \bar{h}_{pq,rs} a_p^\dagger a_q^\dagger a_s a_r + \frac{1}{(3!)^2} \sum_{pqr,stu} \bar{h}_{pqr,stu} a_p^\dagger a_q^\dagger a_r^\dagger a_u a_t a_s + \cdots ,\end{aligned} \tag{3.4.1.1}$$

where $\{\bar{h}_{pq}, \bar{h}_{pq,rs}, \bar{h}_{pqr,stu}, \cdots\}$ are the one-body, antisymmetrized two-body, three-body and so on matrix elements. Using the notation of Ref. [4], in Appendix B.2 we normal-order this Hamiltonian with respect to the reference determinant to give [85]

$$\begin{aligned}\bar{H} = E_0^{\mathrm{CC}} &+ \sum_{pq} F_{pq} \{a_p^\dagger a_q\}_0 + \frac{1}{(2!)^2} \sum_{pq,rs} \chi_{pq,rs} \{a_p^\dagger a_q^\dagger a_s a_r\}_0 \\ &+ \frac{1}{(3!)^2} \sum_{pqr,stu} \chi_{pqr,stu} \{a_p^\dagger a_q^\dagger a_r^\dagger a_u a_t a_s\}_0 + \cdots\end{aligned} \tag{3.4.1.2}$$

where the notation $\{\cdots\}_0$ indicates normal-ordering with respect to the reference, $|\Phi_0\rangle$. The set of effective interaction matrix elements $\{F_{pq}, \chi_{pq,rs}, \chi_{pqr,stu}, \cdots\}$, up to the four-body effective interaction, can be found in Refs [85] and [122]. This is the conventional normal-ordering of $\bar{H}$ usually presented in the context of coupled-cluster theory and is central to the perturbative expansion of the irreducible coupled-cluster self-energy and Bethe-Salpeter kernel with respect to the reference Green's function.

However, in Appendix B.2 we also normal-order the Hamiltonian with respect to the biorthogonal expectation value $\langle\Phi_0|\Phi_0\rangle_{bo} := \langle\tilde{\Psi}_0|\Phi_0\rangle$, defined in Section 3.2, to give

$$\begin{aligned}\bar{H} = E_0^{\mathrm{CC}} &+ \sum_{pq} \tilde{F}_{pq} \{a_p^\dagger a_q\} + \frac{1}{(2!)^2} \sum_{pq,rs} \tilde{\Xi}_{pq,rs} \{a_p^\dagger a_q^\dagger a_s a_r\} \\ &+ \frac{1}{(3!)^2} \sum_{pqr,stu} \tilde{\chi}_{pqr,stu} \{a_p^\dagger a_q^\dagger a_r^\dagger a_u a_t a_s\} + \cdots\end{aligned} \tag{3.4.1.3}$$

to the best of our knowledge, this normal-ordering of $\bar{H}$ has not been reported in the literature before. It is this normal-ordering that will be central to the development of the self-consistent Green's function formalism within coupled-cluster theory. The relationship between all matrix elements $\{\bar{h}_{pq}, \bar{h}_{pq,rs}, \bar{h}_{pqr,stu}, \cdots\}$, $\{F_{pq}, \chi_{pq,rs}, \chi_{pqr,stu}, \cdots\}$ and $\{\tilde{F}_{pq}, \tilde{\Xi}_{pq,rs}, \tilde{\chi}_{pqr,stu}, \cdots\}$ is derived in Appendix B.2. The coupled-cluster amplitude equations are given by the effective interaction elements $\{F_{ai}, \chi_{ab,ij}, \chi_{abc,ijk}, \cdots\}$ which all evaluate to zero at convergence [85]. Since these effective interaction elements vanish, the interaction elements $\{\tilde{F}_{ai}, \tilde{\Xi}_{ab,ij}, \tilde{\chi}_{abc,ijk}, \cdots\}$ also evaluate to zero [4, 7]. All effective interaction matrix elements with four or more lines below the vertex, apart from the two-body

terms $\chi_{ij,ab}$ and $\tilde{\Xi}_{ij,ab}$, vanish as a result of the coupled-cluster similarity transformation. Finally, it is useful to split the similarity transformed Hamiltonian into two terms

$$\begin{aligned}\bar{H} &= F + \bar{H}_1 \\ &= \sum_{pq} f_{pq} a_p^\dagger a_q + \sum_{pq} (\bar{h}_{pq} - f_{pq}) a_p^\dagger a_q + \frac{1}{(2!)^2} \sum_{pq,rs} \bar{h}_{pq,rs} a_p^\dagger a_q^\dagger a_s a_r \\ &+ \frac{1}{(3!)^2} \sum_{pqr,stu} \bar{h}_{pqr,stu} a_p^\dagger a_q^\dagger a_r^\dagger a_u a_t a_s + \cdots\end{aligned} \tag{3.4.1.4}$$

where F is the Fock operator and $\bar{H}_1 = \bar{H} - F$, is the N-body operator containing all the interactions and effects introduced by the similarity transformed Hamiltonian.

3.5 The coupled-cluster representation of the electronic Green's function

As defined in Chapter 2, the zero temperature single-particle electronic Green's function of the hermitian, two-body electronic structure Hamiltonian H, is defined as

$$iG_{pq}^{\mathrm{T}}(t_1 - t_2) = \langle \Psi_0^N | \mathcal{T} \left\{ a_p(t_1) a_q^\dagger(t_2) \right\} | \Psi_0^N \rangle \tag{3.5.0.1}$$

where $|\Psi_0^N\rangle$ is the exact N-electron ground state wavefunction and the time-dependence of the field operators is governed by the electronic structure Hamiltonian: $a_p(t) = e^{iHt} a_p e^{-iHt}$.

Attempts at combining coupled-cluster theory with the Green's function formalism have largely focused on *direct computation* of Eq. 3.5.0.1 for the electronic Green's function using coupled-cluster theory [87–90]. The coupled-cluster representation of the time-domain electronic Green's function can be obtained from the biorthogonal theory developed in Section 3.2 and is written as

$$i\bar{G}_{pq}^{\mathrm{T}}(t_1 - t_2) = \langle \tilde{\Psi}_0 | \mathcal{T} \left\{ \bar{a}_p(t_1) \bar{a}_q^\dagger(t_2) \right\} | \Phi_0 \rangle \ , \tag{3.5.0.2}$$

where $\bar{a}_p(t_1) = e^{i\bar{H}t} \bar{a}_p e^{-i\bar{H}t}$, $\bar{a}_q^\dagger(t_1) = e^{i\bar{H}t} \bar{a}_q^\dagger e^{-i\bar{H}t}$ with $\bar{a}_p = e^{-T} a_p e^T$ and $\bar{a}_p^\dagger = e^{-T} a_p^\dagger e^T$, respectively. The notation $\bar{G}$ is chosen to distinguish the coupled-cluster representation of the electronic Green's function from the electronic Green's function, denoted by G. Performing the similarity transformation on the operators leads to

$$\begin{aligned}\bar{a}_p(t_1) &= a_p(t_1) + e^{i\bar{H}t_1} [a_p, T] e^{-i\bar{H}t_1} \\ &= a_p(t_1) + [a_p, T](t_1) \ ,\end{aligned} \tag{3.5.0.3}$$

where $[a_p, T](t_1) = e^{i\bar{H}t_1}[a_p, T]e^{-i\bar{H}t_1}$. Inserting this relation into the time-ordered expectation value gives

$$\begin{aligned} i\bar{G}^{\mathrm{T}}_{pq}(t_1 - t_2) = &\langle\tilde{\Psi}_0|\mathcal{T}\left\{a_p(t_1)a_q^\dagger(t_2)\right\}|\Phi_0\rangle + \langle\tilde{\Psi}_0|\mathcal{T}\left\{[a_p, T](t_1)a_q^\dagger(t_2)\right\}|\Phi_0\rangle \\ &+ \langle\tilde{\Psi}_0|\mathcal{T}\left\{a_p(t_1)[a_q^\dagger, T](t_2)\right\}|\Phi_0\rangle + \langle\tilde{\Psi}_0|\mathcal{T}\left\{[a_p, T](t_1)[a_q^\dagger, T](t_2)\right\}|\Phi_0\rangle \ . \end{aligned} \tag{3.5.0.4}$$

Due to the commutator of the creation/annihilation operators with T, it is clear that the coupled-cluster representation of the electronic single-particle Green's function is in fact a collection of 'many-particle' Green's functions of specified time-orderings, including up to the N-body Green's function. However, the occupied–virtual (ia) part of the coupled-cluster representation of the electronic Green's function is in fact a single-particle propagator:

$$i\bar{G}^{\mathrm{T}}_{ia}(t_1 - t_2) = \langle\tilde{\Psi}_0|\mathcal{T}\left\{\bar{a}_i(t_1)\bar{a}_a^\dagger(t_2)\right\}|\Phi_0\rangle = \langle\tilde{\Psi}_0|\mathcal{T}\left\{a_i(t_1)a_a^\dagger(t_2)\right\}|\Phi_0\rangle \ . \tag{3.5.0.5}$$

This is because $[a_i, T] = [a_a^\dagger, T] = 0$, remembering that i and a index occupied and virtual spin-orbitals as defined in Section 2.1 of Chapter 2. Through Eq. 3.5.0.4, we see that the full coupled-cluster representation of the electronic Green's function is a complicated combination of many-body Green's functions. However, the many-body Green's functions are explicitly coupled to each other through their exact equations of motion (see Section 3.8) and it is exactly this hierarchy of coupled many-body Green's functions that we want to decouple by introduction of the coupled-cluster self-energy.

To obtain the spectral form of the coupled-cluster representation of the electronic Green's function, we take the Fourier transform of Eq. 3.5.0.2, resolving the identity of $(N \pm 1)$-particle eigenstates of $\bar{H}$, to give:

$$\begin{aligned} \bar{G}_{pq}(\omega) = &\sum_\mu \frac{\langle\tilde{\Psi}_0|\bar{a}_p|\bar{\Psi}_\mu^{N+1}\rangle\langle\tilde{\Psi}_\mu^{N+1}|\bar{a}_q^\dagger|\Phi_0\rangle}{\omega - \varepsilon_\mu^{N+1} + i\eta} \\ &+ \sum_\nu \frac{\langle\tilde{\Psi}_0|\bar{a}_q^\dagger|\bar{\Psi}_\nu^{N-1}\rangle\langle\tilde{\Psi}_\nu^{N-1}|\bar{a}_p|\Phi_0\rangle}{\omega - \varepsilon_\nu^{N-1} - i\eta} \ , \end{aligned} \tag{3.5.0.6}$$

where $\varepsilon_\mu^{N+1} = E_\mu^{N+1} - E_0^N$ and $\varepsilon_\nu^{N-1} = E_0^N - E_\nu^{N-1}$ are the exact addition and removal energies of the system of interacting electrons, within a complete basis when T is not truncated. This is the expression that was first presented by Nooijen and Snijders in Refs [87, 88].

In principle, knowledge of the exact coupled-cluster representation of the electronic Green's function gives the exact single-particle spectrum, coupled-cluster ground state

energy as well as the non-hermitian one-particle reduced density matrix

$$\bar{\gamma}_{pq} = -i\bar{G}^{\mathrm{T}}_{qp}(t - t^{+}) = \langle\tilde{\Psi}_0|\bar{a}^{\dagger}_{p}\bar{a}_{q}|\Phi_0\rangle \ . \tag{3.5.0.7}$$

However, it should be noted that calculation of the ground state energy at any level of approximation for the coupled-cluster representation of the electronic Green's function results in a different ground state energy from that obtained at the same level of approximation of the ground state coupled-cluster equations [87, 88, 99].

Formally the Dyson equation for the coupled-cluster representation of the electronic Green's function is written as

$$\bar{G}^{\mathrm{T}}_{pq}(\omega) = G^{0,\mathrm{T}}_{pq}(\omega) + \sum_{rs} G^{0,\mathrm{T}}_{pr}(\omega)\bar{\Sigma}^{\mathrm{T}}_{rs}(\omega)\bar{G}^{\mathrm{T}}_{sq}(\omega) \ . \tag{3.5.0.8}$$

However, it is important to note that the 'self-energy', $\bar{\Sigma}$, is not the same object as the electronic self-energy, Σ [4]. This is because $\bar{\Sigma}$ is an object that connects G_0 to $\bar{G}$ rather than G of the hermitian electronic structure Hamiltonian. As a result the coupled-cluster self-energy is non-hermitian. Due to the fact that the coupled-cluster representation of the electronic Green's function introduces a fundamental coupling to every N-particle Green's function, the 'self-energy' $\bar{\Sigma}$ entering Eq. 3.5.0.8 cannot be defined in the diagrammatic way as the set of all 1PI diagrams. Therefore, the coupled-cluster representation of the electronic Green's function, $\bar{G}$, does not concern the diagrammatic coupled-cluster self-energy and therefore does not fully connect Green's function and coupled-cluster theories.

3.6 The single-particle coupled-cluster Green's function and self-energy

In this work, we take the similarity transformed Hamiltonian as the fundamental interaction Hamiltonian and use the biorthogonal formulation for non-hermitian Hamiltonians to define the *single-particle* coupled-cluster Green's function (SP-CCGF) as

$$i\tilde{G}^{\mathrm{T}}_{pq}(t_1 - t_2) = \langle\tilde{\Psi}_0|\mathcal{T}\left\{a_p(t_1)a^{\dagger}_{q}(t_2)\right\}|\Phi_0\rangle \ , \tag{3.6.0.1}$$

where the time-dependence of the operators is governed by the similarity transformed Hamiltonian, $\bar{H}$ via Eq. 3.2.2.5. We note that $\bar{G}_{ia}(\omega) = \tilde{G}_{ia}(\omega)$. This is a single-particle propagator that remains coupled to all higher-order many-body Green's function through

its equation-of-motion. It will subsequently be shown that this propagator also contains the exact charged excitation spectrum as well as the coupled-cluster ground-state correlation energy through its associated self-energy. As we will show, this change of perspective allows us to define the irreducible coupled-cluster self-energy directly using techniques from Green's function theory. In the following we refer to G as the electronic Green's function, $\bar{G}$ as the coupled-cluster representation of the electronic Green's function and $\tilde{G}$ as the single-particle coupled-cluster Green's function.

3.6.1 Lehmann representation of the single-particle coupled-cluster Green's function

The explicit *single-particle* coupled-cluster Green's function is defined in Eq. 3.6.0.1. By expanding the time-ordered product, resolving the identity of $(N \pm 1)$-particle eigenstates of $\bar{H}$ and taking the Fourier transform, we find the Lehmann representation of the SP-CCGF:

$$\tilde{G}^{\mathrm{T}}_{pq}(\omega) = \sum_{\mu} \frac{\langle \tilde{\Psi}_0 | a_p | \Psi^{N+1}_{\mu} \rangle \langle \tilde{\Psi}^{N+1}_{\mu} | a^{\dagger}_q | \Phi_0 \rangle}{\omega - \varepsilon^{N+1}_{\mu} + i\eta} + \sum_{\nu} \frac{\langle \tilde{\Psi}_0 | a^{\dagger}_q | \Psi^{N-1}_{\nu} \rangle \langle \tilde{\Psi}^{N-1}_{\nu} | a_p | \Phi_0 \rangle}{\omega - \varepsilon^{N-1}_{\nu} - i\eta} \ . \quad (3.6.1.1)$$

We immediately see that the SP-CCGF contains the exact single-particle spectrum and we will subsequently show how the associated self-energy also contains the exact ground state energy. The only difference between the SP-CCGF and the coupled-cluster representation of the electronic Green's function (Eq. 3.5.0.6) arises in the form of the residues, which in the coupled-cluster representation are different due to the explicit contribution of the higher-order N-particle Green's functions. We introduce the residues of the coupled-cluster propagator defined in Eq. 3.6.1.1 as $\bar{Y}^{\mu}_p = \langle \tilde{\Psi}^{N+1}_{\mu} | a^{\dagger}_p | \Phi_0 \rangle$, $\tilde{Y}^{\mu}_p = \langle \tilde{\Psi}_0 | a_p | \Psi^{N+1}_{\mu} \rangle$, $\bar{X}^{\nu}_p = \langle \tilde{\Psi}^{N-1}_{\nu} | a_p | \Phi_0 \rangle$ and $\tilde{X}^{\nu}_p = \langle \tilde{\Psi}_0 | a^{\dagger}_p | \Psi^{N-1}_{\nu} \rangle$, and re-write the single-particle coupled-cluster Green's function as

$$\tilde{G}^{\mathrm{T}}_{pq}(\omega) = \sum_{\mu} \frac{\tilde{Y}^{\mu}_p \bar{Y}^{\mu}_q}{\omega - \varepsilon^{N+1}_{\mu} + i\eta} + \sum_{\nu} \frac{\tilde{X}^{\nu}_q \bar{X}^{\nu}_p}{\omega - \varepsilon^{N-1}_{\nu} - i\eta} \ . \quad (3.6.1.2)$$

The four blocks of the SP-CCGF are given by:

$$\tilde{G}^{\mathrm{T}}_{ij}(\omega) = \sum_{\nu} \frac{\tilde{X}^{\nu}_j \bar{X}^{\nu}_i}{\omega - \varepsilon^{N-1}_{\nu} - i\eta} \quad (3.6.1.3a)$$

$$\tilde{G}^{\mathrm{T}}_{ab}(\omega) = \sum_{\mu} \frac{\tilde{Y}^{\mu}_a \bar{Y}^{\mu}_b}{\omega - \varepsilon^{N+1}_{\mu} + i\eta} \quad (3.6.1.3b)$$

$$\tilde{G}^{\mathrm{T}}_{ia}(\omega) = \sum_{\mu} \frac{\tilde{Y}^{\mu}_i \bar{Y}^{\mu}_a}{\omega - \varepsilon^{N+1}_{\mu} + i\eta} + \sum_{\nu} \frac{\tilde{X}^{\nu}_a \bar{X}^{\nu}_i}{\omega - \varepsilon^{N-1}_{\nu} - i\eta} \quad (3.6.1.3c)$$

$$\tilde{G}^{\mathrm{T}}_{ai}(\omega) = 0 \ . \quad (3.6.1.3d)$$

Note that $\bar{Y}_i^\mu = \bar{X}_a^\nu = 0$. Therefore, we see that the occupied block contains only backward time contributions, the virtual block contains only forward time contributions, the occupied–virtual block contains both forward and backward time contributions and that the virtual–occupied block vanishes.

3.6.2 The irreducible coupled-cluster self-energy

The perturbative expression for the SP-CCGF is given by

$$i\tilde{G}^{\mathrm{T}}_{pq}(t_1 - t_2) = \langle \Phi_0 | \mathcal{T} \left\{ e^{-i\int_{-\infty}^{\infty} dt \bar{H}_1(t)} a_p(t_1) a_q^\dagger(t_2) \right\} | \Phi_0 \rangle_c, \tag{3.6.2.1}$$

where the operators are implicitly defined in the Heisenberg picture in the first equality and the interaction picture in the perturbative expansion: $a_p(t_1) = e^{iFt} a_p e^{-iFt}$. We have dropped the implicit limit of $\eta \to 0$. This procedure was outlined in Section 3.2 and results in a diagrammatic perturbation theory for the Green's function. The set of diagrams generated by Eq. 3.6.2.1 is reduced by collecting all 1PI diagrams and performing a geometric series summation through the coupled-cluster Dyson equation

$$\tilde{G}^{\mathrm{T}}_{pq}(\omega) = G^{0,\mathrm{T}}_{pq}(\omega) + \sum_{rs} G^{0,\mathrm{T}}_{pr}(\omega) \tilde{\Sigma}^{\mathrm{T}}_{rs}(\omega) \tilde{G}^{\mathrm{T}}_{sq}(\omega), \tag{3.6.2.2}$$

where $G^0_{pq}(\omega)$ is the reference Green's function of the Fock operator and $\tilde{\Sigma}_{pq}(\omega)$ is the coupled-cluster self-energy. As $\tilde{G}_{ia} = \bar{G}_{ia}$, it should be noted that $\tilde{\Sigma}_{ia} = \bar{\Sigma}_{ia}$.

From the Lehmann representation of the coupled-cluster Green's function (Eq. 3.6.1.1), we immediately identify the spectral form of the coupled-cluster self-energy as [4]

$$\begin{aligned} \tilde{\Sigma}^{\mathrm{T}}_{pq}(\omega) &= \tilde{\Sigma}^{\infty}_{pq} + \tilde{\Sigma}^{\mathrm{F}}_{pq}(\omega) + \tilde{\Sigma}^{\mathrm{B}}_{pq}(\omega) \\ &= \tilde{\Sigma}^{\infty}_{pq} + \sum_{JJ'} \tilde{U}_{pJ} \left[(\omega + i\eta)\mathbb{1} - (\bar{\mathbf{K}}^{>} + \bar{\mathbf{C}}^{>}) \right]^{-1}_{JJ'} \bar{U}_{J'q} \\ &\quad + \sum_{AA'} \bar{V}_{pA} \left[(\omega - i\eta)\mathbb{1} - (\bar{\mathbf{K}}^{<} + \bar{\mathbf{C}}^{<}) \right]^{-1}_{AA'} \tilde{V}_{A'q} \end{aligned} \tag{3.6.2.3}$$

where the indices JJ'/AA' label forward-time/backward-time multi-particle-hole ISCs. The matrices $\bar{\mathbf{K}}^{>}_{JJ'} + \bar{\mathbf{C}}^{>}_{JJ'}$ and $\bar{\mathbf{K}}^{<}_{AA'} + \bar{\mathbf{C}}^{<}_{AA'}$ represent the interactions between the different ISCs mediated by the similarity transformed Hamiltonian. The $\bar{\mathbf{K}}$-matrices are block-diagonal by definition ($\bar{\mathbf{K}}^{>}_{JJ'} = \bar{\mathbf{K}}^{>}_{JJ}\delta_{JJ'}$). The quantities $\tilde{U}_{pJ}/\bar{U}_{Jp}$ and $\bar{V}_{pJ}/\tilde{V}_{Ap}$ represent

the coupling matrices that link initial and final single-particle states to the different ISCs. For the occupied-occupied block of the self-energy we have

$$\tilde{\Sigma}^{\mathrm{T}}_{ij}(\omega) = \tilde{\Sigma}^{\infty}_{ij} + \sum_{AA'} \bar{V}_{iA} \left[(\omega - i\eta)\mathbb{1} - (\bar{\mathbf{K}}^{<} + \bar{\mathbf{C}}^{<})\right]^{-1}_{AA'} \tilde{V}_{A'j}. \tag{3.6.2.4}$$

The occupied block of the coupled-cluster self-energy only contains poles above the real axis and is a consequence of backward time propagation alone. The self-energy of the virtual-virtual block is

$$\tilde{\Sigma}^{\mathrm{T}}_{ab}(\omega) = \tilde{\Sigma}^{\infty}_{ab} + \sum_{JJ'} \tilde{U}_{aJ} \left[(\omega + i\eta)\mathbb{1} - (\bar{\mathbf{K}}^{>} + \bar{\mathbf{C}}^{>})\right]^{-1}_{JJ'} \bar{U}_{J'b} \tag{3.6.2.5}$$

and contains poles only beneath the real axis resulting from forward time propagation only. The self-energy of the occupied-virtual block contains the combined forward and backward propagation and has poles both above and below the real axis as

$$\begin{aligned} \tilde{\Sigma}^{\mathrm{T}}_{ia}(\omega) = \tilde{\Sigma}^{\infty}_{ia} &+ \sum_{JJ'} \tilde{U}_{iJ} \left[(\omega + i\eta)\mathbb{1} - (\bar{\mathbf{K}}^{>} + \bar{\mathbf{C}}^{>})\right]^{-1}_{JJ'} \bar{U}_{J'a} \\ &+ \sum_{AA'} \bar{V}_{iA} \left[(\omega - i\eta)\mathbb{1} - (\bar{\mathbf{K}}^{<} + \bar{\mathbf{C}}^{<})\right]^{-1}_{AA'} \tilde{V}_{A'a}. \end{aligned} \tag{3.6.2.6}$$

As $\tilde{G}_{ai}(\omega) = 0$, the self-energy of the virtual-occupied block also vanishes: $\tilde{\Sigma}_{ai}(\omega) = 0$. An important limit is when the cluster operator vanishes, *i.e.* $T = 0$ ($\tilde{G} \to G$). In this case, the coupled-cluster Dyson equation (Eq. 3.6.2.2) reduces to the electronic Dyson equation, where H_1 is the bare two-body Coulomb interaction subtracted by the HF potential. The coupled-cluster self-energy reduces to the two-body electronic self-energy.

For the rest of this Chapter the Green's function and self-energy components are implicitly taken to be real-time-ordered.

3.7 Diagrammatic perturbation expansion of the coupled-cluster self-energy

In this section, we derive the perturbative diagrammatic expansion of the coupled-cluster self-energy functional, $\tilde{\Sigma}[G_0]$, to third-order. The number of diagrams in the perturbative expansion for the coupled-cluster self-energy may be reduced by restricting the diagrammatic expansion to contain only interaction-irreducible diagrams [20]. This results in a combined series that involves renormalization of the propagators and interaction vertices. Diagrams are referred to as interaction-reducible when they can be split into

two diagrams by cutting an interaction vertex into two parts [20, 36]. As long as only interaction-irreducible diagrams are included, where all propagators are dressed, the diagrammatic expansion for the coupled-cluster self-energy is equivalent to replacing the perturbation $\bar{H}_1$ in Eq. 3.6.2.1 with the effective interaction

$$\tilde{\bar{H}}_1 = \sum_{pq}(\tilde{F}_{pq} - f_{pq})a_p^\dagger a_q + \frac{1}{(2!)^2}\sum_{pq,rs}\tilde{\Xi}_{pq,rs}a_p^\dagger a_q^\dagger a_s a_r + \frac{1}{(3!)^2}\sum_{pqr,stu}\tilde{\chi}_{pqr,stu}a_p^\dagger a_q^\dagger a_r^\dagger a_u a_t a_s + \cdots \tag{3.7.0.1}$$

obtained from the normal-ordering of the similarity transformed Hamiltonian with respect to the biorthogonal ground state expectation value (Eq. 3.4.1.3). Obtaining the perturbative expression for the coupled-cluster self-energy in terms of effective interactions resulting from normal-ordering with respect to the reference $|\Phi_0\rangle$, requires the relationships between the effective interactions, which are defined in Appendices B.2 and B.4. The effective interactions arising from normal-ordering with respect to the reference arise when expanding the self-energy with respect to the reference Green's function, G_0. Therefore, the self-energy expansion with respect to the non-interacting propagator is obtained by the expansion of interaction-irreducible interactions that enter 1PI, skeleton self-energy diagrams.

In the following, we employ the antisymmetrized Hugenholtz-Shavitt-Bartlett diagram convention [123]. Diagrammatically, the effective interactions that arise when normal-ordering the Hamiltonian with respect to the reference state are represented by

$= \chi_{pq,rs}$,

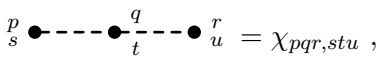

$= \chi_{pqr,stu}$,

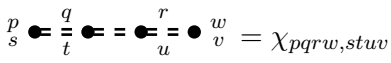

$= \chi_{pqrw,stuv}$,

and so on for the higher-body terms. The effective interactions that arise from normal-ordering the Hamiltonian with respect to the biorthogonal expectation value are obtained by contracting the diagrams above with the corresponding λ-matrices as outlined in Appendix B.2.

3.7.1 First-order diagrams

The first-order contribution to the perturbative expansion is the static term [4]

$$\tilde{\Sigma}^{\infty(0)}_{pq}[G_0] = \quad = \quad F_{pq} - f_{pq} \ . \tag{3.7.1.1}$$

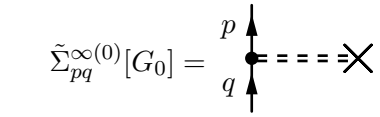

This term was derived in Ref. [4] as the first contribution to the functional derivative of the BCC Lagrangian with respect to the non-interacting Green's function. However, Eq. 3.7.1.1 represents the generalization to coupled-cluster theory formulated about an arbitrary reference state.

Depending on the external time-orderings of the legs, this self-energy contains different sets of diagrams. For simplicity, we take the reference to be the HF state such that the reference Green's function is the HF Green's function. Focusing on the occupied-occupied contribution, we have

$$\tilde{\Sigma}^{\infty(0)}_{ij} = \quad = \quad + \quad + \tag{3.7.1.2}$$

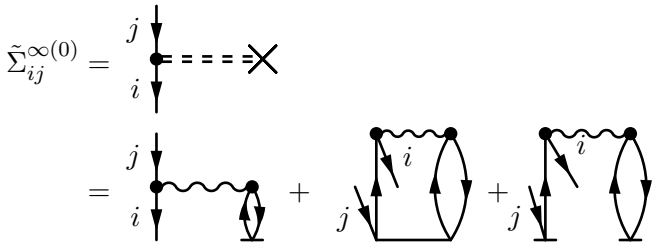

where we have employed the standard Goldstone diagram notation of Ref. [85]. This set of Goldstone diagrams corresponds to the equation

$$\tilde{\Sigma}^{\infty(0)}_{ij} = \frac{1}{2}\sum_{kab} \langle ik||ab\rangle \left(t^{ab}_{jk} + 2t^a_j t^b_k\right) + \sum_{ka} \langle ik||ja\rangle \, t^a_k \ . \tag{3.7.1.3}$$

Likewise, the first-order self-energy of the virtual-virtual states is given by

$$\tilde{\Sigma}^{\infty(0)}_{ab} = \quad = \quad + \quad + \tag{3.7.1.4}$$

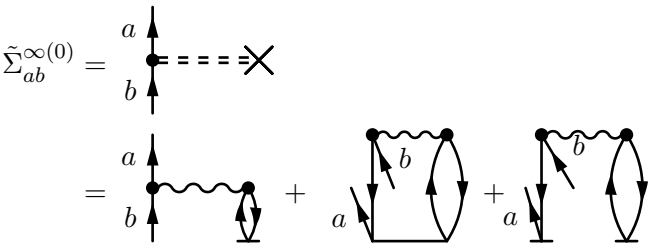

which are written as

$$\tilde{\Sigma}^{\infty(0)}_{ab} = -\frac{1}{2}\sum_{ijc} \langle ij||bc\rangle \left(t^{ac}_{ij} + 2t^a_i t^c_j\right) + \sum_{kc} \langle ak||bc\rangle \, t^c_k \ . \tag{3.7.1.4}$$

The contribution to the occupied-virtual block is given by $\tilde{\Sigma}_{ai}^{\infty(0)} = \langle \Phi_i^a | \bar{H} | \Phi_0 \rangle = 0$, which are the singles amplitude equations. The virtual–occupied self-energy contribution is given by

$\tilde{\Sigma}_{ia}^{\infty(0)} =$  $= \sum_{kb} \langle ik||ab\rangle \, t_k^b \ .$

These terms represent the most important 1PI contribution to the coupled-cluster self-energy [4]. It should be noted that if we work with the Brueckner reference, the first-order contribution decouples the IP/EA sectors of the self-energy. From this analysis, we see the general feature of the coupled-cluster self-energy in that it combines Feynman diagrams in terms of propagators with Goldstone diagrams that represent the interaction vertices arising from the similarity transformed Hamiltonian. When the similarity transformation is not present ($T = 0$), our expression reduces to the perturbative electronic self-energy expansion and hence $\tilde{\Sigma}_{pq}^{T=0,\infty(0)} = \Sigma_{pq}^{\infty(0)} = 0$ as required.

3.7.2 Second-order diagrams

At second-order, both static and frequency-dependent terms arise. The only explicitly frequency-dependent second-order perturbative contribution to the coupled-cluster self-energy is the diagram

$\tilde{\Sigma}^{(2)}[G_0] =$ 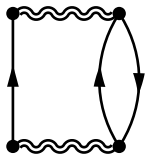 (3.7.2.1)

Fixing the external indices, the Feynman diagram contains two contributions corresponding to forward and backward time orderings

$$\tilde{\Sigma}_{pq}^{(2)}(\omega) = \frac{1}{2}\left(\sum_{abi} \frac{\chi_{pi,ab}\chi_{ab,qi}}{\omega + \epsilon_i - \epsilon_a - \epsilon_b + i\eta} + \sum_{ija} \frac{\chi_{pa,ij}\chi_{ij,qa}}{\omega + \epsilon_a - \epsilon_i - \epsilon_j - i\eta} \right) . \tag{3.7.2.2}$$

If both external indices are in the occupied space, we have

$$\tilde{\Sigma}_{ij}^{(2)}(\omega) = \frac{1}{2}\left(\sum_{kab} \frac{\chi_{ik,ab}\chi_{ab,jk}}{\omega + \epsilon_k - \epsilon_a - \epsilon_b + i\eta} + \sum_{kla} \frac{\chi_{ia,kl}\chi_{kl,ja}}{\omega + \epsilon_a - \epsilon_k - \epsilon_l - i\eta} \right) . \tag{3.7.2.3}$$

However, since the matrix element $\chi_{ab,jk} = \langle \Phi_{jk}^{ab} | \bar{H} | \Phi_0 \rangle = 0$ via the amplitude equations, the forward time contribution of the second-order self-energy vanishes. Therefore, we are left with

$$\tilde{\Sigma}_{ij}^{(2)}(\omega) = \frac{1}{2} \sum_{kla} \frac{\chi_{ia,kl}\chi_{kl,ja}}{\omega + \epsilon_a - \epsilon_k - \epsilon_l - i\eta} \ . \tag{3.7.2.4}$$

Likewise, the second-order contribution to the virtual-virtual block is

$$\tilde{\Sigma}^{(2)}_{ab}(\omega) = \frac{1}{2}\sum_{cdk} \frac{\chi_{ak,cd}\chi_{cd,bk}}{\omega + \epsilon_k - \epsilon_c - \epsilon_d + i\eta} \,. \tag{3.7.2.5}$$

In this case, the backward time-contribution vanishes due to the doubles amplitude equations $\chi_{ac,ij} = 0$. Turning to the second-order contribution corresponding to hole to particle propagation we have $\tilde{\Sigma}^{(2)}_{ai} = 0$. This is because both $\chi_{bc,ij} = \chi_{ab,jk} = 0$. However, both time-orderings remain in the particle to hole block

$$\tilde{\Sigma}^{(2)}_{ia}(\omega) = \frac{1}{2}\left(\sum_{bcj} \frac{\chi_{ij,bc}\chi_{bc,aj}}{\omega + \epsilon_j - \epsilon_b - \epsilon_c + i\eta} + \sum_{jkb} \frac{\chi_{ib,jk}\chi_{jk,ab}}{\omega + \epsilon_b - \epsilon_j - \epsilon_k - i\eta} \right) . \tag{3.7.2.6}$$

Therefore, at second-order, the perturbative expansion of the coupled-cluster self-energy is exactly that of the spectral form outlined in Subsection 3.6.2. Summarising, the forward time dynamical contribution to the coupled-cluster self-energy in the occupied-occupied space vanishes as a result of the similarity transformation. These contributions appear instead in the first-order static term, $\tilde{\Sigma}^{\infty(0)}_{ij}$. This is because the forward time contributions that would appear in the second-order electronic self-energy are instead contained in the doubles amplitudes t^{ab}_{ij} that enter the similarity transformation. Therefore, if we included these forward time contributions in the second-order dynamical self-energy, we would be double-counting these contributions. The same structure is observed for the backward time contribution of the coupled-cluster self-energy in the virtual-virtual space which are now contained in the static contribution, $\tilde{\Sigma}^{\infty(0)}_{ab}$. The occupied-virtual block of the coupled-cluster self-energy must vanish in order to consistently determine the doubles amplitudes that contain these contributions. When $T = 0$, the second-order expression for the coupled-cluster self-energy in Eq. 3.7.2.2 reduces the well known second-order Møller-Plesset (MP2) self-energy [124], *i.e.* $\tilde{\Sigma}^{T=0(2)}_{pq}(\omega) = \Sigma^{\mathrm{MP2}}_{pq}(\omega)$ as $\chi_{pq,rs} \to \langle pq||rs\rangle$.

Other second-order diagrams such as

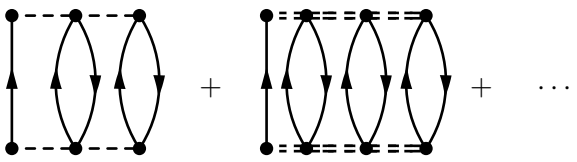

(3.7.2.7)

and so on, containing elements up to N-body from the similarity transformed Hamiltonian, vanish as a result of having four or more lines below any interaction vertex. The coupled-cluster self-energy diagram of Eq. 3.7.2.1 represents an excitation processes whereby

the intermediate scattered states consist of excited states containing two-particle-one-hole (2p1h) and two-hole-one-particle (2h1p) configurations. Likewise, the diagrams of Eq. 3.7.2.7 contain intermediate scattered states of 3p2h/3h2p and 4p3h/4h3p character, which vanish within coupled-cluster theory, but will contribute in the case of a generic N-body interaction Hamiltonian.

The final second-order interaction-reducible diagrams are those where the two-body effective interaction is contracted with the static self-energy and where the three-body effective interaction is contracted with the two-body interaction:

$\tilde{\Sigma}^{\infty(2)}_{pq} =$ 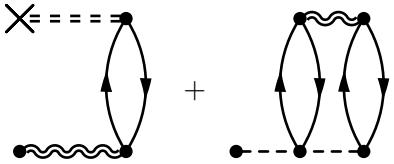 (3.7.2.8)

These are static terms that evaluate to give

$$\tilde{\Sigma}^{\infty(2)}_{pq} = \sum_{kc} \frac{\chi_{pc,qk}\tilde{\Sigma}^{\infty(0)}_{kc}}{(\epsilon_k - \epsilon_c + i\eta)} + \frac{1}{(2!)^2}\sum_{abij} \frac{\chi_{pab,qij}\chi_{ij,ab}}{(\epsilon_i + \epsilon_j - \epsilon_a - \epsilon_b + i\eta)} \,. \tag{3.7.2.9}$$

The contributions resulting from the contraction of the four-body with the three-body effective interaction and so on vanish as a result of containing four or more lines below the interaction vertex. In Brueckner theory, the first term vanishes because $\tilde{\Sigma}^{\infty(0)}_{kc} = 0$ [4].

3.7.3 Third-order diagrams

In order to reduce the number of diagrams depicted at third-order, we present only the 1PI, skeleton and interaction-irreducible coupled-cluster self-energy diagrams. This restriction requires the self-energy to be written in terms of fully dressed Green's functions because the self-energy insertions are already included in the propagator renormalization.

They are depicted below:

$\tilde{\Sigma}^{(3)}[G_0] =$

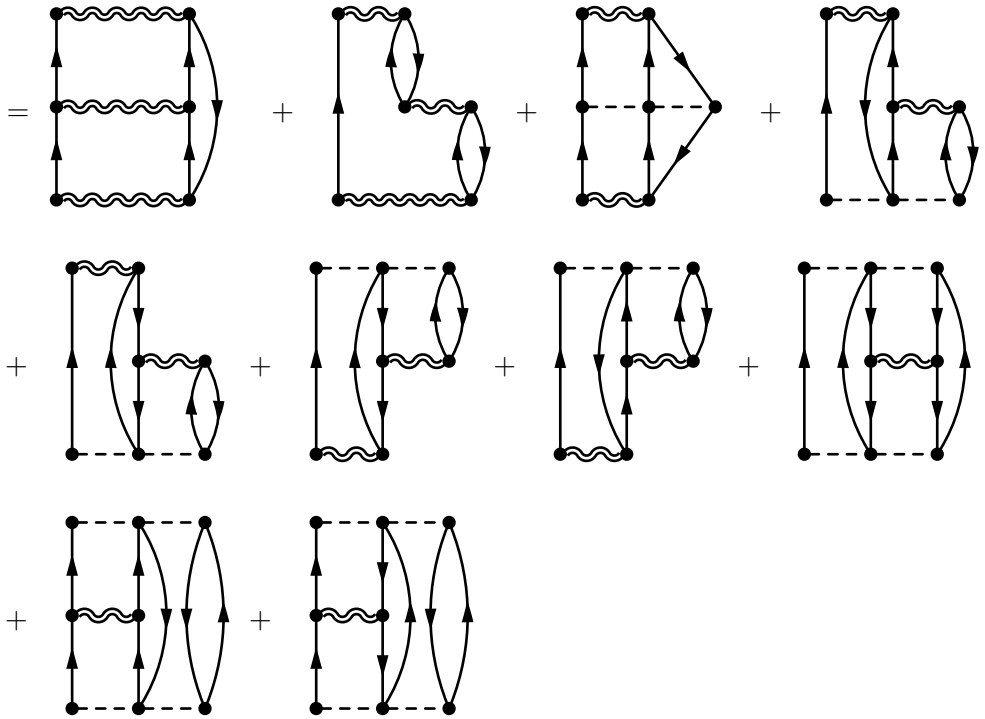

(3.7.3.1)

Typical third-order diagrams of the form:

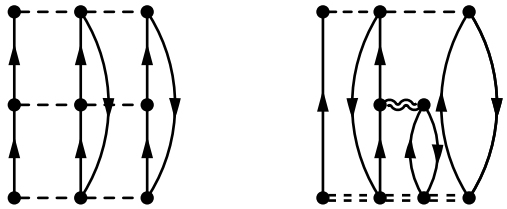

vanish due to the fact that matrix elements of the similarity transformed Hamiltonian with four or more lines below a vertex are zero. Other dynamical third-order contributions such as the diagrams

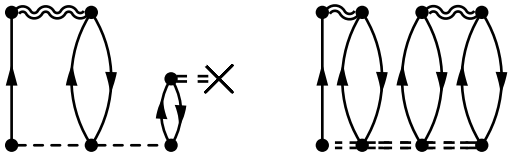

are in fact interaction-reducible as they are obtained by contracting the three-body effective interaction with a single-particle Green's function and the four-body effective interaction with a two-body Green's function. However, these diagrams will appear in the perturbative expansion of the self-energy with respect to G_0, but they do not contribute to the series of third-order 1PI, skeleton and interaction-irreducible diagrams that enter $\tilde{\Sigma}[\tilde{G}]$. These interaction-reducible diagrams are actually contained in the self-consistent renormalized coupled-cluster self-energy expansion at second-order to be presented in Section 3.8.

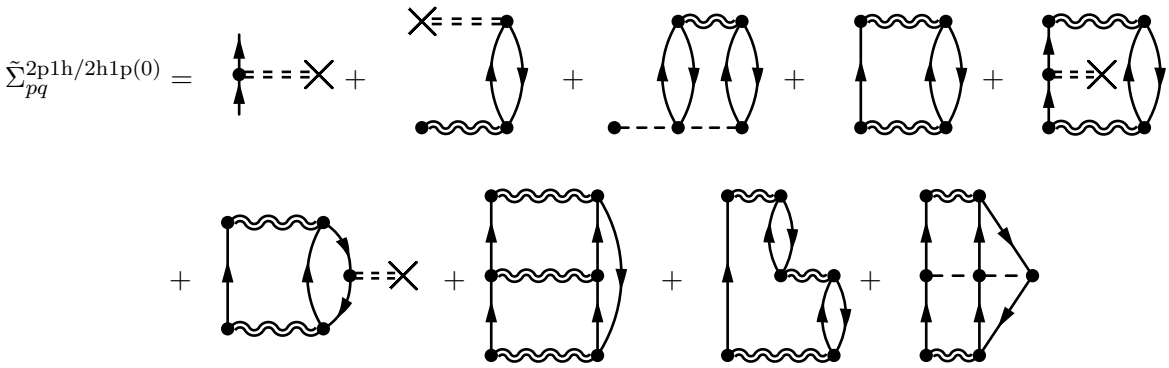

Figure 3.1: The 2p1h/2h1p excitation character restricted third-order one-particle irreducible coupled-cluster self-energy diagrams expressed with respect to the reference Green's function, G_0.

When $T = 0$, the third-order coupled-cluster self-energy exactly reduces to the two skeleton diagrams of the electronic self-energy as

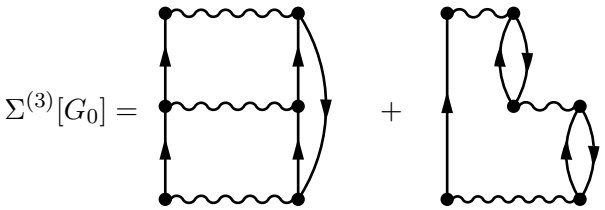

where the interaction line is now the antisymmetrized bare Coulomb interaction. Therefore, we have $\tilde{\Sigma}_{pq}^{T=0(3)}(\omega) = \Sigma_{pq}^{(3)}(\omega)$ as expected.

To demonstrate the evaluation of a typical third-order contribution to the coupled-cluster self-energy, we focus on the third diagram of Eq. 3.7.3.1. In this diagram, from the Feynman rules [13, 14, 17, 20, 36], we have two sets of two equally oriented Green's function lines which give rise to a total symmetry factor $\frac{1}{(2!)^2} = \frac{1}{4}$. There is also one closed fermion loop giving rise to an overall phase factor of -1. The diagram evaluates to

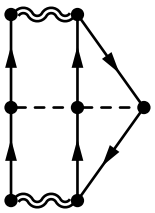

$$= -\frac{(i)^4}{(2!)^2} \sum_{\substack{rstuvx \\ yzwnol}} \int \frac{d\omega_1 d\omega_2 d\omega_3 d\omega_4}{(2\pi)^4} \chi_{pr,st} G^0_{su}(\omega_1) G^0_{tv}(\omega_2) G^0_{wr}(\omega_1 + \omega_2 - \omega)$$

$$\times \chi_{uvx,yzw} G^0_{yn}(\omega_3) G^0_{zo}(\omega_4) \chi_{no,ql} G^0_{lx}(\omega_3 + \omega_4 - \omega) \ . \tag{3.7.3.2}$$

The first three diagrams of Eq. 3.7.3.1 encode excitations that contain mixtures of 2p1h/2h1p states. In the case of three-body interactions, it was proposed that these diagrams make up the dominant contribution to the self-energy at third-order [20, 36]. The rest of the diagrams all contain combinations of 3p2h and 2p1h excitations. Higher-body

excitations are possible in the case of a generic N-body interaction, but vanish within coupled-cluster theory due to the structure of the similarity transformed Hamiltonian [85].

To conclude the perturbative analysis presented in this section, we depict the diagrammatic content of the set of perturbative third-order 1PI coupled-cluster self-energy diagrams restricted to the space of 2p1h/2h1p intermediate excitation states in Figure 3.1. The fifth and sixth diagrams of Figure 3.1 arise by insertion of the static coupled-cluster self-energy diagram (the first diagram) into the second-order dynamical term (the fourth diagram). As a result, they are non-skeleton contributions. The second and third diagrams are static contributions that are interaction-reducible.

3.8 Self-consistent renormalization of the coupled-cluster self-energy

In this Section, we construct the renormalized coupled-cluster self-energy from the exact equation-of-motion for the single-particle coupled-cluster Green's function. Our analysis demonstrates the formally consistent functional-diagrammatic formulation of the non-hermitian CC self-energy. As a result, profound connections are uncovered between the effective interactions generated by the self-consistent Green's function theory and those that arise from the functional derivatives of the BCC Lagrangian presented in Ref. [4]. From this analysis, we also demonstrate how the perturbative series for the self-energy derived in Section 3.7 emerges from the self-consistent formalism.

3.8.1 Renormalized coupled-cluster self-energy

Through its exact equation-of-motion, the single-particle coupled-cluster Green's function is coupled to the 4-point, 6-point, 8-point and so on Green's functions. In the spin-orbital basis, these higher-point Green's functions are defined as

$$i\tilde{G}^{\mathrm{4pt}}_{pq,rs}(t_1,t_2;t_3,t_4) = \langle\tilde{\Psi}_0|\mathcal{T}\left\{a_q(t_2)a_p(t_1)a_r^\dagger(t_3)a_s^\dagger(t_4)\right\}|\Phi_0\rangle \ , \tag{3.8.1.1a}$$

$$i\tilde{G}^{\mathrm{6pt}}_{pqr,stu}(t_1,t_2,t_3;t_4,t_5,t_6) = \langle\tilde{\Psi}_0|\mathcal{T}\left\{a_r(t_3)a_q(t_2)a_p(t_1)a_s^\dagger(t_4)a_t^\dagger(t_5)a_u^\dagger(t_6)\right\}|\Phi_0\rangle \ , \tag{3.8.1.1b}$$

$$i\tilde{G}^{\mathrm{8pt}}_{pqrs,tuvw}(t_1,t_2,t_3,t_4;t_5,t_6,t_7,t_8) = \langle\tilde{\Psi}_0|\mathcal{T}\left\{a_s(t_4)a_r(t_3)a_q(t_2)a_p(t_1)a_t^\dagger(t_5)a_u^\dagger(t_6)a_v^\dagger(t_7)a_w^\dagger(t_8)\right\}|\Phi_0\rangle \ . \tag{3.8.1.1c}$$

The 10-point and higher Green's functions are defined analogously. The relationship between the 4-point Green's function, the two-particle-hole Green's function and the two-particle reduced density matrix is given by

$$\tilde{G}^{\mathrm{4pt}}_{pq,rs}(t^+, t; t', t'^+) = \tilde{G}^{\mathrm{2ph}}_{pq,rs}(t - t') \tag{3.8.1.2a}$$

with

$$\tilde{\Gamma}_{pq,rs} = i\tilde{G}^{\mathrm{2ph}}_{pq,rs}(t - t^+) = \langle \tilde{\Psi}_0 | a_r^\dagger a_s^\dagger a_q a_p | \Phi_0 \rangle \ . \tag{3.8.1.2b}$$

Here, the notation $t - t^+$ denotes evaluation of the second time argument of the Green's function with a positive infinitesimal, *i.e.* $t^+ = t + \eta$, where $\eta \to 0$ from above. Analogous relationships hold between the higher-body Green's functions and corresponding reduced density matrices.

Taking the time-derivative of the first argument of the coupled-cluster Green's function (Eq. 3.6.0.1), using Eq. 3.2.2.5 and the definitions of the higher-order Green's functions, we have

$$\begin{aligned}
\sum_r \left(i\frac{\partial}{\partial t_1}\delta_{pr} - f_{pr} \right) \tilde{G}_{rq}(t_1 - t_2) = \delta_{pq}\delta(t_1 - t_2) &+ \sum_r (\bar{h}_{pr} - f_{pr})\tilde{G}_{rq}(t_1 - t_2) \\
&+ \frac{1}{2!}\sum_{rst} \bar{h}_{pr,st}\tilde{G}^{\mathrm{4pt}}_{st,rq}(t_1, t_1; t_1^+, t_2) \\
&+ \frac{1}{3!\cdot 2!}\sum_{\substack{rs \\ tuv}} \bar{h}_{prs,tuv}\tilde{G}^{\mathrm{6pt}}_{tuv,rsq}(t_1, t_1, t_1; t_1^{++}, t_1^+, t_2) \\
&+ \frac{1}{4!\cdot 3!}\sum_{\substack{rst \\ uvol}} \bar{h}_{prst,uvol}\tilde{G}^{\mathrm{8pt}}_{uvol,rstq}(t_1, t_1, t_1, t_1; t_1^{+++}, t_1^{++}, t_1^+, t_2) \\
&+ \cdots
\end{aligned} \tag{3.8.1.3}$$

In contrast to the electronic Green's function where the interaction Hamilotonian is a two-body operator, the coupled-cluster Green's function is coupled all the way up to the N-body Green's function, since $\bar{H}$ is an N-body operator. Using the functional inverse for the 'non-interacting' Green's function and taking the Fourier transformation of this

expression, we rewrite the equation-of-motion as the Dyson series

$$\begin{aligned}
\tilde{G}_{pq}(\omega) &= G^0_{pq}(\omega) + \sum_{rs} G^0_{pr}(\omega)(\bar{h}_{rs} - f_{rs})\tilde{G}_{sq}(\omega) \\
&- \frac{1}{2!}\sum_{rstu} G^0_{pr}(\omega)\bar{h}_{rs,tu}\int_{-\infty}^{\infty}\frac{d\omega_1 d\omega_2}{(2\pi)^2}\,\tilde{G}^{4\text{pt}}_{tu,qs}(\omega_1,\omega_2;\omega,\omega_1+\omega_2-\omega) \\
&+ \frac{1}{3!\cdot 2!}\sum_{\substack{rst\\uvw}} G^0_{ps}(\omega)\bar{h}_{rst,uvw}\int_{-\infty}^{\infty}\frac{d\omega_1 d\omega_2 d\omega_3 d\omega_4}{(2\pi)^4} \\
&\qquad\qquad \times \tilde{G}^{6\text{pt}}_{uvw,rqt}(\omega_1,\omega_2,\omega_3;\omega_4,\omega,\omega_1+\omega_2+\omega_3-\omega_4-\omega) \\
&- \frac{1}{4!\cdot 3!}\sum_{\substack{rst\\uvol}} G^0_{pn}(\omega)\bar{h}_{nrst,uvol}\int_{-\infty}^{\infty}\frac{d\omega_1 d\omega_2 d\omega_3 d\omega_4 d\omega_5 d\omega_6}{(2\pi)^6} \\
&\qquad\qquad \times \tilde{G}^{8\text{pt}}_{uvol,qrst}(\omega_1,\omega_2,\omega_3,\omega_4;\omega,\omega_5,\omega_6,\omega_1+\omega_2+\omega_3+\omega_4-\omega_5-\omega_6-\omega) \\
&+ \cdots
\end{aligned} \tag{3.8.1.4}$$

where the continuing series implies coupling of the five-body interaction to the 10-point Green's function and so on. Therefore, knowledge of the single-particle Green's function requires the knowledge of all N-point Green's functions. In order to derive the self-consistent expression for the coupled-cluster self-energy, we first introduce expressions for the 4-point, 6-point, 8-point vertices and so on. These interaction vertices contain only 1PI diagrams and are related to the self-consistent equations of motion for the 4-point, 6-point, 8-point Green's functions and so on, respectively. In the frequency domain, the 4-point vertex function is defined as [17, 125]

$$\begin{aligned}
\tilde{G}^{4\text{pt}}_{pq,rs}(\omega_1,\omega_2;\omega_3,\omega_4) &= 2\pi i\Big(\delta(\omega_1-\omega_3)\delta(\omega_2-\omega_4)\tilde{G}_{pr}(\omega_1)\tilde{G}_{qs}(\omega_2) \\
&\quad - \delta(\omega_1-\omega_4)\delta(\omega_2-\omega_3)\tilde{G}_{ps}(\omega_1)\tilde{G}_{qr}(\omega_2)\Big) \\
&\quad - \sum_{tuvw}\tilde{G}_{pt}(\omega_1)\tilde{G}_{qu}(\omega_2)\tilde{\Lambda}^{4\text{pt}}_{tu,vw}(\omega_1,\omega_2;\omega_3,\omega_4)\tilde{G}_{vr}(\omega_3)\tilde{G}_{ws}(\omega_4)\ .
\end{aligned} \tag{3.8.1.5}$$

This equation presents the 4-point Green's function as the sum of the properly antisymmetrized propagation of two independent particles, with $\tilde{\Lambda}^{4\text{pt}}$ representing their effective interaction. The 4-point vertex, $\tilde{\Lambda}^{4\text{pt}}$, is very closely related to the Bethe-Salpeter kernel and 'vertex' of Hedin's equations (see Section 3.12). However, it is constructed from antisymmetrized 1PI diagrams as opposed to the two-particle irreducible diagrams (2PI) which enter the BSE.

Similarly, the exact equation-of-motion for the 6-point Green's function can be written as [17, 20, 125]

$$\begin{aligned}
&\tilde{G}^{6\mathrm{pt}}_{pqr,stu}(\omega_1,\omega_2,\omega_3;\omega_4,\omega_5,\omega_6) = \\
&-(2\pi)^2\mathcal{A}_{[\{p\omega_1,q\omega_2,r\omega_3\}]}\Big[\delta(\omega_1-\omega_4)\delta(\omega_2-\omega_5)\delta(\omega_3-\omega_6)\tilde{G}_{ps}(\omega_1)\tilde{G}_{qt}(\omega_2)\tilde{G}_{ru}(\omega_3)\Big] \\
&-2\pi i\mathcal{P}_{[\{p\omega_1,q\omega_2,r\omega_3\}]}\mathcal{P}_{[\{s\omega_4,t\omega_5,u\omega_6\}]} \\
&\times\left(\delta(\omega_1-\omega_4)\tilde{G}_{ps}(\omega_1)\sum_{vwlo}\tilde{G}_{qv}(\omega_2)\tilde{G}_{rw}(\omega_3)\tilde{\Lambda}^{4\mathrm{pt}}_{vw,lo}(\omega_2,\omega_3;\omega_5,\omega_6)\tilde{G}_{lt}(\omega_5)\tilde{G}_{ou}(\omega_6)\right) \\
&+\sum_{\substack{vwl\\omn}}\tilde{G}_{pv}(\omega_1)\tilde{G}_{qw}(\omega_2)\tilde{G}_{rl}(\omega_3)\tilde{\Lambda}^{6\mathrm{pt}}_{vwl,omn}(\omega_1,\omega_2,\omega_3;\omega_4,\omega_5,\omega_6)\tilde{G}_{os}(\omega_4)\tilde{G}_{mt}(\omega_5)\tilde{G}_{nu}(\omega_6)
\end{aligned} \tag{3.8.1.6}$$

Here, we employ the notation of Ref. [20] where $\mathcal{A}_{[\{p\omega_1,q\omega_2,r\omega_3\}]}$ represents the antisymmetric sum of all possible pairs of permutations of the index-frequency pairs and $\mathcal{P}_{[\{p\omega_1,q\omega_2,r\omega_3\}]}$ sums all cyclic permutations of each index-frequency pair. The antisymmetrized and cyclic permutation summations are required to ensure that the fermionic exchange symmetry is obeyed during multiparticle propagation. In general, there are $n!$ terms that contribute to the independent-particle propagation of n fermions. For a single fermion propagating independently with respect to the coupled propagating of $(n-1)$ interacting fermions gives rise to n^2 equivalent combinations. For the case of the 6-point vertex equation, we have $3! = 6$ independent-particle propagation terms, $3^2 = 9$ terms corresponding to the propagation of a single fermion with two interacting fermions [125]. From this equation, we immediately see the emergence of the coupling of the 6-point vertex function to the 4-point vertex. This is a consequence of the fact that the 6-point vertex is related to the functional derivative of the 4-point vertex with respect to the single-particle Green's function. Continuing this process up to the N-body Green's function and $2N$-point vertex function, yields expressions that couple to all propagators and contain the correct permutation symmetry with respect to the Fermi statistics. All equations involving vertices are exact by definition and inserting the expressions containing the vertex functions, using the definition of the self-energy through the Dyson equation, we obtain the following expression for the irreducible coupled-cluster self-energy

$$
\begin{aligned}
\tilde{\Sigma}_{pq}(\omega) = &\left(\bar{h}_{pq} - i \sum_{rs} \bar{h}_{pr,qs} \tilde{G}_{sr}(t - t^+) + \frac{i}{(2!)^2} \sum_{rstu} \bar{h}_{prs,qtu} \tilde{G}^{\mathrm{2ph}}_{tu,rs}(t - t^+) + \cdots \right) - f_{pq} \\
&+ \frac{1}{2!} \sum_{\substack{stu \\ vwl}} \left(\bar{h}_{ps,tu} - i \sum_{on} \bar{h}_{pso,tun} \tilde{G}_{no}(t - t^+) + \frac{i}{(2!)^2} \sum_{on\epsilon\kappa} \bar{h}_{pson,tu\epsilon\kappa} \tilde{G}^{\mathrm{2ph}}_{\epsilon\kappa,on}(t - t^+) + \cdots \right) \\
&\times \int \frac{d\omega_1 d\omega_2}{(2\pi)^2} \tilde{G}_{tv}(\omega_1) \tilde{G}_{uw}(\omega_2) \tilde{\Lambda}^{\mathrm{4pt}}_{vw,ql}(\omega_1, \omega_2; \omega, \omega_1 + \omega_2 - \omega) \tilde{G}_{ls}(\omega_1 + \omega_2 - \omega) \\
&+ \frac{1}{3! \cdot 2!} \sum_{\substack{st \\ uvw}} \sum_{\substack{l\sigma \\ \alpha\gamma\kappa}} \left(\bar{h}_{spt,uvw} - i \sum_{\beta\epsilon} \bar{h}_{spt\beta,uvw\epsilon} \tilde{G}_{\epsilon\beta}(t - t^+) \right. \\
&\left. + \frac{i}{(2!)^2} \sum_{\beta\epsilon\delta\rho} \bar{h}_{spt\beta\epsilon,uvw\delta\rho} \tilde{G}^{\mathrm{2ph}}_{\delta\rho,\beta\epsilon}(t - t^+) + \cdots \right) \\
&\times \int \frac{d\omega_1 d\omega_2 d\omega_3 d\omega_4}{(2\pi)^4} \tilde{G}_{ul}(\omega_1) \tilde{G}_{v\sigma}(\omega_2) \tilde{G}_{w\alpha}(\omega_3) \tilde{\Lambda}^{\mathrm{6pt}}_{l\sigma\alpha,\gamma q\kappa}(\omega_1, \omega_2, \omega_3; \omega_4, \omega, \omega_1 + \omega_2 + \omega_3 - \omega_4 - \omega) \\
&\qquad \times \tilde{G}_{\gamma s}(\omega_4) \tilde{G}_{\sigma t}(\omega_1 + \omega_2 + \omega_3 - \omega_4 - \omega) \\
&+ \frac{1}{4! \cdot 3!} \sum_{\substack{stu \\ vwol}} \sum_{\substack{\sigma gz \\ y\gamma\epsilon\delta}} \left(\bar{h}_{pstu,vwol} - i \sum_{\alpha\beta} \bar{h}_{pstu\alpha,vwol\beta} \tilde{G}_{\beta\alpha}(t - t^+) \right. \\
&\left. + \frac{i}{(2!)^2} \sum_{\alpha\beta\gamma\phi} \bar{h}_{pstu\alpha\beta,vwol\gamma\phi} \tilde{G}^{\mathrm{2ph}}_{\gamma\phi,\alpha\beta}(t - t^+) + \cdots \right) \\
&\times \int \frac{d\omega_1 d\omega_2 d\omega_3 d\omega_4 d\omega_5 d\omega_6}{(2\pi)^6} \tilde{G}_{v\sigma}(\omega_1) \tilde{G}_{wg}(\omega_2) \tilde{G}_{oz}(\omega_3) \tilde{G}_{ly}(\omega_4) \\
&\qquad \times \tilde{\Lambda}^{\mathrm{8pt}}_{\sigma gzy,q\gamma\epsilon\delta}(\omega_1, \omega_2, \omega_3, \omega_4; \omega, \omega_5, \omega_6, \omega_1 + \omega_2 + \omega_3 + \omega_4 - \omega_5 - \omega_6 - \omega) \\
&\qquad \times \tilde{G}_{\gamma s}(\omega_5) \tilde{G}_{\epsilon t}(\omega_6) \tilde{G}_{\delta u}(\omega_1 + \omega_2 + \omega_3 + \omega_4 - \omega_5 - \omega_6 - \omega) \\
&+ \cdots
\end{aligned}
\tag{3.8.1.7}
$$

From the equation-of-motion for the Green's function this expression continues up to the $2N$-point vertex. Remarkably, as a result of the exact vertex equations, the effective interaction elements appearing here correspond exactly to those of the similarity transformed Hamiltonian normal-ordered with respect to the exact ground state biorthogonal expectation value (Eq. 3.4.1.3). Therefore, we may simplify the above expression to obtain

the fully renormalized coupled-cluster self-energy as

$$\begin{aligned}
\tilde{\Sigma}_{pq}(\omega) &= (\tilde{F}_{pq} - f_{pq}) \\
&+ \frac{1}{2!}\sum_{\substack{stu\\vwl}} \tilde{\Xi}_{ps,tu} \int \frac{d\omega_1 d\omega_2}{(2\pi)^2} \tilde{G}_{tv}(\omega_1)\tilde{G}_{uw}(\omega_2)\tilde{\Lambda}^{4\text{pt}}_{vw,ql}(\omega_1,\omega_2;\omega,\omega_1+\omega_2-\omega)\tilde{G}_{ls}(\omega_1+\omega_2-\omega) \\
&+ \frac{1}{3!\cdot 2!}\sum_{\substack{st\\uvw}}\sum_{\substack{l\sigma\\\alpha\gamma\kappa}} \tilde{\chi}_{spt,uvw} \int \frac{d\omega_1 d\omega_2 d\omega_3 d\omega_4}{(2\pi)^4} \tilde{G}_{ul}(\omega_1)\tilde{G}_{v\sigma}(\omega_2)\tilde{G}_{w\alpha}(\omega_3) \\
&\qquad \times \tilde{\Lambda}^{6\text{pt}}_{l\sigma\alpha,\gamma q\kappa}(\omega_1,\omega_2,\omega_3;\omega_4,\omega,\omega_1+\omega_2+\omega_3-\omega_4-\omega)\tilde{G}_{\gamma s}(\omega_4)\tilde{G}_{\sigma t}(\omega_1+\omega_2+\omega_3-\omega_4-\omega) \\
&+ \frac{1}{4!\cdot 3!}\sum_{\substack{stu\\vwol}}\sum_{\substack{\sigma gz\\y\gamma\epsilon\delta}} \tilde{\chi}_{pstu,vwol} \int \frac{d\omega_1 d\omega_2 d\omega_3 d\omega_4 d\omega_5 d\omega_6}{(2\pi)^6} \tilde{G}_{v\sigma}(\omega_1)\tilde{G}_{wg}(\omega_2)\tilde{G}_{oz}(\omega_3)\tilde{G}_{ly}(\omega_4) \\
&\qquad\qquad \times \tilde{\Lambda}^{8\text{pt}}_{\sigma gzy,q\gamma\epsilon\delta}(\omega_1,\omega_2,\omega_3,\omega_4;\omega,\omega_5,\omega_6,\omega_1+\omega_2+\omega_3+\omega_4-\omega_5-\omega_6-\omega) \\
&\qquad\qquad \times \tilde{G}_{\gamma s}(\omega_5)\tilde{G}_{\epsilon t}(\omega_6)\tilde{G}_{\delta u}(\omega_1+\omega_2+\omega_3+\omega_4-\omega_5-\omega_6-\omega) \\
&+ \cdots
\end{aligned} \tag{3.8.1.8}$$

The diagrammatic representation of this equation is given by

$\tilde{\Sigma}[\tilde{G}] =$ 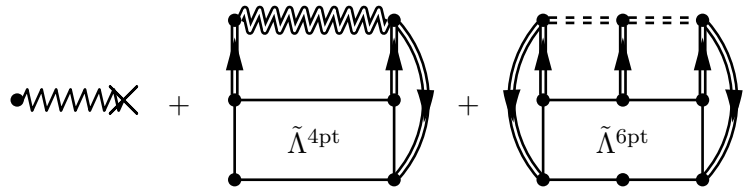 (3.8.1.9)

where the higher-order diagrams are represented by propagators coupled to the five-body interaction and the 10-point vertex function and so on. Here, we have introduced the diagrammatic notation for the 'vertex' functions, $\tilde{\Lambda}^{4/6/8\text{pt}}$. Diagrammatically, through the vertices, the renormalized self-energy is expressed as the sum of all 1PI, interaction-irreducible skeleton diagrams. From the Feynman rules, we see that the correct pre-factors of the self-energy are reproduced. The first vertex diagram has one set of two equally oriented Green's function lines therefore giving a total symmetry factor of $\frac{1}{2!}$. The second vertex diagram contains one set of three and one set of two equally oriented Green's function lines giving rise to the total symmetry factor of $\frac{1}{3!2!}$. The third vertex diagram contains one set of four and one set of three equally oriented Green's function lines giving rise to the total symmetry factor of $\frac{1}{4!3!}$, and so on. This results in the self-consistently

renormalized series for the self-energy functional (up to third order)

$\tilde{\Sigma}[\tilde{G}] =$ 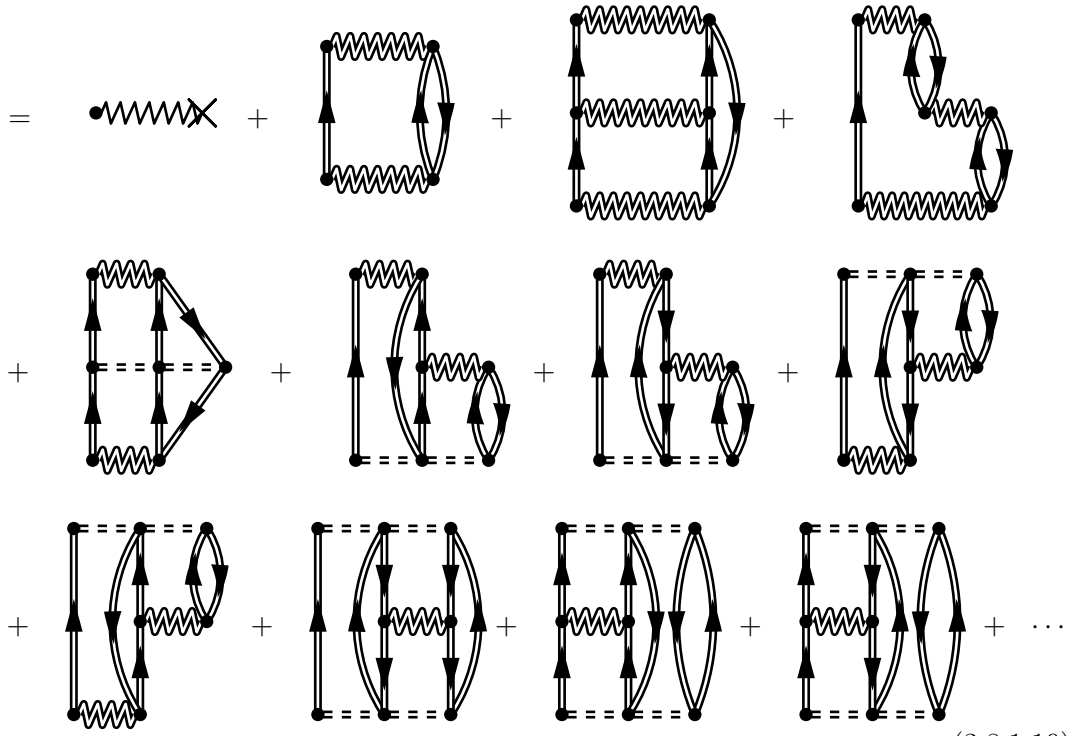 (3.8.1.10)

Subsequently we observe the renormalization of both propagators and interaction vertices as required by the presence of the interaction-irreducible diagrams. This is the result of the implicit normal-ordering of the Hamiltonian generated by the Green's function formalism. Third-order diagrams such as

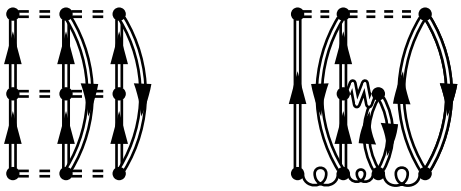

vanish due to the fact that the renormalized three-body, four-body and so on matrix elements of the similarity transformed Hamiltonian that contain four or more lines below a vertex are zero. This is analogous to the corresponding perturbative analysis presented

in Section 3.7. The explicitly static term is given by

$$\tilde{\Sigma}^{\infty}_{pq} = \overset{p}{q}\bullet\!\!\sim\!\!\times = \tilde{F}_{pq} - f_{pq}$$

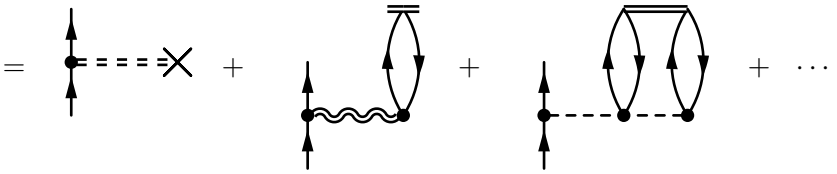

$$= \tilde{\Sigma}^{\infty(0)}_{pq} + \sum_{ia} \lambda^{i}_{a} \chi_{pa,qi} + \frac{1}{(2!)^2} \sum_{ijab} \lambda^{ij}_{ab} \chi_{pab,qij} + \cdots \tag{3.8.1.11}$$

This is exactly the static term first derived in Ref [4] and is given by the functional derivative of the coupled-cluster Lagrangian with respect to the equal-time 'non-interacting' single-particle Green's function. When $T = 0$ (meaning that $\tilde{G}$ is also replaced by G), we find that

$$\begin{aligned}
\lim_{T\to 0} \tilde{\Sigma}^{\infty}_{pq} &= \lim_{T\to 0} \tilde{F}_{pq} - f_{pq} \\
&= h_{pq} - i \sum_{rs} \langle pr||qs\rangle \, G_{sr}(t - t^{+}) - h_{pq} - i \sum_{rs} \langle pr||qs\rangle \, G^{0}_{rs}(t - t^{+}) \\
&= \sum_{rs} \langle pr||qs\rangle \, (\gamma_{rs} - \gamma^{\mathrm{ref}}_{rs}) \\
&= \Sigma^{\infty}_{pq} \, ,
\end{aligned} \tag{3.8.1.12}$$

which is the exact static part of the two-body electronic self-energy [35]. It is important to note that the property $\tilde{F}_{ai} = F_{ai} = 0$ holds for the interaction-irreducible effective interactions. However, $\tilde{F}_{ai}$ is no longer simply the singles amplitude equations but contains all amplitude equations via Eq. 3.8.1.11. The effective two-body interaction is similarly given by the following Goldstone diagram series [4]

$$\tilde{\Xi}_{pq,rs} = \overset{p}{r}\bullet\!\!\sim\!\!\bullet\overset{q}{s}$$

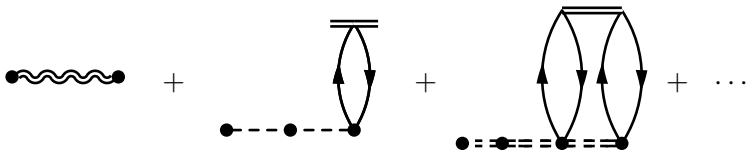

$$= \chi_{pq,rs} + \sum_{ia} \lambda^{i}_{a} \chi_{pqa,rsi} + \frac{1}{(2!)^2} \sum_{ijab} \lambda^{ij}_{ab} \chi_{pqab,rsij} + \cdots \tag{3.8.1.13}$$

Again, $\tilde{\Xi}_{ab,ij} = \chi_{ab,ij} = 0$ due to the coupled-cluster amplitude equations. The three-body

effective interaction is similarly defined as

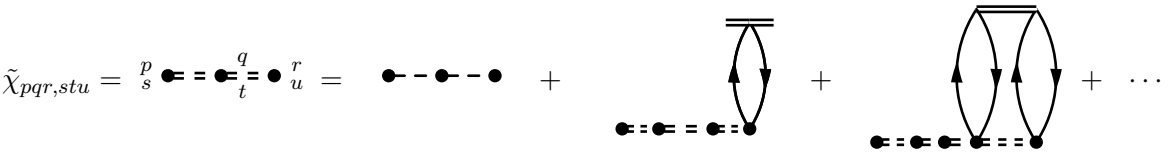

(3.8.1.14)

and so on. The higher-body terms are constructed analogously by contracting the higher-order effective interaction matrix elements $\{\chi\}$ with the corresponding λ-matrices. Within the CCSD approximation, all dressed effective interactions contributions are truncated to contain contractions of terms up to the doubles de-excitation amplitudes, $\{\lambda_{ab}^{ij}\}$, only.

Using the expression for the effective two-body interaction, the corresponding second-order self-consistent coupled-cluster self-energy takes the form

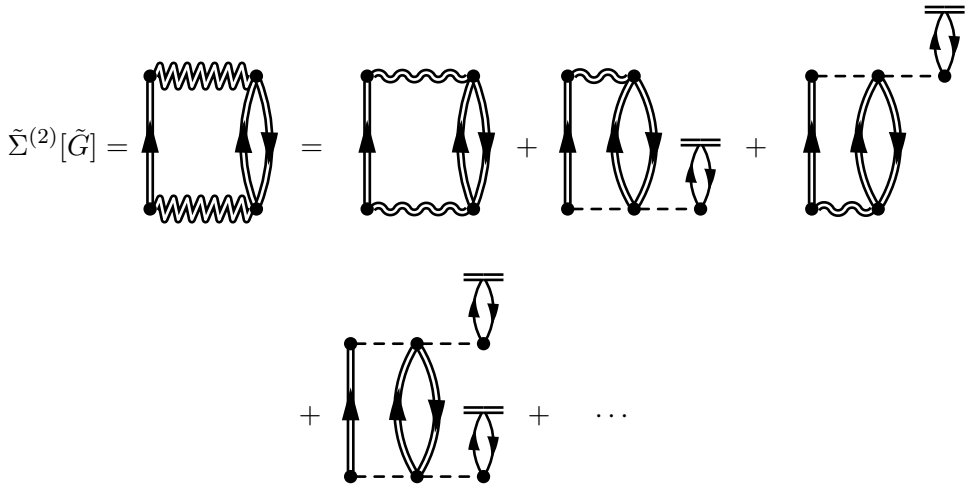

(3.8.1.15)

and so on for the terms containing the higher-body de-excitation amplitudes. Here, we have introduced the mixed Feynman-Goldstone diagram notation to represent the Green's functions and interaction-irreducible matrix elements. The dressed propagators are to be identified as Green's functions, whilst undressed fermion lines contracting with the λ-matrices are to be interpreted as Goldstone diagrams that contribute to the effective interaction, $\tilde{\chi}_{pq,rs}$.

Using the Green's function residues and poles defined in Section 3.6, as an example, we evaluate the second-order self-consistent contribution to the renormalized coupled-cluster self-energy to give

$$\tilde{\Sigma}_{pq}^{(2)}[\tilde{G}](\omega) = \frac{1}{2} \sum_{\substack{rst \\ uvw}} \tilde{\Xi}_{pr,tu} \tilde{G}_{tur,svw}^{\mathrm{2p1h/2h1p}}(\omega) \tilde{\Xi}_{sv,qw}. \tag{3.8.1.16}$$

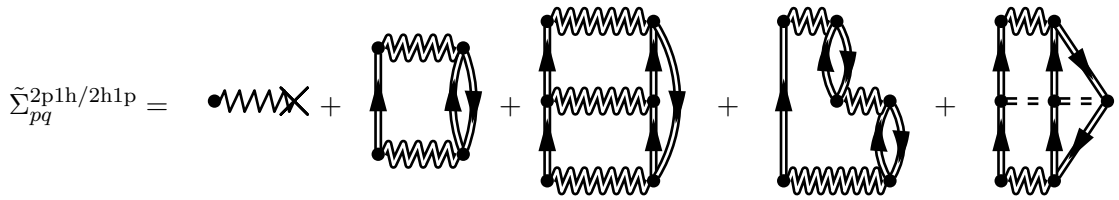

Figure 3.2: The 2p1h/2h1p excitation character restricted third-order one-particle irreducible skeleton coupled-cluster self-energy diagrams expressed with respect to the exact single-particle coupled-cluster Green's function, $\tilde{G}$.

Here, we have identified the resolvents generated in Eq. 3.8.1.16 in terms of the propagator

$$\begin{aligned}\tilde{G}^{\mathrm{2p1h/2h1p}}_{tur,svw}(\omega) = &\sum_{\mu_1\mu_2\nu_1} \frac{(\tilde{Y}^{\mu_1}_{t}\tilde{Y}^{\mu_2}_{u}\tilde{X}^{\nu_1}_{r})\bar{Y}^{\mu_1}_{s}\bar{Y}^{\mu_2}_{v}\bar{X}^{\nu_1}_{w}}{\omega + \varepsilon^{N-1}_{\nu_1} - \varepsilon^{N+1}_{\mu_1} - \varepsilon^{N+1}_{\mu_2} + i\eta} \\ &+ \sum_{\nu_1\nu_2\mu_1} \frac{\bar{X}^{\nu_1}_{t}\bar{X}^{\nu_2}_{u}\bar{Y}^{\mu_1}_{r}(\tilde{X}^{\nu_1}_{s}\tilde{X}^{\nu_2}_{v}\tilde{Y}^{\mu_1}_{w})}{\omega + \varepsilon^{N+1}_{\mu_1} - \varepsilon^{N-1}_{\nu_1} - \varepsilon^{N-1}_{\nu_2} - i\eta},\end{aligned} \tag{3.8.1.17}$$

representing correlated simultaneous charged excitation processes involving three-particles. The space spanned by the indices μ and ν is much larger than the spin-orbital space as they index the removal/addition poles of the Green's function and are directly connected to charged excitation processes.

To conclude this subsection, in Figure 3.2 we depict the diagrammatic content of the set of renormalized third-order 1PI skeleton coupled-cluster self-energy diagrams restricted to the space of 2p1h/2h1p intermediate excitation states. These diagrams contain excitations involving renormalized intermediate states of 2p1h/2h1p excitation character and will therefore constitute the most important contributions to the coupled-cluster self-energy at third-order. All diagrams depicted in Figure 3.2 are 1PI, skeleton and interaction-irreducible.

3.8.2 Recovering the perturbative expansion

To recover the perturbative expansion for the coupled-cluster self-energy requires careful consideration. This is due to the fact that the interaction-irreducible matrix elements of the similarity transformed Hamiltonian also depend on the exact Green's function. The self-consistent self-energy at second-order is composed of two diagrams

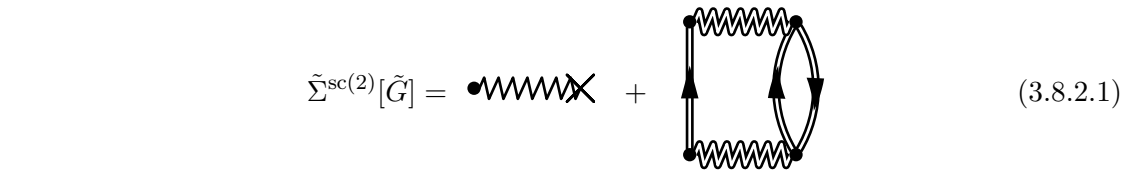

(3.8.2.1)

However, the effective interactions as well as Green's function lines have corresponding Dyson expansions. Diagrammatically, these take the form (see Appendix B.4)

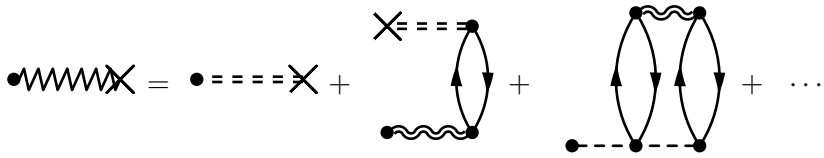

(3.8.2.2)

with

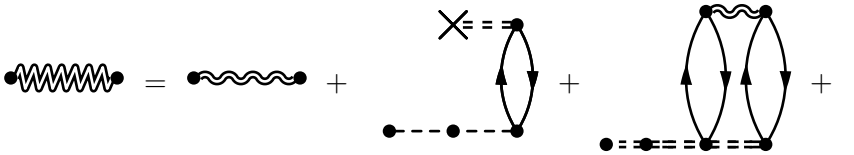

(3.8.2.3)

Now, retaining only terms up to second-order (diagrams containing up to two interaction lines), we insert Eqs 3.8.2.2 and 3.8.2.3 into Eq. 3.8.2.1 to obtain the second-order perturbative expansion of the self-energy as

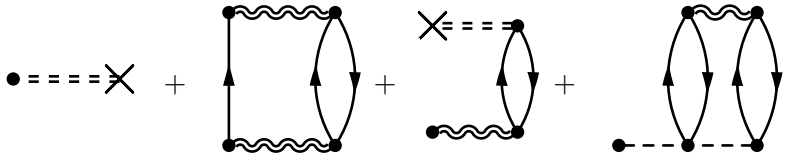

(3.8.2.4)

This is exactly the expression obtained at second order in the perturbative expansion as presented in Section 3.7. All higher-order perturbative diagrams are obtained from the self-consistent expression by successive diagrammatic expansion of exact propagators and interaction vertices.

3.9 The coupled-cluster ground state energy

In this Section, we demonstrate how the coupled-cluster correlation energy may be obtained from the coupled-cluster self-energy. The coupled-cluster ground state energy is given by the expectation value

$$\begin{aligned} E_0^{\mathrm{CC}} &= \langle \Phi_0 | \bar{H} | \Phi_0 \rangle \\ &= \sum_{pq} \bar{h}_{pq} \gamma_{pq}^{\mathrm{ref}} + \frac{1}{(2!)^2} \sum_{pq,rs} \bar{h}_{pq,rs} \Gamma_{pq,rs}^{\mathrm{ref}} + \frac{1}{(3!)^2} \sum_{pqr,stu} \bar{h}_{pqr,stu} \Gamma_{pqr,stu}^{\mathrm{ref}} + \cdots , \end{aligned} \tag{3.9.0.1}$$

From Eq. 3.4.0.9, we have

$$\begin{aligned} E_0^{\mathrm{CC}} &= \sum_i \bar{h}_{ii} + \frac{1}{2} \sum_{ij} \bar{h}_{ij,ij} \\ &= E_0^{\mathrm{ref}} + \frac{1}{4} \sum_{ijab} \langle ij||ab \rangle \left(t_{ij}^{ab} + 2 t_i^a t_j^b \right) + \sum_{ia} f_{ia} t_i^a \\ &= E_0^{\mathrm{ref}} + E_c^{\mathrm{CC}} \ . \end{aligned} \tag{3.9.0.2}$$

All additional higher-body terms evaluate to zero due to the structure of the coupled-cluster similarity transformed Hamiltonian as all matrix elements with four or more lines below the interaction vertex vanish [85]. The ground state energy is also given by the coupled-cluster Lagrangian via

$$\begin{aligned}\mathcal{L}_0^{\mathrm{CC}} &= \langle\tilde{\Psi}_0|\bar{H}|\Phi_0\rangle = \langle\tilde{\Psi}_0|\bar{h}_1|\Phi_0\rangle + \langle\tilde{\Psi}_0|\bar{V}|\Phi_0\rangle + \langle\tilde{\Psi}_0|\bar{W}|\Phi_0\rangle + \cdots \\ &= \sum_{pq}\bar{h}_{pq}\gamma^{\mathrm{ref}}_{pq} + \frac{1}{(2!)^2}\sum_{pq,rs}\bar{h}_{pq,rs}\Gamma^{\mathrm{ref}}_{pq,rs} + \frac{1}{(3!)^2}\sum_{pqr,stu}\bar{h}_{pqr,stu}\Gamma^{\mathrm{ref}}_{pqr,stu} + \cdots \\ &+ \sum_{pq}\bar{h}_{pq}\langle\Lambda|a_p^\dagger a_q|\Phi_0\rangle + \frac{1}{(2!)^2}\sum_{pq,rs}\bar{h}_{pq,rs}\langle\Lambda|a_p^\dagger a_q^\dagger a_s a_r|\Phi_0\rangle \\ &+ \frac{1}{(3!)^2}\sum_{pqr,stu}\bar{h}_{pqr,stu}\langle\Lambda|a_p^\dagger a_q^\dagger a_r^\dagger a_u a_t a_s|\Phi_0\rangle + \cdots\end{aligned} \tag{3.9.0.3}$$

where $\langle\Lambda| = \langle\Phi_0|\,\Lambda$ is the state obtained from application of the de-excitation operator onto the reference. From the equation-of-motion for the single-particle CC Green's function (Eq. 3.8.1.3), it appears that the total ground-state energy cannot be obtained from the self-energy because

$$\begin{aligned}\frac{1}{2}\lim_{\eta\to 0^+}\sum_{pq}\int_{-\infty}^{\infty}\frac{d\omega}{2\pi i}e^{i\eta\omega}\tilde{\Sigma}_{pq}(\omega)\tilde{G}_{qp}(\omega) &= \frac{1}{2}\sum_{pq}(\bar{h}_{pq} - f_{pq})\langle\tilde{\Psi}_0|a_p^\dagger a_q|\Phi_0\rangle \\ &+ \frac{1}{(2!)^2}\sum_{pq,rs}\bar{h}_{pq,rs}\langle\tilde{\Psi}_0|a_p^\dagger a_q^\dagger a_s a_r|\Phi_0\rangle \\ &+ \frac{1}{3!\cdot(2!)^2}\sum_{pqr,stu}\bar{h}_{pqr,stu}\langle\tilde{\Psi}_0|a_p^\dagger a_q^\dagger a_r^\dagger a_u a_t a_s|\Phi_0\rangle \\ &+ \cdots\end{aligned} \tag{3.9.0.4}$$

which equates to

$$\begin{aligned}\frac{1}{2}\lim_{\eta\to 0^+}\sum_{pq}\int_{-\infty}^{\infty}\frac{d\omega}{2\pi i}e^{i\eta\omega}\tilde{\Sigma}_{pq}(\omega)\tilde{G}_{qp}(\omega) &= \frac{1}{2}\langle\Phi_0|(\mathbb{1}+\Lambda)(\bar{h}_1 - F)|\Phi_0\rangle + \langle\Phi_0|(\mathbb{1}+\Lambda)\bar{V}|\Phi_0\rangle \\ &+ \frac{3}{2}\langle\Phi_0|(\mathbb{1}+\Lambda)\bar{W}|\Phi_0\rangle + \cdots\end{aligned} \tag{3.9.0.5}$$

The correct prefactors required to give the coupled-cluster Lagrangian in Eq. 3.9.0.3 are not generated by the equation-of-motion for the single-particle Green's function given in Eq. 3.9.0.5. Therefore the amplitude equations are not correctly reproduced from the equation-of-motion. This is analogous to the fact that the ground state energy of a three-body hermitian interaction Hamiltonian is not obtainable from the equation-of-motion for the single-particle Green's function [20]. However, the coupled-cluster ground state energy is still accessible from the coupled-cluster self-energy. To demonstrate how this is the case,

we evaluate the frequency integral in Eq. 3.9.0.5 analytically by making use of the pole structure of the SP-CCGF and associated coupled-cluster self-energy. As the coupled-cluster self-energy consists of a static and dynamical part, $\tilde{\Sigma}(\omega) = \tilde{\Sigma}^{\infty} + \tilde{\Sigma}^{\mathrm{D}}(\omega)$, we have

$$\begin{aligned} -\frac{i}{2}\lim_{\eta\to 0^+}\sum_{pq}\int_{-\infty}^{\infty}\frac{d\omega}{2\pi}e^{i\eta\omega}\tilde{\Sigma}_{pq}(\omega)\tilde{G}_{qp}(\omega) &= \frac{1}{2}\sum_{pq}\tilde{\Sigma}^{\infty}_{pq}\tilde{\gamma}_{pq} \\ &\quad - \frac{i}{2}\lim_{\eta\to 0^+}\sum_{ij}\int_{-\infty}^{\infty}\frac{d\omega}{2\pi}e^{i\eta\omega}\tilde{\Sigma}^{\mathrm{D}}_{ij}(\omega)\tilde{G}_{ji}(\omega) \\ &\quad - \frac{i}{2}\lim_{\eta\to 0^+}\sum_{ab}\int_{-\infty}^{\infty}\frac{d\omega}{2\pi}e^{i\eta\omega}\tilde{\Sigma}^{\mathrm{D}}_{ab}(\omega)\tilde{G}_{ba}(\omega), \end{aligned} \tag{3.9.0.6}$$

where we have used $\tilde{G}_{ai}(\omega) = \tilde{\Sigma}^{\mathrm{D}}_{ai}(\omega) = 0$. The dynamical part of the self-energy is given by the sum of the forward- and backward-time contribuitons: $\tilde{\Sigma}^{\mathrm{D}} = \tilde{\Sigma}^{\mathrm{F}} + \tilde{\Sigma}^{\mathrm{B}}$. The one-particle reduced density matrix is given by $\tilde{\gamma}_{pq} = \langle\tilde{\Psi}_0|a_p^\dagger a_q|\Phi_0\rangle$. The poles of the occupied-occupied block of the self-energy and Green's function lie above the real axis and the poles of the virtual-virtual block of the self-energy and Green's function lie below the real axis. Therefore, from the residue theorem, the integrals over frequency vanish and we are left only with the static contribution

$$-\frac{i}{2}\lim_{\eta\to 0^+}\sum_{pq}\int_{-\infty}^{\infty}\frac{d\omega}{2\pi}e^{i\eta\omega}\tilde{\Sigma}_{pq}(\omega)\tilde{G}_{qp}(\omega) = \frac{1}{2}\sum_{pq}\tilde{\Sigma}^{\infty}_{pq}\tilde{\gamma}_{pq}\ . \tag{3.9.0.7}$$

From the definition of the one-particle reduced density matrix and the static component of the coupled-cluster self-energy, Eq. 3.9.0.7 evaluates to

$$\begin{aligned} -\frac{i}{2}\lim_{\eta\to 0^+}\sum_{pq}\int_{-\infty}^{\infty}\frac{d\omega}{2\pi}e^{i\eta\omega}\tilde{\Sigma}_{pq}(\omega)\tilde{G}_{qp}(\omega) &= \frac{1}{2}\sum_{i}\tilde{\Sigma}^{\infty}_{ii} + \frac{1}{2}\sum_{ai}\lambda^i_a\tilde{\Sigma}^{\infty(0)}_{ai} \\ &= \frac{1}{2}\sum_{ii}\tilde{\Sigma}^{\infty(0)}_{ii} + \frac{1}{2}\sum_{ika}\lambda^k_a\chi_{ia,ik} + \frac{1}{(2!)^3}\sum_{iklab}\lambda^{kl}_{ab}\chi_{iab,ikl} \\ &\quad + \cdots \\ &\quad + \frac{1}{2}\sum_{ai}\lambda^i_a(F_{ai} - f_{ai})\ , \end{aligned} \tag{3.9.0.8}$$

where we have used Eq. 3.8.1.11 to identify $\tilde{\Sigma}^{\infty}_{ai} = \tilde{\Sigma}^{\infty(0)}_{ai}$. We have also used Eq. 3.8.1.11 to write the second equality of Eq 3.9.0.8, alongside the definition $\tilde{\Sigma}^{\infty(0)}_{pq} = F_{pq} - f_{pq}$, given in Section 3.7. We have derived these equations using a general reference state $|\Phi_0\rangle$, such that $\Sigma^{\infty(0)}_{ai} \neq f_{ai} \neq 0$. Using Eqs 3.9.0.3 and 3.9.0.5, we can write the CC ground state energy as

$$E_0^{\mathrm{CC}} = \frac{1}{2}\sum_{i}\tilde{\Sigma}^{\infty}_{ii} + \frac{1}{2}\sum_{ia}\lambda^i_a(F_{ai} - f_{ai}) + \frac{1}{2}\langle\tilde{\Psi}_0|(\bar{h}_1 + F)|\Phi_0\rangle - \frac{1}{2}\langle\tilde{\Psi}_0|\bar{W}|\Phi_0\rangle + \cdots \tag{3.9.0.9}$$

The third term evaluates to give $\frac{1}{2}\langle\tilde{\Psi}_0|(\bar{h}_1+F)|\Phi_0\rangle = \frac{1}{2}\sum_i(\bar{h}_{ii}+f_{ii}) + \sum_{ai}\lambda_a^i(\bar{h}_{ai}+f_{ai})$. The additional three-body component results in the expression

$$-\frac{1}{2}\langle\tilde{\Psi}_0|\bar{W}|\Phi_0\rangle = -\frac{1}{(2!)^2}\sum_{ijka}\lambda_a^k\bar{h}_{aij,kij} - \frac{1}{(2!)^3}\sum_{kijab}\lambda_{ab}^{ij}\bar{h}_{abk,ijk} - \frac{1}{2\cdot(3!)^2}\sum_{ijkabc}\lambda_{abc}^{ijk}\bar{h}_{abc,ijk}\ . \tag{3.9.0.10}$$

The higher-body terms in Eq. 3.9.0.9 give rise to a similar structure of terms whereby the higher-body interactions are contracted with different de-excitation amplitudes. Using these identities we can simplify Eq. 3.9.0.9 to give

$$\begin{aligned} E_0^{\mathrm{CC}} = &\frac{1}{2}\sum_i\left(h_{ii}+f_{ii}+\tilde{\Sigma}_{ii}^{\infty(0)}+\sum_a h_{ia}t_i^a\right)+\frac{1}{2}\sum_{ia}\lambda_a^i(F_{ai}+\bar{h}_{ai}) \\ &+\frac{1}{2}\sum_{ika}\lambda_a^k\chi_{ai,ki}+\frac{1}{(2!)^3}\sum_{iklab}\lambda_{ab}^{kl}\chi_{abi,kli}+\cdots \\ &-\frac{1}{(2!)^2}\sum_{ijka}\lambda_a^k\bar{h}_{aij,kij}-\frac{1}{(2!)^3}\sum_{kijab}\lambda_{ab}^{ij}\bar{h}_{abk,ijk}-\frac{1}{2\cdot(3!)^2}\sum_{ijkabc}\lambda_{abc}^{ijk}\bar{h}_{abc,ijk}+\cdots \end{aligned} \tag{3.9.0.11}$$

where we have used $\bar{h}_{ii} = h_{ii} + \sum_a h_{ia}t_i^a$. We have also used the antisymmetry of the matrix elements to re-write terms originating from the trace of the static component of the self-energy ($\tilde{\Sigma}_{pq}^{\infty}$) such as: $\chi_{ia,ik} = \chi_{ai,ki}$ and so on. Using the definition of $\tilde{\Sigma}_{ii}^{\infty(0)}$ from Eq. 3.7.1.3, we find

$$\frac{1}{2}\sum_i\tilde{\Sigma}_{ii}^{\infty(0)} = \frac{1}{4}\sum_{ijab}\langle ij||ab\rangle\,(t_{ij}^{ab}+2t_i^at_j^b)+\frac{1}{2}\sum_{ia}f_{ia}t_i^a+\frac{1}{2}\sum_{iaj}\langle ij||ai\rangle\,t_j^a\ , \tag{3.9.0.12}$$

remembering that $f_{ia} \neq 0$ for a general reference state. Using this result, we identify the first term of Eq. 3.9.0.11 as the coupled-cluster ground state energy obtained from the ground state coupled-cluster equations as

$$\begin{aligned} E_0^{\mathrm{CC}} &= \frac{1}{2}\sum_i\left(h_{ii}+f_{ii}+\tilde{\Sigma}_{ii}^{\infty(0)}+\sum_a h_{ia}t_i^a\right) \\ &= E_0^{\mathrm{ref}}+\frac{1}{4}\sum_{ijab}\langle ij||ab\rangle\,(t_{ij}^{ab}+2t_i^at_j^b)+\sum_{ia}f_{ia}t_i^a\ , \end{aligned} \tag{3.9.0.13}$$

where we have used the definition of the reference energy as $E_0^{\mathrm{ref}} = \frac{1}{2}\sum_i(h_{ii}+f_{ii})$. This result is clearly identical to Eq. 3.9.0.2. Therefore, we have

$$\begin{aligned} E_0^{\mathrm{CC}} = E_0^{\mathrm{CC}} &+\frac{1}{2}\sum_{ia}\lambda_a^i(F_{ai}+\bar{h}_{ai})+\frac{1}{2}\sum_{ika}\lambda_a^k\chi_{ai,ki}+\frac{1}{(2!)^3}\sum_{iklab}\lambda_{ab}^{kl}\chi_{abi,kli}+\cdots \\ &-\frac{1}{(2!)^2}\sum_{ijka}\lambda_a^k\bar{h}_{aij,kij}-\frac{1}{(2!)^3}\sum_{kijab}\lambda_{ab}^{ij}\bar{h}_{abk,ijk}-\frac{1}{2\cdot(3!)^2}\sum_{ijkabc}\lambda_{abc}^{ijk}\bar{h}_{abc,ijk}+\cdots \end{aligned} \tag{3.9.0.14}$$

In order for this equation to be correct, we demonstrate in Appendix B.6 that the remaining terms of Eq. 3.9.0.14 vanish as a result of the CC amplitude equations. Combining these results together, Eq. 3.9.0.14 can be re-written as

$$E_0^{\mathrm{CC}} = E_0^{\mathrm{CC}} + \sum_{ia} \lambda_a^i F_{ai} - \frac{1}{2 \cdot (3!)^2} \sum_{ijkabc} \lambda_{abc}^{ijk} \chi_{abc,ijk} + \cdots \tag{3.9.0.15}$$

Written is this form, it is clear that the additional terms in Eq. 3.9.0.15 vanish as they contain exactly the CC amplitude equations, $F_{ai} = \chi_{ab,ij} = \chi_{abc,ijk} = 0$ and so on. Therefore, within the Green's function formalism, the coupled-cluster correlation energy is generally given by the expression

$$E_c^{\mathrm{CC}} = \frac{1}{2} \sum_i \left(\tilde{\Sigma}_{ii}^{\infty(0)} + \sum_a h_{ia} t_i^a \right). \tag{3.9.0.16}$$

In the Brueckner basis, the second term vanishes and the correlation energy is simply given by the first term of the static contribution to the coupled-cluster self-energy [4]. Hence, the coupled-cluster ground state correlation energy is completely determined by the coupled-cluster self-energy. From Eq. 3.9.0.16, we find that the coupled-cluster ground state energy obtained at any level of approximation of the CC self-energy gives the same ground state energy as that obtained at the same level of approximation of the ground state coupled-cluster equations.

3.10 The coupled-cluster Dyson supermatrix

In this Section, we provide an overview of the coupled-cluster quasiparticle equation and Dyson supermatrix. Standard Green's function theory is centered around the frequency-dependent quasiparticle equation (Eq. 2.6.0.3), which gives access to the poles and residues of the Green's function. This allows us to directly combine coupled-cluster theory with the methodology employed in the Green's function formalism, leading us to introduce several approximations for the coupled-cluster self-energy that preserve its correct spectral form.

The Dyson equation for the SP-CCGF can be used to derive the coupled-cluster quasiparticle Hamiltonian using the identity

$$\tilde{H}_{pq}(\omega) = \left(\omega \delta_{pq} - \tilde{G}_{pq}^{-1}(\omega) \right) = f_{pq} + \tilde{\Sigma}_{pq}(\omega) \ , \tag{3.10.0.1}$$

where: $\tilde{G}^{-1}_{pq}(\omega) = [G_0]^{-1}_{pq}(\omega) - \tilde{\Sigma}_{pq}(\omega)$, with $[G_0]^{-1}_{pq}(\omega) = (\omega\delta_{pq} - f_{pq})$. The poles and residues of the SP-CCGF are then given by the eigenvalues and eigenvectors of the self-consistent frequency-dependent coupled-cluster quasiparticle equation:

$$\sum_q \tilde{H}_{pq}(\varepsilon_\gamma)\bar{A}^\gamma_q = \bar{A}^\gamma_p \varepsilon_\gamma \ . \tag{3.10.0.2}$$

Here, γ is a composite index that spans both forward- and backward-time poles and residues of the SP-CCGF: $\gamma = \mu, \nu$. When the full set of 1PI diagrams are included in the coupled-cluster self-energy, the eigenvalues of Eq. 3.10.0.2 are the exact addition and removal energies of the system. As discussed in Section 3.6, the coupled-cluster self-energy is inherently non-hermitian. Therefore, the coupled-cluster quasiparticle Hamiltonian possesses distinct left eigenstates given by

$$\sum_q \tilde{A}^\gamma_q \tilde{H}_{qp}(\varepsilon_\gamma) = \varepsilon_\gamma \tilde{A}^\gamma_p \ . \tag{3.10.0.3}$$

The right and left eigenvectors are related to the SP-CCGF residues defined in Section 3.6 through

$$\bar{A}^{\gamma=\mu,\nu}_p \equiv \begin{cases} \tilde{Y}^\mu_p = \langle \tilde{\Psi}_0 | a_p | \Psi^{N+1}_\mu \rangle \\ \tilde{X}^\nu_p = \langle \tilde{\Psi}^{N-1}_\nu | a_p | \Phi_0 \rangle \end{cases} \tag{3.10.0.4a}$$

$$\tilde{A}^{\gamma=\mu,\nu}_p \equiv \begin{cases} \bar{Y}^\mu_p = \langle \tilde{\Psi}^{N+1}_\mu | a^\dagger_p | \Phi_0 \rangle \\ \bar{X}^\nu_p = \langle \tilde{\Psi}_0 | a^\dagger_p | \Psi^{N-1}_\nu \rangle \end{cases} . \tag{3.10.0.4b}$$

Similarly, the eigenvalues are related to the poles of the SP-CCGF as

$$\varepsilon_{\gamma=\mu,\nu} \equiv \begin{cases} \varepsilon^{N+1}_\mu \\ \varepsilon^{N-1}_\nu \end{cases} , \tag{3.10.0.5}$$

which are at the formally exact removal and addition energies of the system.

Using the spectral form of the CC self-energy, given in Eq. 3.6.2.3, the frequency-dependent coupled-cluster quasiparticle equation (Eq. 3.10.0.2) can be written in terms of the frequency-independent 'upfolded' coupled-cluster Dyson supermatrix eigenvalue problem

$$\begin{pmatrix} \mathbf{f} + \tilde{\mathbf{\Sigma}}^\infty & \tilde{\mathbf{U}} & \bar{\mathbf{V}} \\ \bar{\mathbf{U}} & \bar{\mathbf{K}}^> + \bar{\mathbf{C}}^> & \mathbf{0} \\ \tilde{\mathbf{V}} & \mathbf{0} & \bar{\mathbf{K}}^< + \bar{\mathbf{C}}^< \end{pmatrix} \begin{pmatrix} \bar{\mathbf{A}} \\ \bar{\mathbf{W}}^+ \\ \bar{\mathbf{W}}^- \end{pmatrix} = \varepsilon \begin{pmatrix} \bar{\mathbf{A}} \\ \bar{\mathbf{W}}^+ \\ \bar{\mathbf{W}}^- \end{pmatrix} . \tag{3.10.0.6}$$

Here we have employed matrix notation for the coupling and interactions between the forward and backward time multi-particle-hole ISCs. The eigenvalues, ε, are the exact addition and removal energies of the system. Diagonalization of the coupled-cluster Dyson

supermatrix yields all the forward- and backward-time poles and residues of the SP-CCGF at once. Throughout the rest of this Chapter we denote the CC Dyson supermatrix as $\tilde{\mathbf{D}}^{\mathrm{CC}}$.

Since the coupled-cluster self-energy is non-hermitian, the coupled-cluster Dyson supermatrix also has distinct left and right supereigenvectors. However, the exact CC Dyson supermatrix is pseudo-hermitian, due to the similarity transformed Hamiltonian $\bar{H}$, as it possesses a real spectrum. In Appendix B.5 we show that the imaginary part of the retarded component of the exact coupled-cluster self-energy is *biorthogonally* negative semi-definite. This property follows from the pseudo-hermiticity of the CC Dyson supermatrix and CC self-energy. This constitutes a non-hermitian extension of the negative semi-definite property of the imaginary part of the retarded self-energy (Eq. 2.5.0.4) presented in Chapter 2, which is an important property that ensures the correct causal structure of the theory [40, 41, 126].

The components of the right and left eigenvectors in the space of excited multi-particle-hole ISCs are found as

$$\bar{W}^{+,\gamma}_{J} = \sum_{J''p} \Big(\varepsilon_\gamma \mathbb{1} - (\bar{\mathbf{K}}^{>} + \bar{\mathbf{C}}^{>})\Big)^{-1}_{JJ''} \bar{U}_{J'',p} \bar{A}^{\gamma}_{p} \tag{3.10.0.7a}$$

$$\bar{W}^{-,\gamma}_{A} = \sum_{A''p} \Big(\varepsilon_\gamma \mathbb{1} - (\bar{\mathbf{K}}^{<} + \bar{\mathbf{C}}^{<})\Big)^{-1}_{AA''} \tilde{V}_{A'',p} \bar{A}^{\gamma}_{p} \tag{3.10.0.7b}$$

$$\tilde{W}^{+,\gamma}_{J} = \sum_{pJ''} \tilde{A}^{\gamma}_{p} \tilde{U}_{p,J''} \Big(\varepsilon_\gamma \mathbb{1} - (\bar{\mathbf{K}}^{>} + \bar{\mathbf{C}}^{>})\Big)^{-1}_{J''J} \tag{3.10.0.7c}$$

$$\tilde{W}^{+,\gamma}_{A} = \sum_{pA''} \tilde{A}^{\gamma}_{p} \bar{V}_{p,A''} \Big(\varepsilon_\gamma \mathbb{1} - (\bar{\mathbf{K}}^{<} + \bar{\mathbf{C}}^{<})\Big)^{-1}_{A''A} , \tag{3.10.0.7d}$$

where $\begin{pmatrix} \tilde{\mathbf{A}} & \tilde{\mathbf{W}}^{+} & \tilde{\mathbf{W}}^{-} \end{pmatrix}$ is the left supereigenvector solution. From these formal solutions, it should be noted that the $\bar{W}^{\pm,\gamma}/\tilde{W}^{\pm,\gamma}$ components of the eigenvectors are explicit functions of the corresponding eigenvalue, ε_γ.

If we impose the normalization condition: $\sum_p \tilde{A}^{\gamma}_{p} \bar{A}^{\gamma}_{p} = 1$, the quasiparticle renormalization factor can be found from the inverse of the overlap of the supereigenvectors as

$$\begin{aligned} Z_\gamma &= \left(\sum_p \tilde{A}^{\gamma}_{p} \bar{A}^{\gamma}_{p} + \sum_J \tilde{W}^{+,\gamma}_{J} \bar{W}^{+,\gamma}_{J} + \sum_A \tilde{W}^{-,\gamma}_{A} \bar{W}^{-,\gamma}_{A} \right)^{-1} \\ &= \left(1 - \frac{\partial \tilde{\Sigma}_{\gamma\gamma}(\omega)}{\partial \omega} \bigg|_{\omega=\varepsilon_\gamma} \right)^{-1} . \end{aligned} \tag{3.10.0.8}$$

However, if we instead require that full supereigenvectors be normalized under the biorthogonal inner product then the renormalization factor is simply given by: $Z_\gamma = \sum_p \tilde{A}^{\gamma}_{p} \bar{A}^{\gamma}_{p}$.

From the right and left supereigenvector solutions of the CC Dyson supermatrix (Eq. 3.10.0.6), it is possible to reconstruct the exact SP-CCGF by taking the resolvent of the Dyson supermatrix in the single-particle spin-orbital subspace. For the retarded SP-CCGF, the result is given by

$$\begin{aligned} \tilde{G}^{R}_{pq}(\omega) &= \left((\omega + i\eta)\mathbb{1} - \tilde{\mathbf{D}}^{\mathrm{CC}}\right)^{-1}_{pq} \\ &= \sum_{\gamma=\mu,\nu} \frac{\bar{A}^{\gamma}_{p}\tilde{A}^{\gamma}_{q}}{\omega - \varepsilon_{\gamma} + i\eta} \\ &= \sum_{\mu} \frac{\tilde{Y}^{\mu}_{p}\bar{Y}^{\mu}_{q}}{\omega - \varepsilon^{N+1}_{\mu} + i\eta} + \sum_{\nu} \frac{\tilde{X}^{\nu}_{q}\bar{X}^{\nu}_{p}}{\omega - \varepsilon^{N-1}_{\nu} + i\eta} \,, \end{aligned} \tag{3.10.0.9}$$

where we have used the relationships given in Eqs 3.10.0.4 and 3.10.0.5 to go from the second equality to the third equality. As can be seen, this expression agrees with the exact Lehmann representation given in Eq. 3.6.1.2 (remembering that the difference between the time-ordered and retarded single-particle Green's function is that the retarded propagator simply places all the poles below the real axis [13, 14, 17]).

By introducing the coupled-cluster Dyson supermatrix, we preserve the correct analytical structure of the self-energy required to obtain the correct convergence of the Feynman-Dyson diagrammatic perturbation expansion [123]. This representation forms the basis of the Algebraic Diagrammatic Construction method [35, 36, 41]. In the following subsections, we construct the upfolded Dyson supermatrices for different 2p1h/2h1p CC self-energy approximations that preserve the correct analytic structure. To be consistent with the treatment of 2p1h/2h1p excitations, all coupling and effective interaction matrices appearing in these subsections will be implicitly taken within the CCSD approximation ($T = T_1 + T_2$). These CC self-energy approximations reveal the connection to IP/EA-EOM-CCSD theory and allow us to leverage the connections between Green's function and coupled-cluster theory.

The equations derived in this work are no more complex than those that have been derived in the context of EOM-CC theory [127–129], the Algebraic Diagrammatic Construction method [36, 41] and the Gorkov-Green's function formalism [37, 130]. Therefore, similar hierarchies of approximations and powerful numerical techniques can be ported over for the efficient solution of the coupled-cluster Dyson supermatrix [36, 61, 94, 131–141].

In the following subsections, we will use the fermionic antisymmetry of the effective interaction matrix elements to restrict our sums to be over ordered sets of single-particle Green's

function indices: $(i < j; a)$, $(i < j < k; a < b)$, $(\nu_1 < \nu_2; \mu_1)$, $(\nu_1 < \nu_2 < \nu_3; \mu_1 < \mu_2)$ and so on. We can recover the general case using unrestricted summations by introduction of the relevant symmetry factors of the Feynman diagrams presented in Sections 3.7 and 3.8.

3.10.1 Second-order perturbative and self-consistent approximations

From the second-order perturbative coupled-cluster self-energy (Eq. 3.7.2.2), we see that $J \equiv (i; a < b)/A \equiv (i < j; a)$ are restricted to the space of 2p1h/2h1p excitations such that:

$$\tilde{U}^{(0)}_{p,iab} = \chi_{pi,ab} \tag{3.10.1.1a}$$

$$\bar{U}^{(0)}_{iab,q} = \chi_{ab,qi} \tag{3.10.1.1b}$$

$$\tilde{V}^{(0)}_{ija,q} = \chi_{ij,qa} \tag{3.10.1.1c}$$

$$\bar{V}^{(0)}_{p,ija} = \chi_{pa,ij} \tag{3.10.1.1d}$$

The ISC interaction matrices are given by $\bar{\mathbf{K}}^{>}_{iab,jcd} = (\epsilon_a + \epsilon_b - \epsilon_i)(\delta_{ac}\delta_{bd} - \delta_{ad}\delta_{bc})\delta_{ij}$ and $\bar{\mathbf{K}}^{<}_{ija,klb} = (\epsilon_i + \epsilon_j - \epsilon_a)(\delta_{ik}\delta_{jl} - \delta_{il}\delta_{jk})\delta_{ab}$, respectively. This leads to the following upfolded CC Dyson supermatrix

$$\tilde{\mathbf{D}}^{\mathrm{CC}}_{(2)} = \begin{pmatrix} f_{pq} + \tilde{\Sigma}^{\infty(0)}_{pq} + \tilde{\Sigma}^{\infty(2)}_{pq} & \tilde{U}^{(0)}_{p,iab} & \bar{V}^{(0)}_{p,ija} \\ \bar{U}^{(0)}_{iab,q} & \bar{\mathbf{K}}^{>}_{iab,jcd} & \mathbf{0} \\ \tilde{V}^{(0)}_{ija,q} & \mathbf{0} & \bar{\mathbf{K}}^{<}_{ija,klb} \end{pmatrix}. \tag{3.10.1.2}$$

Alternatively, we also carry out this procedure for the second-order self-consistent, renormalized coupled-cluster self-energy. This self-energy also consists of 2p1h/2h1p excitation character ($J \equiv (\nu_1; \mu_1 < \mu_2)/A \equiv (\nu_1 < \nu_2; \mu_1)$) and gives rise to the following coupling matrices:

$$\tilde{U}^{\mathrm{sc}(2)}_{p,\nu_1\mu_1\mu_2} = \sum_{rtu} \tilde{\Xi}_{pr,tu} \tilde{Y}^{\mu_1}_t \tilde{Y}^{\mu_2}_u \tilde{X}^{\nu_1}_r \tag{3.10.1.3a}$$

$$\bar{U}^{\mathrm{sc}(2)}_{\nu_1\mu_1\mu_2,q} = \sum_{svw} \tilde{\Xi}_{sv,qw} \bar{Y}^{\mu_1}_s \bar{Y}^{\mu_2}_v \bar{X}^{\nu_1}_w \tag{3.10.1.3b}$$

$$\bar{V}^{\mathrm{sc}(2)}_{p,\nu_1\nu_2\mu_1} = \sum_{rtu} \tilde{\Xi}_{pr,tu} \bar{X}^{\nu_1}_t \bar{X}^{\nu_2}_u \bar{Y}^{\mu_1}_r \tag{3.10.1.3c}$$

$$\tilde{V}^{\mathrm{sc}(2)}_{\nu_1\nu_2\mu_1,q} = \sum_{svw} \tilde{\Xi}_{sv,qw} \tilde{X}^{\nu_1}_s \tilde{X}^{\nu_2}_v \tilde{Y}^{\mu_1}_w \ . \tag{3.10.1.3d}$$

The interaction matrices become $\bar{\mathbf{K}}^{>}_{\nu_1\mu_1\mu_2,\nu_2\mu_3\mu_4} = (\varepsilon^{N+1}_{\mu_1} + \varepsilon^{N+1}_{\mu_2} - \varepsilon^{N-1}_{\nu_1})(\delta_{\mu_1\mu_3}\delta_{\mu_2\mu_4} - \delta_{\mu_1\mu_4}\delta_{\mu_2\mu_3})\delta_{\nu_1\nu_2}$ and $\bar{\mathbf{K}}^{<}_{\nu_1\nu_2\mu_1,\nu_3\nu_4\mu_2} = (\varepsilon^{N-1}_{\nu_1} + \varepsilon^{N-1}_{\nu_2} - \varepsilon^{N+1}_{\nu_1})(\delta_{\nu_1\nu_3}\delta_{\nu_2\nu_4} - \delta_{\nu_1\nu_4}\delta_{\nu_2\nu_3})\delta_{\mu_1\mu_2}$. Within this approximation, the resulting coupled-cluster Dyson supermatrix is given by

$$\tilde{\mathbf{D}}^{\mathrm{CC}}_{\mathrm{sc}(2)} = \begin{pmatrix} f_{pq} + \tilde{\Sigma}^{\infty\mathrm{CCSD}}_{pq} & \tilde{U}^{\mathrm{sc}(2)}_{p,\nu_1\mu_1\mu_2} & \bar{V}^{\mathrm{sc}(2)}_{p,\nu_1\nu_2\mu_1} \\ \bar{U}^{\mathrm{sc}(2)}_{\nu_1\mu_1\mu_2,q} & \bar{\mathbf{K}}^{>}_{\nu_1\mu_1\mu_2,\nu_2\mu_3\mu_4} & \mathbf{0} \\ \tilde{V}^{\mathrm{sc}(2)}_{\nu_1\nu_2\mu_1,q} & \mathbf{0} & \bar{\mathbf{K}}^{<}_{\nu_1\nu_2\mu_1,\nu_3\nu_4\mu_2} \end{pmatrix}. \tag{3.10.1.4}$$

The static contribution, $\tilde{\Sigma}_{pq}^{\infty\mathrm{CCSD}}$, is taken within the CCSD approximation to be consistent with the treatment of 2p1h/2h1p excitations contained in the second-order self-energy:

$$\tilde{\Sigma}_{pq}^{\infty\mathrm{CCSD}} = \tilde{\Sigma}_{pq}^{\infty(0)} + \sum_{ia} \lambda_a^i \chi_{pa,qi} + \frac{1}{(2!)^2} \sum_{ijab} \lambda_{ab}^{ij} \chi_{pab,qij} \ . \tag{3.10.1.5}$$

The solution of Eq. 3.10.1.4 requires iterative diagonalization, whereby the coupling and interaction matrices are updated at each step. The zeroth-order iteration is taken as the second-order perturbative supermatrix defined in Eq. 3.10.1.2 and the resulting eigenvectors and eigenvalues are subsequently fed into the definition of the coupling and interaction matrices. This processes is repeated until convergence of the spectrum of $\tilde{\mathbf{D}}_{\mathrm{sc}(2)}^{\mathrm{CC}}$ is achieved.

3.10.2 Coupled-cluster self-energy approximations

The second-order coupled-cluster self-energy contains interactions between ISCs that are fundamentally of 2p1h/2h1p excitation character. This is demonstrated by the fact that the ISCs are parametrized by the ordered sets of single-particle Green's function indices: $J \equiv (i; a < b)/A \equiv (i < j; a)$. We can include the complete set of 2p1h/2h1p interactions between these ISCs by defining the interaction matrices as [4]

$$\bar{\mathbf{K}}_{iab,jcd}^{>} + \bar{\mathbf{C}}_{iab,jcd}^{>(0)} = \langle \Phi_i^{ab} | \bar{H}_N | \Phi_j^{cd} \rangle \tag{3.10.2.1a}$$

$$\bar{\mathbf{K}}_{ija,klb}^{<} + \bar{\mathbf{C}}_{ija,klb}^{<(0)} = - \langle \Phi_{kl}^{b} | \bar{H}_N | \Phi_{ij}^{a} \rangle \ , \tag{3.10.2.1b}$$

where the matrices $\bar{\mathbf{K}}_{iab,jcd}^{>}/\bar{\mathbf{K}}_{ija,klb}^{<}$ are defined in Subsection 3.10.1 and are block-diagonal by definition (see Section 3.6). This approximation corresponds to allowing all particles to propagate independently, to interact pairwise via the static component of the perturbative CC-BSE kernel and finally via the combined three-body interaction of the similarity transformed Hamiltonian normal-ordered with respect to the reference determinant [4, 142, 143]. The explicit expression for the interaction matrices are therefore given by

$$\begin{aligned}\bar{\mathbf{C}}_{iab,jcd}^{>(0)} = {} & \tilde{\Sigma}_{ac}^{\infty(0)} \delta_{ij} \delta_{bd} - \tilde{\Sigma}_{ad}^{\infty(0)} \delta_{ij} \delta_{bc} + \tilde{\Sigma}_{bd}^{\infty(0)} \delta_{ac} \delta_{ij} - \tilde{\Sigma}_{bc}^{\infty(0)} \delta_{ad} \delta_{ij} - \tilde{\Sigma}_{ji}^{\infty(0)} \delta_{ac} \delta_{bd} \\ & + \tilde{\Sigma}_{ji}^{\infty(0)} \delta_{ad} \delta_{bc} + \chi_{ja,ci} \delta_{bd} + \chi_{jb,di} \delta_{ac} + \chi_{ab,cd} \delta_{ij} - \chi_{ja,di} \delta_{bc} - \chi_{jb,ci} \delta_{ad} + \chi_{jab,cid}\end{aligned} \tag{3.10.2.2a}$$

$$\begin{aligned}\bar{\mathbf{C}}_{ija,klb}^{<(0)} = {} & \tilde{\Sigma}_{ik}^{\infty(0)} \delta_{ab} \delta_{jl} - \tilde{\Sigma}_{il}^{\infty(0)} \delta_{ab} \delta_{jk} + \tilde{\Sigma}_{jl}^{\infty(0)} \delta_{ab} \delta_{ik} - \tilde{\Sigma}_{jk}^{\infty(0)} \delta_{ab} \delta_{il} + \tilde{\Sigma}_{ba}^{\infty(0)} \delta_{il} \delta_{jk} \\ & - \tilde{\Sigma}_{ba}^{\infty(0)} \delta_{ik} \delta_{jl} + \chi_{ib,al} \delta_{jk} + \chi_{jb,ak} \delta_{il} - \chi_{ij,kl} \delta_{ab} - \chi_{ib,ak} \delta_{jl} - \chi_{jb,al} \delta_{ik} + \chi_{ijb,kal} \ .\end{aligned} \tag{3.10.2.2b}$$

To include the full set of time-orderings of the coupled-cluster self-energy diagrams corresponding to the interaction matrices defined in Eqs 3.10.2.1 requires us to modify the 2p1h and 2h1p coupling matrices as

$$\begin{aligned}
\tilde{U}^{\mathrm{2p1h(0)}}_{p,iab} &= \chi_{pi,ab} + \frac{1}{2}\sum_{kl}\chi_{pi,kl}\frac{\chi_{kl,ab}}{\epsilon_k+\epsilon_l-\epsilon_a-\epsilon_b} + \sum_{kc}\chi_{pc,ak}\frac{\chi_{ik,bc}}{\epsilon_i+\epsilon_k-\epsilon_b-\epsilon_c} \\
&\quad - \sum_{kc}\chi_{pc,bk}\frac{\chi_{ik,ac}}{\epsilon_i+\epsilon_k-\epsilon_a-\epsilon_c} - \sum_{k}\frac{\chi_{pi,kb}\tilde{\Sigma}^{\infty(0)}_{ka}}{\epsilon_k-\epsilon_a} + \sum_{k}\frac{\chi_{pi,ka}\tilde{\Sigma}^{\infty(0)}_{kb}}{\epsilon_k-\epsilon_b} \\
&\quad + \sum_{c}\frac{\chi_{pc,ab}\tilde{\Sigma}^{\infty(0)}_{ic}}{\epsilon_i-\epsilon_c}\,, \qquad \text{(3.10.2.3a)} \\
\tilde{V}^{\mathrm{2h1p(0)}}_{ija,q} &= \chi_{ij,qa} + \frac{1}{2}\sum_{cd}\frac{\chi_{ij,cd}}{\epsilon_i+\epsilon_j-\epsilon_c-\epsilon_d}\chi_{cd,qa} + \sum_{kc}\frac{\chi_{kj,ca}}{\epsilon_k+\epsilon_j-\epsilon_c-\epsilon_a}\chi_{ic,qk} \\
&\quad - \sum_{kc}\frac{\chi_{ki,ca}}{\epsilon_k+\epsilon_i-\epsilon_c-\epsilon_a}\chi_{jc,qk} + \sum_{c}\frac{\tilde{\Sigma}^{\infty(0)}_{ic}\chi_{cj,qa}}{\epsilon_i-\epsilon_c} - \sum_{c}\frac{\tilde{\Sigma}^{\infty(0)}_{jc}\chi_{ci,qa}}{\epsilon_j-\epsilon_c} \qquad \text{(3.10.2.3b)} \\
&\quad - \sum_{k}\frac{\tilde{\Sigma}^{\infty(0)}_{ka}\chi_{ij,qk}}{\epsilon_k-\epsilon_a}\,.
\end{aligned}$$

In the Brueckner basis, the final three terms of Eqs 3.10.2.3a and 3.10.2.3b vanish. The coupling matrices $\bar{U}^{(0)}_{iab,q}/\bar{V}^{(0)}_{p,ija}$ remain the same as those defined in Subsection 3.10.1. This reflects the inherent non-hermitian structure of the coupled-cluster self-energy. Using the definition of the interaction and coupling matrices defined above leads to the upfolded CC Dyson supermatrix

$$\tilde{\mathbf{D}}^{\mathrm{CC}}_{\mathrm{ADC(2p1h(0))}} = \begin{pmatrix} f_{pq} + \tilde{\Sigma}^{\infty(0)}_{pq} + \tilde{\Sigma}^{\infty(2)}_{pq} & \tilde{U}^{\mathrm{2p1h(0)}}_{p,abi} & \bar{V}^{(0)}_{p,ija} \\ \bar{U}^{(0)}_{cdj,q} & \bar{\mathbf{K}}^{>}_{iab,jcd} + \bar{\mathbf{C}}^{>(0)}_{iab,jcd} & \mathbf{0} \\ \tilde{V}^{\mathrm{2h1p(0)}}_{klb,q} & \mathbf{0} & \bar{\mathbf{K}}^{<}_{ija,klb} + \bar{\mathbf{C}}^{<(0)}_{ija,klb} \end{pmatrix}. \tag{3.10.2.4}$$

This approximation corresponds to the infinite-order summation of the coupled-cluster self-energy diagrams depicted in Figure 3.1 and is closely related to IP/EA-EOM-CC theory truncated to the space of 2p1h/2h1p excitations. However, the upper left block of the coupled-cluster Dyson supermatrix is defined over the combined set of occupied and virtual spin-orbitals. This definition of the interaction and coupling matrices results in the 2p1h(0)/2h1p(0) coupled-cluster self-energy approximation

$$\begin{aligned}
\tilde{\Sigma}^{\mathrm{ADC(2p1h(0))}}_{pq}(\omega) &= \tilde{\Sigma}^{\infty(0)}_{pq} + \tilde{\Sigma}^{\infty(2)}_{pq} \\
&\quad + \frac{1}{(2!)^2}\sum_{\substack{iab\\jcd}}\tilde{U}^{\mathrm{2p1h(0)}}_{p,iab}\Big((\omega+i\eta)\mathbb{1} - (\bar{\mathbf{K}}^{>} + \bar{\mathbf{C}}^{>(0)})\Big)^{-1}_{iab,jcd}\bar{U}^{(0)}_{jcd,q} \\
&\quad + \frac{1}{(2!)^2}\sum_{\substack{kla\\mnb}}\bar{V}^{(0)}_{p,kla}\Big((\omega-i\eta)\mathbb{1} - (\bar{\mathbf{K}}^{<} + \bar{\mathbf{C}}^{<(0)})\Big)^{-1}_{kla,mnb}\tilde{V}^{\mathrm{2h1p(0)}}_{mnb,q}\,.
\end{aligned} \tag{3.10.2.5}$$

Similarly, we can further generalize the 2p1h/2h1p coupled-cluster self-energy approximation by allowing the interaction matrices to be composed of the full effective interactions arising when normal-ordering $\bar{H}$ with respect to the biorthogonal ground state expectation value. This results in the following interaction matrices [4]

$$\begin{aligned}\bar{\mathbf{C}}^{>}_{iab,jcd} = \tilde{\Sigma}^{\infty}_{ac}\delta_{ij}\delta_{bd} - \tilde{\Sigma}^{\infty}_{ad}\delta_{ij}\delta_{bc} + \tilde{\Sigma}^{\infty}_{bd}\delta_{ac}\delta_{ij} - \tilde{\Sigma}^{\infty}_{bc}\delta_{ad}\delta_{ij} - \tilde{\Sigma}^{\infty}_{ji}\delta_{ac}\delta_{bd} + \tilde{\Sigma}^{\infty}_{ji}\delta_{ad}\delta_{bc} \\ + \tilde{\Xi}_{ja,ci}\delta_{bd} + \tilde{\Xi}_{jb,di}\delta_{ac} + \tilde{\Xi}_{ab,cd}\delta_{ij} - \tilde{\Xi}_{ja,di}\delta_{bc} - \tilde{\Xi}_{jb,ci}\delta_{ad} + \tilde{\chi}_{jab,cid}\end{aligned} \tag{3.10.2.6a}$$

$$\begin{aligned}\bar{\mathbf{C}}^{<}_{ija,klb} = \tilde{\Sigma}^{\infty}_{ik}\delta_{ab}\delta_{jl} - \tilde{\Sigma}^{\infty}_{il}\delta_{ab}\delta_{jk} + \tilde{\Sigma}^{\infty}_{jl}\delta_{ab}\delta_{ik} - \tilde{\Sigma}^{\infty}_{jk}\delta_{ab}\delta_{il} + \tilde{\Sigma}^{\infty}_{ba}\delta_{il}\delta_{jk} - \tilde{\Sigma}^{\infty}_{ba}\delta_{ik}\delta_{jl} \\ + \tilde{\Xi}_{ib,al}\delta_{jk} + \tilde{\Xi}_{jb,ak}\delta_{il} - \tilde{\Xi}_{ij,kl}\delta_{ab} - \tilde{\Xi}_{ib,ak}\delta_{jl} - \tilde{\Xi}_{jb,al}\delta_{ik} + \tilde{\chi}_{ijb,kal}\ .\end{aligned} \tag{3.10.2.6b}$$

To reiterate, in order to be consistent with the treatment of the 2p1h/2h1p excitation character of the intermediate state configurations, the static coupled-cluster self-energy contribution and the effective interactions $\tilde{\Xi}_{pq,rs}$ and $\tilde{\chi}_{pqr,stu}$ appearing in Eqs 3.10.2.6a and 3.10.2.6b are taken in the CCSD approximation. Then, we define the coupling matrices to be composed of the renormalized interactions as follows:

$$\begin{aligned}\tilde{U}^{\text{2p1h}}_{p,iab} = \tilde{\Xi}_{pi,ab} + \frac{1}{2}\sum_{kl}\tilde{\Xi}_{pi,kl}\frac{\tilde{\Xi}_{kl,ab}}{\epsilon_k+\epsilon_l-\epsilon_a-\epsilon_b} + \sum_{kc}\tilde{\Xi}_{pc,ak}\frac{\tilde{\Xi}_{ik,bc}}{\epsilon_i+\epsilon_k-\epsilon_b-\epsilon_c} \\ - \sum_{kc}\tilde{\Xi}_{pc,bk}\frac{\tilde{\Xi}_{ik,ac}}{\epsilon_i+\epsilon_k-\epsilon_a-\epsilon_c} - \sum_{k}\frac{\tilde{\Xi}_{pi,kb}\tilde{\Sigma}^{\infty}_{ka}}{\epsilon_k-\epsilon_a} + \sum_{k}\frac{\tilde{\Xi}_{pi,ka}\tilde{\Sigma}^{\infty}_{kb}}{\epsilon_k-\epsilon_b} + \sum_{c}\tilde{\Xi}_{pc,ab}\frac{\tilde{\Sigma}^{\infty}_{ic}}{\epsilon_i-\epsilon_c}\ ,\end{aligned} \tag{3.10.2.7a}$$

$$\bar{U}^{\text{2p1h}}_{iab,q} = \tilde{\Xi}_{ab,qi} \tag{3.10.2.7b}$$

$$\begin{aligned}\tilde{V}^{\text{2h1p}}_{ija,q} = \tilde{\Xi}_{ij,qa} + \frac{1}{2}\sum_{cd}\frac{\tilde{\Xi}_{ij,cd}}{\epsilon_i+\epsilon_j-\epsilon_c-\epsilon_d}\tilde{\Xi}_{cd,qa} + \sum_{kc}\frac{\tilde{\Xi}_{kj,ca}}{\epsilon_k+\epsilon_j-\epsilon_c-\epsilon_a}\tilde{\Xi}_{ic,qk} \\ - \sum_{kc}\frac{\tilde{\Xi}_{ki,ca}}{\epsilon_k+\epsilon_i-\epsilon_c-\epsilon_a}\tilde{\Xi}_{jc,qk} + \sum_{c}\frac{\tilde{\Sigma}^{\infty}_{ic}\tilde{\Xi}_{cj,qa}}{\epsilon_i-\epsilon_c} - \sum_{c}\frac{\tilde{\Sigma}^{\infty}_{jc}\tilde{\Xi}_{ci,qa}}{\epsilon_j-\epsilon_c} - \sum_{k}\frac{\tilde{\Sigma}^{\infty}_{ka}\tilde{\Xi}_{ij,qk}}{\epsilon_k-\epsilon_a}\end{aligned} \tag{3.10.2.7c}$$

$$\bar{V}^{\text{2h1p}}_{p,ija} = \tilde{\Xi}_{pa,ij}\ . \tag{3.10.2.7d}$$

This definition of the coupling matrices ensures that all time-orderings of the 2p1h/2h1p CC self-energy diagrams are included in the CC Dyson supermatrix. The CC Dyson supermatrix within this approximation is given by

$$\tilde{\mathbf{D}}^{\text{CC}}_{\text{ADC(2p1h)}} = \begin{pmatrix} f_{pq} + \tilde{\Sigma}^{\infty\text{CCSD}}_{pq} & \tilde{U}^{\text{2p1h}}_{p,iab} & \bar{V}^{\text{2h1p}}_{p,ija} \\ \bar{U}^{\text{2p1h}}_{jcd,q} & \bar{\mathbf{K}}^{>}_{iab,jcd} + \bar{\mathbf{C}}^{>}_{iab,jcd} & \mathbf{0} \\ \tilde{V}^{\text{2h1p}}_{klb,q} & \mathbf{0} & \bar{\mathbf{K}}^{<}_{ija,klb} + \bar{\mathbf{C}}^{<}_{ija,klb} \end{pmatrix}. \tag{3.10.2.8}$$

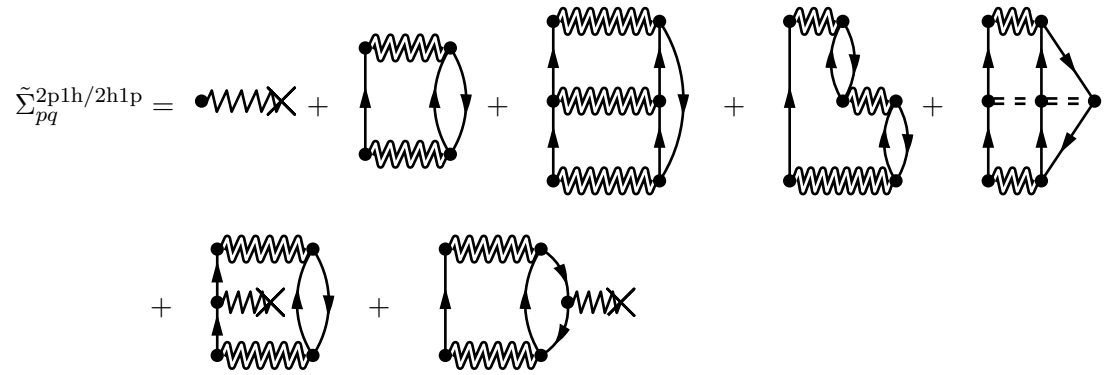

Figure 3.3: The set of third-order 2p1h/2h1p excitation character restricted 1PI coupled-cluster self-energy diagrams that are obtained from the diagrams in Figure 3.2 by replacing the self-consistent propagators with their lowest-order linearized equivalents: $\tilde{G} \rightarrow G_0 + G_0\tilde{\Sigma}^{\infty}G_0$.

The CC Dyson supermatrix approximations, defined in Eqs. 3.10.2.4 and 3.10.2.8, can be viewed as infinite-order summations of coupled-cluster self-energy diagrams. Eq. 3.10.2.4 is constructed from the infinite-order summation of the perturbative coupled-cluster self-energy diagrams depicted in Figure 3.1, whereas Eq. 3.10.2.8 results from the infinite-order summation of the diagrammatic series depicted in Figure 3.3. The coupled-cluster self-energy diagrams depicted in Figure 3.3 are obtained from the self-consistent diagrams presented in Figure 3.2 by retaining the third-order 2p1h/2h1p self-energy diagrams that result upon replacement of the self-consistent propagators with their lowest-order linearized equivalents: $\tilde{G} \rightarrow G_0 + G_0\tilde{\Sigma}^{\infty}G_0$. This replacement gives rise to the sixth and seventh diagrams of Figure 3.3 which are one-particle irreducible contributions, containing interactions vertices that are interaction-irreducible.

Downfolding the CC Dyson supermatrix in Eq. 3.10.2.8 into the single-particle spin-orbital subspace spanned by the upper left block results in the following coupled-cluster self-energy approximation

$$\begin{aligned}\tilde{\Sigma}^{\mathrm{ADC(2p1h)}}_{pq}(\omega) = \tilde{\Sigma}^{\infty\mathrm{CCSD}}_{pq} &+ \frac{1}{(2!)^2}\sum_{\substack{iab\\jcd}} \tilde{U}^{\mathrm{2p1h}}_{p,iab}\Big((\omega+i\eta)\mathbb{1} - (\bar{\mathbf{K}}^{>} + \bar{\mathbf{C}}^{>})\Big)^{-1}_{iab,jcd}\bar{U}^{\mathrm{2p1h}}_{jcd,q} \\ &+ \frac{1}{(2!)^2}\sum_{\substack{kla\\mnb}} \bar{V}^{\mathrm{2h1p}}_{p,kla}\Big((\omega-i\eta)\mathbb{1} - (\bar{\mathbf{K}}^{<} + \bar{\mathbf{C}}^{<})\Big)^{-1}_{kla,mnb}\tilde{V}^{\mathrm{2h1p}}_{mnb,q} \,,\end{aligned} \tag{3.10.2.9}$$

and corresponds to the infinite-order summation of the coupled-cluster self-energy diagrams depicted in Figure 3.3.

Therefore, the coupled-cluster Dyson supermatrices of Eqs 3.10.2.4 and 3.10.2.8 are identical to the third-order Algebraic Diagrammatic Construction method (ADC(3)) applied to the 2p1h/2h1p coupled-cluster self-energy diagrams depicted in Figures 3.1 and 3.3. However, it should be noted that the vanishing different Goldstone time-orderings of the third-order CC self-energy diagrams, as a result of the CC amplitude equations, is in contradistinction to the hermitian ADC(3) electronic Dyson supermatrix construction [35, 41]. In the case of the hermitian electronic self-energy, these different time-orderings are non-zero and give rise to additional contributions to the coupling matrices. The reader is referred to Refs [35, 36, 41] for a comprehensive review of the Algebraic Diagrammatic Construction method.

3.11 Relationship to IP/EA-EOM-CC and G_0W_0 approximations

In this section, we provide an overview of the connections between approximations for the coupled-cluster self-energy, IP/EA-EOM-CC and G_0W_0 theory. Subsequently, we arrive at CC-G_0W_0 theory.

3.11.1 Connection to IP/EA-EOM-CC theory

The IP-EOM-CC method was presented in Section 3.4. The electron removal energies are obtained from the IP-EOM-CC eigenvalue problem given in Eq. 3.4.0.12. Restricting the IP-EOM-CC supermatrix to contain only 2h1p interactions gives the IP-EOM-CCSD approximation [85]:

$$\bar{\mathbf{H}}^{\text{IP-EOM-CCSD}} = -\begin{pmatrix} \langle\Phi_i|\bar{H}_N|\Phi_j\rangle & \langle\Phi_i|\bar{H}_N|\Phi^a_{kl}\rangle \\ \langle\Phi^b_{mn}|\bar{H}_N|\Phi_j\rangle & \langle\Phi^b_{mn}|\bar{H}_N|\Phi^a_{kl}\rangle \end{pmatrix} . \tag{3.11.1.1}$$

By identifying that the upper left block is $-\langle\Phi_i|\bar{H}_N|\Phi_j\rangle = f_{ji} + \tilde{\Sigma}^{\infty(0)}_{ji}$, that in the Brueckner basis, $\langle\Phi_i|\bar{H}_N|\Phi^a_{kl}\rangle = \chi_{kl,ia}$ and $\langle\Phi^b_{mn}|\bar{H}_N|\Phi_j\rangle = \chi_{jb,mn}$, we re-write the IP-EOM-CCSD supermatrix as

$$\bar{\mathbf{H}}^{\text{IP-EOM-CCSD}} = \begin{pmatrix} f_{ji} + \tilde{\Sigma}^{\infty(0)}_{ji} & -\chi_{kl,ia} \\ -\chi_{jb,mn} & \bar{\mathbf{K}}^{<}_{kla,mnb} + \bar{\mathbf{C}}^{<(0)}_{kla,mnb} \end{pmatrix} , \tag{3.11.1.2}$$

where we have used Eq. 3.10.2.1 to identify the interaction matrices as the lower right block of the IP-EOM-CCSD supermatrix. Downfolding this supermatrix into the single-particle occupied-occupied subspace, we have [4, 5]

$$\bar{H}^{\text{EOM-CCSD}}_{ij}(\omega) = f_{ji} + \tilde{\Sigma}^{\infty(0)}_{ji} + \frac{1}{4}\sum_{\substack{kla\\mnb}} \chi_{ja,kl}\Big(\omega\mathbb{1} - (\bar{\mathbf{K}}^{<} + \bar{\mathbf{C}}^{<(0)})\Big)^{-1}_{kla,mnb}\chi_{mn,ib}. \tag{3.11.1.3}$$

Transposing Eq. 3.11.1.3, we identify the effective EOM-CCSD 'non-Dyson self-energy' as:

$$\begin{aligned}\bar{\Sigma}^{\text{EOM-CCSD}}_{ij}(\omega) &= \bar{H}^{\text{EOM-CCSD}}_{ji}(\omega) - f_{ij} \\ &= \tilde{\Sigma}^{\infty(0)}_{ij} + \frac{1}{4}\sum_{\substack{kla\\mnb}} \chi_{ia,kl}\Big(\omega\mathbb{1} - (\bar{\mathbf{K}}^{<} + \bar{\mathbf{C}}^{<(0)})\Big)^{-1}_{kla,mnb}\chi_{mn,jb}.\end{aligned} \tag{3.11.1.4}$$

By comparison with Eq. 3.10.2.5, we see that the IP-EOM-CCSD effective self-energy is related to the transpose of the 2p1h(0) coupled-cluster self-energy restricted to the occupied-occupied block. However, the contribution $\tilde{\Sigma}^{\infty(2)}_{ij}$ does not appear in IP-EOM-CCSD theory. It arises from the correct treatment of the static component in the perturbative expansion of the coupled-cluster self-energy resulting from the Green's function formalism. Additionally, the coupling matrices of the ADC(2p1h(0)) CC self-energy (Eq. 3.10.2.5) contain different time-orderings that are neglected in the IP-EOM-CCSD approximation which is based on a Configuration Interaction expansion. As a result, ADC(2p1h(0)) CC self-energy diagrams such as

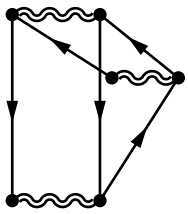

are not included in IP-EOM-CCSD theory. However, it should be noted that the untruncated algebraic-wavefuction based IP/EA-EOM-CC theory and the full set of 1PI coupled-cluster self-energy diagrams are both formally exact approaches for obtaining the charge-excitation spectrum of the similarity-transformed Hamiltonian despite their differing mathematical formulations [4].

3.11.2 The G_0W_0 self-energy and CC-G_0W_0 theory

The dynamical G_0W_0 self-energy is given by [38, 97, 134, 144]

$$\Sigma^{G_0W_0}_{pq}(\omega) = \sum_{a\nu}\frac{W_{p,a\nu}W_{a\nu,q}}{\omega - \Omega_\nu - \epsilon_a + i\eta} + \sum_{i\nu}\frac{W_{p,i\nu}W_{i\nu,q}}{\omega + \Omega_\nu - \epsilon_i - i\eta}\ , \tag{3.11.2.1}$$

where the coupling and interaction matrix elements $W_{p,q\nu}$ and Ω_ν are usually found by solution of the RPA equations within the quasi-boson approximation [19]

$$\begin{pmatrix} \mathbf{A} & \mathbf{B} \\ -\mathbf{B}^* & -\mathbf{A}^* \end{pmatrix} \begin{pmatrix} \mathbf{X} \\ \mathbf{Y} \end{pmatrix} = \mathbf{\Omega} \begin{pmatrix} \mathbf{X} \\ \mathbf{Y} \end{pmatrix} \tag{3.11.2.2}$$

where

$$A_{ia,jb} = (\epsilon_a - \epsilon_i)\,\delta_{ab}\delta_{ij} + \langle ib||aj\rangle \ , \tag{3.11.2.3a}$$

$$B_{ia,jb} = \langle ij||ab\rangle \ , \tag{3.11.2.3b}$$

$$W_{p,q\nu} = \sum_{ia} \Big(\langle pa||qi\rangle\, X^\nu_{ia} + \langle pi||qa\rangle\, Y^\nu_{ia} \Big) \ . \tag{3.11.2.3c}$$

In the G_0W_0 approximation, the exchange interaction is usually separated from the direct interaction and one is left with only the direct RPA (dRPA) equations. Here, we instead choose to work with the antisymmetrized RPA equations to more easily exploit the connections to coupled-cluster theory. The exchange contributions may be trivially removed from our equations to recover the G_0W_0 approximation using dRPA [97, 99]. In terms of the upfolded Dyson supermatrix representation, the G_0W_0 eigenvalue problem takes the form

$$\mathbf{D}^{G_0W_0} = \begin{pmatrix} f_{pq} & W_{p,a\nu} & W_{p,i\nu} \\ W_{a\nu,q} & \mathbf{\Lambda}^{G_0W_0>}_{a\nu,b\nu'} & \mathbf{0} \\ W_{i\nu,q} & \mathbf{0} & \mathbf{\Lambda}^{G_0W_0<}_{i\nu,j\nu'} \end{pmatrix} \tag{3.11.2.4}$$

with

$$\mathbf{\Lambda}^{G_0W_0>}_{a\nu,b\nu'} = (\epsilon_a + \Omega_\nu)\delta_{ab}\delta_{\nu\nu'} \tag{3.11.2.5a}$$

$$\mathbf{\Lambda}^{G_0W_0<}_{i\nu,j\nu'} = (\epsilon_i - \Omega_\nu)\delta_{ij}\delta_{\nu\nu'} \ . \tag{3.11.2.5b}$$

where the index ν is a quasi-boson index that spans a set of values much larger than the spin-orbital index. The RPA eigenvalue problem can be re-written in terms of effective coupled-cluster doubles amplitudes by identifying $\mathbf{T} = \mathbf{Y}\mathbf{X}^{-1}$. Using this expression in the RPA equations (Eq. 3.11.2.2) leads to the ring CCD (rCCD) approximation [4, 100, 145]

$$\mathbf{B}^* + \mathbf{A}^*\mathbf{T} + \mathbf{T}\mathbf{A} + \mathbf{T}\mathbf{B}\mathbf{T} = \mathbf{0} \ , \tag{3.11.2.6}$$

with the RPA Hamiltonian written as

$$H^{\mathrm{RPA}}_{ia,jb} = (\epsilon_a - \epsilon_i)\delta_{ab}\delta_{ij} + \langle ib||aj\rangle + \sum_{kc} \langle ik||ac\rangle\, (t^{cb}_{kj})_{\mathrm{rCCD}}. \tag{3.11.2.7}$$

As a result, the RPA eigenvalue problem becomes

$$\sum_{jb} H^{\mathrm{RPA}}_{ia,jb} X^{\nu}_{jb} = \Omega_{\nu} X^{\nu}_{ia} \ . \tag{3.11.2.8}$$

where the rCCD doubles amplitudes do not retain fermionic anti-symmetry [100].

To demonstrate the connection between the G_0W_0 approximation and the coupled-cluster self-energy, we restrict our analysis of the coupled-cluster self-energy to the space of 2h1p/2p1h excitations. In doing so, we introduce the CC-G_0W_0 Dyson supermatrix as

$$\tilde{\mathbf{D}}^{\text{CC-}G_0W_0} = \begin{pmatrix} f_{pq} + \tilde{\Sigma}^{\infty \mathrm{rCCD}}_{pq} & \chi^{\mathrm{rCCD}}_{pi,ab} & \chi^{\mathrm{rCCD}}_{pa,ij} \\ \chi^{\mathrm{rCCD}}_{ab,qi} & \bar{\mathbf{\Lambda}}^{G_0W_0>}_{iab,jcd} & \mathbf{0} \\ \chi^{\mathrm{rCCD}}_{ij,qa} & \mathbf{0} & \bar{\mathbf{\Lambda}}^{G_0W_0<}_{ija,klb} \end{pmatrix} \tag{3.11.2.9}$$

where the effective interactions $\{\chi^{\mathrm{rCCD}}_{pq,rs}\}$ are found from the two-body matrix elements of $\bar{H}$, but are formed from only the rCCD diagrams and amplitudes. For example, the element $\chi^{\mathrm{rCCD}}_{ia,kl}$ is given by

$$\chi^{\mathrm{rCCD}}_{ia,kl} = \langle ia||kl\rangle + \sum_{cm} \langle im||kc\rangle \, (t^{ca}_{ml})_{\mathrm{rCCD}} \ . \tag{3.11.2.10}$$

The interaction matrices are defined as

$$\bar{\mathbf{\Lambda}}^{G_0W_0>}_{iab,jcd} = (\epsilon_a \delta_{bd} \delta_{ij} + H^{\mathrm{dRPA}}_{ib,jd}) \delta_{ac} \tag{3.11.2.11a}$$

$$\bar{\mathbf{\Lambda}}^{G_0W_0<}_{ija,klb} = (\epsilon_i \delta_{jl} \delta_{ab} - H^{\mathrm{dRPA}}_{ja,lb}) \delta_{ik} \ . \tag{3.11.2.11b}$$

The static contribution, $\tilde{\Sigma}^{\infty \mathrm{rCCD}}_{pq}$, can be evaluated exactly within the rCCD approximation and is given by

$$\tilde{\Sigma}^{\infty \mathrm{rCCD}}_{pq} = \tilde{\Sigma}^{\infty (0) \mathrm{rCCD}}_{pq} + \frac{1}{(2!)^2} \sum_{ijab} \chi^{\mathrm{rCCD}}_{pab,qij} (\lambda^{ij}_{ab})_{\mathrm{rCCD}} \ , \tag{3.11.2.12}$$

where $(\lambda^{ij}_{ab})_{\mathrm{rCCD}}$ are the rCCD de-excitation amplitudes obtained from the rCCD Lagrangian [98]. There are no singles amplitudes in the coupled-cluster doubles approximation. The three-body interaction elements can be found in Ref. [85], an example of which is the element

$$\chi^{\mathrm{rCCD}}_{iab,jkl} = \sum_{n} \chi^{\mathrm{rCCD}}_{in,jk} (t^{ab}_{nl})_{\mathrm{rCCD}} + \sum_{c} \chi^{\mathrm{rCCD}}_{ia,ck} (t^{cb}_{jl})_{\mathrm{rCCD}} \ . \tag{3.11.2.13}$$

Using these coupling and interaction matrix elements, the diagrammatic representation of the CC-G_0W_0 self-energy diagrams contained in the $\tilde{\mathbf{D}}^{\text{CC-}G_0W_0}$ supermatrix is depicted in Figure 3.4. We clearly see that this approximation results in the infinite-order summation

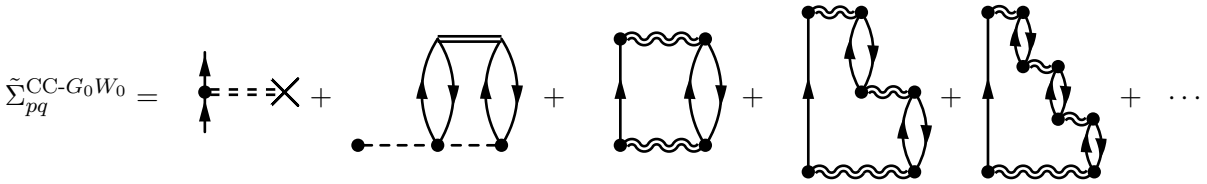

Figure 3.4: Diagrammatic representation of the CC-G_0W_0 self-energy. The bubble diagrams are summed to infinite-order through the $\tilde{\mathbf{D}}^{\text{CC-}G_0W_0}$ supermatrix representation (Eq. 3.11.2.9) and the two-body antisymmetrized effective interactions are evaluated within the rCCD approximation. The non-interacting Green's function lines appearing in the dynamical self-energy diagrams are not fully antisymmetrized with respect to fermionic exchange.

of the coupled-cluster bubble self-energy diagrams, analogous to the G_0W_0 approximation which performs an infinite-order summation of electronic bubble self-energy diagrams.

Finally, from Eq. 3.9.0.16, the ground state correlation energy in CC-G_0W_0 theory is the RPA correlation energy [4, 100]

$$E_c^{\text{CC-}G_0W_0} = \frac{1}{2}\sum_i \tilde{\Sigma}_{ii}^{\infty(0)\text{rCCD}} = \frac{1}{4}\sum_{ij,ab} \langle ij||ab\rangle \, (t_{ij}^{ab})_{\text{rCCD}} \, . \tag{3.11.2.14}$$

Through this reformulation of the G_0W_0 approximation in the framework of coupled-cluster theory, we may now include 'vertex' corrections that go beyond the G_0W_0 approximation, while maintaining the correct spectral form of the self-energy. This is achieved by simply modifying the doubles excitation and de-excitation amplitudes that enter the approximation. For example, using Eq. 3.11.2.9, one may use the full CCSD singles and doubles excitation and de-excitation amplitudes instead of the rCCD amplitudes. This would provide a simple way to extend the G_0W_0 approximation to include effects of singles excitations and go beyond RPA screening by including the complete set of interactions, $\langle \Phi_j^b | \bar{H}_N | \Phi_i^a \rangle$, between singly excited configurations in the definition of the interaction matrices defined in $\bar{\mathbf{\Lambda}}_{iab,jcd}^{G_0W_0>}/\bar{\mathbf{\Lambda}}_{ija,klb}^{G_0W_0<}$ [4].

3.12 The coupled-cluster Bethe-Salpeter Equation

In Chapter 2, it was demonstrated that within the Green's function formalism the Bethe-Salpeter equation (BSE) describes two-particle correlation processes and gives access to neutral and two-particle excitation energies. We can immediately write the

coupled-cluster Bethe-Salpeter equation as

$$\begin{aligned}\tilde{L}_{pq,rs}(t_1,t_2;t_3,t_4) &= \tilde{L}^0_{pq,rs}(t_1,t_2;t_3,t_4) \\ &+ \sum_{tuvw}\int dtdt'dt''dt'''\tilde{L}^0_{pt,ru}(t_1,t;t_3,t')\tilde{\Xi}_{uv,tw}(t',t'';t,t''')\tilde{L}_{wq,vs}(t''',t_2;t'',t_4),\end{aligned} \tag{3.12.0.1}$$

where $\tilde{L}^0_{pq,rs}(t_1,t_2;t_3,t_4) = -i\tilde{G}_{ps}(t_1,t_4)\tilde{G}_{qr}(t_2,t_3)$ corresponds to the propagation of two-independent particles [17], and $\tilde{\Xi}$ is the coupled-cluster Bethe-Salpeter kernel. The correlated four-point linear response function $\tilde{L}$ is defined as

$$\tilde{L}_{pq,rs}(t_1,t_2;t_3,t_4) = \tilde{G}^{\mathrm{4pt}}_{pq,rs}(t_1,t_2;t_3,t_4) - i\tilde{G}_{pr}(t_1,t_3)\tilde{G}_{qs}(t_2,t_4)\ , \tag{3.12.0.2}$$

and can be expressed as the functional derivative of the single-particle Green's function with respect to a fictitious external potential via application of Schwinger's functional derivative technique to the biorthogonal Interaction picture (Section 3.2).

It is important to note that the coupled-cluster BSE is not an equation for the coupled-cluster representation of the electronic 4-point response function, which is defined as

$$\bar{L}_{pq,rs}(t_1,t_2;t_3,t_4) = \bar{G}^{\mathrm{4pt}}_{pq,rs}(t_1,t_2;t_3,t_4) - i\bar{G}_{pr}(t_1,t_3)\bar{G}_{qs}(t_2,t_4)\ ,$$

where

$$i\bar{G}^{\mathrm{4pt}}_{pq,rs}(t_1,t_2;t_3,t_4) = \langle\tilde{\Psi}_0|\mathcal{T}\left\{\bar{a}_q(t_2)\bar{a}_p(t_1)\bar{a}^\dagger_r(t_3)\bar{a}^\dagger_s(t_4)\right\}|\Phi_0\rangle$$

is the coupled-cluster representation of the electronic 4-point Green's function. This is because the coupled-cluster representation of the electronic 4-point electronic response function can only be obtained by direct computation using quantities obtained from ground state and excitation energy equation-of-motion (EE-EOM-CC) coupled-cluster theory, which remains largely unexplored. Instead, the coupled-cluster BSE naturally arises as a result of the coupling between the SP-CCGF and the four-point response function through the diagrammatic coupled-cluster self-energy.

In the real time-domain, the kernel of the coupled-cluster BSE is given by the functional derivative of the coupled-cluster self-energy with respect to the single-paricle coupled-cluster Green's function as

$$\tilde{\Xi}_{pq,rs}(t_1,t_2;t_3,t_4) = i\frac{\delta\tilde{\Sigma}_{pr}(t_1,t_3)}{\delta\tilde{G}_{sq}(t_4,t_2)}\ . \tag{3.12.0.3}$$

The kernel is composed of two-particle irreducible (2PI) diagrams [17]. The BSE is fundamentally different from the corresponding Dyson equation for the single-particle

Green's function because it cannot be cast as a closed form equation for the ph/hp response function. The ph/hp response function is defined as [35]

$$\tilde{L}^{\mathrm{ph}}_{pq,rs}(t_1,t_2) = \tilde{L}_{pq,rs}(t_1,t_2;t_1^+,t_2^+) \ . \tag{3.12.0.4}$$

The Fourier transform of the exact coupled-cluster ph/hp response function (Eq. 3.12.0.4), obtained by resolving the identity of N-particle eigenstates of $\bar{H}$, possess poles at the *exact* neutral excitation spectrum:

$$\tilde{L}^{\mathrm{ph}}_{pq,rs}(\omega) = \sum_{\nu\neq 0}\left(\frac{\langle\tilde{\Psi}_0|a_r^\dagger a_p|\bar{\Psi}^N_\nu\rangle\langle\tilde{\Psi}^N_\nu|a_s^\dagger a_q|\Phi_0\rangle}{\omega-\Omega_\nu+i\eta} - \frac{\langle\tilde{\Psi}_0|a_s^\dagger a_q|\bar{\Psi}^N_\nu\rangle\langle\tilde{\Psi}^N_\nu|a_r^\dagger a_p|\Phi_0\rangle}{\omega+\Omega_\nu-i\eta}\right), \tag{3.12.0.5}$$

where $\Omega_\nu = E^N_\nu - E^N_0$ are the exact neutral excitation energies of the system. Restricting the BSE to that of the ph/hp sector, we have

$$\begin{aligned}\tilde{L}^{\mathrm{ph}}_{pq,rs}(t_1,t_2) &= \tilde{L}^{\mathrm{ph(0)}}_{pq,rs}(t_1,t_2) \\ &\quad + \sum_{tuvw}\int dtdt'dt''dt'''\tilde{L}^0_{pt,ru}(t_1,t;t_1^+,t')\tilde{\Xi}_{uv,tw}(t',t'';t,t''')\tilde{L}_{wq,vs}(t''',t_2;t'',t_2^+) \ .\end{aligned} \tag{3.12.0.6}$$

Analogous to the hermitian theory presented in Chapter 2, the presence of the kernel $\tilde{\Xi}$ means that the BSE always contains a fundamental coupling between the particle-hole, particle-particle and hole-hole response functions [146].

3.12.1 The coupled-cluster Bethe-Salpeter kernel

By taking the functional derivative of the coupled-cluster self-energy defined in Eq. 3.8.1.9 with respect to the coupled-cluster Green's function we generate the coupled-cluster BSE kernel. Diagrammatically, this functional derivative is found by cutting the Green's function and interaction lines in the Feynman diagram series for the renormalized coupled-cluster self-energy. To do this, we first analyze the variation of the interaction lines with respect to the Green's function. In the real-time domain, the static component of the self-energy is given by

$$\begin{aligned}\tilde{\Sigma}^\infty_{pq}(t_1,t_3) &= \tilde{\Sigma}^\infty_{pq}\delta(t_1,t_3) \\ &= \left(\bar{h}_{pq} - i\sum_{rs}\bar{h}_{pr,qs}\tilde{G}_{sr}(t_1-t_1^+) + \frac{i}{4}\sum_{rs,tu}\bar{h}_{prs,qtu}\tilde{G}^{\mathrm{2ph}}_{tu,rs}(t_1-t_1^+)+\cdots\right)\delta(t_1,t_3) \ .\end{aligned} \tag{3.12.1.1}$$

The functional derivative of the static component with respect to the exact Green's function is therefore

$$i\frac{\delta\tilde{\Sigma}^{\infty}_{pr}(t_1,t_3)}{\delta\tilde{G}_{sq}(t_4,t_2)} = \left(\bar{h}_{pq,rs} - i\sum_{rs,tu}\bar{h}_{pqt,rsu}\tilde{G}_{ut}(t_1-t_1^+)+\cdots\right)\delta(t_1,t_3)\delta(t_1,t_2)\delta(t_1^+,t_4) + \tilde{\Xi}^{c}_{pq,rs}(t_1,t_2;t_1^+,t_4)\delta(t_1,t_3)\ , \tag{3.12.1.2}$$

where $\tilde{\Xi}^{c}_{pq,rs}(t_1,t_2;t_1^+,t_4)$ represents the contribution that is dependent on functional derivatives involving the $\tilde{\Lambda}^{2n\mathrm{pt}}$-vertices and is explicitly related to multiparticle correlation effects. This additional term $\tilde{\Xi}^{c}$ is similar in origin to the functional derivative of W with respect to the Green's function in the GW approximation that arises when deriving the electronic GW-BSE kernel. The first term inside the brackets is simply the series for the two-body effective interaction (see Appendix B.2) and so we have

$$\begin{aligned} i\frac{\delta\tilde{\Sigma}^{\infty}_{pr}(t_1,t_3)}{\delta\tilde{G}_{sq}(t_4,t_2)} &= \tilde{\Xi}_{pq,rs}\delta(t_1,t_3)\delta(t_1,t_2)\delta(t_1^+,t_4) \\ &\quad + \tilde{\Xi}^{c}_{pq,rs}(t_1,t_2;t_1^+,t_4)\delta(t_1,t_3)\ . \end{aligned} \tag{3.12.1.3}$$

Therefore, at first-order, the functional derivative is the static two-body effective interaction and arises due to 'independent particle' propagation. The additional term $\tilde{\Xi}^{c}$ must also be accounted for and gives rise to a dynamical contribution.

To derive the additional component $\tilde{\Xi}^{c}$ we adopt a simplified notation whereby the spin-orbital indices and time/frequency arguments are suppressed. With this notation, we write the 4-point and 6-point vertex equations from Eqs 3.8.1.5 and 3.8.1.6 as

$$\tilde{G}^{4\mathrm{pt}} = i\mathcal{A}\{\tilde{G}\tilde{G}\} - \tilde{G}\tilde{G}\tilde{\Lambda}^{4\mathrm{pt}}\tilde{G}\tilde{G} \tag{3.12.1.4}$$

and

$$\tilde{G}^{6\mathrm{pt}} = -\mathcal{A}\{\tilde{G}\tilde{G}\tilde{G}\} - i\mathcal{P}\{\tilde{G}\tilde{G}\tilde{G}\tilde{\Lambda}^{4\mathrm{pt}}\tilde{G}\tilde{G}\} + \tilde{G}\tilde{G}\tilde{G}\tilde{\Lambda}^{6\mathrm{pt}}\tilde{G}\tilde{G}\tilde{G}\ . \tag{3.12.1.5}$$

where $\mathcal{A}$ generates the correct fermionic symmetry associated with independent-particle propagation and $\mathcal{P}$ is the cyclic permutation symmetry required to correctly describe fermionic statistics of two correlated particles propagating with respect to a third independent-particle. Using this simplified notation, the static component of the self-energy becomes

$$\tilde{\Sigma}^{\infty} = \bar{h}^{1b} - i\bar{h}^{2b}\tilde{G} + \frac{i}{4}\bar{h}^{3b}\tilde{G}^{4\mathrm{pt}} - \frac{i}{(3!)^2}\bar{h}^{4b}\tilde{G}^{6\mathrm{pt}} + \cdots \tag{3.12.1.6}$$

where $\bar{h}^{nb}$ represent the n-body matrix elements of the similarity transformed Hamiltonian. The contribution of the functional derivative $\frac{\delta\tilde{\Sigma}^{\infty}}{\delta\tilde{G}}$ due to anti-symmetrized independent-particle propagation gives the static two-body effective interaction, $\tilde{\Xi}^{2b}$. The functional derivatives of the higher-body Green's functions with respect to the single-particle propagator (removing the anti-symmetrized independent-particle propagation) gives rise to the general structure

$$\frac{\delta}{\delta\tilde{G}}\Big(\tilde{G}^{4\text{pt}} - i\mathcal{A}\{\tilde{G}\tilde{G}\}\Big) = -2\tilde{G}\tilde{\Lambda}^{4\text{pt}}\tilde{G}\tilde{G} - \tilde{G}\tilde{G}\frac{\delta\tilde{\Lambda}^{4\text{pt}}}{\delta\tilde{G}}\tilde{G}\tilde{G} \tag{3.12.1.7a}$$

with

$$\begin{aligned}\frac{\delta}{\delta\tilde{G}}\Big(\tilde{G}^{6\text{pt}} + \mathcal{A}\{\tilde{G}\tilde{G}\tilde{G}\}\Big) = &-(3!)^2 i\tilde{G}\tilde{G}\tilde{\Lambda}^{4\text{pt}}\tilde{G}\tilde{G} - 3^2 i\tilde{G}\tilde{G}\tilde{G}\frac{\delta\tilde{\Lambda}^{4\text{pt}}}{\delta\tilde{G}}\tilde{G}\tilde{G} \\ &+ 3\tilde{G}\tilde{G}\tilde{\Lambda}^{6\text{pt}}\tilde{G}\tilde{G}\tilde{G} + \tilde{G}\tilde{G}\tilde{G}\frac{\delta\tilde{\Lambda}^{6\text{pt}}}{\delta\tilde{G}}\tilde{G}\tilde{G}\tilde{G}\end{aligned} \tag{3.12.1.7b}$$

and so on for the higher derivatives. In these equations, the pre-factors represent the number of equivalent terms generated by the different functional derivatives with respect to permutation of the fermionic states. Therefore, the functional derivative of the static component of the coupled-cluster self-energy gives rise to

$$\begin{aligned}i\frac{\delta\tilde{\Sigma}^{\infty}}{\delta\tilde{G}} &= \tilde{\Xi}^{2b} + \frac{1}{(2!)^2}\bar{h}^{3b}\Big(2!\tilde{G}\tilde{\Lambda}^{4\text{pt}}\tilde{G}\tilde{G} + \tilde{G}\tilde{G}\frac{\delta\tilde{\Lambda}^{4\text{pt}}}{\delta\tilde{G}}\tilde{G}\tilde{G}\Big) \\ &+ \frac{1}{(3!)^2}\bar{h}^{4b}\Big(-(3!)^2 i\tilde{G}\tilde{G}\tilde{\Lambda}^{4\text{pt}}\tilde{G}\tilde{G} - 3^2 i\tilde{G}\tilde{G}\tilde{G}\frac{\delta\tilde{\Lambda}^{4\text{pt}}}{\delta\tilde{G}}\tilde{G}\tilde{G} + 3\tilde{G}\tilde{G}\tilde{\Lambda}^{6\text{pt}}\tilde{G}\tilde{G}\tilde{G} + \tilde{G}\tilde{G}\tilde{G}\frac{\delta\tilde{\Lambda}^{6\text{pt}}}{\delta\tilde{G}}\tilde{G}\tilde{G}\tilde{G}\Big) \\ &+ \cdots\end{aligned} \tag{3.12.1.8}$$

Collecting like terms together along with the higher-order contributions arising from functional derivatives of the higher-order Green's functions we have

$$\begin{aligned}i\frac{\delta\tilde{\Sigma}^{\infty}}{\delta\tilde{G}} = \tilde{\Xi}^{2b} &+ \frac{1}{2!}\Big(\bar{h}^{3b} - i\bar{h}^{4b}\tilde{G} + \cdots\Big)\Big(\tilde{G}\tilde{\Lambda}^{4\text{pt}}\tilde{G}\tilde{G}\Big) \\ &+ \frac{1}{(2!)^2}\Big(\bar{h}^{3b} - i\bar{h}^{4b}\tilde{G} + \cdots\Big)\Big(\tilde{G}\tilde{G}\frac{\delta\tilde{\Lambda}^{4\text{pt}}}{\delta\tilde{G}}\tilde{G}\tilde{G}\Big) \\ &+ \frac{1}{(3!)^2}\Big(\bar{h}^{4b} - i\bar{h}^{5b}\tilde{G} + \cdots\Big)\Big(3\tilde{G}\tilde{G}\tilde{\Lambda}^{6\text{pt}}\tilde{G}\tilde{G}\tilde{G} + \tilde{G}\tilde{G}\tilde{G}\frac{\delta\tilde{\Lambda}^{6\text{pt}}}{\delta\tilde{G}}\tilde{G}\tilde{G}\tilde{G}\Big) + \cdots\end{aligned} \tag{3.12.1.9}$$

Identifying the expressions in brackets as the effective interactions that arise when normal-ordering the similarity transformed Hamiltonian with respect to the biorthogonal ground state expectation value, we find

$$\begin{aligned}i\frac{\delta\tilde{\Sigma}^{\infty}}{\delta\tilde{G}} = \tilde{\Xi}^{2b} &+ \frac{1}{2!}\tilde{\chi}^{3b}\Big(\tilde{G}\tilde{\Lambda}^{4\text{pt}}\tilde{G}\tilde{G}\Big) + \frac{1}{(2!)^2}\tilde{\chi}^{3b}\Big(\tilde{G}\tilde{G}\frac{\delta\tilde{\Lambda}^{4\text{pt}}}{\delta\tilde{G}}\tilde{G}\tilde{G}\Big) \\ &+ \frac{1}{3!\cdot 2!}\tilde{\chi}^{4b}\tilde{G}\tilde{G}\Lambda^{6\text{pt}}\tilde{G}\tilde{G}\tilde{G} + \frac{1}{(3!)^2}\tilde{\chi}^{4b}\tilde{G}\tilde{G}\tilde{G}\frac{\delta\Lambda^{6\text{pt}}}{\delta\tilde{G}}\tilde{G}\tilde{G}\tilde{G} + \cdots\end{aligned} \tag{3.12.1.10}$$

where the series continues with the higher-order effective interactions contracting with higher-order vertices in this schematic derivation. At first-order, the explicitly frequency-dependent contribution gives rise to the following diagrams, which correspond to the second term of the right hand side of Eq. 3.12.1.10

$$\tilde{\Xi}^{c(1)}_{pq,rs} \quad = \quad + \tag{3.12.1.11}$$

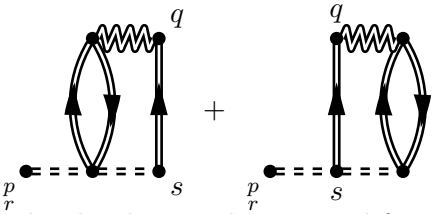

Here, we have re-inserted the spin-orbital indices and accounted for the different external index permutations. Diagrammatically, this term arises from cutting the Green's function lines in the following diagram contributing to the static component of the self-energy:

$$\tilde{\Sigma}^{\infty(c,1)}_{pr} = \tag{3.12.1.12}$$

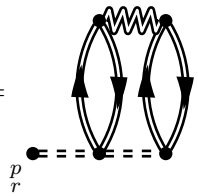

This diagram appears when expanding the 4-point Green's function in the expression for $\tilde{\Sigma}^{\infty}$ through the four-point vertex equation (Eq. 3.8.1.5). The resulting contribution is explicitly dynamical. A similar expression holds for the two-body effective interaction elements

$$i\frac{\delta\tilde{\Xi}_{pq,rs}}{\delta\tilde{G}_{ut}(t_4,t_2)}\delta(t_1,t_3) = \tilde{\chi}_{pqt,rsu}\delta(t_1,t_3)\delta(t_1,t_2)\delta(t_1^+,t_4) + \tilde{\chi}^{c}_{pqt,rsu}(t_1,t_2;t_1^+t_4)\delta(t_1,t_3)\ . \tag{3.12.1.13}$$

Using our simplified notation, we find

$$\begin{aligned} i\frac{\delta\tilde{\Xi}^{2b}}{\delta\tilde{G}} &= \tilde{\chi}^{3b} + \frac{1}{2!}\tilde{\chi}^{4b}\Big(\tilde{G}\tilde{\Lambda}^{4\mathrm{pt}}\tilde{G}\tilde{G}\Big) + \frac{1}{(2!)^2}\tilde{\chi}^{4b}\Big(\tilde{G}\tilde{G}\frac{\delta\tilde{\Lambda}^{4\mathrm{pt}}}{\delta\tilde{G}}\tilde{G}\tilde{G}\Big) \\ &\quad + \frac{1}{3!\cdot 2!}\tilde{\chi}^{5b}\tilde{G}\tilde{G}\Lambda^{6\mathrm{pt}}\tilde{G}\tilde{G}\tilde{G} + \frac{1}{(3!)^2}\tilde{\chi}^{5b}\tilde{G}\tilde{G}\tilde{G}\frac{\delta\Lambda^{6\mathrm{pt}}}{\delta\tilde{G}}\tilde{G}\tilde{G}\tilde{G} + \cdots \end{aligned} \tag{3.12.1.14}$$

and so on for the derivatives of higher-body interactions. In the case of a three-body Hamiltonian, this derivative would only generate the bare three-body interaction, $i\frac{\delta\tilde{\Xi}^{2b}}{\delta\tilde{G}} = \tilde{\chi}^{3b} = \bar{h}^{3b}$, as there are no higher-body interactions present. Using these results, the corresponding expansion for the coupled-cluster BSE kernel is given by the following series of Feynman diagrams (up to second-order)

$\tilde{\Xi}_{pq,rs}[\tilde{G}] =$

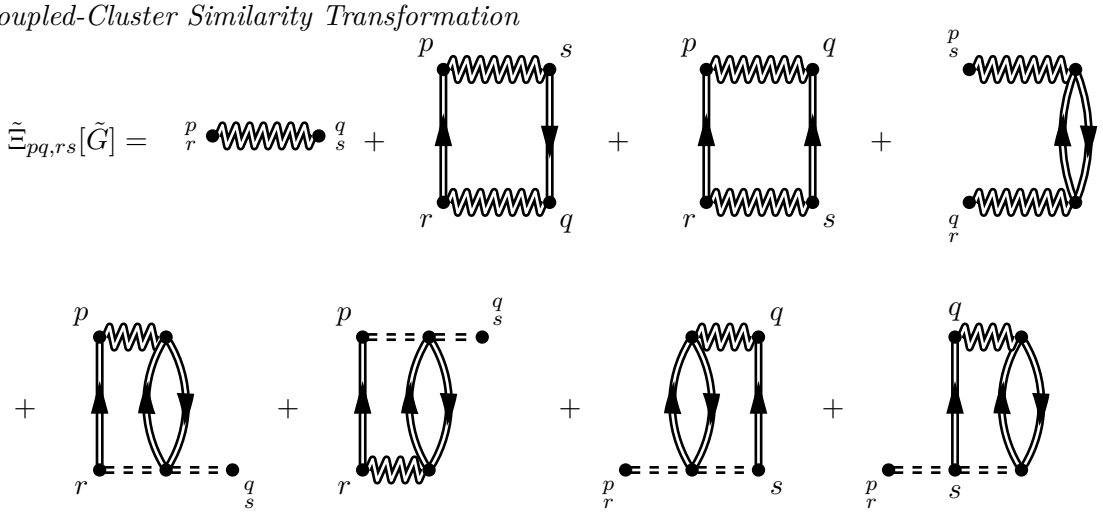

(3.12.1.15)

We obtain the perturbative expansion, $\tilde{\Xi}[G_0]$, to second-order by inserting Eq. 3.8.2.3 into Eq. 3.12.1.15 while replacing all effective interactions and Green's functions by their reference counterparts: $\tilde{\chi} \to \chi$, $\tilde{G} \to G_0$. As can be seen from the general diagrammatic series, the CC-BSE kernel reduces to the electronic BSE kernel when $T = 0$ and the effects of the similarity transformation are removed. The second, third and fourth diagrams of the first line of Eq. 3.12.1.15 arise by cutting the Green's function lines of the second-order dynamical self-energy diagram of Eq. 3.8.1.15. The fifth and sixth diagrams of Eq. 3.12.1.15 appear when taking the functional derivative of the two-body effective interaction lines appearing in the second-order self-energy diagram. They are the first-order contributions according to Eq. 3.12.1.13. The final two diagrams of Eq. 3.12.1.15 are those that arise due to derivatives of the static component of the self-energy as outlined in Eq. 3.12.1.11.

We can also take the functional derivative of the vanishing second-order self-energy diagram (see Section 3.7)

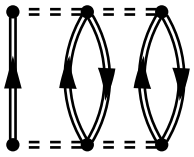

and find that this gives rise to the BSE kernel diagrams

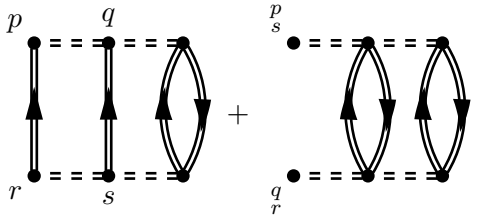

However, as these diagrams have four Green's function lines below the three-body vertex, they also vanish due to the coupled-cluster similarity transformation. If we take the functional derivative of the two-body interaction in Eq. 3.12.1.12, at first-order we generate the complementary exchange diagram

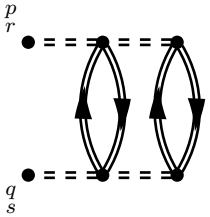

which also vanishes. At first-order, the functional derivative of the three-body effective interaction in Eq. 3.12.1.12 gives rise to the diagram

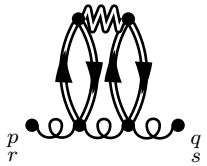

which explicitly contains the 4-body effective interaction. Depending on the ordering of the external indices, this diagram may not vanish and will give a non-zero contribution to the CC-BSE kernel.

From our analysis, we see that the diagrams of the Bethe-Salpeter kernel generated by an N-body interaction result from functional derivatives of different components of the self-energy. We note that the corresponding expression for the 6-point vertex function is obtained by the functional derivative of the BSE kernel with respect to the single-particle Green's function, $\tilde{\Lambda}^{6\text{pt}} \sim i\frac{\delta\tilde{\Xi}}{\delta\tilde{G}}$, and so on for the higher-order vertices. These relationships arise as the 6-point Green's function is generated from the functional derivative of the 4-point Green's function and so on.

Using the general analysis presented in this work, we can generate the diagrammatic series for the coupled-cluster BSE kernel order-by-order. When restricted to the Tamm-Dancoff approximation, the perturbative expansion of the coupled-cluster BSE kernel derived here is closely related to the EE-EOM-CC eigenvalue problem. To conclude this section, we write the terms appearing in the second-order perturbative expansion of the CC-BSE kernel as

$$\tilde{\Xi}^{(2)}_{pq,rs}(\omega) = \chi_{pq,rs} + \sum_{kc} \frac{\chi_{pqc,rsk}\tilde{\Sigma}^{\infty(0)}_{kc}}{\epsilon_k - \epsilon_c} + \frac{1}{(2!)^2}\sum_{abij} \frac{\chi_{pqab,rsij}\chi_{ij,ab}}{\epsilon_i - \epsilon_j - \epsilon_a - \epsilon_b} + \sum_{kc} \frac{\chi_{pk,sc}\chi_{cq,rk}}{\omega - (\epsilon_c - \epsilon_k) + i\eta}$$
$$+ \sum_{kc} \frac{\chi_{pc,ks}\chi_{kq,rc}}{\omega - (\epsilon_k - \epsilon_c) - i\eta} - \frac{1}{2}\sum_{kl} \frac{\chi_{pq,kl}\chi_{kl,rs}}{\omega - (\epsilon_k + \epsilon_l) - i\eta} + \frac{1}{2}\sum_{cd} \frac{\chi_{pq,cd}\chi_{cd,rs}}{\omega - (\epsilon_c + \epsilon_d) + i\eta}$$
$$+ \frac{1}{2}\sum_{abk} \frac{(\chi_{abq,rks}\chi_{pk,ab} + \chi_{pkq,abs}\chi_{ab,rk} + \chi_{pab,rks}\chi_{kq,ab} + \chi_{pab,rsk}\chi_{qk,ab})}{\omega + \epsilon_k - \epsilon_a - \epsilon_b + i\eta}$$
$$+ \frac{1}{2}\sum_{kla} \frac{(\chi_{klq,ras}\chi_{pa,kl} + \chi_{paq,kls}\chi_{kl,ra} + \chi_{pkl,ras}\chi_{aq,kl} + \chi_{pkl,rsa}\chi_{qa,kl})}{\omega + \epsilon_a - \epsilon_k - \epsilon_l - i\eta} \,. \tag{3.12.1.16}$$

Here, the first three terms arise due to the perturbative expansion of the two-body effective interaction (see Eq. 3.8.2.3). The remaining terms correspond to the remaining diagrams of Eq. 3.12.1.15 where the Green's function and interaction lines are replaced by G_0 and χ equivalents. We clearly see the similarity between the fourth, fifth, sixth and seventh terms of Eq. 3.12.1.16 and those obtained within the second-order perturbative approximation for the electronic BSE kernel [52–54, 96]. Using Eq. 3.12.1.16 for the CC-BSE kernel, we can formulate closed equations for the particle-hole response function which give access to neutral excitation energies. This is reserved for future work.

3.13 Conclusions

In summary, we have presented the diagrammatic theory of the irreducible self-energy and Bethe-Salpeter kernel that is generated by a general N-body hermitian or non-hermitian interaction Hamiltonian. We have centered our analysis around the non-hermitian coupled-cluster similarity transformed Hamiltonian.

To generate a consistent functional-diagrammatic theory of the coupled-cluster self-energy, we introduce the single-particle Green's function $\tilde{G}$, of a general N-body non-hermitian interaction within the biorthogonal quantum theory. We extend the GML theorem to include adiabatic generation of the right and left ground states of a psuedo-hermitian Hamiltonian, which leads to the perturbative expansion of the non-hermitian single-particle Green's function. Using our extended GML theorem, we define the non-hermitian Dyson equation and generate the perturbative expansion for the coupled-cluster self-energy, $\tilde{\Sigma}[G_0]$. From the exact equation-of-motion for the single-particle CC Green's

function we reveal the structure of the self-consistent renormalized coupled-cluster self-energy, $\tilde{\Sigma}[\tilde{G}]$ and demonstrate how the perturbative self-energy is generated from this functional. The analysis presented in this work clearly demonstrates the emergence of different effective interactions that appear when expanding the self-energy with respect to either the non-interacting or the exact Green's function. These interactions correspond to those appearing when normal-ordering the Hamiltonian with respect to the reference or exact ground state. Further, we show how the electronic self-energy emerges when the similarity transformation of the electronic structure Hamiltonian is removed.

We subsequently derive the coupled-cluster Dyson supermatrix from the exact, analytic spectral representation of the coupled-cluster self-energy and present several approximate expressions for the coupled-cluster self-energy that are restricted to the space of 2p1h/2h1p excitations. In the process, we have firmly demonstrated the relationship and connections between the coupled-cluster self-energy, IP/EA-EOM-CC theory and the G_0W_0 approximation. This analysis lead us to introduce CC-G_0W_0 theory which combines aspects of the G_0W_0 approximation with the coupled-cluster self-energy presented in Section 3.8. This is a novel approximation that will be explored in future work. Our formulation also allows us to explore approximations beyond G_0W_0 theory by using the full CCSD singles and doubles excitation and de-excitation amplitudes in place of the rCCD amplitudes. Use of the full CCSD amplitudes goes beyond RPA screening by including the complete set of interactions, $\langle \Phi_j^b | \bar{H}_N | \Phi_i^a \rangle$, between singly excited configurations [4].

Finally, we derive the coupled-cluster BSE kernel in terms of the functional derivative of the coupled-cluster self-energy with respect to the single-particle coupled-cluster Green's function. We demonstrate that diagrams of the CC-BSE kernel are generated both by cutting Green's function lines in self-energy diagrams whilst also taking derivatives of the interaction vertices. These diagrams are closely related to the terms that arise within EE-EOM-CC theory once further approximations are made in defining an effective kernel that depends only on a single frequency using the analysis presented in Chapter 2 [50, 53, 54].

Of particular interest in the context of non-hermitian quantum systems are $\mathcal{PT}$-symmetric Hamiltonians. However, in certain parameter regimes, not every eigenstate is also $\mathcal{PT}$-symmetric with a corresponding real eigenvalue solution [70, 78]. It has been well established that a $\mathcal{PT}$-broken phase can exist where eigenstates take on complex

eigenvalues [66, 111, 115, 116]. The Green's function formalism presented here is rooted in the biorthogonal theory whereby the left and right eigenstates of the Hamiltonian are dealt with explicitly. As a result, our approach is not concerned with the construction of a $\mathcal{PT}$-symmetric metric for the Hilbert space. Therefore, our formalism allows for the calculation of the full spectra of a generic non-hermitian Hamiltonian, including complex eigenvalues corresponding to a $\mathcal{PT}$-broken phase. This is also supported by the fact that the CC similarity transformed Hamiltonian does not possess $\mathcal{PT}$-symmetry. In fact, the presence of complex solutions can occur in truncated CC theories [147, 148], although their interpretation in the context of CC theory indicates a deficiency in the similarity-transformation rather than the presence a $\mathcal{PT}$-broken phase.

The formalism presented in this Chapter provides the rigorous theoretical foundation for many possible implementations as a result of different approximations of the coupled-cluster amplitude equations. A potential further application of the formalism presented in this work would be to generate the self-energy and BSE kernel for the transcorrelated Hamiltonian [149–152]. The theory presented in this work provides a unified and complete description of the seemingly disconnected approaches of coupled-cluster theory and the Green's function formalism. Our findings should form the basis for improved formulations of Green's function theory for systems of many interacting particles.

"Sometimes it happens that the most insane thought, the most impossible conception, will become so fixed in one's head that at length one believes the thought or the conception to be reality."

— Fyodor Dostoevsky

4

Exact Relationship Between Coupled-Cluster Doubles Theory and The Electronic Self-Energy

This Chapter contains work that contributed to the publication of Ref. [5]. The analytic HF and *GW* solutions for the Hubbard dimer also contributed to the publication of Ref. [1].

Contents

4.1 Introduction

In contrast to wavefunction based approaches, Green's function methods simultaneously encode excited and ground state many-body correlation. This is reflected by the fact that exact ground state properties as well as the single-particle charged excitation spectrum can be obtained from the same single-particle Green's function as demonstrated in Chapter 2 [13, 14, 17]. As stated at length in Chapter 3, recently there has been significant interest in identifying and leveraging connections between coupled-cluster and Green's function theory [4, 7, 61, 95–97, 99, 134, 138–140, 144, 153]. In this Chapter, we uncover the exact connection between the electronic self-energy and the coupled-cluster doubles

amplitude equations by showing how, under certain approximations, the Dyson supermatrix formulation can be recast to give the CCD amplitude equations. This complements the analysis presented in Chapter 3 by further cementing the connection between the Green's function formalism and coupled-cluster theory. We employ a real canonical spin-orbital basis throughout the Chapter and all Green's function and self-energy components are time-ordered as we are at zero temperature.

4.2 Third-order Algebraic Diagrammatic Construction method

The third-order Algebraic Diagrammatic Construction method, ADC(3), provides an infinite-order partial summation of a third-order diagrammatic perturbation expansion of the electronic self-energy [36, 41]. It combines diagonalization of the Dyson supermatrix with perturbation expansions of the coupling and interaction matrix elements of the self-energy. For a complete account of the ADC(n) method, the reader is again referred to Refs [35, 36, 41]. Here, we simply state the results. The forward-time coupling matrices (see Sections 2.5 and 2.6 of Chapter 2) are defined as

$$U^{\dagger}_{p,iab} = \langle pi||ab\rangle + \frac{1}{2}\sum_{kl}\langle pi||kl\rangle\,(t^{ab}_{kl})_{\mathrm{MP2}} - \sum_{kc}\langle pc||bk\rangle\,(t^{ac}_{ki})_{\mathrm{MP2}} + \sum_{kc}\langle pc||ak\rangle\,(t^{bc}_{ki})_{\mathrm{MP2}}\ , \tag{4.2.0.1a}$$

with the backward-time contributions as

$$V_{p,ija} = \langle pa||ij\rangle + \frac{1}{2}\sum_{bc}\langle pa||bc\rangle\,(t^{bc}_{ij})_{\mathrm{MP2}} - \sum_{kb}\langle pk||jb\rangle\,(t^{ba}_{ki})_{\mathrm{MP2}} + \sum_{kb}\langle pk||ib\rangle\,(t^{ba}_{kj})_{\mathrm{MP2}}\ . \tag{4.2.0.1b}$$

Here, we introduce the MP2 CCD amplitude notation as $(t^{ab}_{ij})_{\mathrm{MP2}} = -\frac{\langle ab||ij\rangle}{\Delta^{ab}_{ij}}$, with $\Delta^{ab}_{ij} = \epsilon_a + \epsilon_b - \epsilon_i - \epsilon_j$ and $\langle pq||rs\rangle = v_{pq,rs} - v_{pq,sr}$ representing the anti-symmetrized two-electron repulsion integrals. The forward-time interaction matrices are given by

$$\begin{aligned}(\mathbf{K}^{>,\mathrm{2p1h}}_{iab,jcd} + \mathbf{C}^{>,\mathrm{2p1h}}_{iab,jcd}) = (\epsilon_a + \epsilon_b - \epsilon_i)(\delta_{ac}\delta_{bd} - \delta_{ad}\delta_{bc})\delta_{ij} + \langle ab||cd\rangle\,\delta_{ij} + \langle jb||di\rangle\,\delta_{ac} \\ - \langle jb||ci\rangle\,\delta_{ad} + \langle ja||ci\rangle\,\delta_{bd} - \langle ja||di\rangle\,\delta_{bc}\ ,\end{aligned} \tag{4.2.0.2a}$$

with the backward-time interaction matrices as

$$\begin{aligned}(\mathbf{K}^{<,\mathrm{2h1p}}_{ija,klb} + \mathbf{C}^{<,\mathrm{2h1p}}_{ija,klb}) = (\epsilon_i + \epsilon_j - \epsilon_a)\delta_{ab}(\delta_{ik}\delta_{jl} - \delta_{il}\delta_{jk}) - \langle ij||kl\rangle\,\delta_{ab} - \langle jb||al\rangle\,\delta_{ik} \\ + \langle jb||ak\rangle\,\delta_{il} + \langle ib||al\rangle\,\delta_{jk} - \langle ib||ak\rangle\,\delta_{jl}\ .\end{aligned} \tag{4.2.0.2b}$$

Using these expressions for the coupling and interaction matrices in the Dyson supermatrix

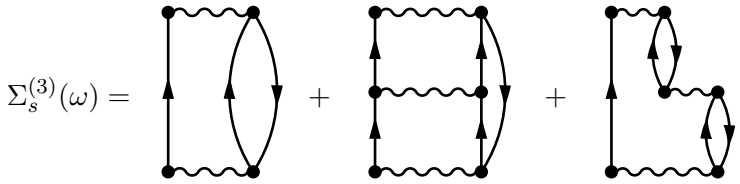

Figure 4.1: The third-order one-particle irreducible skeleton electronic self-energy diagrams. The ADC(3) Dyson supermatrix performs an infinite-order summation of these terms.

representation (Eq. 2.6.0.10) corresponds to an infinite-order summation of the electronic self-energy diagrams depicted in Figure 4.1. To identify the connection to coupled-cluster doubles theory, we define $\Sigma^{\infty} = 0$, as the reference zeroth-order Hamiltonian is the Fock operator.

4.3 Coupled-cluster doubles theory from the electronic self-energy

In the following we show that the connection between the electronic self-energy and the CCD amplitude equations can be derived by decoupling the forward and backward time self-energy components along with separating the particle-hole sectors. The decoupling of the different time directions and particle-hole sectors is commonly referred to as a non-Dyson self-energy approximation [99, 123, 134, 154].

The connections presented in this Section are related to but distinct from the diagrammatic coupled-cluster self-energy, recently introduced in Refs [4] and [7] and presented in Chapter 3, which is defined over the complete set of occupied and virtual orbitals. As a result, the non-Dyson electronic self-energy uncovered in this work that yields the exact CCD amplitude equations cannot be derived by taking functional derivatives of a diagrammatic expansion for the CC ground-state energy.

We refer to the non-Dyson electronic self-energy approximation introduced in this Chapter as the *particle-hole-time decoupled self-energy*. For the occupied states, we have

$$\bar{\Sigma}_{ij}(\omega) = \sum_{\substack{ka>b \\ lc>d}} \bar{U}_{i,kab}\Big((\omega + i\eta)\mathbb{1} - (\mathbf{K}^{>}_{\mathrm{2p1h}} + \mathbf{C}^{>}_{\mathrm{2p1h}})\Big)^{-1}_{kab,lcd} U_{lcd,j} \tag{4.3.0.1}$$

where all backward-time contributions are decoupled. This is motivated by the fact that the coupled-cluster excitation operators contain only hole to particle excitations and so are restricted to only contain forward-time propagation: $T_2 = \sum_{\substack{b>a \\ j>i}} t_{ij}^{ab} a_a^\dagger a_b^\dagger a_j a_i$.

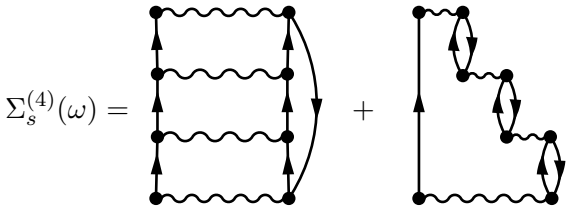

Figure 4.2: The fourth-order one-particle irreducible skeleton electronic self-energy diagrams contained in the full CCD equations when their contribution is included in the set of 2p1h/2h1p interaction matrices.

Additionally, we also neglect all forward-time self-energy diagrams that contain internal backward-time propagation of the intermediate Green's function lines from the final interaction vertex such that: $\bar{U}_{i,jab} = \langle ij||ab\rangle$. This procedures ensures that the correct set of only forward-time ordered Feynman-Goldstone self-energy diagrams are included in the particle-hole-time decoupled self-energy. However, the form of the second coupling matrix, $U_{lcd,j}$ remains the same as defined in Eq. 4.2.0.1a. In general, this breaks the hermiticity of the coupling elements of the electronic self-energy. This retention of specific forward-time ordered diagrams is closely related to well-known approximations for the polarization propagator [144]. The full set of time-orderings contained in the ADC(3) supermatrix contain both forward- and backward-time bubble, exchange and ladder polarization insertions. This is also the case in the GW-RPA approximation whereby both forward- and backward-time bubble diagrams are present [99, 144]. The inclusion of both time-orderings of these polarization diagrams is particularly important to describe both electronic relaxation and correlation processes.

By particle-hole symmetry, we have the particle-hole-time decoupled self-energy of the virtual states as

$$\bar{\Sigma}^{\mathrm{B}}_{ab}(\omega) = \sum_{\substack{i>jc \\ k>ld}} \bar{V}_{a,ijc}\Big((\omega - i\eta)\mathbb{1} - (\mathbf{K}^{<}_{\mathrm{2h1p}} + \mathbf{C}^{<}_{\mathrm{2h1p}})\Big)^{-1}_{ijc,kld} V^{\dagger}_{kld,b} \ , \tag{4.3.0.2}$$

where now we decouple all forward-time contributions and neglect all diagrams that contain internal forward-time propagation of the intermediate Green's function lines from the final interaction verex such that: $\bar{V}_{a,ijc} = \langle ac||ij\rangle$. The second coupling matrix element, $V^{\dagger}_{kld,b}$, remains the same as defined in Eq. 4.2.0.1b. Decoupling the particle-hole sectors requires: $\bar{\Sigma}_{ia} = \bar{\Sigma}_{ai} = 0$.

4. Exact Relationship Between Coupled-Cluster Doubles Theory and The Electronic Self-Energy

Focusing on the particle-hole-time decoupled self-energy of the occupied-occupied block, Eq. 4.3.0.1, we have the upfolded supermatrix eigenvalue problem

$$\begin{pmatrix} \epsilon_i \delta_{ij} & \bar{U}_{i,jab} \\ U_{kcd,i} & (\mathbf{K}^{>,\mathrm{2p1h}}_{iab,jcd} + \mathbf{C}^{>,\mathrm{2p1h}}_{iab,jcd}) \end{pmatrix} \begin{pmatrix} X_i^\nu \\ Y_{iab}^\nu \end{pmatrix} = \begin{pmatrix} X_i^\nu \\ Y_{iab}^\nu \end{pmatrix} \varepsilon_\nu \ . \tag{4.3.0.3}$$

Now, we introduce the doubles amplitudes through the follow identity: $t_{ij}^{ab} = \sum_\nu Y_{jab}^\nu (X^{-1})_i^\nu$. In matrix notation, we write $(\mathbf{T})_{ij}^{ab} = (\mathbf{Y}\mathbf{X}^{-1})_{ij}^{ab} = t_{ij}^{ab}$. Using this identity with Eq. 4.3.0.3, we have

$$\begin{pmatrix} \mathbf{f} & \bar{\mathbf{U}} \\ \mathbf{U} & \mathbf{K}^{>,\mathrm{2p1h}} + \mathbf{C}^{>,\mathrm{2p1h}} \end{pmatrix} \begin{pmatrix} \mathbb{1} \\ \mathbf{T} \end{pmatrix} = \begin{pmatrix} \mathbb{1} \\ \mathbf{T} \end{pmatrix} \mathbf{X}\mathcal{E}\mathbf{X}^{-1} \ . \tag{4.3.0.4}$$

These simultaneous equations give the extended Fock operator and the self-energy Riccati equation:

$$\mathbf{F}\mathbf{X} = \mathbf{X}\mathcal{E} \tag{4.3.0.5a}$$

$$\mathbf{U} + (\mathbf{K}^{>}_{\mathrm{2p1h}} + \mathbf{C}^{>}_{\mathrm{2p1h}})\mathbf{T} - \mathbf{T}\mathbf{F} = \mathbf{0} \ , \tag{4.3.0.5b}$$

where $\mathbf{F} = \mathbf{f} + \bar{\mathbf{U}}\mathbf{T}$ is the extended Fock operator. In explicit matrix notation, the extended Fock operator is written as

$$F_{ij} = \epsilon_i \delta_{ij} + \frac{1}{2} \sum_{kab} \langle ik||ab\rangle \, t_{jk}^{ab} \ . \tag{4.3.0.6}$$

The extended Fock operator is exactly of the form of the upper left block in IP-EOM-CCD theory: $F_{ij} = -\langle \Phi_j | \bar{H}_N | \Phi_i \rangle$, where $\bar{H}_N = e^{-T_2} H e^{T_2} - E_0^{\mathrm{CC}}$ is the normal-ordered CCD similarity transformed Hamiltonian [4, 7, 155]. Eq. 4.3.0.6 is also found by neglecting the T_1 amplitudes appearing in Refs [122, 127, 135, 137]. Using the coupling and interaction matrix elements defined above in Eqs 4.2.0.1a and 4.2.0.2a, the self-energy Riccati equation is explicitly written as

$$\begin{aligned} &\langle ab||ij\rangle + \frac{1}{2}\sum_{kl} (t_{kl}^{ab})_{\mathrm{MP2}} \langle ij||kl\rangle - \sum_{kc} \langle kb||ic\rangle \, (t_{kj}^{ac})_{\mathrm{MP2}} + \sum_{kc} \langle ka||ic\rangle \, (t_{kj}^{bc})_{\mathrm{MP2}} + \Delta_{ij}^{ab} t_{ij}^{ab} \\ &+ \frac{1}{2}\sum_{cd} \langle ab||cd\rangle \, t_{ij}^{cd} - \sum_{kc} \langle kb||jc\rangle \, t_{ik}^{ac} + \sum_{kc} \langle ka||jc\rangle \, t_{ik}^{bc} - \frac{1}{2}\sum_{klcd} t_{ik}^{cd} \langle kl||cd\rangle \, t_{jl}^{ab} = 0 \ . \end{aligned} \tag{4.3.0.7}$$

The self-energy Riccati equation as defined in Eq 4.3.0.5b represents a subset of the full CCD equations [85]:

$$\begin{aligned}
&\langle ab||ij\rangle + \Delta_{ij}^{ab} t_{ij}^{ab} + \frac{1}{2}\sum_{cd}\langle ab||cd\rangle\, t_{ij}^{cd} + \frac{1}{2}\sum_{kl}\langle ij||kl\rangle\, t_{kl}^{ab} \\
&- \sum_{kc}\Big(\langle kb||jc\rangle\, t_{ik}^{ac} - \langle ka||jc\rangle\, t_{ik}^{bc} + \langle ak||ci\rangle\, t_{jk}^{bc} - \langle bk||ci\rangle\, t_{jk}^{ac}\Big) \\
&+ \sum_{klcd}\langle kl||cd\rangle\, \Big(\frac{1}{4}t_{kl}^{ab}t_{ij}^{cd} - \frac{1}{2}(t_{ik}^{ab}t_{jl}^{cd} + t_{ik}^{cd}t_{jl}^{ab} + t_{ij}^{ac}t_{kl}^{bd} + t_{ij}^{bd}t_{kl}^{ac}) + (t_{ik}^{ac}t_{jl}^{bd} + t_{ik}^{bd}t_{jl}^{ac})\Big) = 0\ .
\end{aligned} \tag{4.3.0.8}$$

As can be seen by analysis of Eq. 4.3.0.8, the self-energy CCD amplitude equations given in Eq. 4.3.0.7 are missing several additional terms. These missing contributions include the particle-particle ladder terms, the full antisymmetrized ring diagrams as well as the six additional quadratic terms. Another difference is that only the MP2 doubles amplitudes appear in the hole-hole ladder and ring terms of the self-energy amplitude equations. These effectively represent a first iteration of the CCD equations using the MP2 amplitudes as an initial guess.

We note that the approach presented in this Chapter shares some similarities to the rCCD amplitude equations, first derived in Ref. [100]. However, the rCCD amplitude equations are given by [19, 98, 100, 144, 145]

$$\langle ab||ij\rangle + \Delta_{ij}^{ab} t_{ij}^{ab} - \sum_{kc}\langle kb||jc\rangle\, t_{ik}^{ac} - \sum_{kc}\langle ka||ic\rangle\, t_{jk}^{bc} + \sum_{klcd} t_{ik}^{ac}\langle kl||cd\rangle\, t_{jl}^{bd} = 0\ , \tag{4.3.0.9}$$

and originate from the RPA eigenvalue problem. The RPA approximation only contains ring diagram contributions to the CCD equations that are not antisymmetrized with respect to exchange of the external indices.

To obtain the full CCD equations from the electronic self-energy, we must transform the coupling and interaction matrices to become self-consistently dependent on the corresponding amplitude solutions. For the coupling matrices, Eq. 4.2.0.1a, this simply corresponds to replacing all MP2 amplitudes with the exact doubles amplitudes to be determined: $(t_{ij}^{ab})_{\mathrm{MP2}} \rightarrow t_{ij}^{ab}$. This results in the 'self-consistent' coupling matrix elements:

$$U_{abj,p}^{\mathrm{sc}} = \langle ab||pj\rangle + \frac{1}{2}\sum_{kl} t_{kl}^{ab}\langle pj||kl\rangle - \sum_{kc}\langle kb||pc\rangle\, t_{kj}^{ac} + \sum_{kc}\langle ka||pc\rangle\, t_{kj}^{bc}\ . \tag{4.3.0.10}$$

These coupling matrix elements can be viewed in terms of a self-consistent Green's function theory whereby the solution is updated iteratively. For the interaction matrices, the

following self-consistent updates are necessary:

$$\epsilon_i \delta_{ij} \rightarrow \epsilon_i \delta_{ij} + \frac{1}{2} \sum_{kcd} \langle ik||cd\rangle \, t_{jk}^{cd} \tag{4.3.0.11a}$$

$$\epsilon_a \delta_{ab} \rightarrow \epsilon_a \delta_{ab} - \frac{1}{2} \sum_{ijc} \langle ij||bc\rangle \, t_{ij}^{ca} \tag{4.3.0.11b}$$

$$\langle ab||cd\rangle \rightarrow \langle ab||cd\rangle + \frac{1}{2} \sum_{kl} \langle kl||cd\rangle \, t_{kl}^{ab} \tag{4.3.0.11c}$$

$$\langle ja||bi\rangle \rightarrow \langle ja||bi\rangle + \sum_{kc} \langle jk||bc\rangle \, t_{ik}^{ac} \ . \tag{4.3.0.11d}$$

Including these additional terms in the interaction matrices, $(\mathbf{K}^{>,\mathrm{2p1h}}_{iab,jcd} + \mathbf{C}^{>,\mathrm{2p1h}}_{iab,jcd})$, (see Eq. 4.2.0.2a) that enter the self-energy Riccati equation (Eq. 4.3.0.5b) gives rise to the six additional quadratic terms required to generate the full CCD equations given in Eq. 4.3.0.8. The additional terms, generated by the replacements given in Eqs 4.3.0.11, can be viewed as self-consistent fourth-order electronic self-energy diagrams that contain contributions in the 2p1h/2h1p excitation space (see Figure 4.2 and Appendix C.1) that are present in the ADC(4) construction [41]. However, in the perturbative ADC(4) construction their contribution is restricted to contain MP2 doubles amplitudes only and necessarily requires the expansion of the Dyson supermatrix to include 3p2h/3h2p intermediate state configurations [35, 41]. The self-energy Riccati equation, Eq. 4.3.0.5b, resulting from the replacements made in Eqs 4.3.0.10 and 4.3.0.11 to the coupling and interaction matrices gives the full CCD amplitude equations. These results demonstrate that the full CCD equations can be viewed as an infinite partial summation through fourth-order of perturbation theory in the electronic self-energy when restricted to 2p1h/2h1p excitation character of the Intermediate State Configurations. The Feynman-Goldstone diagrams for the particle-hole-time decoupled self-energy that generate the full CCD amplitude equations are given in Appendix C.1. To the best of our knowledge, this is the first time that the *complete* CCD amplitude equations have been derived within the Green's function formalism.

In Chapter 3, it was stated that the singles amplitudes, $\{t_i^a\}$, can be formally eliminated by the use of Brueckner orbitals whereby the spin-orbitals are determined simultaneously with the optimization of the cluster amplitudes [86, 118–120, 155]. This orbital rotation determined by the singles amplitude equations is termed BCC theory. Therefore, upon rotation to the Brueckner orbitals the derivation of the doubles amplitude equations

presented above is unchanged. Additionally, the formalism presented in this work can also be extended to derive the higher body BCCDT amplitude equations by retention and identification of the correct time-ordered self-energy diagrams contained in the higher-order ADC(n) approximations.

The ground state correlation energy is found from the relation

$$\begin{aligned} E_0^N &= \frac{1}{2}\mathrm{tr}\mathbf{X}\boldsymbol{\mathcal{E}}\mathbf{X}^{-1} + \frac{1}{2}\mathrm{tr}[\mathbf{h}] \\ &= E_0^{\mathrm{HF}} + \frac{1}{2}\mathrm{tr}[\bar{\mathbf{U}}\mathbf{T}] \\ &= E_0^{\mathrm{HF}} + \frac{1}{4}\sum_{ijab}\langle ij||ab\rangle\, t_{ij}^{ab} \ , \end{aligned} \tag{4.3.0.12}$$

where we have used the identity: $\mathbf{X}\boldsymbol{\mathcal{E}}\mathbf{X}^{-1} = \mathbf{F}$ from Eq. 4.3.0.6 to go from the first line to second line of Eq. 4.3.0.12. This expression is exactly equivalent to that obtained from CCD theory. Eq. 4.3.0.12 demonstrates that we can obtain ground state correlation energies from Green's function theory that can be cast exactly in terms of CCD theory.

The doubles amplitude equations generated by the particle-hole-time decoupled self-energy for the virtual block can be found in Appendix C.2 and are identical through particle-hole symmetry.

The relationship to the IP-EOM-CCD eigenvalue problem can be seen by coupling the self-consistent backward-time particle-hole-time decoupled self-energy (see Eq. 4.3.0.2 and Appendix C.2) to the occupied-occupied block of the self-energy while maintaining the particle-hole separation. This coupling is necessary to account for the negation of the full time-orderings of the coupling matrices of the forward-time particle-hole-time decoupled self-energy (see Eq. 4.3.0.1) in order to obtain accurate approximations for the removal excitation energies. Inclusion of these terms results in equations that are analogous to those of IP-EOM-CCD theory [127–129, 135–137]. As particle-hole separation is maintained, the resulting self-energy approximation is still of the non-Dyson form. Therefore, the presence of the lambda de-excitation amplitudes, $\{\lambda_\mu\}$ required to construct the left eigenstate of $\bar{H}$, that appear in Refs [4] and [7] (see Chapter 3) in the diagrammatic coupled-cluster self-energy do not appear here. As the non-Dyson approximation is kept, the connection can be explicitly made to IP/EA-EOM-CCD theory, where the particle-hole sectors are decoupled. The coupling of backward-time components to the

particle-hole-time decoupled self-energy of the occupied-occupied block gives the additional particle-hole decoupled self-energy contribution

$$\bar{\Sigma}^{\mathrm{B}}_{ij}(\omega) = \sum_{\substack{k>la \\ m>nb}} V^{\mathrm{sc}}_{i,kla}\Big((\omega - i\eta)\mathbb{1} - (\bar{\mathbf{K}}^{<}_{\mathrm{2h1p}} + \bar{\mathbf{C}}^{<}_{\mathrm{2h1p}})\Big)^{-1}_{kla,mnb} \bar{V}^{\dagger}_{mnb,j}, \tag{4.3.0.13}$$

where we define the transformed coupling elements from the self-consistent coupling matrices given in Appendix C.2. The coupling matrix elements are exactly equal to the blocks of the CCD similarity transformed Hamiltonian: $V_{i,kla} = \langle \Phi^a_{kl}|\bar{H}_N|\Phi_i\rangle$ and $\bar{V}^{\dagger}_{mnb,j} = \langle \Phi_j|\bar{H}_N|\Phi^b_{mn}\rangle$ [85, 99]. The interaction matrices are almost identical to the matrix elements of the CCD similarity transformed Hamiltonian in the basis of 2h1p determinants: $(\bar{\mathbf{K}}^{<,\mathrm{2h1p}}_{ija,klb} + \bar{\mathbf{C}}^{<,\mathrm{2h1p}}_{ija,klb}) \approx -\langle \Phi^b_{kl}|\bar{H}_N|\Phi^a_{ij}\rangle$. However, the explicit three-body interaction, $\chi_{ijb,kal}$, that arises in IP-EOM-CCD theory is not present in the modified interaction matrices (see Eq. C.2.0.8) [4, 7, 127, 135, 137, 156]. We maintain particle-hole separability such that $\bar{\Sigma}_{ia} = \bar{\Sigma}_{ai} = 0$. The result of this re-coupling is the effective particle-hole decoupled quasiparticle Hamiltonian

$$\hat{H}^{\text{IP-EOM-CCD}}_{ij}(\omega) = F_{ij} + \bar{\Sigma}^{\mathrm{B}}_{ij}(\omega)\ , \tag{4.3.0.14}$$

from which we have the upfolded supermatrix representation:

$$\bar{\mathbf{D}}^{\text{IP-EOM-CCD}} = \begin{pmatrix} \mathbf{f} + \bar{\mathbf{U}}\mathbf{T} & \mathbf{V}^{\mathrm{sc}} \\ \bar{\mathbf{V}}^{\dagger} & \bar{\mathbf{K}}^{<}_{\mathrm{2h1p}} + \bar{\mathbf{C}}^{<}_{\mathrm{2h1p}} \end{pmatrix}. \tag{4.3.0.15}$$

Explicitly, we can write this supermatrix in the suggestive form

$$\bar{\mathbf{D}}^{\text{IP-EOM-CCD}} = \begin{pmatrix} -\langle \Phi_j|\bar{H}_N|\Phi_i\rangle & -\langle \Phi^a_{kl}|\bar{H}_N|\Phi_i\rangle \\ -\langle \Phi_j|\bar{H}_N|\Phi^b_{mn}\rangle & -\langle \Phi^b_{mn}|\bar{H}_N|\Phi^a_{kl}\rangle \end{pmatrix}, \tag{4.3.0.16}$$

remembering that the interaction matrices (bottom right block of the supermatrix) do not include the three-body CC interaction. In Chapter 3, we showed that supermatrices of the form of Eqs 4.3.0.15/4.3.0.16 have structures that are analogous to the IP-EOM-CCD supermatrix. Therefore, the eigenvalues of $\bar{\mathbf{D}}^{\text{IP-EOM-CCD}}$ provide access to approximate electron removal energies. However, the residues of the single-particle Green's function are not obtained within this approximation as the particle-hole sectors remain decoupled. The relationship to EA-EOM-CCD theory can be derived in an entirely analogous manner by coupling the forward time self-energy contributions to the virtual states (see Eq. 4.3.0.2) while maintaining particle-hole separability.

4.4 Exact solution of the Hubbard Dimer

We apply the formalism presented in this Chapter to the exactly solvable Hubbard dimer at half filling. The Hubbard model is parametrized by the ratio $\frac{U}{t}$, which provides a measure of the 'correlation strength'. The parameters U and t represent the on-site repulsion and the coupling strength between nearest neighbour sites, respectively [157]. The CCD amplitude equations are exact for the Hubbard dimer and their quadratic Riccati equation yields two solutions:

$$(t_{ii}^{aa})_{\pm} = \frac{4t \pm c}{U} \ , \tag{4.4.0.1}$$

where $c = \sqrt{U^2 + 16t^2}$. The CCD amplitude is the negative solution, $(t_{ii}^{aa})_{-}$, which gives the exact ground state correlation energy: $E_c = \frac{U}{2}(t_{ii}^{aa})_{-} = 2t - \frac{c}{2}$.

In Ref. [1], we demonstrated that the second-order MP2 self-energy is exact for the Hubbard dimer. From the MP2 self-energy, the corresponding Dyson supermatrix for this system splits into the following eigenvalue problems for the occupied and virtual blocks respectively

$$\begin{pmatrix} \epsilon_i & \frac{U}{2} \\ \frac{U}{2} & 2\epsilon_a - \epsilon_i \end{pmatrix} \begin{pmatrix} X \\ Y \end{pmatrix} = \begin{pmatrix} X \\ Y \end{pmatrix} \varepsilon^{\mathrm{h}} \tag{4.4.0.2a}$$

$$\begin{pmatrix} \epsilon_a & \frac{U}{2} \\ \frac{U}{2} & 2\epsilon_i - \epsilon_a \end{pmatrix} \begin{pmatrix} \tilde{X} \\ \tilde{Y} \end{pmatrix} = \begin{pmatrix} \tilde{X} \\ \tilde{Y} \end{pmatrix} \varepsilon^{\mathrm{p}} \tag{4.4.0.2b}$$

where $\epsilon_{i/a} = \frac{U}{2} \mp t$ are the HF reference energies of the occupied/virtual states, respectively.

Multiplying Eq. 4.4.0.2a by X^{-1}, we obtain the extended Fock operator and self-energy Riccati equation as

$$\epsilon_i + \frac{U}{2} t_{ii}^{aa} = \varepsilon^{\mathrm{h}} \tag{4.4.0.3a}$$

$$\frac{U}{2} + 2(\epsilon_a - \epsilon_i) t_{ii}^{aa} - \frac{U}{2}(t_{ii}^{aa})^2 = 0 \ , \tag{4.4.0.3b}$$

where we have used the identity: $t_{ii}^{aa} = Y \cdot X^{-1}$. The self-energy Riccati equation, Eq. 4.4.0.3b, is the exact CCD amplitude equation:

$$\frac{U}{2}(t_{ii}^{aa})^2 - 4t(t_{ii}^{aa}) - \frac{U}{2} = 0 \ , \tag{4.4.0.4}$$

and yields two solutions: $(t_{ii}^{aa})_{\pm} = \frac{1}{U}(4t \pm c)$. The corresponding hole eigenvalues and super-eigenvectors of the quasiparticle and satellite solutions are found by substitution

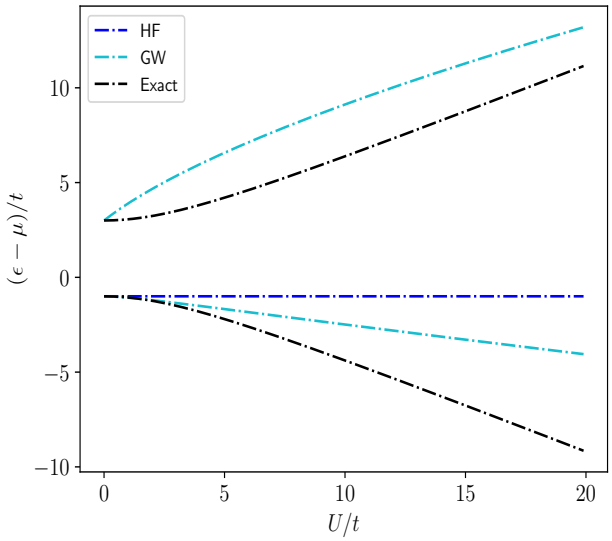

Figure 4.3: Hole quasiparticle and satellite energies of the Hubbard dimer as a function of $\frac{U}{t}$ relative to the chemical potential, $\mu = \frac{U}{2}$. The particle states are related to the hole states by particle-hole symmetry.

of the CCD amplitude solutions, $(t_{ii}^{aa})_{\pm}$, into Eq. 4.4.0.3a to give

$$\varepsilon_{\mathrm{QP}}^{\mathrm{h}} = \epsilon_i + \frac{U}{2}(t_{ii}^{aa})_- \quad ; \quad \mathbf{v}_{\mathrm{QP}}^{\mathrm{h}} = \begin{pmatrix} 1 \\ (t_{ii}^{aa})_- \end{pmatrix} \tag{4.4.0.5a}$$

$$\varepsilon_{\mathrm{sat}}^{\mathrm{h}} = \epsilon_i + \frac{U}{2}(t_{ii}^{aa})_+ \quad ; \quad \mathbf{v}_{\mathrm{sat}}^{\mathrm{h}} = \begin{pmatrix} 1 \\ (t_{ii}^{aa})_+ \end{pmatrix} . \tag{4.4.0.5b}$$

The CCD amplitude is the lower component of the $\mathbf{v}_{\mathrm{QP}}^{\mathrm{h}}$ vector of the hole quasiparticle solution: $(t_{ii}^{aa})_- = \frac{4t-c}{U}$. From Eq. 2.6.0.9, the inverse of the norm of the vector is exactly the hole quasiparticle renormalization factor: $Z_h^{\mathrm{QP}} = \left(\mathbf{v}_{\mathrm{QP}}^{\mathrm{h}\dagger}\mathbf{v}_{\mathrm{QP}}^{\mathrm{h}}\right)^{-1} = \left(1 + (t_{ii}^{aa})_-^2\right)^{-1} = \frac{1}{2} + \frac{2t}{c}$. The hole satellite solution contains a lower component of the eigenvector, $\mathbf{v}_{\mathrm{sat}}^{\mathrm{h}}$, that is exactly the positive CCD amplitude solution: $(t_{ii}^{aa})_+ = \frac{1}{U}(4t+c)$, with the satellite renormalization factor as $Z_h^{\mathrm{sat}} = \left(1 + (t_{ii}^{aa})_+^2\right)^{-1} = \frac{1}{2} - \frac{2t}{c}$. As expected, the renormalization factor for the quasiparticle is larger than that of the satellite, $Z_h^{\mathrm{QP}} > Z_h^{\mathrm{sat}}$. Using Eq. 4.3.0.12 for the ground state correlation energy gives the exact ground state correlation energy of the Hubbard dimer [63, 64, 158, 159].

For the particle solutions, the amplitude equations are directly connected to the hole solutions via particle-hole symmetry (see Appendix C.2). The corresponding particle

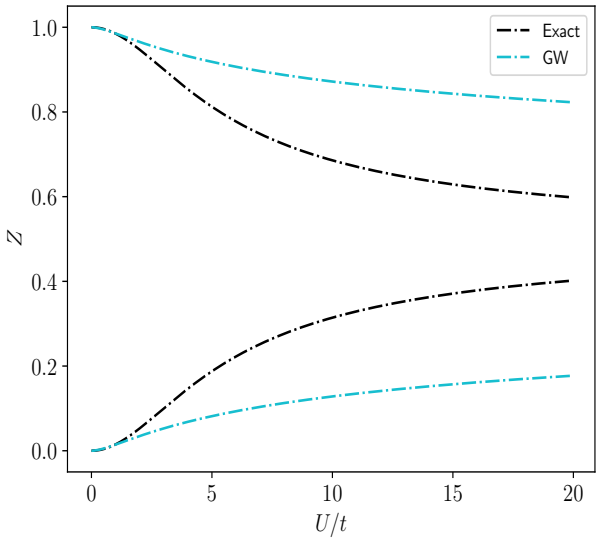

Figure 4.4: $Z^{\mathrm{QP/sat}}_{\mathrm{p/h}}$ renormalization factors for the Hubbard dimer as a function of $\frac{U}{t}$.

eigenvalues and super-eigenvectors of the quasiparticle and satellite solutions are given by

$$\varepsilon^{\mathrm{p}}_{\mathrm{QP}} = \epsilon_a - \frac{U}{2}(t^{aa}_{ii})_- \quad ; \quad \mathbf{v}^{\mathrm{p}}_{\mathrm{QP}} = \begin{pmatrix} 1 \\ -(t^{aa}_{ii})^*_- \end{pmatrix} \tag{4.4.0.6a}$$

$$\varepsilon^{\mathrm{p}}_{\mathrm{sat}} = \epsilon_a - \frac{U}{2}(t^{aa}_{ii})_+ \quad ; \quad \mathbf{v}^{\mathrm{p}}_{\mathrm{sat}} = \begin{pmatrix} 1 \\ -(t^{aa}_{ii})^*_+ \end{pmatrix} , \tag{4.4.0.6b}$$

where we have used the relation from Appendix C.2: $\tilde{t}^{aa}_{ii} = \tilde{Y} \cdot \tilde{X}^{-1} = -(t^{aa}_{ii})^*$. The quasiparticle renormalization factor is again $Z^{\mathrm{QP}}_p = \left(1 + (t^{aa}_{ii})^2_-\right)^{-1}$. The satellite particle solution gives the lower component of the $\mathbf{v}^{\mathrm{p}}_{\mathrm{sat}}$ vector as the negative of the positive CCD solution: $-(t^{ab}_{ij})_+$, with the renormalization factor given by $Z^{\mathrm{sat}}_p = \left(1 + (t^{aa}_{ii})^2_+\right)^{-1}$. Again, the renormalization factor of the quasiparticle is larger than that of the satellite, $Z^{\mathrm{QP}}_p > Z^{\mathrm{sat}}_p$. Using these expressions is it simple to verify that $Z^{\mathrm{QP}}_{h/p} + Z^{\mathrm{sat}}_{h/p} = 1$, as required by the sum rule.

Substituting the expression for the CCD amplitudes (Eq. 4.4.0.1) obtained from the self-energy Riccati equation (Eq. 4.4.0.3b) into Eqs 4.4.0.5 and 4.4.0.6, we see that the particle and hole quasiparticle/satellite energies and renormalization factors are exact for the Hubbard dimer [1, 142, 143, 160]. The satellite and quasiparticle energies are exactly of the form of the extended Fock operators defined in Eqs 4.3.0.6 and C.2.0.3. These results concretely demonstrate that different CCD amplitude solutions can correspond to satellite excited states resulting from particle removal and addition processes. From

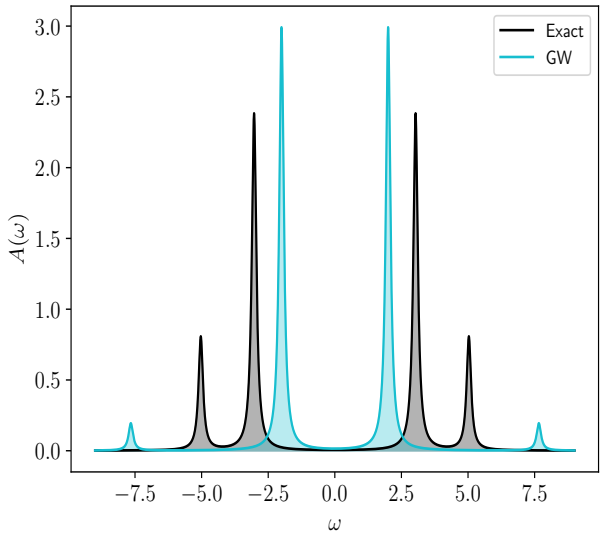

Figure 4.5: Exact and *GW* spectral functions obtained for the Hubbard dimer at $\frac{U}{t} = 7$. The exact spectral function is obtained from Eq. 4.4.0.7 as $A(\omega) = -\frac{1}{\pi}\sum_p \mathrm{Im}G^{\mathrm{R}}_{pp}(\omega)$.

our formulation, we can explicitly write the exact single-particle Green's function in terms of the CCD amplitudes:

$$\begin{aligned} G^{\mathrm{R}}_{ii}(\omega) = &\left(1 + (t^{aa}_{ii})^2_-\right)^{-1} \frac{1}{\omega - (\epsilon_i + \frac{U}{2}(t^{aa}_{ii})_-) + i\eta} \\ &+ \left(1 + (t^{aa}_{ii})^2_+\right)^{-1} \frac{1}{\omega - (\epsilon_i + \frac{U}{2}(t^{aa}_{ii})_+) + i\eta} \end{aligned} \tag{4.4.0.7a}$$

$$\begin{aligned} G^{\mathrm{R}}_{aa}(\omega) = &\left(1 + (t^{aa}_{ii})^2_-\right)^{-1} \frac{1}{\omega - (\epsilon_a - \frac{U}{2}(t^{aa}_{ii})_-) + i\eta} \\ &+ \left(1 + (t^{aa}_{ii})^2_+\right)^{-1} \frac{1}{\omega - (\epsilon_a - \frac{U}{2}(t^{aa}_{ii})_+) + i\eta} \end{aligned} . \tag{4.4.0.7b}$$

In Figures 4.3 and 4.4, we plot the poles and weights of the exact Green's function given in Eq. 4.4.0.7 against the HF and *GW* approximations obtained from Ref. [1]. In Figure 4.3, we see that the quasiparticle *GW* solutions are close to the exact quasiparticle solutions obtained within our formalism for values of $\frac{U}{t}$ up to 3. Beyond this point, the quasiparticle *GW* solutions begin to diverge away from the exact results as the essential correlated physics of electron localization is not recovered. In Figure 4.3, we also see that the *GW* satellite solutions are completely qualitatively wrong. This is a result of the fact that the *GW* approximation cannot handle the increasing multireference character of the underlying ground and excited state wavefunctions as the correlation strength $\frac{U}{t}$ increases [1, 161].

In Figure 4.4, we plot the quasiparticle and satellite renormalization factors as a function of $\frac{U}{t}$. We find that the *GW* solutions diverge quickly from the exact results even in the

weakly correlated regime as a result of the strong multireference character of the ground and excited state wavefunctions [1]. In Figure 4.5, we show the exact and *GW* spectral functions, evaluated at $\frac{U}{t} = 7$, obtained from the trace of the imaginary part of the corresponding Green's function. From analysis of the spectral function, we clearly see the qualitatively incorrect satellite peaks and strengths obtained from the *GW* approximation relative to the exact solution obtained from Eq. 4.4.0.7. Additionally, we see that the *GW* quasiparticle peaks are in qualitatively better agreement with the exact solution, but that their relative peak strength is larger as a result of the underestimation of the satellite weights.

4.5 Summary

In summary, we have firmly demonstrated the connection between the electronic self-energy and coupled-cluster doubles theory. To do so, we decouple the particle-hole as well as forward- and backward-time sectors of the electronic self-energy. Our formal insights have demonstrated that CCD theory represents a self-consistent, infinite-order summation of fourth-order electronic self-energy diagrams restricted to the space of 2p1h/2h1p excitations. The relationship to the IP/EA-EOM-CCD eigenvalue problem can be revealed be coupling reverse-time self-energy contributions to either the occupied or virtual sectors while maintaining particle-hole separability. Finally, using the formalism developed in this paper, we reconstruct the exact Green's function of the Hubbard dimer in terms of the CCD amplitudes. We hope that our findings will help stimulate renewed work towards combining Green's function and coupled-cluster theories for ground and excited state many-body correlation [132, 141]. Further directions of this work would be to develop a hermitian ADC(3) self-energy approximation that contains the exact CCD amplitudes obtained from a ground state coupled-cluster calculation. This would allow for the use of ground state coupled-cluster amplitudes, that contain infinite-order partial summations of the forward-time self-energy diagrams derived in this work, within the hermitian structure of the conventional Green's function formalism to obtain charged excitation spectra. In principle, the relationships identified here can also be used to generate novel CCD approximations from the *GW* approximation. The extension of the analysis presented here to the derivation of the coupled doubles and triples amplitude equations is reserved for future work.

Part II

Electron–Phonon Interactions

"I see myself as doomed, pitiful – An awful realisation that I have been fooling myself all my life thinking there was a next thing to do to keep the show going and actually I'm just a sick clown and so is everybody else..."

— Jack Kerouac

5

Electron-Phonon and Exciton-Phonon Interactions: Green's Function Theory For Continuous Systems

This Chapter provides a overview of the role of analytic continuation in systems that have continuous energy eigenstates, alongside how to treat electron-phonon and exciton-phonon interactions in infinite solids using the methods of quantum field theory. This Chapter also contains work that contributed to the publication of Refs [3, 6, 162], as well as work that will be submitted for publication.

Throughout this Chapter we will employ notation commonly used by the condensed matter physics community. The indices $\{v, v', \cdots\}$ will denote electronic valence bands, $\{c, c', \cdots\}$ will denote electronic conduction band indices, $\{n, n', \cdots\}$ will denote general electronic band indices and $\{\mathbf{k}, \mathbf{k}', \cdots\}$ will correspond to the electronic momenta. The indices and wavevectors $\{\nu, \nu', \cdots\}$ and $\{\mathbf{q}, \mathbf{q}', \cdots\}$ will denote phonon modes and momenta, respectively.

Contents

5.1 Branch cuts, the second Riemann sheet and resonant states

In Chapter 2, we derived the Lehmann representation of the Green's function corresponding to a system of many interacting particles governed by a hermitian interaction Hamiltonian. In the process, we were lead to introduce the general Green's function defined over the complex plane: $G(s)$. Through analytic continuation, we demonstrated how the general Green's function can be used to obtain the physical retarded/advanced Green's functions on the real axis. In addition, we showed that there is a fundamental difference in the structure of the Green's function for finite and continuous systems. For systems in the thermodynamic limit, the Green's function develops a branch cut discontinuity on the real axis due to the continuum of energy states accessible when the system is excited. This is reflected by the fact that the imaginary part of the Green's function becomes a smooth function of frequency.

In the most general case, a retarded Green's function can be written as the sum over simple poles (corresponding to bound states) and an integral over the spectral function describing the continuum energy states that appear above a certain energy threshold:

$$G^{\mathrm{R}}(\omega) = \sum_{\lambda} \frac{Z_\lambda}{\omega - \varepsilon_\lambda + i\eta} + \int_{E_{\mathrm{th}}}^{\infty} d\omega' \frac{\mathcal{A}(\omega')}{\omega - \omega' + i\eta} \ . \tag{5.1.0.1}$$

Here, we have made chosen the continuum contribution to appear above an energy threshold, E_{th}. By analytic continuation, we can write the expression for the general Green's function as

$$G(s) = \sum_{\lambda} \frac{Z_\lambda}{s - \varepsilon_\lambda} + \int_{E_{\mathrm{th}}}^{\infty} d\omega' \frac{\mathcal{A}(\omega')}{s - \omega'} \ . \tag{5.1.0.2}$$

Importantly, the retarded and advanced components can be obtained by evaluation of this function from either above or below the real axis: $G(\omega + i\eta) = G^{\mathrm{R}}(\omega)$ and $G(\omega - i\eta) =$

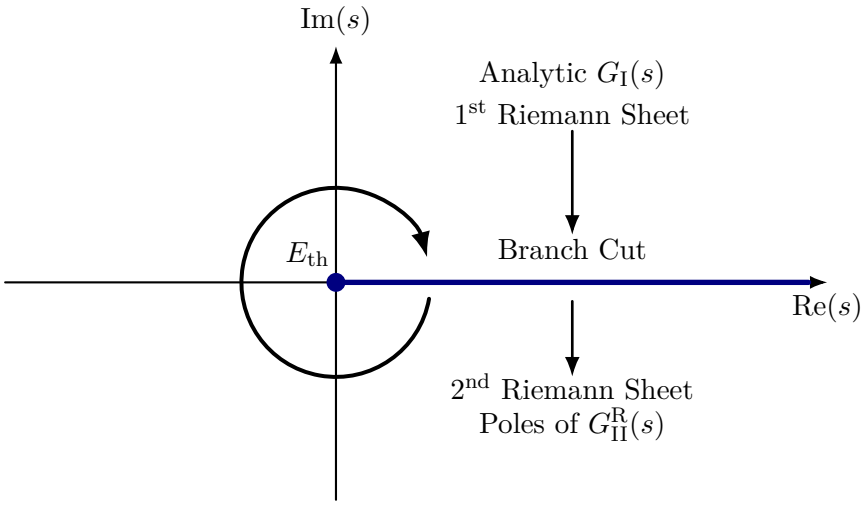

Figure 5.1: Branch cut and relationship to the analytically continued Green's function: $G^{\mathrm{R}}_{\mathrm{II}}(s)$. The branch cut indicates that the propagator becomes a multi-valued function in the complex plane, requiring a multi-Riemann sheet construction for its analytic continuation.

$G^{\mathrm{A}}(\omega)$, where $\eta \to 0^+$ from above. The complex function $G(s)$ is single valued everywhere except along the real axis where it contains a discontinuity given by the spectral function:

$$\lim_{\eta \to 0^+} [G(\omega - i\eta) - G(\omega + i\eta)] = 2\pi i \mathcal{A}(\omega) \ . \tag{5.1.0.3}$$

Eq. 5.1.0.3 demonstrates that $G(s)$ is not single-valued and therefore must contain a branch cut along the real axis from $[E_{\mathrm{th}}, \infty)$. This is depicted in Figure 5.1 where we introduce the branch cut along the real axis to ensure that the Green's function remains single valued for the closed path in the complex plane that *avoids* the branch cut discontinuity. However, we can analytically continue the function *through* the branch cut and onto the second Riemann sheet.

The second Riemann sheet is obtained from the first Riemann sheet by choice of how the branch cut is made. By choosing the branch cut such that the first Riemann sheet is constrained to describe only the retarded component when moving in a closed loop in the complex plane, we can analytically continue the Green's function through the branch cut with the retarded boundary conditions. Therefore, we label the Green's function on the first Riemann sheet as $G_{\mathrm{I}}(s)$ and the analytically continued Green's function of the second sheet as $G_{\mathrm{II}}(s)$. Traveling *through* the branch cut takes the complex function onto the second Riemann sheet which is simply another complex plane glued to the 'seam' where the branch cut occurs. This is also displayed in Figure 5.1, where we depict how analytic continuation through the branch cut takes us onto the second Riemann sheet. It

is clear that the analytically continued function is not equal to the original general Green's function of the first 'physical' Riemann sheet: $G_{\mathrm{I}}(s) \neq G_{\mathrm{II}}(s)$. However, the analytic continuation must obey the boundary conditions when going through the branch cut:

$$G_{\mathrm{II}}(\omega - i\eta) = G_{\mathrm{I}}(\omega + i\eta) = G^{\mathrm{R}}(\omega) \tag{5.1.0.4a}$$

$$G_{\mathrm{II}}(\omega + i\eta) = G_{\mathrm{I}}(\omega - i\eta) = G^{\mathrm{A}}(\omega) \ . \tag{5.1.0.4b}$$

These boundary conditions are required in order for the functions to be defined continuously across the sheets. Using the boundary conditions, we can re-write the branch cut discontinuity as

$$\lim_{\eta \to 0^+} [G_{\mathrm{II}}(\omega + i\eta) - G_{\mathrm{I}}(\omega + i\eta)] = 2\pi i \mathcal{A}(\omega) \ . \tag{5.1.0.5}$$

This equation can also be analytically continued to give

$$G_{\mathrm{II}}(s) = G_{\mathrm{I}}(s) + 2\pi i \mathcal{A}(s) \ , \tag{5.1.0.6}$$

where the analytically continued spectral function is given by $\mathcal{A}(s)$. Focusing on the continuum contribution to Eq. 5.1.0.2, we can write

$$G_{\mathrm{I}}(s) = \int_{E_{\mathrm{th}}+i0^+}^{\infty+i0^+} dz \frac{\mathcal{A}(z)}{s-z} \ , \tag{5.1.0.7}$$

where $z = \omega' + i0^+$. Here, the notation 0^+ indicates that the integral is taken an infinitesimal distance above the branch cut. This is the physical Green's function of the first Riemann sheet which is defined above the branch cut on the real axis. We can analytically continue this expression to the second Riemann sheet by moving through the branch cut to get:

$$G_{\mathrm{II}}(s) = \int_{E_{\mathrm{th}}-i0^+}^{\infty-i0^+} dz \frac{A(z)}{s-z} \ , \tag{5.1.0.8}$$

where now $z = \omega' - i0^+$ and the integral runs an infinitesimal distance below the branch cut on the second Riemann sheet. It is important to note that this corresponds to an analytic continuation of the retarded Green's function. The Green's functions on both Riemann sheets contain the same branch cut structure on the real axis and simply passing through the branch cut takes you from one sheet to the other.

$G_{\mathrm{I}}(s)$ does not contain any simple poles off the real axis (only poles on the real axis corresponding to bound states) and is a meromorphic function everywhere in the complex plane except at the branch cut location where it is discontinuous. The same is not true for

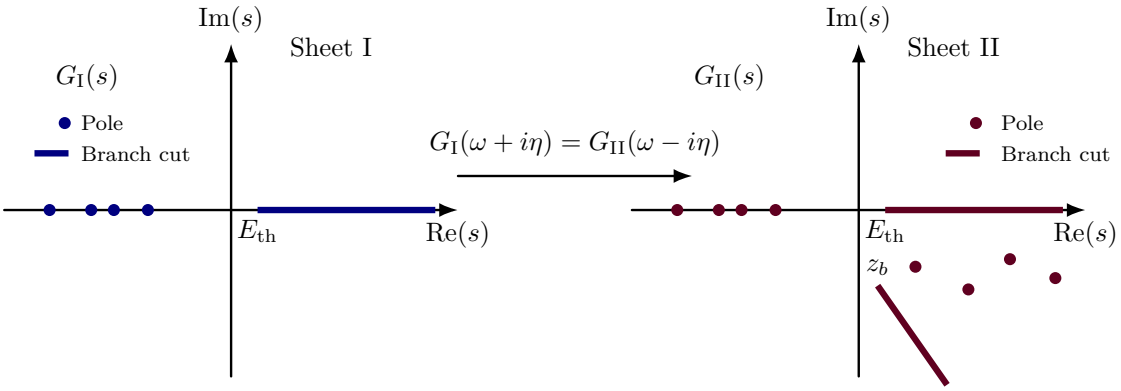

Figure 5.2: Analytic continuation from the physical sheet (Sheet I) to the second Riemann sheet (Sheet II) by traveling through the branch cut from above.

$G_{\rm II}(s)$, which contains the branch cut on the real axis as well as complex poles and branch cuts beneath the real axis [163]. The reason that the poles and branch cuts of $G_{\rm II}(s)$ all appear below the real axis is due to causality. This is directly related to the fact that, on the real axis, $\mathrm{Im}\Sigma^{\rm R}(\omega) \leq 0$, which pushes the poles into the lower half of the complex plane and is directly related to the analytic continuation of the spectral function given in Eq. 5.1.0.7. The relationship between the analytic structure of $G_{\rm I}(s)$ and $G_{\rm II}(s)$ is depicted in Figure 5.2.

To generate an exact analytic expression for the second sheet Green's function, we write the closed contour integral:

$$\oint_{\mathcal{C}} dw\ f(s,w)\ , \tag{5.1.0.9}$$

where $f(s,w) = \frac{\mathcal{A}(w)}{s-w}$ and $\mathcal{C}$ is the closed contour on the second Riemann sheet that runs along the branch cut just below the real axis and wraps around the lower half of the complex plane, encircling the poles of $f(s,w)$ and avoiding the branch cut discontinuities where the function becomes multi-valued. By the residue theorem, we can immediately write

$$\oint_{\mathcal{C}} dw\ f(s,w) = \sum_j \frac{\tilde{Z}_j}{s - z_j}\ , \tag{5.1.0.10}$$

where z_j and $\tilde{Z}_j$ are the complex poles and residues of the analytically continued spectral function, $\mathcal{A}(w)$. Due to causality, $\mathrm{Im}z_j \leq 0$ as the poles of the analytically continued function are pushed into the lower half of the plane. By splitting the contour into the sum of the real axis branch cut contribution and the 'background' term which contains the contributions generated by avoiding the branch cuts of $f(s,w)$, we can immediately write

$$G_{\rm II}(s) = \sum_j \frac{\tilde{Z}_j}{s - z_j} + G_{\rm II}^{\rm bg}(s)\ , \tag{5.1.0.11}$$

where $G_{\mathrm{II}}^{\mathrm{bg}}(s) = -\int_{\mathcal{C}_{\mathrm{cuts}}} dw f(s,w)$ is the 'background' continuum term dependent on the branch cut structure of $f(s,w)$. Using the boundary continuation for the analytic continuation (Eq. 5.1.0.4), we can immediately write the expression for the continuum contribution to the physical retarded Green's function from G_{II} as

$$G^{\mathrm{R}}(\omega) = \sum_j \frac{\tilde{Z}_j}{\omega - z_j} + G_{\mathrm{II}}^{\mathrm{bg}}(\omega - i\eta) \ . \tag{5.1.0.12}$$

Therefore, we can re-write the Lehmann representation of the retarded Green's function in terms of the analytically continued function as

$$\sum_\lambda \frac{Z_\lambda}{\omega - \varepsilon_\lambda + i\eta} + \int_{E_{\mathrm{th}}}^{\infty} d\omega' \frac{\mathcal{A}(\omega')}{\omega - \omega' + i\eta} = \sum_\lambda \frac{Z_\lambda}{\omega - \varepsilon_\lambda + i\eta} + \sum_j \frac{\tilde{Z}_j}{\omega - z_j} + G_{\mathrm{II}}^{\mathrm{bg}}(\omega - i\eta) \ . \tag{5.1.0.13}$$

Using this exact relationship, the exact spectral function is given by

$$\begin{aligned} \mathcal{A}(\omega) &= -\frac{1}{\pi}\mathrm{Im}G^{\mathrm{R}}(\omega) \\ &= \sum_\lambda Z_\lambda \delta(\omega - \varepsilon_\lambda) \\ &+ \frac{1}{\pi}\sum_j \left(\frac{\mathrm{Im}z_j \mathrm{Re}\tilde{Z}_j}{(\omega - \mathrm{Re}z_j)^2 + \mathrm{Im}z_j^2} - \frac{\mathrm{Im}\tilde{Z}_j(\omega - \mathrm{Re}z_j)}{(\omega - \mathrm{Re}z_j)^2 + \mathrm{Im}z_j^2} \right) + \mathcal{A}_{\mathrm{II}}^{\mathrm{bg}}(\omega) \geq 0 \ , \end{aligned} \tag{5.1.0.14}$$

where $\mathcal{A}_{\mathrm{II}}^{\mathrm{bg}}(\omega) = -\frac{1}{\pi}\mathrm{Im}G_{\mathrm{II}}^{\mathrm{bg}}(\omega - i\eta)$. Eq. 5.1.0.14 is an exact identity and therefore requires the spectral function to be positive semi-definite. However, as the residues and poles of G_{II} are complex, the second term containing the sum over these poles can become negative around specific peaks depending on the magnitude and sign of the imaginary component of $\tilde{Z}_j$. When this happens, it is clear from Eq. 5.1.0.14 that the 'background' contribution $\mathcal{A}_{\mathrm{II}}^{\mathrm{bg}}(\omega)$ will provide a positive contribution which will cancel these negative contributions, ensuring that the spectral function remains positive semi-definite. In general, the second term of Eq. 5.1.0.14 can give rise to asymmetric 'Lorentzian-like' line shapes in the spectral function [46]. This was first discussed by Toyozawa in Refs [164, 165] in the context of exciton-phonon interactions but the detailed analysis of the analytic continuation and the positive continuum contribution, $\mathcal{A}_{\mathrm{II}}^{\mathrm{bg}}$, was not presented.

With this analysis, we can now fully understand the pole condition of the single-particle Green's function for continuous systems that contain a branch cut on the real axis. The pole condition is determined by

$$\mathrm{det}G^{\mathrm{R},-1}(\omega) = \mathrm{det}G_{\mathrm{II}}^{-1}(\omega - i\eta) = 0 \ . \tag{5.1.0.15}$$

From Eq. 5.1.0.12, we see that this condition locates exactly the poles and residues of the second Riemann sheet Green's function. Therefore, the pole condition of Eq. 5.1.0.15 is used to determine the complex pole contribution to the analytically continued second sheet Green's function:

$$G_{\mathrm{II}}^{\mathrm{p}}(s) = \sum_j \frac{\tilde{Z}_j}{s - z_j} \ . \tag{5.1.0.16}$$

There is a deep relationship between the condition of Eq. 5.1.0.15 and the pole positions of the analytically continued $\mathcal{S}$-matrix. In fact, they are directly related to each other through the fact that the $\mathcal{S}$-matrix can be written as [3, 163]

$$\mathcal{S}(s) = \mathbb{1} - iT(s) \ , \tag{5.1.0.17}$$

where

$$T(s) = V + VG_{\mathrm{II}}(s)V, \tag{5.1.0.18}$$

with $G_{\mathrm{II}}(s) = (s - H)^{-1}$. Therefore, the poles of $\mathcal{S}$-matrix are identical to those of the T-matrix, which are inherited from the Dyson equation as the poles of $G_{\mathrm{II}}(s)$. From the optical theorem, in the isolated simple pole and exponential decay regime, the scattering rate of a state is then given by the imaginary part of the pole of the second sheet Green's function:

$$\gamma_j = -2\mathrm{Im}z_j = 2|\mathrm{Im}z_j| \geq 0 \ . \tag{5.1.0.19}$$

Therefore, the poles of the second sheet Green's function correspond exactly to metastable, resonance states that are transient excitations that spontaneously decay into the continuum with a rate corresponding to twice their imaginary part.

Through the Dyson equation, the branch cut structure of the Green's function can be viewed directly as a consequence of the branch cut structure of the self-energy. As demonstrated in Chapter 2, the self-energy on the first Riemann sheet can be written in its spectral form as

$$\Sigma_{\mathrm{I}}(s) = \Sigma_{pq}^{\infty} + \sum_\nu \frac{V_\nu V_\nu^\dagger}{s - \sigma_\nu} + \int_{E_{\mathrm{th}}}^{\infty} d\omega' \frac{\Gamma(\omega')}{s - \omega'} \ , \tag{5.1.0.20}$$

where $\Gamma(\omega)$ is the scattering function given by the discontinuity of the self-energy on the real axis. As is the case for the single-particle Green's function, the second term of Eq. 5.1.0.20 represents the unitary evolution of the closed system giving rise to bound

states. Using our analysis of the analytic continuation of the Green's function through the branch cut, we can immediately write the analytic continuation of the self-energy through the branch cut and onto the second Riemann sheet as

$$\Sigma_{\mathrm{II}}(s) = \int_{E_{\mathrm{th}}-i0^+}^{\infty-i0^+} dz \frac{\Gamma(z)}{s-z} \ , \tag{5.1.0.21}$$

with

$$\Sigma_{\mathrm{II}}(\omega+i\eta) - \Sigma_{\mathrm{I}}(\omega+i\eta) = 2\pi i \Gamma(\omega) \ . \tag{5.1.0.22}$$

On the second sheet, due to causality, the poles of the self-energy lie below the real axis. Therefore, we can immediately write the analytic continuation of the self-energy as

$$\Sigma_{\mathrm{II}}(s) = \Sigma_{pq}^{\infty} + \sum_{\nu} \frac{V_\nu V_\nu^\dagger}{s-\sigma_\nu} + \sum_{\lambda} \frac{\tilde{M}_\lambda}{s-w_\lambda} + \Sigma_{\mathrm{II}}^{\mathrm{bg}}(s), \tag{5.1.0.23}$$

where w_λ and $\tilde{M}_\lambda$ are the complex poles and residues of the analytically continued self-energy, with $\mathrm{Im} w_\lambda \leq 0$. $\Sigma_{\mathrm{II}}^{\mathrm{bg}}$ is the background contribution that arises due to the branch cut structure of the analytic continuation of $\Gamma(s)$. From the analytic continuation boundary condition, the retarded self-energy is therefore given by

$$\Sigma^{\mathrm{R}}(\omega) = \Sigma_{pq}^{\infty} + \sum_{\nu} \frac{V_\nu V_\nu^\dagger}{\omega-\sigma_\nu+i\eta} + \sum_{\lambda} \frac{\tilde{M}_\lambda}{\omega-w_\lambda} + \Sigma_{\mathrm{II}}^{\mathrm{bg}}(\omega-i\eta) \ . \tag{5.1.0.24}$$

With this continuation, we can immediately write the scattering function as

$$\begin{aligned}
\Gamma(\omega) &= -\frac{1}{\pi}\mathrm{Im}\Sigma^{\mathrm{R}}(\omega) \\
&= \sum_{\nu} V_\nu V_\nu^\dagger \delta(\omega-\sigma_\nu) \\
&+ \frac{1}{\pi}\sum_{\lambda}\left(\frac{\mathrm{Im}w_\lambda \mathrm{Re}\tilde{M}_\lambda}{(\omega-\mathrm{Re}w_\lambda)^2+\mathrm{Im}w_\lambda^2} - \frac{\mathrm{Im}\tilde{M}_\lambda(\omega-\mathrm{Re}w_\lambda)}{(\omega-\mathrm{Re}w_\lambda)^2+\mathrm{Im}w_\lambda^2}\right) + \Gamma_{\mathrm{II}}^{\mathrm{bg}}(\omega) \geq 0 \ ,
\end{aligned} \tag{5.1.0.25}$$

where $\Gamma_{\mathrm{II}}^{\mathrm{bg}}(\omega) = -\frac{1}{\pi}\mathrm{Im}\Sigma_{\mathrm{II}}^{\mathrm{bg}}(\omega-i\eta)$. Similarly, depending on the magnitude of the real and imaginary parts of residues of the pole terms of the analytic continuation of the self-energy, the scattering function can become negative. However, the background continuum contribution will provide a positive contribution that will ensure that the overall scattering function remains positive semi-definite.

Finally, the states obtained by solution of the pole condition of the second sheet Green's function are given by the eigenstates of the Dyson equation:

$$\left(h + \Sigma_{\mathrm{II}}(z_j)\right)|\psi_{\mathrm{R}}^j\rangle = z_j |\psi_{\mathrm{R}}^j\rangle \tag{5.1.0.26}$$

and

$$\left(h + \Sigma^{\dagger}_{\mathrm{II}}(z_j)\right) |\tilde{\psi}^j_{\mathrm{L}}\rangle = z^*_j \, |\tilde{\psi}^j_{\mathrm{L}}\rangle \tag{5.1.0.27}$$

which can be used to reconstruct the second sheet Green's function as

$$G_{\mathrm{II}}(s) = \sum_j \frac{|\psi^j_{\mathrm{R}}\rangle \langle\tilde{\psi}^j_{\mathrm{L}}|}{s - z_j} \ . \tag{5.1.0.28}$$

From the biorthogonal theory of quantum mechanics presented in Chapter 3, the states, $\{|\psi^j_{\mathrm{R}}\rangle, |\tilde{\psi}^j_{\mathrm{L}}\rangle\}$, can be viewed as binormalized pairs. In the context of scattering theory, the left and right eigenstates are referred to as Gamow states and are non-normalizable in the physical Hilbert space [163, 166–168]. The time evolution of Gamow states automatically implies irreversibility as $\mathrm{Im} z_j < 0$, meaning that they represent the spontaneous and irreversible decay of resonant states into the continuum, enforced by the retarded boundary condition [43, 168]. It is important to note that solution of Eq. 5.1.0.26 gives rise to scattering rates and energy renormalizations that go beyond the first Born approximation as they involve the full diagonalization of the dynamical self-energy.

5.2 The electron-nuclear Hamiltonian

A system of interacting electrons and nuclei is given by the Hamiltonian [13–15, 17, 169]

$$\begin{aligned} H = &- \int d\mathbf{x} \psi^{\dagger}(\mathbf{x}) \frac{\nabla^2}{2} \psi(\mathbf{x}) + \frac{1}{2} \int d\mathbf{x} d\mathbf{x}' \psi^{\dagger}(\mathbf{x}) \psi^{\dagger}(\mathbf{x}') v(\mathbf{r}, \mathbf{r}') \psi(\mathbf{x}') \psi(\mathbf{x}) + \sum_{\kappa} \frac{|\mathbf{P}_{\kappa}|^2}{2M_{\kappa}} \\ &+ \int d\mathbf{x} \psi^{\dagger}(\mathbf{x}) \psi(\mathbf{x}) \phi(\mathbf{r}, \mathbf{R}) + E_{\mathrm{nuc}}(\mathbf{R}) \ , \end{aligned} \tag{5.2.0.1}$$

where $v(\mathbf{r}, \mathbf{r}') = \frac{1}{|\mathbf{r} - \mathbf{r}'|}$ is the bare Coulomb interaction and $\mathbf{x} = (\mathbf{r}, \sigma)$ is the composite space-spin coordinate with $\int d\mathbf{x} = \sum_{\sigma} \int d\mathbf{r}$ as given in Chapters 1 and 2. $\{M_{\kappa}\}$, $\{Z_{\kappa}\}$ and $\{\mathbf{R}_{\kappa}\}$ are the are the nuclear masses, charges and position operators, respectively. The nuclear repulsion energy is given by $E_{\mathrm{nuc}}(\mathbf{R}) = \frac{1}{2} \sum_{\kappa \neq \kappa'} \frac{Z_{\kappa} Z_{\kappa'}}{|\mathbf{R}_{\kappa} - \mathbf{R}_{\kappa'}|}$. The scalar electric field that results in the electron-nuclear interaction is given by

$$\phi(\mathbf{r}, \mathbf{R}) = - \sum_{\kappa} \frac{Z_{\kappa}}{|\mathbf{r} - \mathbf{R}_{\kappa}|} \ . \tag{5.2.0.2}$$

At equilibrium, we can approximate the nuclear repulsion energy by its second-order Taylor expansion with respect to the equilibrium nuclear positions:

$$E_{\mathrm{nuc}}(\mathbf{R}) \approx E_{\mathrm{nuc}}(\mathbf{R}_{\mathrm{eq}}) + \sum_{\kappa\alpha} \left. \frac{\partial E_{\mathrm{nuc}}(\mathbf{R})}{\partial R_{\kappa\alpha}} \right|_{\mathbf{R}=\mathbf{R}_{\mathrm{eq}}} U_{\kappa\alpha} + \frac{1}{2} \sum_{\kappa\alpha\kappa'\beta} \left. \frac{\partial^2 E_{\mathrm{nuc}}(\mathbf{R})}{\partial R_{\kappa\alpha} \partial R_{\kappa'\beta}} \right|_{\mathbf{R}=\mathbf{R}_{\mathrm{eq}}} U_{\kappa\alpha} U_{\kappa'\beta} \tag{5.2.0.3}$$

where $U_{\kappa\alpha} = R_{\kappa\alpha} - R^{\text{eq}}_{\kappa\alpha}$, is the nuclear displacement of the κ-th nucleus about the equilibrium position, with α corresponding to the cartesian component of the vector. We can then also approximate the electron-nuclear interaction to second-order in the lattice displacements as

$$\phi(\mathbf{r},\mathbf{R}) \approx \phi(\mathbf{r},\mathbf{R}_{\text{eq}}) + \sum_{\kappa\alpha} \frac{\partial\phi(\mathbf{r},\mathbf{R})}{\partial R_{\kappa\alpha}}\bigg|_{\mathbf{R}=\mathbf{R}_{\text{eq}}} U_{\kappa\alpha} + \frac{1}{2}\sum_{\kappa\alpha\kappa'\beta} \frac{\partial^2\phi(\mathbf{r},\mathbf{R})}{\partial R_{\kappa\alpha}\partial R_{\kappa'\beta}}\bigg|_{\mathbf{R}=\mathbf{R}_{\text{eq}}} U_{\kappa\alpha}U_{\kappa'\beta} \ . \tag{5.2.0.4}$$

By defining the electron-nuclear and Debye-Waller (DW) couplings as $g^{\text{b}}_{\kappa\alpha}(\mathbf{r}) = \frac{\partial\phi(\mathbf{r},\mathbf{R})}{\partial R_{\kappa\alpha}}\Big|_{\mathbf{R}=\mathbf{R}_{\text{eq}}}$ and $g^{\text{DW}}_{\kappa\alpha,\kappa'\beta}(\mathbf{r}) = \frac{\partial^2\phi(\mathbf{r},\mathbf{R})}{\partial R_{\kappa\alpha}\partial R_{\kappa'\beta}}\Big|_{\mathbf{R}=\mathbf{R}_{\text{eq}}}$, respectively, we can re-write this expression as

$$\phi(\mathbf{r},\mathbf{R}) \approx \phi(\mathbf{r}) + \sum_{\kappa\alpha} g^{\text{b}}_{\kappa\alpha}(\mathbf{r})U_{\kappa\alpha} + \frac{1}{2}\sum_{\kappa\alpha\kappa'\beta} g^{\text{DW}}_{\kappa\alpha,\kappa'\beta}(\mathbf{r})U_{\kappa\alpha}U_{\kappa'\beta} \ . \tag{5.2.0.5}$$

We used the notation g^{b} to emphasize that the electron-nuclear coupling is given by the derivative of the 'bare' Coulomb interaction between the electrons and nuclei. Importantly, including the second-order term in the Taylor expansion of the electron-nuclear interaction gives rise to the DW interaction [17]. In certain circumstances, the DW interaction can be significant and responsible for band structure renormalization effects [169–175]. However, the DW contribution is commonly neglected in the literature on electron-phonon interactions in semiconductors and metallic systems as it gives rise to a frequency-independent contribution to the electronic self-energy and will not substantially contribute to states near the Fermi surface [169]. Therefore, considering the effects of including the DW interaction on exciton-phonon interactions is beyond the scope of this thesis.

With these identifications, we can re-write the electron-nuclear interaction Hamiltonian as

$$H = H_{el} + \sum_{\kappa\alpha}\int d\mathbf{x}\psi^{\dagger}(\mathbf{x})g^{\text{b}}_{\kappa\alpha}(\mathbf{r})\psi(\mathbf{x})U_{\kappa\alpha} + \sum_{\kappa}\frac{|\mathbf{P}_{\kappa}|^2}{2M_{\kappa}} + \frac{1}{2}\sum_{\kappa\alpha\kappa'\beta} U_{\kappa\alpha}C_{\kappa\alpha,\kappa'\beta}U_{\kappa'\beta} \ , \tag{5.2.0.6}$$

where H_{el} is the electronic structure Hamiltonian defined in Eq. 2.1.0.1 of chapter 2. We have neglected the additive constant of the equilibrium nuclear energy and defined the Dynamical matrix: $C_{\kappa\alpha,\kappa'\beta} = \frac{\partial^2 E_{\text{nuc}}(\mathbf{R})}{\partial R_{\kappa\alpha}\partial R_{\kappa'\beta}}\Big|_{\mathbf{R}=\mathbf{R}_{\text{eq}}} + \int d\mathbf{r} n_e(\mathbf{r}) g^{\text{DW}}_{\kappa\alpha,\kappa'\beta}(\mathbf{r})$; we have kept the DW contribution for completeness.

To describe the electrons and nuclei in an infinite solid, we use Born-von-Kármán (BvK) boundary conditions in which periodic boundary conditions are applied to a large

supercell containing N_p unit cells which are indexed by $\mathbf{R}_p$ direct lattice vectors [169]. Therefore, the position of a nucleus is specified by $U_{\kappa\alpha p} = U_{\kappa\alpha} + R_{\alpha p}$, where $U_{\kappa\alpha}$ is the position of the nucleus in the unit cell. The periodicity of the infinite solid essentially amounts to replacing $\kappa \to \kappa p$ in Eq. 5.2.0.6 to indicate summations over the direct lattice thereby including the periodic copies of the unit cell. The details of this construction can be found in Appendix A.5.

5.2.1 Phonons and the electron-phonon interaction

In an infinite solid, the phonon Hamiltonian is given by the nuclear contribution to Eq. 5.2.0.6 as

$$H_{ph} = \sum_{\kappa p} \frac{|\mathbf{P}_{\kappa p}|^2}{2M_\kappa} + \frac{1}{2} \sum_{\substack{\kappa\alpha p \\ \kappa'\beta p'}} U_{\kappa\alpha p} C_{\kappa\alpha p,\kappa'\beta p'} U_{\kappa'\beta p'} \ . \tag{5.2.1.1}$$

The translational symmetry of the lattice implies $C_{\kappa\alpha p,\kappa'\beta p'} = C_{\kappa\alpha,\kappa'\beta}(\mathbf{R}_p - \mathbf{R}_{p'})$ such that we may take the Fourier transform of the dynamical matrix as

$$C_{\kappa\alpha,\kappa'\beta}(\mathbf{q}) = \frac{1}{\sqrt{M_\kappa M_{\kappa'}}} \sum_p e^{i\mathbf{q}\cdot\mathbf{R}_p} C_{\kappa\alpha,\kappa'\beta}(\mathbf{R}_p), \tag{5.2.1.2}$$

where the expansion has been chosen about the reference unit cell indexed as $\mathbf{R}_{p'} = \mathbf{0}$. The eigenvalues and eigenvectors of the Fourier transformed Dynamical matrix give the normal modes and phonon frequencies of the solid:

$$\sum_{\kappa'\beta} C_{\kappa\alpha,\kappa'\beta}(\mathbf{q}) \xi_{\kappa'\beta,\nu}(\mathbf{q}) = \omega^2_{\mathbf{q}\nu} \xi_{\kappa\alpha,\nu}(\mathbf{q}) \ . \tag{5.2.1.3}$$

It is clear that the index ν spans the product of states $N_\alpha N_\kappa = 3N$, where N is the number of nuclei contained in the unit cell. The phonon normal modes, $\{\xi_{\kappa\alpha,\nu}(\mathbf{q})\}$, form a complete set at each $\mathbf{q}$-point and

$$\sum_{\nu} \xi^*_{\kappa'\beta,\nu}(\mathbf{q}) \xi_{\kappa\alpha,\nu}(\mathbf{q}) = \delta_{\kappa\kappa'}\delta_{\alpha\beta} \ , \tag{5.2.1.4a}$$

$$\sum_{\kappa\alpha} \xi^*_{\kappa\alpha,\nu'}(\mathbf{q}') \xi_{\kappa\alpha,\nu}(\mathbf{q}) = \delta_{\nu\nu'}\delta_{\mathbf{q}\mathbf{q}'} \ , \tag{5.2.1.4b}$$

with the eigenvectors and eigenvalues related by $\xi_{\kappa\alpha,\nu}(\mathbf{q}) = \xi^*_{\kappa\alpha,\nu}(-\mathbf{q})$ and $\omega^2_{\mathbf{q}\nu} = \omega^2_{-\mathbf{q}\nu}$, respectively. Using the complete set of phonon eigenvectors, we can expand the nuclear displacements as

$$U_{\kappa\alpha p} = \frac{1}{\sqrt{M_\kappa N_p}} \sum_{\mathbf{q}\nu} e^{i\mathbf{q}\cdot\mathbf{R}_p} \xi_{\kappa\alpha,\nu}(\mathbf{q}) U_{\mathbf{q}\nu} \ . \tag{5.2.1.5}$$

Using this transformation and the equivalent for the phonon momenta, we can write

$$H_{ph} = \frac{1}{2}\sum_{\mathbf{q}\nu}\left(P^{\dagger}_{\mathbf{q}\nu}P_{\mathbf{q}\nu} + \omega^{2}_{\mathbf{q}\nu}U^{\dagger}_{\mathbf{q}\nu}U_{\mathbf{q}\nu}\right) \ , \tag{5.2.1.6}$$

where we have used the property $P^{\dagger}_{\mathbf{q}\nu} = P_{-\mathbf{q}\nu}$ and $U^{\dagger}_{\mathbf{q}\nu} = U_{-\mathbf{q}\nu}$. Finally, by introduction of the bosonic field operators: $\left[a_{\mathbf{q}\nu}, a^{\dagger}_{\mathbf{q}'\nu'}\right] = \delta_{\mathbf{q}\mathbf{q}'}\delta_{\nu\nu'}$, we define $U_{\mathbf{q}\nu} = \frac{1}{\sqrt{2\omega_{\mathbf{q}\nu}}}(a_{\mathbf{q}\nu} + a^{\dagger}_{-\mathbf{q}\nu})$ and $P_{\mathbf{q}\nu} = -i\sqrt{\frac{\omega_{\mathbf{q}\nu}}{2}}(a_{\mathbf{q}\nu} - a^{\dagger}_{-\mathbf{q}\nu})$, such that we can re-write the Hamiltonian as

$$H_{ph} = \sum_{\mathbf{q}\nu}\omega_{\mathbf{q}\nu}\left(a^{\dagger}_{\mathbf{q}\nu}a_{\mathbf{q}\nu} + \frac{1}{2}\right) \ . \tag{5.2.1.7}$$

Physically, the bosonic phonon operators $a^{\dagger}_{\mathbf{q}\nu}/a_{\mathbf{q}\nu}$ act to create/annihilate phonon states at wavevector $\mathbf{q}$ in the vibrational mode ν. Using the phonon creation and annihilation operators, we can re-write the electron-nuclear interaction Hamiltonian in Eq. 5.2.0.6 as

$$H = H_{\mathrm{el}} + \sum_{\mathbf{q}\nu}\omega_{\mathbf{q}\nu}\left(a^{\dagger}_{\mathbf{q}\nu}a_{\mathbf{q}\nu} + \frac{1}{2}\right) + \sum_{\substack{nn'\\ \mathbf{k}'\mathbf{q}\nu}} g^{\mathrm{b}}_{nn'\nu}(\mathbf{k}', \mathbf{q})c^{\dagger}_{n\mathbf{k}'+\mathbf{q}}c_{n'\mathbf{k}'}A_{\mathbf{q}\nu} \ , \tag{5.2.1.8}$$

where $c^{\dagger}_{n\mathbf{k}}/c_{n\mathbf{k}}$ act to create/annihilate an electron in the single-particle Bloch state, $\psi_{n\mathbf{k}}(\mathbf{r}) = e^{i\mathbf{k}\cdot\mathbf{r}}u_{n\mathbf{k}}(\mathbf{r})$, where $u_{n\mathbf{k}}(\mathbf{r})$ is the cell-periodic component of the single-particle wavefunction. $A_{\mathbf{q}\nu} = a_{\mathbf{q}\nu} + a^{\dagger}_{-\mathbf{q}\nu}$ is the phonon displacement operator and $g^{\mathrm{b}}_{mn,\nu}(\mathbf{k}, \mathbf{q}) = \langle m\mathbf{k}+\mathbf{q}|g_{\mathbf{q}\nu}(\mathbf{r})|n\mathbf{k}\rangle$ are the electron-phonon coupling elements [169] expressed with respect to the normal modes of the solid. The electron-phonon coupling element is obtained by Fourier transform of the real space representation using the phonon eigenvectors as

$$g^{\mathrm{b}}_{\mathbf{q}\nu}(\mathbf{r}) = \frac{1}{\sqrt{N_p}}\sum_{\kappa\alpha p}\frac{1}{\sqrt{M_\kappa}}e^{i\mathbf{q}\cdot\mathbf{R}_p}\xi_{\kappa\alpha,\nu}(\mathbf{q})g^{\mathrm{b}}_{\kappa\alpha p}(\mathbf{r}) \ . \tag{5.2.1.9}$$

Finally, by treating the electron-electron interaction at the mean-field level (Hartree-Fock or Kohn-Sham DFT), we obtain the electron-phonon interaction Hamiltonian as

$$H_{ep} = \sum_{n\mathbf{k}}\epsilon_{n\mathbf{k}}c^{\dagger}_{n\mathbf{k}}c_{n\mathbf{k}} + \sum_{\mathbf{q}\nu}\omega_{\mathbf{q}\nu}\left(a^{\dagger}_{\mathbf{q}\nu}a_{\mathbf{q}\nu} + \frac{1}{2}\right) + \sum_{\substack{nn'\\ \mathbf{k}'\mathbf{q}\nu}} g_{nn'\nu}(\mathbf{k}', \mathbf{q})c^{\dagger}_{n\mathbf{k}'+\mathbf{q}}c_{n'\mathbf{k}'}A_{\mathbf{q}\nu} \ , \tag{5.2.1.10}$$

where now the electron-phonon coupling elements are defined with respect to the derivative of the self-consistent field potential (V_{SCF})

$$g_{\kappa\alpha}(\mathbf{r}) = \left.\frac{\partial V_{\mathrm{SCF}}(\mathbf{r}, \mathbf{R})}{\partial R_{\kappa\alpha}}\right|_{\mathbf{R}=\mathbf{R}_{\mathrm{eq}}} \ , \tag{5.2.1.11}$$

and the Dynamical matrix contains an additional contribution from the electronic ground state energy: $C^{\mathrm{el}}_{\kappa\alpha,\kappa\beta} = \left.\frac{\partial^2 E_{\mathrm{el}}}{\partial R_{\kappa\alpha}\partial R_{\kappa'\beta}}\right|_{\mathbf{R}=\mathbf{R}_{\mathrm{eq}}}$. This is approach is taken in density functional perturbation theory (DFPT) [169, 176].

5.3 The Hedin-Baym equations and screened Coulomb interaction

The electron-phonon Hamiltonian of Eq. 5.2.1.10 was obtained by neglecting the full effects of the two-body electron-electron Coulomb interaction. However, in order to include both the effects of electronic correlation resulting from the combined motion of the nuclei and harmonic lattice vibrations requires us to work with the full coupled quantum field theory of electron-nuclear interactions [38, 177]. The Hedin-Baym equations provide us with exactly this and constitute a formally exact set of coupled integro-differential equations for the electronic and nuclear Green's functions [38, 169, 177]. One of the central quantities entering the Hedin-Baym equations is the screened Coulomb interaction which accounts for the retardation of the interaction experienced between two electrons due to the combined polarization of the electron and nuclear densities. As this chapter is specifically focused on the *electronic* degrees of freedom, we will focus our analysis on the effects induced by the nuclear motion on the screening of the electron-electron interaction.

The screened Coulomb interaction, induced by the polarization of both the electrons and nuclei ($P = P_{\text{el}} + P_n$), is given by

$$\begin{aligned} W &= v + vPW \\ &= v + vP_{\text{el}}W + vP_nW \ . \end{aligned} \tag{5.3.0.1}$$

It is straightforward to re-write this equation in terms of the electronic polarization by defining

$$\begin{aligned} W_{\text{el}} &= \epsilon_{\text{el}}^{-1} v \\ &= v + vP_{\text{el}}W_{\text{el}} \ , \end{aligned} \tag{5.3.0.2}$$

where $\epsilon_{\text{el}}^{-1}$ is the inverse electronic dielectric response function. Using the electronic contribution to the screened Coloumb interaction we can rearrange Eq. 5.3.0.1 to give

$$\begin{aligned} W &= W_{\text{el}} + W_{\text{el}}P_nW \\ &= W_{\text{el}} + W_{\text{el}}P_n^* v \ , \end{aligned} \tag{5.3.0.3}$$

where in the last equality we have introduced the reducible nuclear polarization propagator, $P_n^* = P_n\epsilon^{-1}$, where ϵ^{-1} is the total inverse dielectric response function that includes the effects due to both the electronic and nuclear degrees of freedom. By introduction of an

external field that couples to both the electronic and nuclear densities (ϕ), using Schwinger's functional derivative technique: $P_n^* = \frac{\delta n_n}{\delta \phi}$, it is possible to re-write Eq. 5.3.0.3 as [169]

$$W = W_{\text{el}} + W_{\text{el}} \frac{\delta n_n}{\delta \phi} v \ , \tag{5.3.0.4}$$

where n_n is the nuclear density. Using the chain-rule, by introduction of an external potential that couples only to the nuclear density (J), we can re-write this expression as

$$W = W_{\text{el}} + W_{\text{el}} \frac{\delta n}{\delta J} v \ , \tag{5.3.0.5}$$

where $n = n_{\text{el}} + n_n$ is now the combined electronic and nuclear density. This expression can then be simplified by identification of the nuclear density-density correlation function ($\bar{D}$) as $\frac{\delta n}{\delta J} = \frac{\delta n_n}{\delta J} \epsilon_{\text{el}}^{-1} = \bar{D} \epsilon_{\text{el}}^{-1}$:

$$\begin{aligned} W &= W_{\text{el}} + W_{\text{el}} \bar{D} W_{\text{el}} \\ W_{ph} &= W_{\text{el}} \bar{D} W_{\text{el}} \ . \end{aligned} \tag{5.3.0.6}$$

Therefore, we see that the screened Coulomb interaction decomposes exactly into the sum of electronic (W_{el}) and nuclear (W_{ph}) contributions. In real space, the nuclear contribution to the screened Coloumb interaction is written as

$$W_{ph}(1,2) = \int d3d4 \ W_{\text{el}}(1,3) \bar{D}(3,4) W_{\text{el}}(4,2) \tag{5.3.0.7}$$

where $\bar{D}(1,2) = -i \left\langle \mathcal{T}_\gamma \left\{ (n_n(1) - \langle n_n(1) \rangle)(n_n(2) - \langle n_n(2) \rangle) \right\} \right\rangle$. By truncating the nuclear density operator to second-order in the atomic displacements about their equilibrium positions, Baym [177] and Maksimov [178] showed that the propagator can be written as

$$\bar{D}(1,2) = \sum_{\substack{\kappa\alpha p \\ \kappa'\beta p'}} Z_\kappa Z_{\kappa'} \frac{\partial}{\partial r_{1\alpha}} \delta(\mathbf{r}_1 - \mathbf{R}_{\kappa p}^{\text{eq}}) D_{\kappa\alpha p, \kappa'\beta p'}(z_1, z_2) \frac{\partial}{\partial r_{2\beta}} \delta(\mathbf{r}_2 - \mathbf{R}_{\kappa' p'}^{\text{eq}}) \ , \tag{5.3.0.8}$$

where we have introduced $D_{\kappa\alpha p, \kappa'\beta p'}(z_1, z_2) = -i \left\langle \mathcal{T} \left\{ U_{\kappa\alpha p}(z_1) U_{\kappa'\beta p'}(z_2) \right\} \right\rangle$ as the phonon propagator. Inserting Eq. 5.3.0.8 into Eq. 5.3.0.7, using the derivative property of the Dirac delta distribution and taking the Fourier transformation to the frequency domain, it is straightforward to show that

$$W_{ph}^{\text{R}}(\mathbf{r}_1, \mathbf{r}_2; \omega) = \sum_{\substack{\kappa\alpha p \\ \kappa'\beta p'}} g_{\kappa\alpha p}^{\text{R}}(\mathbf{r}_1; \omega) D_{\kappa\alpha p, \kappa'\beta p'}^{\text{R}}(\omega) g_{\kappa'\beta p'}^{\text{R}}(\mathbf{r}_2; \omega) \ , \tag{5.3.0.9}$$

where we have defined the dynamically screened electron-phonon vertex as

$$g_{\kappa\alpha p}^{\text{R}}(\mathbf{r}_1; \omega) = \int d\mathbf{r}_2 \epsilon_{\text{el}}^{-1,\text{R}}(\mathbf{r}_1, \mathbf{r}_2; \omega) g_{\kappa\alpha p}^{\text{b}}(\mathbf{r}_2) \ . \tag{5.3.0.10}$$

Transforming to the phonon eigenmode representation and electronic Bloch basis, the screened Coulomb interaction takes the form

$$W^{ph,\mathrm{R}}_{n\mathbf{k}n'\mathbf{k}',n''\mathbf{k}'n'''\mathbf{k}}(\omega) = \sum_{\nu\nu'} g^{\mathrm{R,cc}}_{n_1n''\nu}(\mathbf{k},\mathbf{k}'-\mathbf{k};\omega) D^{\mathrm{R}}_{\mathbf{q}\nu,\mathbf{q}\nu'}(\omega) g^{\mathrm{R}}_{n'n'''\nu'}(\mathbf{k},\mathbf{k}'-\mathbf{k};\omega) \ , \quad (5.3.0.11)$$

where the phonon propagator is now given by $D_{\mathbf{q}\nu,\mathbf{q}\nu'}(z_1,z_2) = -i\left\langle \mathcal{T}\left\{A_{\mathbf{q}\nu}(z_1)A_{\mathbf{q}\nu'}(z_2)\right\}\right\rangle$. The screened electron-phonon vertex is defined as $g^{\mathrm{R}}_{nm\nu}(\mathbf{k},\mathbf{k}'-\mathbf{k};\omega) = \langle n\mathbf{k}'|g^{\mathrm{R}}_{\mathbf{k}'-\mathbf{k}\nu}(\mathbf{r};\omega)|m\mathbf{k}\rangle$, where we use the notation g^{cc} to indicate that this vertex only contains the complex conjugation of the bare electron-phonon vertex in Eq. 5.3.0.10 and not also of the electronic inverse dielectric function. This notation follows that of Ref. [169], where it is also noted that this subtle detail is frequently overlooked in the prior literature on electron-phonon interactions.

To lowest order in the electron-phonon interaction, we can simplify Eq. 5.3.0.11 by neglecting the frequency-dependence of the screened electron-phonon vertex: $g_{\kappa\alpha p}(\mathbf{r};\omega) \approx g_{\kappa\alpha p}(\mathbf{r};\omega=0) = g_{\kappa\alpha p}(\mathbf{r})$. In addition, we also make the 'adiabatic' approximation for the phonon propagator: $D \approx D^0$. With these two approximations, the expression for the phonon contribution to the screened Coulomb interaction in the electronic Bloch basis becomes

$$W^{ph(0),\mathrm{R}}_{n\mathbf{k}n'\mathbf{k}',n''\mathbf{k}'n'''\mathbf{k}}(\omega) = \sum_{\nu} g^{*}_{n''n\nu}(\mathbf{k},\mathbf{k}'-\mathbf{k}) g_{n'n'''\nu}(\mathbf{k},\mathbf{k}'-\mathbf{k}) D^{0,\mathrm{R}}_{\mathbf{k}'-\mathbf{k}\nu}(\omega). \quad (5.3.0.12)$$

This expression can also be obtained from the coherent state path integral by integrating out the phonon field [16]. In Eq. 5.3.0.12, the full complex conjugate of the electron-phonon vertex appears as the inverse electronic dielectric function is real at $\omega = 0$ [169]. At equilibrium and at zero temperature, the Fourier transform of the phonon propagator is given by

$$D^{0,\mathrm{R}}_{\mathbf{q}\nu}(\omega) = \left(\frac{1}{\omega - \omega_{\mathbf{q}\nu} + i\eta} - \frac{1}{\omega + \omega_{\mathbf{q}\nu} + i\eta}\right) \ . \quad (5.3.0.13)$$

Importantly, the phonon contribution to the screened Coloumb interaction provides an additive contribution to the electronic self-energy through the Hedin-Baym equations [38, 177]:

$$\Sigma_{ep}(1,2) = i \int d3d4 \ G(1,3)\Gamma(3,2;4)W_{ph}(4,1) \ . \quad (5.3.0.14)$$

5.3.1 Electron-phonon Fan-Migdal self-energy

By introduction of the phonon contribution to the screened interaction, the lowest-order expression for the dynamical electron-phonon self-energy is given by

$$\Sigma^{ep}_{n\mathbf{k},n'\mathbf{k}'}(z_1,z_2) = i \sum_{\substack{n_1\mathbf{k}_1\\ n_2\mathbf{k}_2}} W^{ph}_{n\mathbf{k}n_1\mathbf{k}_1,n_2\mathbf{k}_2n'\mathbf{k}'}(z_1,z_2) G_{n_2\mathbf{k}_2,n_1\mathbf{k}_1}(z_1,z_2) \ . \tag{5.3.1.1}$$

The GW_{ph} Feynman diagram corresponding to this approximation is depicted in Figure 5.3. Using the expression for W_{ph} given in Eq. 5.3.0.12 and the replacing the interacting Green's function with its non-interacting counterpart, at equilibrium and finite temperature, we obtain the retarded Fan-Migdal electron-phonon self-energy (FMd) self-energy using the Langreth rules (see Appendix A.1) [14, 169]:

$$\begin{aligned}\Sigma^{\mathrm{FMd},R}_{n\mathbf{k},n'\mathbf{k}'}(\omega,T) =& \delta_{\mathbf{k}\mathbf{k}'} \sum_{n''\nu} \int_{\mathrm{BZ}} \frac{d\mathbf{q}}{\Omega_{\mathrm{BZ}}} \ g^*_{n''n\nu}(\mathbf{k},\mathbf{q}) g_{n''n'\nu}(\mathbf{k},\mathbf{q}) \\ & \left[\frac{N_B(\omega_\nu(\mathbf{q})) + 1 - f(\epsilon_{n''}(\mathbf{k}+\mathbf{q}))}{\omega - \epsilon_{n''}(\mathbf{k}+\mathbf{q}) - \omega_\nu(\mathbf{q}) + i\eta} + \frac{N_B(\omega_\nu(\mathbf{q})) + f(\epsilon_{n''}(\mathbf{k}+\mathbf{q}))}{\omega - \epsilon_{n''}(\mathbf{k}+\mathbf{q}) + \omega_\nu(\mathbf{q}) + i\eta} \right] ,\end{aligned} \tag{5.3.1.2}$$

where $N_B(\omega) = (e^{\beta\omega} - 1)^{-1}$ is the Bose-Einstein occupation factor. Here, we have written the summation over the $\mathbf{q}$-points as an integral over the first Brillouin zone and explicitly indicated that the phonon and electronic dispersions are continuous functions of their respective wavevectors in order to emphasize the continuous nature of reciprocal space in the thermodynamic limit.

In the thermodynamic limit, as demonstrated in section 5.1, the single-particle Green's function and self-energy develop branch cuts on the real axis, giving rise to smooth imaginary parts over a given energy interval. The finite imaginary part of the FMd electron-phonon self-energy arises from the scattering of electrons due to phonon emission and absorption. Physically, this is due to the lifetime of the electronic state as it scatters into the continuum of final states accessible resulting from the lattice degrees of freedom.

At a given energy, the imaginary part of the FMd electron-phonon self-energy is directly proportional to the first Born approximation for the scattering rate of an electronic state:

$$\begin{aligned}\mathrm{Im}\Sigma^{\mathrm{FMd},R}_{n\mathbf{k},n\mathbf{k}}(\omega,T) =& -\pi \sum_{n''\nu\pm} \int_{\mathrm{BZ}} \frac{d\mathbf{q}}{\Omega_{\mathrm{BZ}}} \ |g_{n''n\nu}(\mathbf{k},\mathbf{q})|^2 \\ & \left[\left(N_B(\omega_\nu(\mathbf{q})) + \frac{1}{2} \pm \frac{1}{2} \mp f(\epsilon_{n''}(\mathbf{k}+\mathbf{q})) \right) \delta\Big(\omega - \epsilon_{n''}(\mathbf{k}+\mathbf{q}) \mp \omega_\nu(\mathbf{q})\Big) \right] .\end{aligned} \tag{5.3.1.3}$$

$\Sigma^{\mathrm{FMd}}_{nn'}(\omega) =$ 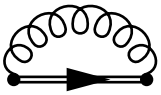

Figure 5.3: Dynamical GW_{ph} Fan-Migdal self-energy contribution.

Here, the $\pm$ notation indicates the sum over both phonon emission and absorption channels. Due to the continuous energies accessible to the electron by scattering with phonons, $\mathrm{Im}\Sigma^{\mathrm{FMd},R}_{n\mathbf{k},n'\mathbf{k}}(\omega, T)$ becomes a smooth function of the frequency. It is clear that the Fan-Migdal electron-phonon self-energy approximation is fully causal as $\mathrm{Im}\Sigma^{\mathrm{FMd},R}_{n\mathbf{k},n\mathbf{k}}(\omega, T) \leq 0$.

Physically, an electron propagating through a crystal drags the polarization of the lattice along with it. This is the origin of the phonon contribution to the screened interaction, W_{ph}. In some cases, if the coupling of the electron and the nuclei is sufficiently strong, this can result in the distortion of the lattice. When this happens, the quasiparticle formed by the combined carrier and lattice distortion is called a polaron [169, 179, 180]. However, capturing the potential distortions of the lattice is typically not possible within perturbation theory, requiring more sophisticated techniques based on variational canonical transformations (Lang-Firsov [8, 14, 181, 182]), the introduction of more sophisticated self-consistent many-body approaches [179, 180, 183–186] or using diagrammatic Monte-Carlo methods [187–189]. In addition, it is clear that the polarization of the lattice induced by an electron will be opposite to that induced by a hole due to their opposite formal charge. This will have important consequences for the dynamics of excitons. These polaronic contributions are clearly not captured by the perturbative Fan-Migdal self-energy given in Eq. 5.3.1.2.

5.4 The Bethe-Salpeter equation including electron-phonon interactions

Excitons are correlated quasiparticles that are commonly generated by photoexcitation of electron-hole pairs in semiconductors and insulators. The composite bound electron-hole pair is inherently correlated as a result of the attractive screened Coulomb interaction they experience [58, 59, 190]. Exciton formation and dissociation at finite temperatures is of central importance for the functioning of optoelectronic devices such as light-emitting

diodes and solar cells. Their dynamics are also central to the efficiency of photochemical reactions [6, 191–198]. In the presence of a weak external electric field, exciton dissociation to free charge carriers and radiative recombination can be induced by exciton-phonon interactions [197, 199–201]. Phonon-driven exciton dissociation, whereby an exciton scatters to a free electron-hole pair by interaction with phonons is of particular importance in semiconductors and insulators [2, 3, 6].

The *ab initio* Bethe-Salpeter equation (BSE) is one of the central theoretical frameworks used to understand and predict the properties of correlated electron-hole pairs in materials from first principles [58, 59]. In the electron-hole pair basis, within the TDA as outlined in Chapter 2 (see Eq. 2.7.4.7), the clamped-ion BSE for a solid, in reciprocal space, is given by [3, 59, 60, 202]

$$\Delta_{c\mathbf{k}+\mathbf{Q},v\mathbf{k}} A^{S\mathbf{Q}}_{vc\mathbf{k}} + \sum_{v'c'\mathbf{k}'} K^{eh}_{vc\mathbf{k}\mathbf{Q},v'c'\mathbf{k}'\mathbf{Q}}(\Omega_{S\mathbf{Q}}) A^{S\mathbf{Q}}_{v'c'\mathbf{k}'} = \Omega_{S\mathbf{Q}} A^{S\mathbf{Q}}_{vc\mathbf{k}}, \tag{5.4.0.1}$$

where $\Delta_{c\mathbf{k}+\mathbf{Q},v\mathbf{k}} = \epsilon_{c\mathbf{k}+\mathbf{Q}} - \epsilon_{v\mathbf{k}}$ are the eigenvalues of an independent-particle Hamiltonian, corresponding to the energy differences between conduction (c) and valence (v) band electronic states. Eq. 5.4.0.1 is written in the $(\mathbf{k}+\mathbf{Q})$-convention whereby the electron (conduction band) states are defined with momenta $\mathbf{Q}$ relative to the hole (valence band) states. The independent-particle eigenvalues are usually evaluated within the 'clamped-ion' GW_{el} approximation. Here, we have introduced the electron-hole pair notation such that the BSE kernel takes the form: $K^{eh}_{vc\mathbf{k}\mathbf{Q},v'c'\mathbf{k}'\mathbf{Q}}(\omega) \equiv K^{eh}_{c\mathbf{k}+\mathbf{Q}v'\mathbf{k}',v\mathbf{k}c'\mathbf{k}'+\mathbf{Q}}(\omega)$. The exciton eigenvalues are given by $\Omega_{S\mathbf{Q}}$, with $A^{S\mathbf{Q}}_{vc\mathbf{k}}$ corresponding to the coefficients of the exciton wavefunction with principle quantum number S and centre-of-mass momentum $\mathbf{Q}$. In the free electron-hole pair basis, the exciton wavefunction is written as [202]

$$|S\mathbf{Q}\rangle = \sum_{vc\mathbf{k}} A^{S\mathbf{Q}}_{vc\mathbf{k}} \, |vc\mathbf{k}+\mathbf{Q}\mathbf{k}\rangle \ , \tag{5.4.0.2}$$

where $|vc\mathbf{k}+\mathbf{Q}\mathbf{k}\rangle$ is the electron-hole-pair state. In the position representation, the electron-hole pair basis wavefunction is given by $\langle \mathbf{r}_h\mathbf{r}_e|vc\mathbf{k}+\mathbf{Q}\mathbf{k}\rangle = \psi_{c\mathbf{k}+\mathbf{Q}}(\mathbf{r}_e)\psi^*_{v\mathbf{k}}(\mathbf{r}_h)$, such that the exciton wavefunction is written as

$$\Psi_{S\mathbf{Q}}(\mathbf{r}_e,\mathbf{r}_h) = \sum_{vc\mathbf{k}} A^{S\mathbf{Q}}_{vc\mathbf{k}} \psi_{c\mathbf{k}+\mathbf{Q}}(\mathbf{r}_e)\psi^*_{v\mathbf{k}}(\mathbf{r}_h) \ , \tag{5.4.0.3}$$

where $\mathbf{r}_e/\mathbf{r}_h$ denote the electron/hole coordinates, respectively.

The electron-hole interaction kernel, $K^{eh}(\omega)$, consists of a direct contribution and an exchange contribution [59]. When working within the GW_{el} approximation, the direct interaction is taken to be the frequency-dependent, screened Coulomb interaction. This term is attractive and results in the formation of bound excited states. The exchange contribution is repulsive and gives rise to the exciton singlet-triplet splitting [59]. Commonly, the clamped-ion electron-hole interaction is evaluated within the static approximation, $W_{\text{el}}(\omega = 0)$, which in many circumstances constitutes a good approximation [2, 58, 59, 203–207]. In this case, the finite momentum GW-BSE equation can be written as

$$\sum_{v'c'\mathbf{k}'} H^{\text{BSE}}_{vc\mathbf{kQ},v'c'\mathbf{k}'\mathbf{Q}} A^{S\mathbf{Q}}_{v'c'\mathbf{k}'} = \Omega_{S\mathbf{Q}} A^{S\mathbf{Q}}_{vc\mathbf{k}} \ , \tag{5.4.0.4}$$

where $H^{\text{BSE}}_{vc\mathbf{kQ},v'c'\mathbf{k}'\mathbf{Q}} = \Delta_{c\mathbf{k}+\mathbf{Q},v\mathbf{k}}\delta_{vc\mathbf{k},v'c'\mathbf{k}'} + K^{eh,\infty}_{vc\mathbf{kQ},v'c'\mathbf{k}'\mathbf{Q}}$, with $K^{eh,\infty}_{vc\mathbf{kQ},v'c'\mathbf{k}'\mathbf{Q}} = v_{c\mathbf{k}+\mathbf{Q}v'\mathbf{k}',v\mathbf{k}c'\mathbf{k}'+\mathbf{Q}} - W^{\text{el}}_{c\mathbf{k}+\mathbf{Q}v'\mathbf{k}',c'\mathbf{k}'+\mathbf{Q}v\mathbf{k}}(\omega = 0)$ [58, 59]. As discussed in Chapter 2, the independent-particle electronic eigenvalues are also taken within the GW_{el} approximation. In the case of optical excitations, the exciton states formed are generally assumed to have zero center-of-mass momentum ($\mathbf{Q} = \mathbf{0}$). Within this approximation, the clamped-ion BSE (Eq. 5.4.0.1) reduces to

$$\Delta_{c\mathbf{k},v\mathbf{k}} A^{S}_{vc\mathbf{k}} + \sum_{v'c'\mathbf{k}'} K^{eh}_{vc\mathbf{k},v'c'\mathbf{k}'}(\Omega_S) A^{S}_{v'c'\mathbf{k}'} = \Omega_S A^{S}_{vc\mathbf{k}}, \tag{5.4.0.5}$$

where we have kept the full frequency-dependence of the electron-hole interaction.

5.4.1 Phonon contribution to the BSE kernel

From Chapter 2, the contribution of the electron-phonon interaction to the BSE kernel is given by the functional derivative of the electron-phonon self-energy with respect to the electronic Green's function:

$$\Xi^{ph}_{pq,rs}(z_1, z_2; z_3, z_4) = i\frac{\delta\Sigma^{ep}_{pr}(z_1, z_3)}{\delta G_{sq}(z_4, z_2)} \ . \tag{5.4.1.1}$$

By making the approximation for the electron-phonon self-energy given in Eq. 5.3.1.1, reinserting the wavevector dependence of all quantities and restricting the indices to the resonant block of the BSE, we see that this contribution is given by

$$\Xi^{ph}_{c\mathbf{k}v'\mathbf{k}',v\mathbf{k}c'\mathbf{k}'}(z_1, z_2; z_3, z_4) = -W^{ph}_{c\mathbf{k}v'\mathbf{k}',c'\mathbf{k}'v\mathbf{k}}(z_1, z_3)\delta(z_4, z_1)\delta(z_2, z_3) \ , \tag{5.4.1.2}$$

where we have neglected the contribution of the functional derivative of W^{ph} with respect to the Green's function. Using the analysis from chapter 2, using the phonon exchange

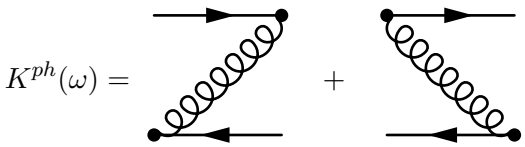

Figure 5.4: Phonon exchange diagrams contained in the *ab initio* phonon-screened BSE interaction kernel, K^{ph}.

diagrams depicted in Figure 5.4, we can generate the expression for the 'closed' frequency-dependent BSE kernel as

$$K^{ph}_{c\mathbf{k}v'\mathbf{k}',v\mathbf{k}c'\mathbf{k}'}(z_1,z_2) = -i\Big[L^{G_0}_{c'\mathbf{k}'v\mathbf{k},v\mathbf{k}c'\mathbf{k}'}(z_1,z_2) + L^{G_0}_{c\mathbf{k}v'\mathbf{k}',v'\mathbf{k}'c\mathbf{k}}(z_1,z_2)\Big]W^{ph}_{c\mathbf{k}v'\mathbf{k}',c'\mathbf{k}'v\mathbf{k}}(z_2,z_1)\ . \tag{5.4.1.3}$$

For the retarded component at finite temperature, we can directly evaluate this diagram using the Langreth rules to give

$$K^{ph,R}_{c\mathbf{k}v'\mathbf{k}',v\mathbf{k}c'\mathbf{k}'}(t_1,t_2) = -i\Big[L^{G_0,\mathrm{R}}_{c'\mathbf{k}'v\mathbf{k},v\mathbf{k}c'\mathbf{k}'}(t_1,t_2) + L^{G_0,\mathrm{R}}_{c\mathbf{k}v'\mathbf{k}',v'\mathbf{k}'c\mathbf{k}}(t_1,t_2)\Big]W^{ph,<}_{c\mathbf{k}v'\mathbf{k}',c'\mathbf{k}'v\mathbf{k}}(t_2,t_1) \tag{5.4.1.4}$$

Using the phonon contribution to the screened interaction given by Eq. 5.3.0.12, we have

$$W^{ph(0),<}_{c\mathbf{k}v'\mathbf{k}',c'\mathbf{k}'v\mathbf{k}}(\omega) = -\sum_{\nu} g_{cc'\nu}(\mathbf{k}',\mathbf{k}-\mathbf{k}')g^{*}_{vv'\nu}(\mathbf{k}',\mathbf{k}-\mathbf{k}')D^{0,<}_{\mathbf{k}-\mathbf{k}'\nu}(\omega) \tag{5.4.1.5}$$

where, at finite temperature the phonon propagator is given by $D^{0,<}_{\mathbf{q}\nu}(\omega) = -2\pi i\Big[(N_B(\omega_{\mathbf{q}\nu})+1)\delta(\omega+\omega_{\mathbf{q}\nu}) + N_B(\omega_{\mathbf{q}\nu})\delta(\omega-\omega_{\mathbf{q}\nu})\Big]$ and we have used the relationship: $g_{nm\nu}(\mathbf{k},\mathbf{k}'-\mathbf{k}) = g^{*}_{mn\nu}(\mathbf{k}',\mathbf{k}-\mathbf{k}')$.

Taking the Fourier transform of Eq. 5.4.1.4 gives the finite temperature expression for the interaction phonon screening contribution to the BSE kernel first derived in Refs [2, 205]:

$$K^{ph,\mathrm{R}}_{vc\mathbf{k},v'c'\mathbf{k}'}(\omega,T) = -\sum_{\nu,\pm} g_{cc'\nu}(\mathbf{k}',\mathbf{k}-\mathbf{k}')g^{*}_{vv'\nu}(\mathbf{k}',\mathbf{k}-\mathbf{k}')\Big(N_B(\omega_{\mathbf{k}-\mathbf{k}'\nu}) + \frac{1}{2} \pm \frac{1}{2}\Big)$$
$$\left[\frac{1}{\omega - \Delta_{c\mathbf{k},v'\mathbf{k}'} \mp \omega_{\mathbf{k}-\mathbf{k}'\nu} + i\eta} + \frac{1}{\omega - \Delta_{c'\mathbf{k}',v\mathbf{k}} \mp \omega_{\mathbf{k}-\mathbf{k}'\nu} + i\eta}\right]. \tag{5.4.1.6}$$

However, in this Chapter we have derived Eq. 5.4.1.6 by directly working on the equilibrium Keldysh contour instead of using analytic continuation from the Matsubara axis. Here, we have made the large band gap approximation, outlined in Chapter 2, which means we can neglect the Fermi-Dirac occupation factors of the electronic states. By rotation into

the basis of clamped-ion exciton states: $K^{ph,\mathrm{R}}_{SS'}(\omega,T) = \sum_{\substack{vc\mathbf{k}\\v'c'\mathbf{k}'}} A^{S*}_{vc\mathbf{k}} K^{ph,\mathrm{R}}_{vc\mathbf{k},v'c'\mathbf{k}'}(\omega,T) A^{S'}_{v'c'\mathbf{k}'}$, we arrive at the expression [2, 3, 6, 205]

$$K^{ph,\mathrm{R}}_{SS'}(\omega,T) = -\sum_{\substack{vc\mathbf{k}\\v'c'\mathbf{k}'\\\nu,\pm}} A^{S*}_{vc\mathbf{k}} g^{*}_{vv'\nu}(\mathbf{k}',\mathbf{k}-\mathbf{k}') g_{cc'\nu}(\mathbf{k}',\mathbf{k}-\mathbf{k}') A^{S'}_{v'c'\mathbf{k}'} \left(N_B(\omega_{\mathbf{k}-\mathbf{k}'\nu}) + \frac{1}{2} \pm \frac{1}{2}\right) \left[\frac{1}{\omega - \Delta_{c\mathbf{k},v'\mathbf{k}'} \mp \omega_{\mathbf{k}-\mathbf{k}'\nu} + i\eta} + \frac{1}{\omega - \Delta_{c'\mathbf{k}',v\mathbf{k}} \mp \omega_{\mathbf{k}-\mathbf{k}'\nu} + i\eta}\right], \tag{5.4.1.7}$$

Physically, the imaginary part of $K^{ph,\mathrm{R}}_{SS}$ is related to the dissociative scattering of exciton states to free electron-hole pairs driven by phonon emission and absorption:

$$\mathrm{Im}K^{ph,\mathrm{R}}_{SS}(\omega,T) = \pi \sum_{\substack{vc\mathbf{k}\\v'c'\mathbf{k}'\\\nu,\pm}} A^{S*}_{vc\mathbf{k}} g^{*}_{vv'\nu}(\mathbf{k}',\mathbf{k}-\mathbf{k}') g_{cc'\nu}(\mathbf{k}',\mathbf{k}-\mathbf{k}') A^{S}_{v'c'\mathbf{k}'} \left(N_B(\omega_{\mathbf{k}-\mathbf{k}'\nu}) + \frac{1}{2} \pm \frac{1}{2}\right) \left[\delta\left(\omega - \Delta_{c\mathbf{k},v'\mathbf{k}'} \mp \omega_{\mathbf{k}-\mathbf{k}'\nu}\right) + \delta\left(\omega - \Delta_{c'\mathbf{k}',v\mathbf{k}} \mp \omega_{\mathbf{k}-\mathbf{k}'\nu}\right)\right]. \tag{5.4.1.8}$$

In contrast to the FMd electron-phonon self-energy (Eq. 5.3.1.3), the sign of the imaginary part of $K^{ph,R}_{SS}$ is not determined. This reflects the fact that the kernel is a two-particle interaction rather than a retarded self-energy, as the kernel encodes interference effects between two-particles which are dependent on the electronic phases of the individual states. It is important to note that the analysis presented here equally applies to the 'clamped-ion' electron-electron dynamical BSE kernel [61, 96] as well as the exciton-polariton interaction kernel [208].

5.4.2 Including dynamical self-energy contributions

To include the effects of the electron-phonon self-energy on the single-particle Green's functions that also enter the BSE, at lowest-order in the interaction we must evaluate the Feynman diagrams shown in Figure 5.5. At equilibrium and finite temperature, these diagrams evaluate to give

$$K^{\Sigma^{\mathrm{FMd}},\mathrm{R}}_{c\mathbf{k}v'\mathbf{k}',v\mathbf{k}c'\mathbf{k}'}(\omega,T) = \Sigma^{\mathrm{FMd,e}}_{c\mathbf{k},c'\mathbf{k}'}(\omega+\epsilon_{v\mathbf{k}},T)\delta_{\mathbf{k}\mathbf{k}'}\delta_{vv'} - \Sigma^{\mathrm{FMd,h}}_{v'\mathbf{k}',v\mathbf{k}}(\epsilon_{c\mathbf{k}}-\omega,T)\delta_{\mathbf{k}\mathbf{k}'}\delta_{cc'}\ , \tag{5.4.2.1}$$

where

$$\Sigma^{\mathrm{FMd,e}}_{c\mathbf{k},c'\mathbf{k}'}(\omega,T) = \delta_{\mathbf{k}\mathbf{k}'} \sum_{c''\mathbf{q}\nu} g^{*}_{c''c\nu}(\mathbf{k},\mathbf{q}) g_{c''c'\nu}(\mathbf{k},\mathbf{q}) \left[\frac{N_B(\omega_{\mathbf{q}\nu})+1}{\omega - \epsilon_{c''\mathbf{k}+\mathbf{q}} - \omega_{\mathbf{q}\nu} + i\eta} + \frac{N_B(\omega_{\mathbf{q}\nu})}{\omega - \epsilon_{c''\mathbf{k}+\mathbf{q}} + \omega_{\mathbf{q}\nu} + i\eta}\right] \tag{5.4.2.2a}$$

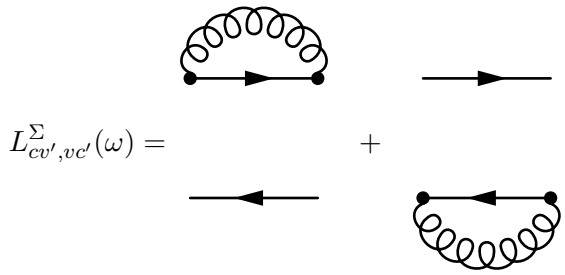

Figure 5.5: Dynamical self-energy diagrams generated by the independent particle propagation term of the BSE.

and

$$\Sigma^{\mathrm{FMd,h}}_{v'\mathbf{k}',v\mathbf{k}}(\omega,T) = \delta_{\mathbf{k}\mathbf{k}'} \sum_{v''\mathbf{q}\nu} g^{*}_{v''v'\nu}(\mathbf{k},\mathbf{q}) g_{v''v\nu}(\mathbf{k},\mathbf{q}) \left[\frac{N_B(\omega_{\mathbf{q}\nu})+1}{\omega - \epsilon_{v''\mathbf{k}+\mathbf{q}} - \omega_{\mathbf{q}\nu} - i\eta} + \frac{N_B(\omega_{\mathbf{q}\nu})}{\omega - \epsilon_{v''\mathbf{k}+\mathbf{q}} + \omega_{\mathbf{q}\nu} - i\eta} \right] . \tag{5.4.2.2b}$$

As can be seen, the two diagrams are constrained within the TDA such that they include only specific time-orderings of the Green's function lines in Figure 5.5. This constrains the self-energy contributions to be composed of only forward time-ordered diagrams for the conduction band states and only backward time-ordered diagrams for the valence states. This is reflected in Eqs 5.4.2.2a and 5.4.2.2b by the fact that the self-energy contributions for the conduction and hole states contain summations only over either conduction or valence intermediate states. Using these two diagrams, we arrive at the generalized interaction kernel given by the sum of the dynamical self-energy and phonon exchange diagrams

$$K^{\mathrm{TDA,R}}_{vc\mathbf{k},v'c'\mathbf{k}'}(\omega,T) = K^{\Sigma^{\mathrm{FMd}},\mathrm{TDA}}_{vc\mathbf{k},v'c'\mathbf{k}'}(\omega,T) + K^{ph,\mathrm{R}}_{vc\mathbf{k},v'c'\mathbf{k}'}(\omega,T) \ . \tag{5.4.2.3}$$

We use the notation $K^{\mathrm{TDA,R}}_{vc\mathbf{k},v'c'\mathbf{k}'}$ to indicate that the dynamical self-energy contributions are included within the TDA. We can combine both terms in the form of a single matrix element to give

$$K^{\mathrm{TDA,R}}_{vc\mathbf{k},v'c'\mathbf{k}'}(\omega,T) = \sum_{\substack{c''\mathbf{k}'' \\ v''\mathbf{k}''' \\ \nu,\pm}} \frac{M_{vc\mathbf{k},v''c''\mathbf{k}''\mathbf{k}'''\nu} M^{*}_{v'c'\mathbf{k}',v''c''\mathbf{k}''\mathbf{k}'''\nu}}{\omega - \Delta_{c''\mathbf{k}'',v''\mathbf{k}'''} \mp \omega_{\mathbf{k}''-\mathbf{k}'''\nu} + i\eta} \Big(N_B(\omega_{\mathbf{k}''-\mathbf{k}'''\nu}) \pm \frac{1}{2} + \frac{1}{2} \Big), \tag{5.4.2.4}$$

where

$$M_{vc\mathbf{k},v''c''\mathbf{k}''\mathbf{k}'''\nu} = g_{cc''\nu}(\mathbf{k}'',\mathbf{k}-\mathbf{k}'')\delta_{vv''}\delta_{\mathbf{k}\mathbf{k}'''} - g^{*}_{vv''\nu}(\mathbf{k}''',\mathbf{k}-\mathbf{k}''')\delta_{cc''}\delta_{\mathbf{k}\mathbf{k}''} \ . \tag{5.4.2.5}$$

It is straightforward to verify that expansion of this matrix element gives exactly the diagrams of Figures 5.4 and 5.5. By inclusion of the dynamical electron-phonon self-energy contributions to the single-particle propagators, we find that the imaginary part

of the kernel recovers a definite sign:

$$\begin{aligned}\mathrm{Im}K^{\mathrm{TDA,R}}_{vc\mathbf{k},vc\mathbf{k}}(\omega,T) = -\pi \sum_{\substack{c''\mathbf{k}'' \\ v''\mathbf{k}''' \\ \nu,\pm}} |M_{vc\mathbf{k},v''c''\mathbf{k}''\mathbf{k}'''\nu}|^2 \Big(N_B(\omega_{\mathbf{k}''-\mathbf{k}'''\nu}) \pm \frac{1}{2} + \frac{1}{2}\Big) \\ \times \delta\left(\omega - \Delta_{c''\mathbf{k}'',v''\mathbf{k}'''} \mp \omega_{\mathbf{k}''-\mathbf{k}'''\nu}\right) \ .\end{aligned} \tag{5.4.2.6}$$

As $\mathrm{Im}K^{\mathrm{TDA,R}}_{vc\mathbf{k},vc\mathbf{k}}(\omega,T) \leq 0$, we can immediately find that $K^{\mathrm{TDA,R}}_{vc\mathbf{k},vc\mathbf{k}}(\omega,T)$ constitutes a fully causal approximation. Transformation of this kernel to the 'clamped-ion' exciton basis: $K^{\mathrm{TDA,R}}_{SS'}(\omega) = \sum_{\substack{vc\mathbf{k} \\ v'c'\mathbf{k}'}} A^{S*}_{vc\mathbf{k}} K^{\mathrm{TDA,R}}_{vc\mathbf{k},v'c'\mathbf{k}'}(\omega) A^{S'}_{v'c'\mathbf{k}'}$, we find that

$$K^{\mathrm{TDA,R}}_{SS'}(\omega,T) = \sum_{\substack{c''\mathbf{k}'' \\ v''\mathbf{k}''' \\ \nu,\pm}} \frac{M_{S,v''c''\mathbf{k}''\mathbf{k}'''\nu} M^*_{S',v''c''\mathbf{k}''\mathbf{k}'''\nu}}{\omega - \Delta_{c''\mathbf{k}'',v''\mathbf{k}'''} \mp \omega_{\mathbf{k}''-\mathbf{k}'''\nu} + i\eta} \Big(N_B(\omega_{\mathbf{k}''-\mathbf{k}'''\nu}) \pm \frac{1}{2} + \frac{1}{2}\Big), \tag{5.4.2.7}$$

where the rotated matrix elements are defined as

$$M_{S,v''c''\mathbf{k}''\mathbf{k}'''\nu} = \sum_{c_1} A^{S*}_{v''c_1\mathbf{k}'''} g_{c_1c''\nu}(\mathbf{k}'', \mathbf{k}''' - \mathbf{k}'') - \sum_{v_1} A^{S*}_{v_1c''\mathbf{k}''} g^*_{v_1v''\nu}(\mathbf{k}''', \mathbf{k}'' - \mathbf{k}''') \ . \tag{5.4.2.8}$$

As stated, the interaction kernel $K^{\mathrm{TDA,R}}(\omega,T)$ contains specific time-ordered electron-phonon Fan-Migdal self-energy contributions. However, for the case of electron-electron interactions, it is found that this approximation can severely affect the eigenvalues of the computed excitation energies [96, 134]. In addition, polaronic effects have been neglected in this approximation. Depending on the nature of the interference between the electron and hole polarons, their renormalized effects may cancel each other out within this regime [181, 209]. This polaron interference can be viewed as the result of the overlap of the separate electron and hole lattice distortion clouds as they are brought closer to form a bound exciton. As the electron-hole distance decreases, the lattice relaxation is reduced relative to the free electron and hole polarons as the lattice is constrained by the opposing lattice distortions. Therefore, as a first approximation, previous work partially neglects the effects of this band renormalization entirely [2, 181, 182, 205, 209]. Potential future directions for including these localization effects in the calculation of exciton renormalization will require a better understanding of polaron interference effects [179, 180].

5.5 Causality and phonon-driven exciton dissociation

The imaginary part of $K_{SS}^{\mathrm{TDA,R}}(\omega,T)$ kernel is given by

$$\begin{aligned}\mathrm{Im}K_{SS}^{\mathrm{TDA,R}}(\omega,T) = -\pi \sum_{\substack{c''\mathbf{k}'' \\ v''\mathbf{k}''' \\ \nu,\pm}} |M_{S,v''c''\mathbf{k}''\mathbf{k}'''\nu}|^2 \Big(N_B(\omega_{\mathbf{k}''-\mathbf{k}'''\nu}) \pm \frac{1}{2} + \frac{1}{2}\Big) \\ \times \delta(\omega - \Delta_{c''\mathbf{k}'',v''\mathbf{k}'''} \mp \omega_{\mathbf{k}''-\mathbf{k}'''\nu}),\end{aligned} \tag{5.5.0.1}$$

which is clearly negative semi-definite: $\mathrm{Im}K_{SS}^{\mathrm{TDA,R}}(\omega) \leq 0$. Using Eq. 5.4.2.3, we find that

$$-\mathrm{Im}K_{SS}^{\mathrm{TDA,R}}(\omega,T) = -\mathrm{Im}K_{SS}^{\Sigma^{\mathrm{FMd}},\mathrm{TDA}}(\omega,T) - \mathrm{Im}K_{SS}^{ph,\mathrm{R}}(\omega,T) \geq 0 \tag{5.5.0.2}$$

from which we immediately conclude

$$-\mathrm{Im}K_{SS}^{\Sigma^{\mathrm{FMd}},\mathrm{TDA}}(\omega,T) \geq \mathrm{Im}K_{SS}^{ph,\mathrm{R}}(\omega,T) \quad \forall\ \omega,T\ . \tag{5.5.0.3}$$

In Ref. [3] we rigorously demonstrated, using rearrangement collision theory [210], that $-\mathrm{Im}K_{SS}^{\mathrm{TDA,R}}(\Omega_S)$ is directly proportional to the first Born approximation for the phonon-driven dissociation rate for a zero momentum exciton:

$$\begin{aligned}\gamma_S(T) = 2\pi \sum_{\substack{vc\mathbf{k}c'c'' \\ \mathbf{q}\nu\pm}} A_{vc\mathbf{k}}^{S*} g_{c''c\nu}^*(\mathbf{k},\mathbf{q}) g_{c''c'\nu}(\mathbf{k},\mathbf{q}) A_{vc'\mathbf{k}}^{S} \left(N_B(\omega_{\mathbf{q}\nu}) + \frac{1}{2} \pm \frac{1}{2}\right) \\ \delta(\Omega_S - (\epsilon_{c''\mathbf{k}+\mathbf{q}} - \epsilon_{v\mathbf{k}}) \mp \omega_{\mathbf{q}\nu}) \\ + 2\pi \sum_{\substack{vc\mathbf{k}v'v'' \\ \mathbf{q}\nu\pm}} A_{vc\mathbf{k}}^{S*} g_{v''v\nu}^*(\mathbf{k},\mathbf{q}) g_{v''v'\nu}(\mathbf{k},\mathbf{q}) A_{v'c\mathbf{k}}^{S} \left(N_B(\omega_{\mathbf{q}\nu}) + \frac{1}{2} \pm \frac{1}{2}\right) \\ \delta(\Omega_S - (\epsilon_{c\mathbf{k}} - \epsilon_{v''\mathbf{k}+\mathbf{q}}) \mp \omega_{\mathbf{q}\nu}) \\ - 2\pi \sum_{\substack{vc\mathbf{k} \\ v'c'\mathbf{k}' \\ \nu,\pm}} A_{vc\mathbf{k}}^{S*} g_{vv'\nu}^*(\mathbf{k}',\mathbf{k}-\mathbf{k}') g_{cc'\nu}(\mathbf{k}',\mathbf{k}-\mathbf{k}') A_{v'c'\mathbf{k}'}^{S} \left(N_B(\omega_{\mathbf{k}-\mathbf{k}'\nu}) + \frac{1}{2} \pm \frac{1}{2}\right) \\ \left[\delta\left(\Omega_S - \Delta_{c\mathbf{k},v'\mathbf{k}'} \mp \omega_{\mathbf{k}-\mathbf{k}'\nu}\right) + \delta\left(\Omega_S - \Delta_{c'\mathbf{k}',v\mathbf{k}} \mp \omega_{\mathbf{k}-\mathbf{k}'\nu}\right)\right],\end{aligned} \tag{5.5.0.4}$$

where $\gamma_S = -2\mathrm{Im}K_{SS}^{\mathrm{TDA,R}}(\Omega_S) \geq 0$. It is clear from their relationship to the dynamical self-energy that the first two terms of Eq. 5.5.0.4 directly arise due to the lifetime of the individual electronic states that the exciton is composed from. Therefore, we can define the contribution

$$\begin{aligned}\gamma_S^{\mathrm{ehFMd}} &= -2\mathrm{Im}K_{SS}^{\Sigma^{\mathrm{FMd}},\mathrm{TDA}}(\Omega_S,T) \\ &= -2\sum_{vc\mathbf{k}c'} A_{vc\mathbf{k}}^{S*} \mathrm{Im}\Sigma_{c\mathbf{k},c'\mathbf{k}}^{\mathrm{FMd,e}}(\Omega_S - \epsilon_{v\mathbf{k}},T) A_{vc'\mathbf{k}}^{S} \\ &+ 2\sum_{vc\mathbf{k}v'} A_{vc\mathbf{k}}^{S*} \mathrm{Im}\Sigma_{v'\mathbf{k},v\mathbf{k}}^{\mathrm{FMd,h}}(\epsilon_{c\mathbf{k}} - \Omega_S,T) A_{v'c\mathbf{k}}^{S}\ ,\end{aligned} \tag{5.5.0.5}$$

where we have used the notation γ_S^{ehFMd} to indicate the lifetime of the corresponding electron and hole-polaron states [3]. Similarly, we also define the interference contribution as [3]

$$\begin{aligned}\gamma_S^{\text{xeh}}(T) &= -2\text{Im}K_{SS}^{ph}(\Omega_S,T)\\ &= -2\pi \sum_{\substack{vc\mathbf{k}\\ v'c'\mathbf{k}'\\ \nu,\pm}} A_{vc\mathbf{k}}^{S*} g_{vv'\nu}^*(\mathbf{k}',\mathbf{k}-\mathbf{k}') g_{cc'\nu}(\mathbf{k}',\mathbf{k}-\mathbf{k}') A_{v'c'\mathbf{k}'}^{S} \Big(N_B(\omega_{\mathbf{k}-\mathbf{k}'\nu}) + \frac{1}{2} \pm \frac{1}{2}\Big)\\ &\qquad \Big[\delta\left(\Omega_S - \Delta_{c\mathbf{k},v'\mathbf{k}'} \mp \omega_{\mathbf{k}-\mathbf{k}'\nu}\right) + \delta\left(\Omega_S - \Delta_{c'\mathbf{k}',v\mathbf{k}} \mp \omega_{\mathbf{k}-\mathbf{k}'\nu}\right)\Big]\end{aligned} \tag{5.5.0.6}$$

to write the dissociation rate as

$$\gamma_S(T) = |\gamma_S^{\text{ehFMd}}(T) + \gamma_S^{\text{xeh}}(T)| \ . \tag{5.5.0.7}$$

As the sign of $\text{Im}K_{SS}^{ph}$ is not determined, it is clear that the sign of $\gamma_S^{\text{xeh}}(T)$ also inherits the same property. However, if we make the approximation that the polaron renormalization of the Fan-Migdal self-energy results in (infinitely) long lived electron/hole-polaron quasiparticle states, we may simplify the dissociation rate by neglecting the imaginary part of the FM self-energy. In this case, we can write the correlated first Born approximation for the electron-hole dissociation rate as

$$\gamma_S(T) \approx |\gamma_S^{\text{xeh}}(T)| = 2|\text{Im}K_{SS}^{ph,R}(\Omega_S,T)| \ , \tag{5.5.0.8}$$

where $|\text{Im}K_{SS}^{ph,R}(\Omega_S,T)|$ ensures that the rate is positive semi-definite within this approximation.

The phonon-screened BSE eigenvalue problem, written in the 'clamped-ion' exciton eigenbasis of Eq. 5.4.0.4, is given by

$$\sum_{S'} \Big(\Omega_S \delta_{SS'} + K_{SS'}^{ph,\text{R}}(\tilde{\Omega}_{\mathcal{S}},T)\Big)\bar{U}_{S'}^{\mathcal{S}}(T) = \tilde{\Omega}_{\mathcal{S}}(T)\bar{U}_S^{\mathcal{S}}(T) \ . \tag{5.5.0.9}$$

As $K_{SS}^{ph,\text{R}}(\omega,T)$ is a two-particle dynamical interaction kernel that is not required to be causal, the eigenvalue solutions of Eq. 5.5.0.9 come in complex conjugate pairs, $\{\tilde{\Omega}_{\mathcal{S}}, \tilde{\Omega}_{\mathcal{S}}^*\}$. This is because the secular equation that determines the eigenvalues of Eq. 5.5.0.9 yields a polynomial equation that contains only real coefficients. As a result, the corresponding pole solutions lie in both halves of the complex plane. Therefore, the physical exciton resonance solution corresponds to the retarded pole, given by the eigenvalue with a negative imaginary part: $\text{Im}\tilde{\Omega}_{\mathcal{S}} \leq 0$. The conjugate solution in the upper half-plane is nonphysical and simply

arises due to the analytic structure of the secular equation rather than indicating a real physical instability of the system. Therefore, the retarded pole can be viewed as an approximate resonance state of the exciton state as a result of interaction with phonons. The real part, $\mathrm{Re}\tilde{\Omega}_{\mathcal{S}}$, corresponds to the renormalization of the exciton as a result of the screening due to phonons while the imaginary part, $|\mathrm{Im}\tilde{\Omega}_{\mathcal{S}}|$, is proportional to the approximate self-consistent linewidth of the exciton due to phonon-driven dissociation scattering to long-lived free electron-hole pairs.

5.6 Including missing reverse-time contributions

As stated in Section 5.4, the dynamical self-energy diagrams depicted in Figure 5.5 do not include the full set of time-orderings of the FMd electron-phonon self-energy. At first-order, inclusion of missing reverse-time contributions gives rise to the following static contribution:

$$
\begin{aligned}
K^{\mathrm{FM},\infty}_{vc\mathbf{k},v'c'\mathbf{k}'}(T) = \frac{\delta_{vv'}\delta_{\mathbf{k}\mathbf{k}'}}{2} \sum_{v''\mathbf{q}\nu\pm} & g_{v''c'\nu}(\mathbf{k},\mathbf{q}) g^{*}_{v''c\nu}(\mathbf{k},\mathbf{q}) \left(N_B(\omega_{\mathbf{q}\nu}) \pm \frac{1}{2} + \frac{1}{2} \right) \\
& \left[\frac{1}{\epsilon_{c\mathbf{k}} - \epsilon_{v''\mathbf{k}+\mathbf{q}} \pm \omega_{\mathbf{q}\nu} + i\eta} + \frac{1}{\epsilon_{c'\mathbf{k}} - \epsilon_{v''\mathbf{k}+\mathbf{q}} \pm \omega_{\mathbf{q}\nu} + i\eta} \right] \\
- \frac{\delta_{cc'}\delta_{\mathbf{k}\mathbf{k}'}}{2} \sum_{c''\mathbf{q}\nu\pm} & g_{c''v\nu}(\mathbf{k},\mathbf{q}) g^{*}_{c''v'\nu}(\mathbf{k},\mathbf{q}) \left(N_B(\omega_{\mathbf{q}\nu}) \pm \frac{1}{2} + \frac{1}{2} \right) \\
& \left[\frac{1}{\epsilon_{v'\mathbf{k}} - \epsilon_{c''\mathbf{k}+\mathbf{q}} \mp \omega_{\mathbf{q}\nu} + i\eta} + \frac{1}{\epsilon_{v\mathbf{k}} - \epsilon_{c''\mathbf{k}+\mathbf{q}} \mp \omega_{\mathbf{q}\nu} + i\eta} \right] .
\end{aligned}
\tag{5.6.0.1}
$$

The diagrams associated with these missing time-orderings are depicted in Figure 5.6 and clearly contain the propagation of intermediate states that cannot be projected onto the space of electron-hole pairs and hence are not captured within the TDA. This term was first derived in Ref. [211] but its connection to the reverse-time contributions of the Fan-Migdal electron-phonon self-energy was not discussed. The derivation of these contributions in this thesis was arrived at completely independently using the Keldysh contour formulation. In particular, we find that Eq. 5.6.0.1 also contains a branch cut on the real axis and can give rise to a finite imaginary part as a result of electron-phonon scattering. However, the analysis of these contributions is beyond the scope of this thesis and requires future study.

Inclusion of the reverse-time components of the FMd electron-phonon self-energy gives the complete first-order expression for the dynamical BSE including the effects of the

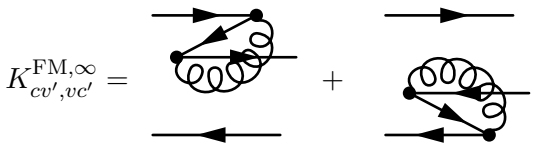

Figure 5.6: Missing reverse-time self-energy diagrams generated by the independent particle propagation term of the BSE. These contributions are not captured with the Tamm-Dancoff approximation.

electron-phonon interaction within the TDA:

$$\hat{H}^{\text{ep,BSE}}_{vc\mathbf{k},v'c'\mathbf{k}'}(\omega,T) = H^{\text{BSE}}_{vc\mathbf{k},v'c'\mathbf{k}'} + K^{\Sigma^{\text{FMd}},\text{TDA}}_{vc\mathbf{k},v'c'\mathbf{k}'}(\omega,T) + K^{ph,\text{R}}_{vc\mathbf{k},v'c'\mathbf{k}'}(\omega,T) + K^{\text{FM},\infty}_{vc\mathbf{k},v'c'\mathbf{k}'}(T) \ . \tag{5.6.0.2}$$

We are currently exploring including these reverse-time contributions in order to provide a complete theory of exciton-phonon interactions in infinite solids.

5.7 Exciton-phonon Fan-Migdal self-energy

In the previous sections, we extended the BSE to include electron-phonon interactions by introduction of the phonon contribution to the screened Coulomb interaction, W_{ph}. In this section, we instead consider an alternative approach based on the effective field theory of excitons that are linearly coupled to a bath of phonons [211]:

$$H_{\text{xct-ph}} = \sum_{S\mathbf{Q}} \Omega_{S\mathbf{Q}} O^{\dagger}_{S\mathbf{Q}} O_{S\mathbf{Q}} + \sum_{\mathbf{q}\nu} \omega_{\mathbf{q}\nu} a^{\dagger}_{\mathbf{q}\nu} a_{\mathbf{q}\nu} + \sum_{\substack{SS'\mathbf{Q}'\\ \mathbf{q}\nu}} G_{SS'\nu}(\mathbf{Q}',\mathbf{q}) O^{\dagger}_{S\mathbf{Q}'+\mathbf{q}} O_{S'\mathbf{Q}'} A_{\mathbf{q}\nu} \ , \tag{5.7.0.1}$$

where $O^{\dagger}_{S\mathbf{Q}}/O_{S\mathbf{Q}}$ are Bosonic creation/annihilation operators that act to create/annihilate 'clamped-ion' Bloch exciton states (the eigenstates of Eq. 5.4.0.4) and we have defined the composite 'exciton-phonon' vertex: $G_{SS'\nu}(\mathbf{Q}',\mathbf{q}) = \langle S\mathbf{Q}'+\mathbf{q}|g_{\mathbf{q}\nu}|S'\mathbf{Q}'\rangle$. Expansion of the exciton-phonon coupling matrix in the electron-hole pair basis we have [211, 212]

$$G_{SS'\nu}(\mathbf{Q}',\mathbf{q}) = \sum_{vcc'\mathbf{k}'} A^{S\mathbf{Q}'+\mathbf{q}*}_{vc\mathbf{k}'} g_{cc'\nu}(\mathbf{k}'+\mathbf{Q}',\mathbf{q}) A^{S'\mathbf{Q}'}_{vc'\mathbf{k}'} - \sum_{vcv'\mathbf{k}'} A^{S\mathbf{Q}'+\mathbf{q}*}_{vc\mathbf{k}'} g_{v'v\nu}(\mathbf{k}',\mathbf{q}) A^{S'\mathbf{Q}'}_{v'c\mathbf{k}'+\mathbf{q}}. \tag{5.7.0.2}$$

The effective field theory of Eq. 5.7.0.1 is valid only in the dilute exciton density limit whereby the field commutation relations are approximately valid: $\left[O_{S\mathbf{Q}}, O^{\dagger}_{S'\mathbf{Q}'}\right] = \delta_{SS'}\delta_{\mathbf{Q}\mathbf{Q}'}$.

The effective Hamiltonian gives rise to the following Dyson equation for the exciton-phonon propagator

$$\mathbf{L}(s,T) = \mathbf{L}^{\mathrm{el}}(s,T) + \mathbf{L}^{\mathrm{el}}(s,T)\mathbf{\Xi}(s,T)\mathbf{L}(s,T) \ , \tag{5.7.0.3}$$

where the 'non-interacting' clamped-ion exciton propagator corresponds to the solution of the eigenvalue problem of Eq. 5.4.0.4:

$$\begin{aligned} L^{\mathrm{el,R}}_{S\mathbf{Q},S'\mathbf{Q}'}(\omega) &= \sum_{\substack{vc\mathbf{k} \\ v'c'\mathbf{k}'}} A^{S\mathbf{Q}*}_{vc\mathbf{k}} L^{\mathrm{el,R}}_{c\mathbf{k}v'\mathbf{k}',v\mathbf{k}c'\mathbf{k}'}(\omega) A^{S'\mathbf{Q}'}_{v'c'\mathbf{k}'} \\ &= \frac{\delta_{SS'}\delta_{\mathbf{Q}\mathbf{Q}'}}{\omega - \Omega_{S\mathbf{Q}} + i\eta} \ . \end{aligned} \tag{5.7.0.4}$$

It is important to realise that the effective field theory of Eq. 5.7.0.1 results in the mapping of the two-particle BSE to an effective one-particle theory whereby the two-particle interaction has been mapped to an effective 'one-particle' self-energy kernel. This structure is emphasized by the emergence of the exciton-phonon Dyson equation of Eq. 5.7.0.3.

To lowest-order in the effective exciton-phonon interaction, the exciton-phonon self-energy can be immediately inferred from the structure of the Hamiltonian in Eq. 5.7.0.1 as the '$L_{\mathrm{el}}W_{ph}$' exciton-phonon Fan-Migdal self-energy:

$$\Xi^{\mathrm{FMd}}_{S\mathbf{Q},S'\mathbf{Q}'}(z_1,z_2) = i \sum_{\substack{S_1\mathbf{Q}_1 \\ S_2\mathbf{Q}_2}} W^{ph(0)}_{S\mathbf{Q}S_1\mathbf{Q}_1,S_2\mathbf{Q}_2S'\mathbf{Q}'}(z_1,z_2) L^{\mathrm{el}}_{S_2\mathbf{Q}_2,S_1\mathbf{Q}_1}(z_1,z_2) \ , \tag{5.7.0.5}$$

where we have defined the phonon contribution to the exciton screened Coulomb interaction as

$$W^{ph(0)}_{S\mathbf{Q}S_1\mathbf{Q}',S_2\mathbf{Q}'S'\mathbf{Q}}(z_1,z_2) = \sum_{\nu} G^{*}_{S_2S\nu}(\mathbf{Q},\mathbf{Q}'-\mathbf{Q}) G^{*}_{S_1S'\nu}(\mathbf{Q},\mathbf{Q}'-\mathbf{Q}) D^{(0)}_{\mathbf{Q}'-\mathbf{Q}\nu}(z_1,z_2) \ . \tag{5.7.0.6}$$

At finite temperature, using the Langreth rules, we find the retarded component of the self-energy as

$$\Xi^{\mathrm{FMd,R}}_{S\mathbf{Q},S'\mathbf{Q}'}(t_1,t_2) = i \sum_{\substack{S_1\mathbf{Q}_1 \\ S_2\mathbf{Q}_2}} L^{\mathrm{el},R}_{S_2\mathbf{Q}_2,S_1\mathbf{Q}_1}(t_1,t_2) W^{ph(0),<}_{S\mathbf{Q}S_1\mathbf{Q}_1,S_2\mathbf{Q}_2S'\mathbf{Q}'}(t_1,t_2) \ , \tag{5.7.0.7}$$

which upon Fourier transformation gives rise to

$$\Xi^{\mathrm{FMd,R}}_{S\mathbf{Q},S'\mathbf{Q}'}(\omega,T) = \delta_{\mathbf{Q}\mathbf{Q}'} \sum_{S_1\mathbf{q}\nu\pm} \frac{G^{*}_{S_1S\nu}(\mathbf{Q},\mathbf{q}) G_{S_1S'\nu}(\mathbf{Q},\mathbf{q})}{\omega - \Omega_{S_1\mathbf{Q}+\mathbf{q}} \mp \omega_{\mathbf{q}\nu} + i\eta} \left(N_B(\omega_{\mathbf{q}\nu}) \pm \frac{1}{2} + \frac{1}{2} \right) \ . \tag{5.7.0.8}$$

It is clear that the exciton-phonon Fan-Migdal self-energy gives rise to th branch cut structure of the exciton Green's function on the real axis as a result of exciton-phonon

scattering to a continuum of final states. The imaginary part of the exciton-phonon Fan-Migdal self-energy describes the first Born approximation for the scattering between clamped-ion BSE exciton states driven by phonon emission and absorption [3, 211–214]:

$$\mathrm{Im}\Xi^{\mathrm{FMd,R}}_{S\mathbf{Q},S\mathbf{Q}}(\omega,T) = -\pi \sum_{S_1\mathbf{q}\nu\pm} |G_{SS_1\nu}(\mathbf{Q},\mathbf{q})|^2 \left(N_B(\omega_{\mathbf{q}\nu}) \pm \frac{1}{2} + \frac{1}{2}\right) \delta\left(\omega - \Omega_{S_1\mathbf{Q}+\mathbf{q}} \mp \omega_{\mathbf{q}\nu}\right) \ . \tag{5.7.0.9}$$

As can be seen, the self-energy is fully causal as $\mathrm{Im}\Xi^{\mathrm{FMd,R}}_{S\mathbf{Q},S\mathbf{Q}}(\omega,T) \leq 0$. The resulting pole condition for the exciton propagator is given by the expression

$$\mathrm{det}\mathbf{L}^{-1}(s,T) = \mathrm{det}\left(\mathbf{L}^{\mathrm{el},-1}(s,T) - \mathbf{\Xi}(s,T)\right) = 0 \ , \tag{5.7.0.10}$$

which gives rise to the frequency-dependent eigenvalue problem corresponding to the effective field theory of Eq. 5.7.0.1:

$$\sum_{S'\mathbf{Q}'} \left(\Omega_{S\mathbf{Q}}\delta_{SS'}\delta_{\mathbf{Q}\mathbf{Q}'} + \Xi_{S\mathbf{Q},S'\mathbf{Q}'}(\tilde{\Omega}_{\mathcal{S}},T)\right) \tilde{U}^{\mathcal{S}}_{S'\mathbf{Q}'}(T) = \tilde{\Omega}_{\mathcal{S}}\tilde{U}^{\mathcal{S}}_{S\mathbf{Q}}(T) \ . \tag{5.7.0.11}$$

In Chapter 6, we will provide a rigorous proof of the exact connection between the exciton-phonon Fan-Migdal self-energy and the Bethe-Salpter equation including electron-phonon interactions through the Dyson supermatrix formulation.

When I have fears that I may cease to be,
Before my pen has gleaned my teeming brain,
Before high-piled books, in charactery,
Hold like rich garners the full ripened grain;
When I behold, upon the night's starred face,
Huge cloudy symbols of a high romance,
And think that I may never live to trace
Their shadows with the magic hand of chance;
And when I feel, fair creature of an hour,
That I shall never look upon thee more,
Never have relish in the faery power
Of unreflecting love—then on the shore
Of the wide world I stand alone and think,
Till love and fame to nothingness do sink.

— John Keats

6 Dyson Supermatrix Formulation for Lattice Screening of Excitons at Finite Temperatures

This Chapter contains work that contributed to the publication of Refs [3, 6, 162]. At the time of writing, the main results of this Chapter are contained in Refs. [10] and [11] that are about to be submitted for review.

Contents

6.1 Introduction

The Green's function formalism has found applications across a wide range of disciplines, from high energy and nuclear physics to condensed matter physics and more recently to quantum chemistry [2, 4, 20, 36, 41, 57–59, 61, 134, 205, 211, 213, 215, 216]. Over the

past two decades, *ab initio* calculations of the properties of quasiparticles such as electrons, polarons, excitons and more, have proven to be a powerful means for understanding and predicting correlated spectroscopic phenomena in molecules and materials [57, 58, 169, 217–222]. In periodic solids, these state-of-the-art *ab initio* calculations typically involve solution of Eq. 2.6.0.3, with a self-energy approximated with low order perturbation theory [179, 180, 183–185, 208, 223–226]. The dynamical self-energy is commonly taken within a diagonal approximation and its frequency-dependence is often treated approximately. It is exceedingly rare that the entire spectrum of the quasiparticle equation is computed. However, understanding the dynamical properties of quasiparticles requires the full solution of Eq. 2.6.0.3, for example to determine transport properties and accurate scattering rates. Additionally, even obtaining an accurate ground state energy from the single-particle Green's function, from the Galitskii-Migdal formula [227], requires the accurate computation of all poles and residues of Eq. 2.6.0.3 [5, 132, 133]. Therefore, to extend the physical information accessible from the Green's function formalism, we must devise novel algorithms for the accurate solution of Eq. 2.6.0.3.

While conceptually and formally elegant, the explicit frequency-dependence of Eq. 2.6.0.3 results in significant numerical instabilities that are not easily and systematically controllable [61, 132–134]. In particular, it is highly non-trivial and challenging to find satellite solutions numerically [228]. Outside of the diagonal approximation, converging to all the different solutions to Eq. 2.6.0.3 requires careful initial starting guesses and iterative numerical algorithm design. This results in significant constraints on what properties can be computed. Furthermore, increasing the number of basis states that enter the dynamical interaction kernel, results in a substantial increase in the computational resources required to iteratively converge to all the different solutions.

In the context of nuclear theory and quantum chemistry, significant progress has been made to recast Eq. 2.6.0.3 in a form that is more amenable to numerical computation. This was initiated by the Algebraic Diagrammatic Construction method [41], whereby a systematic approach to including 'vertex' self-energy corrections to infinite-order was presented [5, 7, 36]. This formulation is centered around the reconstruction of Eq. 2.6.0.3 in terms of the frequency-independent Dyson supermatrix. The frequency-independent Dyson supermatrix allows for the computation of all solutions to Eq. 2.6.0.3 in a single

diagonalization. The trade-off is that the diagonalization of this matrix can become computationally prohibitive due to its size. In spite of this difficulty, several algorithmic advances have been made in order to make this formulation computationally feasible and scalable for finite systems of interacting particles at zero temperature [61, 107, 108, 131, 133, 134]. However, to the best of our knowledge, no form has been reported for extended periodic solids at finite temperatures.

While energy renormalizations, scattering rates and cross-sections are routinely computed from *ab initio* for a variety of physical mechanisms, they are typically computed within the first Born approximation [208, 221, 229–234]. Recently, there has been growing interest in computing self-consistent electron-phonon [235, 236] and exciton-phonon [6, 237] scattering rates in materials, demonstrating that for several systems, a self-consistent treatment is necessary. Self-consistent scattering rates include interactions beyond the first Born approximation. This is because a given perturbation is summed to infinite-order through iterative solution of the Lippmann-Schwinger equation within a given approximation for the self-energy.

In this work, we demonstrate how the Dyson supermatrix formalism can be extended to finite temperatures and applied to solid state systems. We construct Dyson supermatrices for electron-phonon and exciton-phonon interactions, thereby applying, for the first time, the Algebraic Diagrammatic Construction method [35, 41] to the electron-phonon interaction at finite temperatures. Our general formulation allows for the computation of energy renormalizations, scattering rates and spectral functions at finite temperatures in the thermodynamic limit. The temperature-dependent self-consistent scattering rate of a given state is simply extracted as the imaginary part of the corresponding eigenvalue of the Dyson supermatrix. While the focus of this Chapter is on the finite-temperature Dyson supermatrix formulation of the Bethe-Salpeter equation for exciton-phonon interactions within the Tamm-Dancoff approximation, our approach is general and can be applied to a any physical phenomena that are described by equations of a similar form to Eq. 2.6.0.3.

This Chapter is organized as follows. In Section 6.2, we discuss the frequency-dependent phonon screening contribution to the Bethe-Salpeter kernel and demonstrate how, within the Tamm-Dancoff approximation, it can be recast in terms of a frequency-independent Dyson supermatrix. In Section 6.3, we also provide the Dyson supermatrix construction

whereby the dynamical Fan-Migdal electron-phonon self-energy is also included within the TDA. In Section 6.4, we subsequently demonstrate the exact connection between the supermatrix formulation presented in Section 6.3 and the exciton-phonon Fan-Migdal self-energy derived in Chapter 5. In Section 6.5, we provide a detailed analysis between our approach to calculating scattering rates and common quasiparticle approximations employed in the literature. In Section 6.6, we outline the computational details of our implementation, providing an overview of the temperature-dependent block Lanczos algorithm that is particularly well suited for sparse, non-hermitian eigenvalue problems and critical for rendering these calculations computationally tractable. In Section 6.7, we apply our formalism to a three-dimensional model system to compute self-consistent exciton binding energies and dissociation rates resulting from the inclusion of the dynamical effects due to phonon screening. In Section 6.8, we then apply our formalism to compute, from first principles, non-perturbative temperature-dependent phonon-driven exciton dissociation rates and energy renormalizations for the heterogeneous semiconductors GaN, CdS and $BiVO_4$. Finally, in Section 6.9 we summarize our findings and provide outlook for future work.

6.2 Phonon screening Dyson supermatrix formulation

In this Section, we provide the Dyson supermatrix construction for the phonon screening contribution to the BSE kernel presented in Chapter 5 at zero and finite temperatures.

6.2.1 Zero temperature Dyson supermatrix formulation

In a recent series of papers [2, 3, 6, 205, 226], we have introduced the *ab initio* contribution of phonon screening to the BSE (see Eq. 5.4.0.5 of Chapter 5). At equilibrium and at zero temperature, this interaction kernel is given by [2, 6, 205]

$$K^{ph}_{vc\mathbf{k},v'c'\mathbf{k}'}(\omega) = -\sum_{\nu} g_{cc'\nu}(\mathbf{k}', \mathbf{k}-\mathbf{k}') g^{*}_{vv'\nu}(\mathbf{k}', \mathbf{k}-\mathbf{k}') \left[\frac{1}{\omega - \Delta_{c\mathbf{k},v'\mathbf{k}'} - \omega_{\mathbf{k}-\mathbf{k}'\nu} + i\eta} + \frac{1}{\omega - \Delta_{c'\mathbf{k}',v\mathbf{k}} - \omega_{\mathbf{k}-\mathbf{k}'\nu} + i\eta} \right], \tag{6.2.1.1}$$

The interaction kernel K^{ph} encodes the contribution of phonon screening of excitons via exchange of phonons between conduction and valence band electron and its imaginary

part gives a measure of the phonon-driven exciton dissociation rate [2, 3, 6]. The corresponding Feynman diagrams representing phonon exchange are given in Figure 5.4. At zero temperature, Eq. 6.2.1.1 only includes the phonon emission channel, whereby the scattering channel involves the emission of a phonon only. Including this frequency-dependent interaction kernel, $K^{ph}(\omega)$, in the BSE eigenvalue problem (Eq. 5.4.0.5), we arrive at the phonon-screened BSE eigenvalue problem [2, 6]

$$\sum_{v'c'\mathbf{k}'} \Big(H^{\mathrm{BSE}}_{vc\mathbf{k},v'c'\mathbf{k}'} + K^{ph}_{vc\mathbf{k},v'c'\mathbf{k}'}(\tilde{\Omega}_{\mathcal{S}}) \Big) \bar{A}^{\mathcal{S}}_{v'c'\mathbf{k}'} = \tilde{\Omega}_{\mathcal{S}} \bar{A}^{\mathcal{S}}_{vc\mathbf{k}}. \tag{6.2.1.2}$$

Eq. 6.2.1.2 is a frequency-dependent self-consistent eigenvalue problem that yields the renormalized exciton eigenvalues and 'Dyson orbitals' that include the effects of phonon screening on the electron-hole interaction. Typically, self-consistent eigenvalue problems of this form are solved by iterative diagonalization that targets each excited state until a convergence threshold is reached. This process yields the so-called quasiparticle solutions. Quasiparticle solutions are those that correspond to a large quasiparticle renormalization factor, $Z_{\mathcal{S}}$, and therefore have a large spectral weight. Satellite solutions are those that possess a much weaker spectral weight. While it is fairly straightforward to converge the eigenvalue problem of Eq. 6.2.1.2 to find the quasiparticle solutions, it is typically much more challenging to converge to the satellite solutions. As $K^{ph}(\omega)$ is a complex kernel consisting of real and imaginary parts, we have a distinct left eigenvalue equation:

$$\sum_{v'c'\mathbf{k}'} \tilde{A}^{\mathcal{S}}_{v'c'\mathbf{k}'} \Big(H^{\mathrm{BSE}}_{vc\mathbf{k},v'c'\mathbf{k}'} + K^{ph}_{vc\mathbf{k},v'c'\mathbf{k}'}(\tilde{\Omega}_{\mathcal{S}}) \Big) = \tilde{A}^{\mathcal{S}}_{vc\mathbf{k}} \tilde{\Omega}_{\mathcal{S}}. \tag{6.2.1.3}$$

The eigenvalues of Eqs 6.2.1.2 and 6.2.1.3 are complex with the real part corresponding to the energy of the exciton state including the effects of phonon screening and the imaginary part is proportional to the phonon-driven exciton dissociation rate [2, 3, 6].

Using the same approach outlined in Chapter 2, we can write Eq. 6.2.1.2 in terms of the zero temperature Dyson supermatrix

$$\mathbf{D}^{ph} = \begin{pmatrix} H^{\mathrm{BSE}}_{vc\mathbf{k},v'c'\mathbf{k}'} & M^{(I)}_{vc\mathbf{k},v'c'\mathbf{k}'\mathbf{k}''\nu} & M^{(II)}_{vc\mathbf{k},v'c'\mathbf{k}'\mathbf{k}''\nu} \\ \tilde{M}^{(I)}_{v'c'\mathbf{k}'\mathbf{k}''\nu,vc\mathbf{k}} & \Lambda^{(+)}_{vc\mathbf{k}\mathbf{k}'\nu,v'c'\mathbf{k}''\mathbf{k}'''\nu'} & \mathbf{0} \\ \tilde{M}^{(II)}_{v'c'\mathbf{k}'\mathbf{k}''\nu,vc\mathbf{k}} & \mathbf{0} & \Lambda^{(+)}_{vc\mathbf{k}\mathbf{k}'\nu,v'c'\mathbf{k}''\mathbf{k}'''\nu'} \end{pmatrix}, \tag{6.2.1.4}$$

where we define the coupling and interaction matrices as

$$M^{(I)}_{vc\mathbf{k},v''c''\mathbf{k}''\mathbf{k}'''\nu} = -g^*_{vv''\nu}(\mathbf{k}''', \mathbf{k} - \mathbf{k}''')\delta_{cc''}\delta_{\mathbf{k}\mathbf{k}''} \tag{6.2.1.5a}$$

$$\tilde{M}^{(I)}_{v''c''\mathbf{k}''\mathbf{k}'''\nu,v'c'\mathbf{k}'} = g_{c''c'\nu}(\mathbf{k}', \mathbf{k}'' - \mathbf{k}')\delta_{v''v'}\delta_{\mathbf{k}'''\mathbf{k}'} \tag{6.2.1.5b}$$

$$M^{(II)}_{vc\mathbf{k},v''c''\mathbf{k}''\mathbf{k}'''\nu} = -g_{cc''\nu}(\mathbf{k}'', \mathbf{k} - \mathbf{k}'')\delta_{vv''}\delta_{\mathbf{k}\mathbf{k}'''} \tag{6.2.1.5c}$$

$$\tilde{M}^{(II)}_{v''c''\mathbf{k}''\mathbf{k}'''\nu,v'c'\mathbf{k}'} = g^*_{v''v'\nu}(\mathbf{k}', \mathbf{k}''' - \mathbf{k}')\delta_{c''c'}\delta_{\mathbf{k}''\mathbf{k}'} \tag{6.2.1.5d}$$

$$\Lambda^{(+)}_{vc\mathbf{k}\mathbf{k}'\nu,v'c'\mathbf{k}''\mathbf{k}'''\nu'} = (\Delta_{c\mathbf{k},v\mathbf{k}'} + \omega_{\mathbf{k}-\mathbf{k}'\nu})\delta_{vv'}\delta_{cc'}\delta_{\mathbf{k}\mathbf{k}''}\delta_{\mathbf{k}'\mathbf{k}'''}\delta_{\nu\nu'}. \tag{6.2.1.5e}$$

The matrices $\mathbf{M}^{(I)/(II)}$ and $\tilde{\mathbf{M}}^{(I)/(II)}$ are referred to as coupling matrices while the matrix $\mathbf{\Lambda}^{(+)}$ is the interaction matrix. In comparison with Chapter 2 the Green's function index is now: $n\mathbf{k} \rightarrow vc\mathbf{k}$ and the composite ISC index becomes: $J \equiv vc\mathbf{k}\mathbf{k}'\nu$. In deriving the expressions for the coupling matrices in Eqs 6.2.1.5, we have used the property that $g_{mn\nu}(\mathbf{k}, \mathbf{k}' - \mathbf{k}) = g^*_{nm\nu}(\mathbf{k}', \mathbf{k} - \mathbf{k}')$. The supermatrix in Eq. 6.2.1.4 is the result of application of the Algebraic Diagrammatic Construction method for the polarization propagator [35, 36, 41, 133] using the phonon exchange diagrams of Figure 5.4.

The dimensions of the matrix $\mathbf{D}^{ph}$ are much larger than those of the original frequency-dependent self-consistent eigenvalue problem and the supereigenvectors of $\mathbf{D}^{ph}$ have the form

$$\mathbf{D}^{ph}\begin{pmatrix} \bar{A}^{\mathcal{S}}_{vc\mathbf{k}} \\ W^{\mathcal{S},+}_{vc\mathbf{k}\mathbf{k}'\nu} \\ W^{\mathcal{S},-}_{vc\mathbf{k}\mathbf{k}'\nu} \end{pmatrix} = \tilde{\Omega}_{\mathcal{S}}\begin{pmatrix} \bar{A}^{\mathcal{S}}_{vc\mathbf{k}} \\ W^{\mathcal{S},+}_{vc\mathbf{k}\mathbf{k}'\nu} \\ W^{\mathcal{S},-}_{vc\mathbf{k}\mathbf{k}'\nu} \end{pmatrix} . \tag{6.2.1.6}$$

Here, the first row of the supereigenvector, $\bar{A}^{\mathcal{S}}_{vc\mathbf{k}}$, is exactly the eigenvector of the dynamical BSE of Eq. 6.2.1.2. The second and third rows, $W^{\mathcal{S},+}_{vc\mathbf{k}\mathbf{k}'\nu}$ and $W^{\mathcal{S},-}_{vc\mathbf{k}\mathbf{k}'\nu}$, are related to multiparticle propagator residues which contain effects due to the combined electron-hole-pair-phonon (EHPP) propagation as outlined in Appendix D.2. As $\mathbf{D}^{ph}$ is non-hermitian, we denote the left super-eigenvector solution of Eq. 6.2.1.6 by $\begin{pmatrix} \tilde{\mathbf{A}}_{\mathcal{S}} & \tilde{\mathbf{W}}^{+}_{\mathcal{S}} & \tilde{\mathbf{W}}^{-}_{\mathcal{S}} \end{pmatrix}$. The biorthogonal normalization condition requires that the inner product of the left and right eigenvectors is equal to one. As stated in Chapter 5, the eigenvalue solutions of Eq. 6.2.1.6 occur in complex conjugate pairs due to the real coefficients of the characteristic polynomial that determines the eigenvalues.

Using the biorthogonal normalization condition, the inner product of the upper component of the super-eigenvectors gives the quasiparticle renormalization factor as [5, 7]

$$Z_{\mathcal{S}} = \sum_{vc\mathbf{k}} \tilde{A}^{\mathcal{S}}_{vc\mathbf{k}} \bar{A}^{\mathcal{S}}_{vc\mathbf{k}} = \left(1 - \frac{\partial K^{ph}_{\mathcal{S}\mathcal{S}}(\omega)}{\partial \omega}\bigg|_{\omega=\tilde{\Omega}_{\mathcal{S}}} \right)^{-1} . \tag{6.2.1.7}$$

Here, $K^{ph}_{\mathcal{S}\mathcal{S}}(\omega) = \sum_{\substack{vc\mathbf{k} \\ v'c'\mathbf{k}'}} \tilde{A}^{\mathcal{S}}_{vc\mathbf{k}} K^{ph}_{vc\mathbf{k},v'c'\mathbf{k}'}(\omega) \bar{A}^{\mathcal{S}}_{v'c'\mathbf{k}'}$ is the expression for the phonon screened kernel in the biorthogonal eigenbasis of Eq. 6.2.1.2. It is important to note that the quasiparticle renormalization factor defined in Eq. 6.2.1.7 is the exact renormalization factor corresponding to a given self-energy approximation and not obtained from a linearized equation. From the biorthogonal normalization condition, we have

$$1 = Z_{\mathcal{S}} + \sum_{vc\mathbf{k}\mathbf{k}'\nu} \left(\tilde{W}^{\mathcal{S},+}_{vc\mathbf{k}\mathbf{k}'\nu} W^{\mathcal{S},+}_{vc\mathbf{k}\mathbf{k}'\nu} + \tilde{W}^{\mathcal{S},-}_{vc\mathbf{k}\mathbf{k}'\nu} W^{\mathcal{S},-}_{vc\mathbf{k}\mathbf{k}'\nu} \right) . \tag{6.2.1.8}$$

6.2.2 Rotating to the 'clamped-ion' exciton basis

The eigenstates of the clamped-ion BSE (Eq. 5.4.0.5) formally constitute a complete set of states in the electron-hole pair subspace and can be used to rotate the phonon-screened BSE (Eq. 6.2.1.2) into the exciton basis to give

$$\sum_{S'} \left(\Omega_S \delta_{SS'} + K^{ph}_{SS'}(\tilde{\Omega}_{\mathcal{S}}) \right) \bar{U}^{\mathcal{S}}_{S'} = \tilde{\Omega}_{\mathcal{S}} \bar{U}^{\mathcal{S}}_{S} . \tag{6.2.2.1}$$

where the phonon-screening kernel has been rotated into the exciton basis via: $K^{ph}_{SS'}(\omega) = \sum_{\substack{vc\mathbf{k} \\ v'c'\mathbf{k}'}} A^{S*}_{vc\mathbf{k}} K^{ph}_{vc\mathbf{k},v'c'\mathbf{k}'}(\omega) A^{S'}_{v'c'\mathbf{k}'}$. The relationship between the eigenvectors of Eqs 6.2.1.6 and 6.2.2.1 can be used to express the right phonon screened exciton wavefunctions as $|\bar{\mathcal{S}}\rangle = \sum_{S'} \bar{U}^{\mathcal{S}}_{S'} |S'\rangle = \sum_{vc\mathbf{k}} \sum_{S'} \bar{U}^{\mathcal{S}}_{S'} A^{S'}_{vc\mathbf{k}} |vc\mathbf{k}\rangle$. This implies

$$\bar{A}^{\mathcal{S}}_{vc\mathbf{k}} = \sum_{S'} \bar{U}^{\mathcal{S}}_{S'} A^{S'}_{vc\mathbf{k}} . \tag{6.2.2.2}$$

The left eigenvector solutions of Eq. 6.2.2.1 are similarly related to the left eigenvectors of Eq. 6.2.1.2 as

$$\tilde{A}^{\mathcal{S}}_{vc\mathbf{k}} = \sum_{S'} A^{S'*}_{vc\mathbf{k}} \tilde{U}^{\mathcal{S}}_{S'} . \tag{6.2.2.3}$$

Using the clamped-ion BSE exciton basis, we can construct the Dyson supermatrix in the exciton basis by rotating the coupling matrices as

$$\begin{aligned} M^{(I)}_{S,v''c''\mathbf{k}''\mathbf{k}'''\nu} &= \sum_{v_1 c_1 \mathbf{k}_1} A^{S*}_{v_1 c_1 \mathbf{k}_1} M^{(I)}_{v_1 c_1 \mathbf{k}_1, v''c''\mathbf{k}''\mathbf{k}'''\nu} \\ &= -\sum_{v_1} A^{S*}_{v_1 c''\mathbf{k}''} g^{*}_{v_1 v''\nu}(\mathbf{k}''', \mathbf{k}'' - \mathbf{k}''') . \end{aligned} \tag{6.2.2.4}$$

We can perform the same procedure for the other coupling blocks (see Appendix D.1) and this leads to the following supermatrix structure

$$\mathbf{D}^{ph} = \begin{pmatrix} \Omega_S \delta_{SS'} & M^{(I)}_{S,J'} & M^{(II)}_{S,J'} \\ \tilde{M}^{(I)}_{J,S'} & \mathbf{\Lambda}^{(+)}_{JJ'} & \mathbf{0} \\ \tilde{M}^{(II)}_{J,S'} & \mathbf{0} & \mathbf{\Lambda}^{(+)}_{JJ'} \end{pmatrix} , \tag{6.2.2.5}$$

where we have re-introduced the composite index J for notational clarity. Formally, if the complete set of clamped-ion exciton states were included in the change-of-basis, the supermatrix defined in Eq. 6.2.2.5 yields the same eigenvalues as Eq. 6.2.1.4. However, the advantage of rotating to the exciton basis is that it can be used to reduce the dimensionality of the Dyson supermatrix. This is because, in practice, the number of exciton states computed, N_S, is typically much smaller than the total number of free electron-hole pair states, $N_c \times N_v \times N_{\mathbf{k}}$. Therefore, we can reduce the computational cost associated with the diagonalization of $\mathbf{D}^{ph}$ by rotation of the upper left block and coupling elements to the clamped-ion BSE basis. This simplification can be viewed as a physically motivated Singular Value Decomposition (SVD) of the coupling matrices, reducing the dimensionality of the coupling blocks of the supermatrix [216].

By rotating to the 'clamped-ion' exciton basis, the Lehmann representation of the phonon screened exciton Green's function can be obtained from the eigenvalues and super-eigenvectors of Eq 6.2.2.5 as

$$\begin{aligned} L^R_{SS'}(s) &= \left(s\mathbb{1} - \mathbf{D}^{ph}\right)^{-1}_{SS'} \\ &= \sum_{\mathcal{S}} \frac{\bar{U}^{\mathcal{S}}_S \tilde{U}^{\mathcal{S}}_{S'}}{s - \tilde{\Omega}_{\mathcal{S}}} \, . \end{aligned} \tag{6.2.2.6}$$

The exciton spectral function is obtained from the Lehmann representation of the exciton Green's function by using the relationship: $\mathcal{A}^{\text{ex}}(\omega) = -\frac{1}{\pi}\text{Im tr}L^{\text{R}}(\omega)$. This yields

$$\begin{aligned} \mathcal{A}^{\text{ex}}(\omega) &= -\frac{1}{\pi}\text{Im}\sum_{\mathcal{S}} \frac{Z_{\mathcal{S}}}{\omega - \tilde{\Omega}_{\mathcal{S}} + i\eta} \\ &= \frac{1}{\pi}\sum_{\mathcal{S}} \left(\frac{\text{Im}\tilde{\Omega}_{\mathcal{S}}\text{Re}Z_{\mathcal{S}}}{(\omega - \text{Re}\tilde{\Omega}_{\mathcal{S}})^2 + (\text{Im}\tilde{\Omega}_{\mathcal{S}})^2} - \frac{\text{Im}Z_{\mathcal{S}}(\omega - \text{Re}\tilde{\Omega}_{\mathcal{S}})}{(\omega - \text{Re}\tilde{\Omega}_{\mathcal{S}})^2 + (\text{Im}\tilde{\Omega}_{\mathcal{S}})^2} \right) \end{aligned} \tag{6.2.2.7}$$

where we have used the identity: $\sum_S \bar{U}^{\mathcal{S}}_S \tilde{U}^{\mathcal{S}}_S = Z_{\mathcal{S}}$, which can be obtained by substituting Eqs 6.2.2.2 and 6.2.2.3 into Eq. 6.2.1.7.

6.2.3 Finite temperature Dyson supermatrix formulation

At equilibrium and at finite temperature, the temperature-dependent phonon screening kernel in the clamped-ion BSE exciton basis is given by Eq. 5.4.1.7. At finite temperatures we see the emergence of the absorption channel as exciton-phonon scattering can now be due to phonon absorption as well as emission. The corresponding temperature- and frequency-dependent eigenvalue problem is written as

$$\sum_{S'} \Big(\Omega_S \delta_{SS'} + K^{ph}_{SS'}(\tilde{\Omega}_{\mathcal{S}}, T)\Big)\bar{U}^{\mathcal{S}}_{S'}(T) = \tilde{\Omega}_{\mathcal{S}}(T)\bar{U}^{\mathcal{S}}_{S}(T) \ . \tag{6.2.3.1}$$

It is important to note that, at finite temperatures, the eigenvalues and eigenvector solutions are explicitly temperature-dependent as the self-consistent eigenvalue problem must be solved separately at each temperature. We can directly write the finite-temperature frequency-independent Dyson supermatrix as

$$\mathbf{D}^{ph}(T) = \begin{pmatrix} \Omega_S \delta_{SS'} & M^{(I)}_{S,J'}(T) & M^{(II)}_{S,J'}(T) & N^{(I)}_{S,J'}(T) & N^{(II)}_{S,J'}(T) \\ \tilde{M}^{(I)}_{J,S'}(T) & \mathbf{\Lambda}^{(+)}_{JJ'} & \mathbf{0} & \mathbf{0} & \mathbf{0} \\ \tilde{M}^{(II)}_{J,S'}(T) & \mathbf{0} & \mathbf{\Lambda}^{(+)}_{JJ'} & \mathbf{0} & \mathbf{0} \\ \tilde{N}^{(I)}_{J,S'}(T) & \mathbf{0} & \mathbf{0} & \mathbf{\Lambda}^{(-)}_{JJ'} & \mathbf{0} \\ \tilde{N}^{(II)}_{J,S'}(T) & \mathbf{0} & \mathbf{0} & \mathbf{0} & \mathbf{\Lambda}^{(-)}_{JJ'} \end{pmatrix}, \tag{6.2.3.2}$$

where the temperature-dependent couplings and absoption interaction matrix are defined in Appendix D.4.

In principle we can obtain all quasiparticle and satellite energies at a given finite temperature from a single diagonalization of Eq. 6.2.3.2. The emergence of the absorption channel at finite temperatures results in a supermatrix that is almost twice as large as that required for the zero temperature case. However, in Section 6.6, we will show how we can exploit the sparse supermatrix structure of Eq. 6.2.3.2 by employing Krylov subspace expansions alongside the generalized Davidson algorithm to compute its spectrum. In the zero temperature limit, the Bose-Einstein occupation factors vanish and Eq. 6.2.3.2 reduces to Eq. 6.2.2.5. At higher temperatures, the $K^{ph}(\omega, T)$ interaction kernel displays an increase in the coupling to the electron-phonon interaction as demonstrated by the temperature-dependence of the coupling matrices. This is simply a consequence of the increase in the Bose-Einstein occupation factors as the temperature increases.

It must be emphasized again that the eigenvalues of Eqs 6.2.3.1 and 6.2.3.2 are formally identical. However, as demonstrated in Appendix D.2, in principle, the Dyson supermatrix representation gives access to more information, such as multiparticle correlation and spectral functions. Further, the frequency-independent supermatrix representation is numerically more stable. This is due to the complex structure of the self-energy, which can oscillate wildly in the vicinity of its poles, making it difficult to converge calculations to satellite solutions [133, 228]. Additionally, it is not even guaranteed that all solutions to Eq 6.2.3.1 will be found. In stark contrast, a single diagonalization of Eq. 6.2.3.2 yields all poles of the corresponding propagator.

We can directly compute the temperature-dependent phonon screened exciton Green's function

$$L^{R}_{SS'}(\omega, T) = \sum_{\mathcal{S}} \frac{\bar{U}^{\mathcal{S}}_{S}(T)\tilde{U}^{\mathcal{S}}_{S'}(T)}{\omega - \tilde{\Omega}_{\mathcal{S}}(T) + i\eta} \tag{6.2.3.3a}$$

and spectral function as

$$\mathcal{A}^{\mathrm{ex}}(\omega, T) = -\frac{1}{\pi}\mathrm{Im}\sum_{\mathcal{S}} \frac{Z_{\mathcal{S}}(T)}{\omega - \tilde{\Omega}_{\mathcal{S}}(T) + i\eta} \ , \tag{6.2.3.3b}$$

where we have indicated the implicit dependence on temperature that the eigenvalues and eigenvectors possess as a result of Eqs 6.2.3.1 and 6.2.3.2. Due to the fact that the two-particle interaction kernel, K^{ph}, is not fully causal the renormalization factors $Z_{\mathcal{S}}$ do not provide a true probability measure of the spectral weight of a given pole. However, the complex resonance eigenvalues that lie beneath the real axis still provide an accurate approximation to the energy renormalization and scattering rate of an exciton.

6.3 Inclusion of TDA self-energy contributions

We can also derive the Dyson supermatrix representation of the TDA kernel given by Eq. 5.4.2.4 of Chapter 5. This kernel includes the effects of electron-phonon scattering on the single-particle propagators themselves. The corresponding temperature-dependent Dyson supermatrix is

$$\mathbf{D}^{\mathrm{TDA}}_{ph}(T) = \begin{pmatrix} H^{\mathrm{BSE}}_{vc\mathbf{k},v'c'\mathbf{k}'} & V^{(+)}_{vc\mathbf{k},J'}(T) & V^{(-)}_{vc\mathbf{k},J'}(T) \\ V^{(+)*}_{v'c'\mathbf{k}',J}(T) & \mathbf{\Lambda}^{(+)}_{JJ'} & \mathbf{0} \\ V^{(-)*}_{v'c'\mathbf{k}',J}(T) & \mathbf{0} & \mathbf{\Lambda}^{(-)}_{JJ'} \end{pmatrix}, \tag{6.3.0.1}$$

where we have defined

$$V^{(+)}_{vc\mathbf{k},J}(T) = M^{(I)}_{vc\mathbf{k},J}(T) - M^{(II)}_{vc\mathbf{k},J}(T)$$
$$= \left(g_{cc''\nu}(\mathbf{k}'', \mathbf{k}-\mathbf{k}'')\delta_{vv''}\delta_{\mathbf{k}\mathbf{k}'''} - g^{*}_{vv''\nu}(\mathbf{k}''', \mathbf{k}-\mathbf{k}''')\delta_{cc''}\delta_{\mathbf{k}\mathbf{k}''}\right)\sqrt{N_B(\omega_{\mathbf{k}''-\mathbf{k}'''\nu})+1} \tag{6.3.0.2}$$

and

$$V^{(-)}_{vc\mathbf{k},J} = N^{(I)}_{vc\mathbf{k},J}(T) - N^{(II)}_{vc\mathbf{k},J}(T)$$
$$= \left(g_{cc''\nu}(\mathbf{k}'', \mathbf{k}-\mathbf{k}'')\delta_{vv''}\delta_{\mathbf{k}\mathbf{k}'''} - g^{*}_{vv''\nu}(\mathbf{k}''', \mathbf{k}-\mathbf{k}''')\delta_{cc''}\delta_{\mathbf{k}\mathbf{k}''}\right)\sqrt{N_B(\omega_{\mathbf{k}''-\mathbf{k}'''\nu})}\,, \tag{6.3.0.3}$$

where the composite index here is defined as $J \equiv v''c''\mathbf{k}''\mathbf{k}'''\nu$. It is important to note that the $\mathbf{D}^{\mathrm{TDA}}_{ph}(T)$ is of identical form to the exact finite temperature Dyson supermatrix formalism presented in Chapter 2. In contrast to the phonon screened Dyson supermatrix $\mathbf{D}^{ph}(T)$ of Eq. 6.2.3.2, the TDA supermatrix coupling matrices contain both the conduction and valence band electron-phonon coupling elements. Additionally, this supermatrix representation is hermitian as inclusion of the self-energy contributions to the single-particle propagators restores the causality of the kernel. However, as stated in Chapter 5, the self-energy correction included in the TDA kernel is specifically time-ordered and restricted to include only specific self-energy contributions. This can clearly be seen in Eq. 5.4.2.1 where only specific forward- and backward-time contributions to the Fan-Migdal electron-phonon self-energy are included. In the case of electron-electron interactions, the time restriction of the self-energy corrections has been observed to result in significant errors in the calculated excitation energies [61, 96]. This is because restriction of the time-orderings that enter a self-energy approximation can severely affect the energies of the single-particle states, resulting in less accurate neutral excitation energies. Therefore, despite the attractive hermitian and causal structure of Eq. 6.3.0.1, the missing reverse-time self-energy contributions can affect the accuracy of the calculated resonant states.

6.4 Connection to the Fan-Migdal exciton-phonon self-energy

To demonstrate the connection to the Fan-Migdal exciton-phonon self-energy presented in Section 5.7 of Chapter 5, we must first extend the $\mathbf{D}^{\mathrm{TDA}}_{ph}(T)$ supermatrix representation to account for finite momentum exciton states. Working in the $(\mathbf{k}+\mathbf{Q})$-convention, whereby

the conduction band wavevector is specified by the centre-of-mass exciton momentum wavevector $\mathbf{Q}$, we must extend the size of the coupling matrices as:

$$V^{(+)}_{vc\mathbf{k}'\mathbf{Q},v''c'''\mathbf{k}'''\mathbf{Q}'\mathbf{Q}_1\nu}(T) = \Big(g_{cc''\nu}(\mathbf{k}''' + \mathbf{Q}', \mathbf{k}' - \mathbf{k}''' + \mathbf{Q} - \mathbf{Q}')\delta_{vv''}\delta_{\mathbf{k}'\mathbf{k}'''} - g^*_{vv''\nu}(\mathbf{k}''', \mathbf{k}' - \mathbf{k}''')\delta_{cc''}\delta_{\mathbf{k}'+\mathbf{Q},\mathbf{k}'''+\mathbf{Q}'}\Big)\sqrt{N_B(\omega_{\mathbf{Q}'-\mathbf{Q}\nu}) + 1}\delta_{\mathbf{Q}\mathbf{Q}_1} \tag{6.4.0.1}$$

and

$$V^{(-)}_{vc\mathbf{k}'\mathbf{Q},v''c'''\mathbf{k}'''\mathbf{Q}'\mathbf{Q}_1\nu}(T) = \Big(g_{cc''\nu}(\mathbf{k}''' + \mathbf{Q}', \mathbf{k}' - \mathbf{k}''' + \mathbf{Q} - \mathbf{Q}')\delta_{vv''}\delta_{\mathbf{k}'\mathbf{k}'''} - g^*_{vv''\nu}(\mathbf{k}''', \mathbf{k}' - \mathbf{k}''')\delta_{cc''}\delta_{\mathbf{k}'+\mathbf{Q},\mathbf{k}'''+\mathbf{Q}'}\Big)\sqrt{N_B(\omega_{\mathbf{Q}'-\mathbf{Q}\nu})}\delta_{\mathbf{Q}\mathbf{Q}_1} \tag{6.4.0.2}$$

where $\mathbf{k} = \mathbf{k}' + \mathbf{Q}$ and $\mathbf{k}'' = \mathbf{k}''' + \mathbf{Q}'$ correspond to the momenta of the electron state. We see that the configuration space has increased in size due to the presence of the additional wavevector $\mathbf{Q}_1$. This is required in order to specify the additional exciton scattering accessible to finite momentum exciton states. The corresponding interaction matrices are also increased to account for the finite momentum scattering as

$$\mathbf{\Lambda}^{(+)}_{vc\mathbf{k}\mathbf{Q}\mathbf{Q}_1\nu,v'c'\mathbf{k}''\mathbf{Q}'\mathbf{Q}_2\nu'} = (\Delta_{c\mathbf{k}+\mathbf{Q},v\mathbf{k}} + \omega_{\mathbf{Q}-\mathbf{Q}_1\nu})\delta_{vv'}\delta_{cc'}\delta_{\nu\nu'}\delta_{\mathbf{k}\mathbf{k}''}\delta_{\mathbf{Q}\mathbf{Q}'}\delta_{\mathbf{Q}_1\mathbf{Q}_2}\ . \tag{6.4.0.3}$$

and

$$\mathbf{\Lambda}^{(-)}_{vc\mathbf{k}\mathbf{Q}\mathbf{Q}_1\nu,v'c'\mathbf{k}''\mathbf{Q}'\mathbf{Q}_2\nu'} = (\Delta_{c\mathbf{k}+\mathbf{Q},v\mathbf{k}} - \omega_{\mathbf{Q}-\mathbf{Q}_1\nu})\delta_{vv'}\delta_{cc'}\delta_{\nu\nu'}\delta_{\mathbf{k}\mathbf{k}''}\delta_{\mathbf{Q}\mathbf{Q}'}\delta_{\mathbf{Q}_1\mathbf{Q}_2}\ . \tag{6.4.0.4}$$

This gives rise to the finite momentum representation

$$\mathbf{D}^{\mathrm{TDA}}_{ph,\mathbf{Q}}(T) = \begin{pmatrix} H^{\mathrm{BSE}}_{vc\mathbf{k}\mathbf{Q},v'c'\mathbf{k}'\mathbf{Q}'} & V^{(+)}_{vc\mathbf{k}\mathbf{Q},P'}(T) & V^{(-)}_{vc\mathbf{k}\mathbf{Q},P'}(T) \\ V^{(+)*}_{v'c'\mathbf{k}'\mathbf{Q}',P}(T) & \mathbf{\Lambda}^{(+)}_{PP'} & \mathbf{0} \\ V^{(-)*}_{v'c'\mathbf{k}'\mathbf{Q}',P}(T) & \mathbf{0} & \mathbf{\Lambda}^{(-)}_{PP'} \end{pmatrix} \tag{6.4.0.5}$$

where we have introduced the finite momentum composite index: $P \equiv vc\mathbf{k}\mathbf{Q}\mathbf{Q}_1\nu$.

Now that we have introduced the finite momentum extension of Eq. 6.3.0.1 to yield the supermatrix of Eq. 6.4.0.5, we can demonstrate its exact connection to the Fan-Migdal exciton-phonon self-energy. To do so, we allow the intermediate scattered states to interact through the clamped-ion instantaneous electron-hole interaction to infinite-order by modification of the interaction matrices:

$$\mathbf{\Lambda}^{(\pm),eh}_{vc\mathbf{k}\mathbf{Q}\mathbf{Q}_1\nu,v'c'\mathbf{k}''\mathbf{Q}'\mathbf{Q}_2\nu'} = \mathbf{\Lambda}^{(\pm)}_{vc\mathbf{k}\mathbf{Q}\mathbf{Q}_1\nu,v'c'\mathbf{k}''\mathbf{Q}'\mathbf{Q}_2\nu'} + K^{eh,\infty}_{vc\mathbf{k}\mathbf{Q},v'c'\mathbf{k}''\mathbf{Q}}\delta_{\nu\nu'}\delta_{\mathbf{Q}_1\mathbf{Q}_2}\delta_{\mathbf{Q}\mathbf{Q}'}\ . \tag{6.4.0.6}$$

This modification means that the interaction matrices are no longer block diagonal. The resulting finite momentum supermatrix including the electron-hole interactions to infinite order in the intermediate scattering states is given by

$$\mathbf{D}^{\mathrm{TDA,eh}}_{ph,\mathbf{Q}}(T) = \begin{pmatrix} H^{\mathrm{BSE}}_{vc\mathbf{k}\mathbf{Q},v'c'\mathbf{k}'\mathbf{Q}'} & V^{(+)}_{vc\mathbf{k}\mathbf{Q},P'}(T) & V^{(-)}_{vc\mathbf{k}\mathbf{Q},P'}(T) \\ V^{(+)*}_{v'c'\mathbf{k}'\mathbf{Q}',P}(T) & \mathbf{\Lambda}^{(+),eh}_{PP'} & \mathbf{0} \\ V^{(-)*}_{v'c'\mathbf{k}'\mathbf{Q}',P}(T) & \mathbf{0} & \mathbf{\Lambda}^{(-),eh}_{PP'} \end{pmatrix} . \tag{6.4.0.7}$$

Now, we can show that the finite momentum supermatrix that includes the electron-hole interaction to infinite-order in the intermediate scattering states (Eq. 6.4.0.7) is exactly equivalent to the Fan-Migdal exciton-phonon self-energy.

We can rotate into the eigenbasis of the modified interaction matrices $\mathbf{\Lambda}^{(\pm),eh}$ by introduction of the exciton-phonon-pair product states: $|S\mathbf{Q}'\mathbf{Q}_1\nu\rangle$ with corresponding eigenvalues $\Omega_{S\mathbf{Q}'} + \omega_{\mathbf{Q}_1-\mathbf{Q}'}$. This rotation results in the formation of block diagonal interaction matrices

$$\mathbf{\Lambda}^{(\pm),eh}_{S\mathbf{Q}\mathbf{Q}_1\nu,S'\mathbf{Q}'\mathbf{Q}_2\nu'} = (\Omega_{S\mathbf{Q}'} \pm \omega_{\mathbf{Q}_1-\mathbf{Q}'})\delta_{SS'}\delta_{\mathbf{Q}\mathbf{Q}'}\delta_{\mathbf{Q}_1\mathbf{Q}_2}\delta_{\nu\nu'} . \tag{6.4.0.8}$$

With the introduction of the exciton-phonon-pair product states, we can express them with respect to the free electron-hole-pair phonon states as

$$|S\mathbf{Q}'\mathbf{Q}_1\nu\rangle = \sum_{vc\mathbf{k}'} A^{S\mathbf{Q}'}_{vc\mathbf{k}'} |vc\mathbf{k}'\mathbf{Q}'\mathbf{Q}_1\nu\rangle \tag{6.4.0.9}$$

Rotation into the eigenbasis of the interaction matrices requires us to rotate the coupling matrices into the same basis. We also know that the finite momentum exciton states form the eigenbasis of the upper left block of Eq. 6.4.0.7. Therefore, we can rotate the entire matrix into the eigenbasis of the BSE and the modified interaction matrices by corresponding rotation of the coupling matrices as:

$$M^{(+)}_{S\mathbf{Q},S'\mathbf{Q}'\mathbf{Q}_1\nu}(T) = \sum_{\substack{vc\mathbf{k}' \\ v''c''\mathbf{k}'''}} A^{S\mathbf{Q}*}_{vc\mathbf{k}'} V^{(+)}_{vc\mathbf{k}'\mathbf{Q},v''c''\mathbf{k}'''\mathbf{Q}'\mathbf{Q}_1\nu}(T) A^{S'\mathbf{Q}'}_{v''c''\mathbf{k}''} , \tag{6.4.0.10}$$

and likewise for the $M^{(-)}_{S\mathbf{Q},S'\mathbf{Q}'\mathbf{Q}_1\nu}(T)$ block. Therefore, rotation of the coupling matrices

exactly yields the composite exciton-phonon scattering matrix as

$$\begin{aligned}
&\sum_{\substack{vc\mathbf{k}'\\ v''c''\mathbf{k}'''}} A^{S\mathbf{Q}*}_{vc\mathbf{k}'} V^{(+)}_{vc\mathbf{k}'\mathbf{Q},v''c''\mathbf{k}'''\mathbf{Q}'\mathbf{Q}_1\nu}(T) A^{S'\mathbf{Q}'}_{v''c''\mathbf{k}''} \\
&= \left(\sum_{vcc''\mathbf{k}'} A^{S\mathbf{Q}'+\mathbf{q}*}_{vc\mathbf{k}'} g_{cc''\nu}(\mathbf{k}'+\mathbf{Q}',\mathbf{q}) A^{S'\mathbf{Q}'}_{vc''\mathbf{k}'} - \sum_{vcv''\mathbf{k}'} A^{S\mathbf{Q}'+\mathbf{q}*}_{vc\mathbf{k}'} g_{v''v\nu}(\mathbf{k}',\mathbf{q}) A^{S'\mathbf{Q}'}_{v''c\mathbf{k}+\mathbf{q}} \right) \\
&\sqrt{N_B(\omega_{\mathbf{Q}'-\mathbf{Q}\nu})+1}\delta_{\mathbf{Q}\mathbf{Q}_1} \\
&= G_{SS'\nu}(\mathbf{Q}',\mathbf{Q}-\mathbf{Q}')\sqrt{N_B(\omega_{\mathbf{Q}'-\mathbf{Q}\nu})+1}\delta_{\mathbf{Q}\mathbf{Q}_1} \ ,
\end{aligned} \tag{6.4.0.11}$$

where we have used Eq. 5.7.0.2 to indentify the exciton-phonon composite scattering matrix. The result for the $M^{(-)}_{S\mathbf{Q},S'\mathbf{Q}'\mathbf{Q}_1\nu}(T)$ block can be obtained by the analogous rotation. Therefore, the rotated supermatrix becomes

$$\mathbf{D}^{\mathrm{TDA,eh}}_{ph,\mathbf{Q}}(T) = \begin{pmatrix} H^{\mathrm{BSE}}_{S\mathbf{Q},S'\mathbf{Q}'} & M^{(+)}_{S\mathbf{Q},\lambda'}(T) & M^{(-)}_{S\mathbf{Q},\lambda'}(T) \\ M^{(+)*}_{S'\mathbf{Q}',\lambda}(T) & \mathbf{\Lambda}^{(+),eh}_{\lambda\lambda'} & \mathbf{0} \\ M^{(-)*}_{S'\mathbf{Q}',\lambda}(T) & \mathbf{0} & \mathbf{\Lambda}^{(-),eh}_{\lambda\lambda'} \end{pmatrix} \ , \tag{6.4.0.12}$$

where we have introduced the exciton-phonon-pair composite index as $\lambda \equiv S\mathbf{Q}\mathbf{Q}_1\nu$. Downfolding this matrix into the exciton subspace, we have

$$\begin{aligned}
\hat{H}^{\mathrm{TDA,eh}}_{ph,\mathbf{Q}}(s,T) &= H^{\mathrm{BSE}}_{S\mathbf{Q},S'\mathbf{Q}'} + \sum_{\pm\lambda\lambda'} M^{(\pm)}_{S\mathbf{Q},\lambda}(T) \left(s\mathbb{1} - \mathbf{\Lambda}^{(\pm),eh} \right)^{-1}_{\lambda\lambda'} M^{(\pm)*}_{S'\mathbf{Q}',\lambda}(T) \\
&= \Omega_{S\mathbf{Q}}\delta_{S\mathbf{Q},S'\mathbf{Q}'} + \Xi^{\mathrm{FMd}}_{S\mathbf{Q},S'\mathbf{Q}'}(s,T) \ .
\end{aligned} \tag{6.4.0.13}$$

Therefore, we have demonstrated that the supermatrices of Eqs 6.4.0.7 and 6.4.0.12 are exactly equivalent to the exciton-phonon Fan-Migdal self-energy formulation. Clearly this supermatrix describes scattering between excitons driven by the electron-phonon interaction. However, directly from the considerations of the previous subsection, despite the fact that this supermatrix now includes the electron-hole interaction to infinite-order in the scattering, it does not include the complete time-orderings of the underlying *electron-phonon* Fan-Migdal self-energy for the single-particle states. Therefore, this approximation is also expected to suffer from the same reasons identified in the previous subsection. This, coupled with the severe computational scaling involved in the computation of finite-momentum exciton states means that we will we focus our subsequent numerical analysis on the phonon screened Dyson supermatrix, $\mathbf{D}^{ph}(T)$.

An interesting direction for future work would be to provide a complete study of the exciton-phonon kernel that is not constrained within the TDA. This would involve the introduction of terms that fully account for time-orderings of the self-energy of the

underlying single-particle Green's functions. As identified in Section 5.6 of Chapter 5, a first step towards this would be the inclusion of the static term rotated into the exciton basis: $K^{\mathrm{FM},\infty}_{S\mathbf{Q},S'\mathbf{Q}'} = \sum_{vc\mathbf{k}} A^{S\mathbf{Q}*}_{vc\mathbf{k}} K^{\mathrm{FM},\infty}_{vc\mathbf{k}\mathbf{Q},v'c'\mathbf{k}'\mathbf{Q}'} A^{S'\mathbf{Q}'}_{v'c'\mathbf{k}'}$ to give:

$$\mathbf{D}^{\mathrm{ADC,eh}}_{ph,\mathbf{Q}}(T) = \begin{pmatrix} H^{\mathrm{BSE}}_{S\mathbf{Q},S'\mathbf{Q}'} + K^{\mathrm{FM},\infty}_{S\mathbf{Q},S'\mathbf{Q}'} & M^{(+)}_{S\mathbf{Q},\lambda'}(T) & M^{(-)}_{S\mathbf{Q},\lambda'}(T) \\ M^{(+)*}_{S'\mathbf{Q}',\lambda}(T) & \mathbf{\Lambda}^{(+),eh}_{\lambda\lambda'} & \mathbf{0} \\ M^{(-)*}_{S'\mathbf{Q}',\lambda}(T) & \mathbf{0} & \mathbf{\Lambda}^{(-),eh}_{\lambda\lambda'} \end{pmatrix} . \tag{6.4.0.14}$$

Exploration and numerical analysis of this approximation is beyond the scope of this thesis and is reserved for future work.

6.5 Phonon-driven exciton dissociation rates

As demonstrated in Chapter 5, the imaginary part of the eigenvalues of $\mathbf{D}^{ph}(T)$ are related to the self-consistent temperature-dependent phonon-driven exciton dissociation rate to infinitely long-lived electron-hole pairs:

$$\gamma^{\mathrm{sc}}_{\mathcal{S}}(T) = 2|\mathrm{Im}\tilde{\Omega}_{\mathcal{S}}(T)| \, . \tag{6.5.0.1}$$

Clearly, in the frequency-dependent representation (Eq. 6.2.3.1), this relationship gives rise to a self-consistent equation for the imaginary part. However, as the eigenvalues of $\mathbf{D}^{ph}(T)$ are identical to those obtained from the self-consistent frequency-dependent equation, we can compute the scattering rate simply by taking the imaginary part of the computed eigenvalue. Eq. 6.5.0.1 is a correlated dissociation rate that goes beyond the first Born approximation as it is obtained by diagonalization of the BSE including the phonon-exchange interaction. Therefore, the scattering rate can be viewed as containing contributions to infinite-order through exact solution of the Lippmann-Schwinger equation within this self-energy approximation [3]. The lifetime of the given state is simply given by the reciprocal of the scattering rate as: $\tau_{\mathcal{S}} = \gamma^{-1}_{\mathcal{S}}$. The corresponding first Born approximation for this scattering rate was derived in Chapter 5 and is given by: $\gamma^{\mathrm{xeh}}_{S}(T) = 2|\mathrm{Im}K^{ph,R}_{SS}(\Omega_S,T)|$ [2, 3].

Eq. 6.5.0.1 represents the formally exact relationship between scattering rates and solutions of the Dyson equation. It is approximate once the corresponding self-energy approximation is given. It is important to demonstrate exactly how our supermatrix

approach differs from approximations that separate the real and imaginary parts of the self-energy when solving the Dyson equation. The exact solution of the Dyson equation consists of real and imaginary parts, $\tilde{\Omega}_{\mathcal{S}} = \mathrm{Re}\tilde{\Omega}_{\mathcal{S}} + i\mathrm{Im}\tilde{\Omega}_{\mathcal{S}}$. Focusing on the phonon-screening contribution to the BSE, we can write the quasiparticle equation as

$$\left[(\mathrm{Re}\tilde{\Omega}_{\mathcal{S}} + i\mathrm{Im}\tilde{\Omega}_{\mathcal{S}})\mathbb{1} - \hat{H}_{\mathrm{BSE}} - \hat{K}^{ph}(\mathrm{Re}\tilde{\Omega}_{\mathcal{S}} + i\mathrm{Im}\tilde{\Omega}_{\mathcal{S}})\right]|\Psi_{\mathcal{S}}\rangle = 0, \tag{6.5.0.2}$$

where we have not chosen a specific basis representation. By assuming that $\mathrm{Re}\tilde{\Omega}_{\mathcal{S}} \gg \mathrm{Im}\tilde{\Omega}_{\mathcal{S}}$, we can perform a Taylor expansion of the phonon screening kernel about the real part of the eigenvalue, $\hat{K}^{ph}(\tilde{\Omega}_{\mathcal{S}}) \approx \hat{K}^{ph}(\mathrm{Re}\tilde{\Omega}_{\mathcal{S}}) + i\mathrm{Im}\tilde{\Omega}_{\mathcal{S}}\frac{\partial}{\partial\omega}\Big|_{\omega=\mathrm{Re}\tilde{\Omega}_{\mathcal{S}}}\hat{K}^{ph}(\omega)$. Using this expansion and the fact that the kernel evaluated at the real part also has a non-zero imaginary part contribution [3], we can write the approximate expression

$$\begin{aligned}&\left[\bar{\Omega}_{\mathcal{S}}\mathbb{1} - \hat{H}_{\mathrm{BSE}} - \mathrm{Re}\hat{K}^{ph}(\bar{\Omega}_{\mathcal{S}})\right]|\Psi_{\mathcal{S}}\rangle \\ &+ i\left[\mathrm{Im}\tilde{\Omega}_{\mathcal{S}}\left(\mathbb{1} - \frac{\partial\mathrm{Re}\hat{K}^{ph}(\omega)}{\partial\omega}\Big|_{\omega=\bar{\Omega}_{\mathcal{S}}}\right) - \mathrm{Im}\hat{K}^{ph}(\bar{\Omega}_{\mathcal{S}})\right]|\Psi_{\mathcal{S}}\rangle \approx 0\ .\end{aligned} \tag{6.5.0.3}$$

Here we have neglected the contribution arising from $\mathrm{Im}\tilde{\Omega}_{\mathcal{S}}\frac{\partial}{\partial\omega}\Big|_{\omega=\mathrm{Re}\tilde{\Omega}_{\mathcal{S}}}\mathrm{Im}\hat{K}^{ph}(\omega)$ to the real part of Eq. 6.5.0.3 and re-defined the real-part of the eigenvalue as $\bar{\Omega}_{\mathcal{S}} = \mathrm{Re}\tilde{\Omega}_{\mathcal{S}}$. By making the further approximation that the quasiparticle solutions are eigenstates of the real-part of Eq. 6.5.0.3, we arrive at the following approximate decomposition of the quasiparticle equation:

$$\left[\bar{\Omega}_{\mathcal{S}}\mathbb{1} - \hat{H}_{\mathrm{BSE}} - \mathrm{Re}\hat{K}^{ph}(\bar{\Omega}_{\mathcal{S}})\right]|\Psi_{\mathcal{S}}\rangle \approx 0 \tag{6.5.0.4a}$$

$$\left[\mathrm{Im}\tilde{\Omega}_{\mathcal{S}}\left(\mathbb{1} - \frac{\partial\mathrm{Re}\hat{K}^{ph}(\omega)}{\partial\omega}\Big|_{\omega=\bar{\Omega}_{\mathcal{S}}}\right) - \mathrm{Im}\hat{K}^{ph}(\bar{\Omega}_{\mathcal{S}})\right]|\Psi_{\mathcal{S}}\rangle \approx 0 \tag{6.5.0.4b}$$

In matrix notation, reinserting the temperature-dependence of all quantities, we can write these two-equations in the clamped-ion exciton basis as

$$\sum_{S'}\Big(\Omega_S\delta_{SS'} + \mathrm{Re}K^{ph}_{SS'}(\bar{\Omega}_{\mathcal{S}}, T)\Big)U^{\mathcal{S}}_{S'}(T) = \bar{\Omega}_{\mathcal{S}}(T)U^{\mathcal{S}}_{S}(T) \tag{6.5.0.5a}$$

with

$$|\mathrm{Im}\tilde{\Omega}_{\mathcal{S}}(T)| \approx \left|Z^*_{\mathcal{S}}\left(\sum_{SS'}U^{\mathcal{S}*}_{S}(T)\mathrm{Im}K^{ph}_{SS'}(\bar{\Omega}_{\mathcal{S}}, T)U^{\mathcal{S}}_{S}(T)\right)\right|, \tag{6.5.0.5b}$$

where the approximate quasiparticle renormalization factor is given by

$$Z^*_{\mathcal{S}} = \left(1 - \frac{\partial\mathrm{Re}K^{ph}_{\mathcal{S}\mathcal{S}}(\omega, T)}{\partial\omega}\Big|_{\omega=\bar{\Omega}_{\mathcal{S}}}\right)^{-1}. \tag{6.5.0.6}$$

Here, $K^{ph}_{\mathcal{SS}}(\omega,T) = \sum_{SS'} U^{\mathcal{S}*}_{S} K^{ph}_{SS'}(\omega,T) U^{\mathcal{S}}_{S}$ is the expression for the phonon screening kernel in the eigenbasis of Eq. 6.5.0.5a. It should be noted that Eq. 6.5.0.6 is an approximation to the full renormalization factor defined in Eq. 6.2.1.7. Therefore, from the exact relationship given in Eq. 6.5.0.1, we can write the approximate phonon-driven exciton dissociation rate as

$$\gamma^{\mathrm{sc}}_{\mathcal{S}}(T) \approx 2\left| Z^{*}_{\mathcal{S}} \left(\sum_{SS'} U^{\mathcal{S}*}_{S}(T) \mathrm{Im} K^{ph}_{SS'}(\bar{\Omega}_{\mathcal{S}},T) U^{\mathcal{S}}_{S}(T) \right) \right| . \tag{6.5.0.7}$$

Notably, this approximate expression is only valid in the limit where $\mathrm{Re}\tilde{\Omega}_S \gg \mathrm{Im}\tilde{\Omega}_S$, meaning that the resulting excitations are assumed to be long-lived. Furthermore, due to the computational complexity of the frequency-dependent representation, it is common that Eqs 6.5.0.5 are taken within a diagonal approximation: $\mathrm{Re}K^{ph}_{SS'}(\bar{\Omega}_{\mathcal{S}},T) \approx \delta_{SS'}\mathrm{Re}K^{ph}_{SS}(\bar{\Omega}_{\mathcal{S}},T)$, and that the approximate renormalization factor, $Z^{*}_{\mathcal{S}}$ is neglected entirely. Our analysis clearly demonstrates that obtaining solutions to the quasiparticle equation by direct computation of the eigenvalues of the Dyson supermatrix is conceptually simpler, removing the need to introduce fundamental assumptions about the potential character of the solutions. This is in contrast to the approach given in Eqs 6.5.0.5 and the further subsequent approximations commonly resulting from the frequency-dependent formulation.

6.6 Krylov Subspaces and Block Lanczos Algorithm

The large size of the Dyson supermatrices derived in Eqs 6.2.2.5 and 6.2.3.2 is the direct consequence of the large configuration spaces spanned by the $\mathbf{\Lambda}^{(+)}$ and $\mathbf{\Lambda}^{(-)}$ matrices. In general, both the $\mathbf{\Lambda}^{(+)}$ and $\mathbf{\Lambda}^{(-)}$ interaction matrices are of size $N_c N_v N^2_{\mathbf{k}} N_\nu \times N_c N_v N^2_{\mathbf{k}} N_\nu$. This means that they are typically of the order of $10^7 \times 10^7$ for real materials, resulting in the total Dyson supermatrix size of $10^8 \times 10^8$ [11]. However, the $\mathbf{\Lambda}^{(+)}$, $\mathbf{\Lambda}^{(-)}$ and $\mathbf{D}^{ph}$ matrices are significantly sparse. Despite their sparse structure, full diagonalization of the non-hermitian Dyson supermatrix is currently computationally unfeasible. In order to circumvent these numerical difficulties, we extend the approach outlined in Refs [133] and [131] to construct $\mathbf{D}^{ph}(T)$ using a Krylov subspace expansion. In addition, in Appendix D.5, we also provide an overview of the generalized Davidson algorithm which can be used to explicitly diagonalize the full $\mathbf{D}^{ph}(T)$ supermatrix about a given set of target eigenvalues.

To systematically control the growth of the configuration space of the interaction matrices, $\mathbf{\Lambda}^{(+)}$ and $\mathbf{\Lambda}^{(-)}$, we need to find an efficient dense representation of their sparse structure (see Eqs D.4.0.1e and D.3.0.1f). As the $\mathbf{\Lambda}^{(+)}$ and $\mathbf{\Lambda}^{(-)}$ are both hermitian, the most efficient way to do this is to construct an orthonormal basis for these matrices within their respective Krylov subspaces by utilizing the block Lanczos algorithm [94, 131, 133, 238–241]. If $\mathbf{\Lambda}^{(+)}$ and $\mathbf{\Lambda}^{(-)}$ were both non-hermitian, we could simply extend the algorithm by constructing a biorthogonal basis of the Krylov subspace.

A Krylov subspace of order n of $\mathbf{\Lambda}^{(+)}$ is given by the successive application of the first $(n-1)$ powers of the matrix into some starting vector $\mathbf{v}_0$:

$$\mathcal{K}_n(\mathbf{\Lambda}^{(+)};\mathbf{v}_0) \equiv \text{span}\{\mathbf{v}_0, \mathbf{\Lambda}^{(+)}\mathbf{v}_0, (\mathbf{\Lambda}^{(+)})^2\mathbf{v}_0, \cdots, (\mathbf{\Lambda}^{(+)})^{n-1}\mathbf{v}_0\} \ . \tag{6.6.0.1}$$

To construct the orthonormal basis $\{\mathbf{q}_i; i = 1, 2, \cdots n\}$ corresponding to $\mathcal{K}_n(\mathbf{\Lambda}^{(+)};\mathbf{v}_0)$ we employ the block Lanczos method. We fix the initial starting vector $\mathbf{v}_0$, and orthogonalize the rest of Krylov basis as follows:

$$\begin{aligned} \mathbf{q}_1 &\equiv \mathbf{v}_0 \\ \mathbf{\Lambda}^{(+)}\mathbf{q}_1 &= \lambda_{11}\mathbf{q}_1 + \lambda_{21}\mathbf{q}_2 \\ &\vdots \\ \mathbf{\Lambda}^{(+)}\mathbf{q}_{n-1} &= \lambda_{1(n-1)}\mathbf{q}_1 + \cdots + \lambda_{n(n-1)}\mathbf{q}_n \ . \end{aligned} \tag{6.6.0.2}$$

It is straightforward to show that this expansion leads to the tridiagonal hermitian structure:

$$\mathbf{q}_i^\dagger \mathbf{\Lambda}^{(+)}\mathbf{q}_j = \lambda_{ij} = (\lambda_{ji})^* \ , \tag{6.6.0.3}$$

with $\lambda_{ij} = 0$ for $|i-j| > 2$. By collecting the Lanczos basis vectors into a matrix, $\mathcal{L}_1$, we can define the Krylov subspace resolution of the identity as

$$\mathbb{1}_{\mathcal{L}} = \mathcal{L}_1\mathcal{L}_1^\dagger \ . \tag{6.6.0.4}$$

Using the Lanczos basis, we can project the full $\mathbf{\Lambda}^{(+)}$ matrix onto the Krylov subspace by

$$\tilde{\mathbf{\Lambda}}_n^{(+)} = \mathcal{L}_1^\dagger \mathbf{\Lambda}^{(+)}\mathcal{L}_1 \ . \tag{6.6.0.5}$$

The resulting matrix, $\tilde{\mathbf{\Lambda}}_n^{(+)}$, is a tridiagonal and hermitian matrix of much smaller dimension. We can also perform a separate block Lanczos procedure for the $\mathbf{\Lambda}^{(-)}$ interaction block to give an analogous tridiagonal hermitian projected matrix

$$\tilde{\mathbf{\Lambda}}_n^{(-)} = \mathcal{L}_2^\dagger \mathbf{\Lambda}^{(-)}\mathcal{L}_2 \ . \tag{6.6.0.6}$$

Combining both block Lanczos procedures, we can project the full Dyson supermatrix into the Krylov subspace by introducing the projector

$$\mathbf{S}(T) = \begin{pmatrix} \mathbb{1} & \mathbf{0} & \mathbf{0} & \mathbf{0} & \mathbf{0} \\ \mathbf{0} & \mathcal{L}_1 & \mathbf{0} & \mathbf{0} & \mathbf{0} \\ \mathbf{0} & \mathbf{0} & \mathcal{L}_1 & \mathbf{0} & \mathbf{0} \\ \mathbf{0} & \mathbf{0} & \mathbf{0} & \mathcal{L}_2 & \mathbf{0} \\ \mathbf{0} & \mathbf{0} & \mathbf{0} & \mathbf{0} & \mathcal{L}_2 \end{pmatrix} \tag{6.6.0.7}$$

which gives rise to the Lanczos-basis Dyson supermatrix representation

$$\begin{aligned} \mathbf{D}^{ph}_{\mathcal{L}_n}(T) &= \mathbf{S}^{\dagger}(T)\mathbf{D}^{ph}(T)\mathbf{S}(T) \\ &= \begin{pmatrix} \mathbf{H}_{\mathrm{BSE}} & \mathbf{M}^{(I)}\mathcal{L}_1 & \mathbf{M}^{(II)}\mathcal{L}_1 & \mathbf{N}^{(I)}\mathcal{L}_2 & \mathbf{N}^{(II)}\mathcal{L}_2 \\ \mathcal{L}_1^{\dagger}\tilde{\mathbf{M}}^{(I)} & \tilde{\mathbf{\Lambda}}_n^{(+)} & \mathbf{0} & \mathbf{0} & \mathbf{0} \\ \mathcal{L}_1^{\dagger}\tilde{\mathbf{M}}^{(II)} & \mathbf{0} & \tilde{\mathbf{\Lambda}}_n^{(+)} & \mathbf{0} & \mathbf{0} \\ \mathcal{L}_2^{\dagger}\tilde{\mathbf{N}}^{(I)} & \mathbf{0} & \mathbf{0} & \tilde{\mathbf{\Lambda}}_n^{(-)} & \mathbf{0} \\ \mathcal{L}_2^{\dagger}\tilde{\mathbf{N}}^{(II)} & \mathbf{0} & \mathbf{0} & \mathbf{0} & \tilde{\mathbf{\Lambda}}_n^{(-)} \end{pmatrix}. \end{aligned} \tag{6.6.0.8}$$

The Lanczos-basis Dyson supermatrix in Eq. 6.6.0.8 is much smaller than the original $\mathbf{D}^{ph}(T)$ supermatrix. As a result, one can view the Lanczos construction as a very effective data compression of the original sparse matrices. Crucially, as the dimension of the Krylov subspace is increased to the dimensionality of the full $\mathbf{\Lambda}^{(+)}$ and $\mathbf{\Lambda}^{(-)}$ matrices, the Krylov subspace will span the same space as the initial lower interaction block of the initial supermatrix, $\mathbf{D}^{ph}(T)$. Therefore, the 'exact' untruncated basis result will be obtained from the Lanczos method by increasing the basis set size. The Lanczos algorithm clearly generates a set of mutually orthonormal basis vectors that span the full original space [131, 133]. However, the numerical precision on computers can reduce the efficiency of the method as the orthogonality can only be obtained to within machine precision. Therefore, as the number of iterations increases, the Lanczos basis vectors will lose orthogonality and the subspace construction can result in the production of eigenvalues that have already been converged [131–133]. However, such instability issues that occur at each iteration can be overcome by the use of either a complete or a selective reorthonormalization of the Lanczos basis vectors among themselves [242].

Downfolding the Lanczos subspace representation into the electron-hole subspace gives

rise to the subspace phonon screening interaction kernel

$$\begin{aligned}\mathbf{K}^{ph}_{\mathcal{L}_n}(\omega,T) = &\mathbf{M}^{(I)}\mathcal{L}_1\Big(\omega\mathbb{1}-\tilde{\mathbf{\Lambda}}^{(+)}_n\Big)^{-1}\mathcal{L}_1^\dagger\tilde{\mathbf{M}}^{(I)}\\ &+\mathbf{M}^{(II)}\mathcal{L}_1\Big(\omega\mathbb{1}-\tilde{\mathbf{\Lambda}}^{(+)}_n\Big)^{-1}\mathcal{L}_1^\dagger\tilde{\mathbf{M}}^{(II)}\\ &+\mathbf{N}^{(I)}\mathcal{L}_2\Big(\omega\mathbb{1}-\tilde{\mathbf{\Lambda}}^{(-)}_n\Big)^{-1}\mathcal{L}_2^\dagger\tilde{\mathbf{N}}^{(I)}\\ &+\mathbf{N}^{(II)}\mathcal{L}_2\Big(\omega\mathbb{1}-\tilde{\mathbf{\Lambda}}^{(-)}_n\Big)^{-1}\mathcal{L}_2^\dagger\tilde{\mathbf{N}}^{(II)}\ .\end{aligned} \tag{6.6.0.9}$$

Once constructed, the reduced size of the $\mathbf{D}^{ph}_{\mathcal{L}_n}$ supermatrix means that it can be fully diagonalized within the Lanczos subspace. If the initial vector $\mathbf{v}_0$ is provides a good starting point for the algorithm, the resulting spectrum of $\mathbf{D}^{ph}_{\mathcal{L}_n}$ provides an excellent approximation to the full, untruncated $\mathbf{D}^{ph}$ supermatrix. In practice, as demonstrated in Section 6.7, only a few hundred Lanczos vectors are required in order to faithfully reproduce the overall spectral features of the full untruncated supermatrix.

In order that only a few hundred Lanczos vectors are required to provide an accurate representation of the full supermatrix means that the initial starting vector, $\mathbf{v}_0$, needs to capture the relevant degrees of freedom that couple the upper left $\mathbf{H}_{\text{BSE}}$ matrix to the EHPP states responsible for the phonon screening. By initializing the starting vector as the result of the coupling of the EHPP states due to the wings of the supermatrix, we choose the initial vector to be the vector

$$\mathbf{v}_0 = \begin{pmatrix} \tilde{\mathbf{M}}^{(I)}(T) & \tilde{\mathbf{M}}^{(II)}(T) \end{pmatrix}\ , \tag{6.6.0.10}$$

in which each block component is a matrix of dimension $(N_cN_vN_\nu(N_{\mathbf{k}})^2, N_S)$. As a result, block application of $\mathbf{\Lambda}^{(+)}$ on this initial vector provides an extremely effective representation for the Krylov subspace. In particular, as the matrices $\mathbf{\Lambda}^{(+)}$, $\tilde{\mathbf{M}}^{(I)}(T)$ and $\tilde{\mathbf{M}}^{(II)}(T)$ are sparse, the construction of the Lanczos subspace is efficient and only a few hundred Lanczos vectors are required to construct an accurate subspace representation of the full supermatrix. The number of Lanczos vectors employed is denoted by N_L.

In this work, as we are dealing with a temperature-dependent supermatrix eigenvalue problem, we extend the Lanczos approach to construct the Lanczos subspaces at each given temperature. This is required as the coupling blocks are now temperature-dependent (see Appendix D.4) meaning that the coupling between the exciton and EHPP subspaces can be significantly modified at different temperatures.

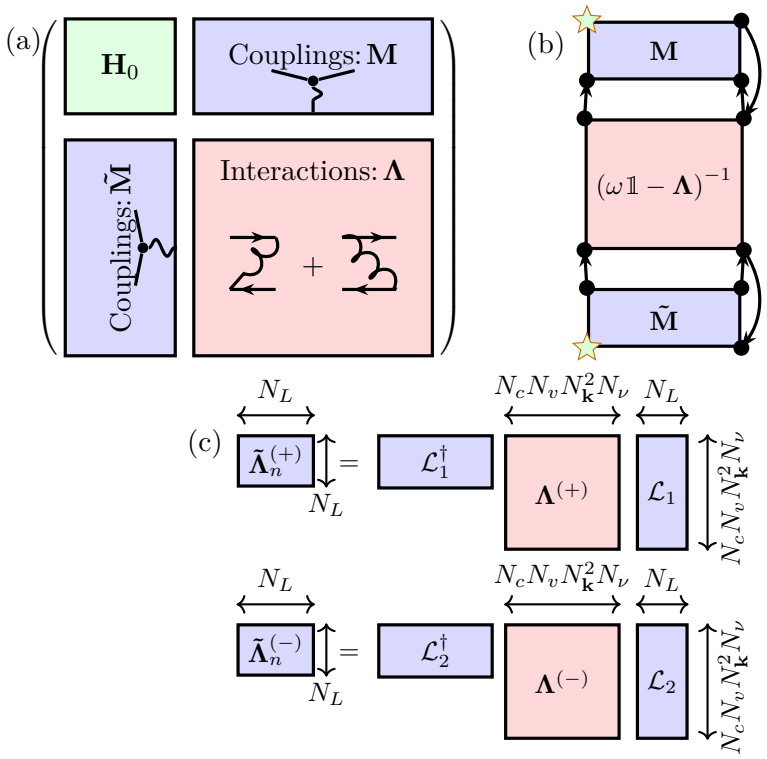

Figure 6.1: (a) Schematic of the Dyson supermatrix representation. Here we indicate the specific phonon exchange diagrams (K^{ph}) considered in this work. (b) Schematic of the dynamical self-energy of the Dyson supermatrix. The green stars indicate how the coupling matrices connect to the subspace of $\mathbf{H}_0$ and the arrows indicate how the coupling and interaction matrices are contracted together. (c) Lanczos projections of $\mathbf{\Lambda}^{(\pm)}$ into the Krylov subspace of dimension N_L.

To summarize, in principle, a target eigenvalue solution of the full Dyson supermatrix will agree with the same target solution of the self-consistent frequency-dependent eigenvalue problem. The Lanczos projected solution will display systematically improvable agreement with the same target eigenvalue as the number of Lanczos vectors approaches the full dimensionality of the space. Finally, the generalized Davidson target solution will also display systematically improvable agreement as the preconditioned subspace grows. In the calculations that follow, we use these internal consistency checks to ensure that our results are accurate and fully converged.

6.7 Application to a model system

In the Wannier-Mott limit, excitons in many three-dimensional polar semi-conductors can be accurately modelled within the hydrogenic exciton approximation [2, 3, 205, 243]. Un-

der these approximations, the two-band electronic clamped-ion BSE Hamiltonian becomes

$$H^{\text{BSE}}_{\mathbf{k},\mathbf{k}'} = \left(E_g + \frac{|\mathbf{k}|^2}{2\mu}\right)\delta_{\mathbf{k}\mathbf{k}'} - \frac{4\pi}{NV\epsilon_\infty}\frac{1}{|\mathbf{k}-\mathbf{k}'|^2} \ . \tag{6.7.0.1}$$

Here, V is the unit cell volume and N is the number of unit cells in the Born-von-Kàrman supercell. This hydrogenic model Hamiltonian can be solved analytically, and the lowest energy (1s) state has the following closed-form expression for the exciton coefficients:

$$A_{\mathbf{k}} = \frac{(2a_0)^{\frac{3}{2}}}{\sqrt{NV\pi}} \cdot \frac{1}{(1+a_0^2|\mathbf{k}|^2)^2} \ , \tag{6.7.0.2}$$

where $a_0 = \sqrt{\frac{1}{2E_B\mu}}$ is the exciton Bohr radius, $E_B^S = E_g - \Omega_S$, the exciton binding energy (in this case for the 1s state) and $\mu = \frac{m_e m_h}{m_e+m_h}$, the exciton reduced mass.

In three-dimensional polar semiconductor systems, the dominant electron-phonon coupling mechanism is given by the Fröhlich interaction. The Fröhlich interaction is a result of the coupling between the polar longitudinal optical (LO) phonon mode and electronic charge density [244]. In reciprocal space, the Fröhlich electron-phonon coupling element is given by [2, 3, 205, 244]

$$g^F_{\mathbf{q}} = \frac{i}{|\mathbf{q}|}\sqrt{\frac{2\pi\omega_{LO}}{NV}\left(\frac{1}{\epsilon_\infty} - \frac{1}{\epsilon_0}\right)} \ , \tag{6.7.0.3}$$

where $\epsilon_{\infty/0}$ are the high/low frequency dielectric constants and ω_{LO} is the frequency of the dispersionless LO phonon responsible for the Fröhlich interaction. Using these approximations, which we refer to as the Wannier-Mott-Fröhlich model, the corresponding phonon-screened upfolded Dyson supermatrix coupling and interaction matrices in the exciton basis are defined in Appendix D.1. The finite temperature model supermatrix is simply given by substituting the model expressions for the exciton coefficients and Fröhlich interaction into the expressions for the coupling and interaction matrices given in Appendix D.4. The Bose-Einstein occupation factors for the model are found by the replacement $N_B(\omega_{\mathbf{k}'''-\mathbf{k}''\nu}) \rightarrow N_B(\omega_{LO})$.

The resulting eigenvalue problem for the model at finite temperatures is given by

$$\mathbf{D}^{ph}(T)\mathbf{V}_{\mathcal{S}}(T) = -\tilde{\Omega}^{\mathcal{S}}_B(T)\mathbf{V}_{\mathcal{S}}(T) \ , \tag{6.7.0.4}$$

where $\tilde{\Omega}^{\mathcal{S}}_B(T) = E_g - \tilde{\Omega}_{\mathcal{S}}(T)$ is the temperature-dependent renormalized exciton energy relative to the band gap and $\mathbf{V}_{\mathcal{S}}(T)$ is the supereigenvector solution. Here, we have subtracted the energy of the band gap to give the exciton binding energy, E_B^S. The real

part of the eigenvalue corresponds to the renormalized exciton binding energy, $\mathrm{Re}\tilde{\Omega}_B^{\mathcal{S}}(T) = \tilde{E}_B^{\mathcal{S}}(T)$. The imaginary part corresponds to the self-consistent phonon-driven exciton dissociation rate: $\gamma_{\mathcal{S}}(T) = 2|\mathrm{Im}\tilde{\Omega}_B^{\mathcal{S}}(T)|$.

It is important to understand the sparse structure of the coupling and interaction matrix elements of the Wannier-Mott-Fröhlich model $\mathbf{D}^{ph}$ supermatrix. The interaction matrices are trivially sparse as they are simply diagonal matrices. However, the coupling blocks for the model are also sparse. To see this, the 1s coupling block is given by

$$\begin{aligned} M^{(I)}_{1s,\mathbf{k}''\mathbf{k}'''} &= -A^{*}_{\mathbf{k}''} g^{F*}_{\mathbf{k}''-\mathbf{k}'''} \\ &= \frac{C}{(1+a_0^2|\mathbf{k}''|^2)^2|\mathbf{k}''-\mathbf{k}'''|} \ , \end{aligned} \tag{6.7.0.5}$$

where $C = \frac{i(2a_0)^{\frac{3}{2}}}{NV\pi} \cdot \sqrt{2\pi\omega_{LO}\left(\frac{1}{\epsilon_\infty} - \frac{1}{\epsilon_0}\right)}$ is the constant of prefactors. From this expression, we see that as the distance between the $\mathbf{k}$-blocks of $M^{(I)}_{1s,\mathbf{k}''\mathbf{k}'''}$ (given by $|\mathbf{k}''-\mathbf{k}'''|$) increases, the coupling elements decay sharply to zero. This behaviour is analogous for the rest of the coupling matrix elements and also present in *ab initio* coupling matrix elements. Therefore, the model Dyson supermatrix possesses an extremely sparse structure that is particularly amenable to both the Lanczos and generalized Davidson algorithms.

The first-order 'single-shot' perturbative correction to Eq. 6.7.0.4 is obtained from Rayleigh-Schrödinger (RS) perturbation theory: $\tilde{\Omega}_S(T) = \Omega_S + \mathrm{Re}K^{ph}_{SS}(\Omega_S, T)$ [2, 205]. The imaginary part, $\mathrm{Im}K^{ph}_{SS}(\Omega_S, T)$, is directly proportional to the first Born approximation for the phonon-driven exciton dissociation rate [3]. In subsection 6.7.1, we will present a comparison of the 'single-shot' RS approach with the solutions obtained from diagonalization of the Dyson supermatrix $\mathbf{D}^{ph}$, to demonstrate the qualitative differences between these approaches.

We choose to apply our method to study CdS, which is a system that is known to be accurately modeled within the Wannier-Mott and Fröhlich approximations [2]. As such, we use parameters calculated in Ref. [2]: $E_B = 39$ meV, $\omega_{LO} = 34$ meV, $\varepsilon_\infty = 6.2$, $\varepsilon_0 = 10.4$, $m_e = 0.12$ and $m_h = 2.01$. We also employ the patched sampling technique developed in Ref. [245], which is necessary to efficiently converge the exciton binding energy with a minimal number of $\mathbf{k}$-points. We employ Γ-centered patches, with a cutoff coordinate of 0.05 (in crystal coordinates), drawn from a fine grid of $100 \times 100 \times 100$ $\mathbf{k}$-points [2]. This corresponds to a patch containing 1331 $\mathbf{k}$-points, which we find to

be more than sufficient to converge our model calculations. Finally, the model exciton subspace consists of the 1s and 2s solutions.

$(N_{\mathbf{k}})^2$	$\dim(\mathbf{D}^{ph})$	$\dim(\mathbf{D}^{ph}(T))$	$\dim(\mathbf{D}^{ph}_{\mathcal{K}_n}(T))$
1,771,561	3,543,124	7,086,246	802

Table 6.1: Dimensions of the model Dyson supermatrices.

In Table D.1, we depict the dimensionality of the model phonon screened zero- and finite-temperature Dyson supermatrices as well as the finite temperature Krylov subspace representation formed from $N_L = 200$ basis vectors. Both the zero and finite temperature Dyson supermatrices are enormous and can only be diagonalized using the generalized Davidson algorithm (see Appendix D.5). However, the Lanczos representation of the Dyson supermatrix can be fully diagonalized using conventional diagonalization routines and its resulting spectrum can be obtained to high accuracy. At zero temperature, we find that $N_L = 400$ Lanczos basis vectors are enough to converge the supermatrix eigenvalue results to within numerical precision of the result obtained from the full exact diagonalization. However, at finite temperatures, using only $N_L = 200$ basis vectors, we find the lowest state to be fully converged to within 0.01 meV. This is shown in Table 6.2, where we display the 1s eigenvalue obtained from the exact diagonalization and Lanczos subspace projection at 200K.

T = 200K	Exact	Lanczos
$\mathrm{Re}\tilde{\Omega}^{\mathcal{S}}_B$ (meV)	-24.89	-24.89
$\mathrm{Im}\tilde{\Omega}^{\mathcal{S}}_B$ (meV)	-2.25	-2.24

Table 6.2: Eigenvalue of the 1s state at 200K obtained from the exact diagonalization and Lanczos projection ($N_L = 200$), respectively.

6.7.1 Results and discussion

In Figure 6.2, we plot a comparison of the change in the exciton binding energy and the dissociation rate for the 1s state obtained from the single-shot Rayleigh-Schrödinger perturbation theory with the Dyson supermatrix solution as a function of temperature.

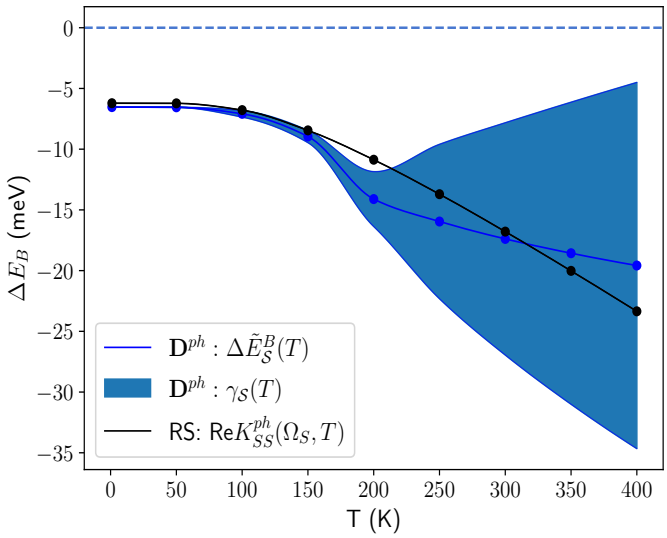

Figure 6.2: Change in the exciton binding energy of the lowest state and the scattering rate obtained from the $\mathbf{D}^{ph}(T)$ and RS solutions as a function of temperature.

The change in the exciton binding energy is simply given by: $\Delta E_B = \Omega_S - \tilde{E}^{\mathcal{S}}_B$. Therefore, the change in the binding energy provides a simple measure of how the effects of phonon screening can modify the energy of a given state. A negative value of the change in the exciton binding energy means that the contribution of phonon screening pushes the energy of the phonon-screened exciton state closer to the conduction band continuum.

At low temperatures, the energy change of the RS and supermatrix solutions for the 1s state are very close in energy, giving a binding energy change of around 6.5 meV at zero temperature. However, the energy change as a function of the temperature for the supermatrix solution is more complex as its temperature dependence is not simply governed by the Bose occupation factor of the LO phonon. This can be seen by working in the frequency-dependent representation. In the Wannier-Mott-Fröhlich model, the phonon screening kernel contains denominator contributions of the form

$$E_B + \Delta E_B + \frac{|\mathbf{k}|^2}{2m_e} + \frac{|\mathbf{k}'|^2}{2m_h} - \omega_{LO} \tag{6.7.1.1a}$$

and

$$E_B + \Delta E_B + \frac{|\mathbf{k}|^2}{2m_e} + \frac{|\mathbf{k}'|^2}{2m_h} + \omega_{LO} \ , \tag{6.7.1.1b}$$

for the emission an absorption channels, respectively. It should be noted that there are other contributions to Eqs 6.7.1.1 where $\mathbf{k} \leftrightarrow \mathbf{k}'$. The 'single-shot' RS solution also contains these contributions but the self-consistent dependence on ΔE_B is removed. However, the

supermatrix solution is equivalent to the self-consistent solution (as demonstrated in Section 6.2) and therefore, at each temperature, Eqs 6.7.1.1 vary depending on the value obtained for ΔE_B. Furthermore, from Eq. 6.7.0.5, we expect that the energy renormalization will be largest when the corresponding $|\mathbf{k}-\mathbf{k}'|$ vector in Eqs 6.7.1.1 is small. This means that contributions to the energy renormalization will be largest when the difference between the renormalized binding energy and the LO phonon frequency ω_{LO} is small.

At low temperatures, we see a slightly larger decrease in the binding energy change for the supermatrix solution as the difference between the LO phonon frequency and the renormalized energy is smaller than that for the RS solution. This results in larger contributions from the decrease in $|\mathbf{k}-\mathbf{k}'|$ that is connected to the coupling matrices. However, as the temperature increases, the slope of the supermatrix solution decreases. This occurs because, as the binding energy change increases, contributions from Eq. 6.7.1.1a can become negative. This results in terms that can act to slightly offset the effects of Eq. 6.7.1.1b, which remain positive. Further, the large binding energy renormalization change also acts self-consistently to reduce the strength of the effective Fröhlich couplings to the exciton state for both the emission and absorption channels through Eq. 6.7.0.5. In contrast, the RS solution shows a constant gradient change as a result of the fixed energy differences that enter the K^{ph} kernel with the constant increase of the LO occupation factor. Therefore, at high temperatures, the constant energy differences present in the RS approach, combined with the increase in the LO occupation factors, means that the RS solution begins to display a larger binding energy renormalization.

In the Wannier-Mott model, the exciton is formed from parabolic conduction and valence bands corresponding to a system with a direct band gap. Therefore, as the energy renormalization of the exciton increases, this can become large enough to resolve the crossing equation:

$$E_B + \Delta E_B + \frac{|\mathbf{k}|^2}{2m_e} + \frac{|\mathbf{k}'|^2}{2m_h} - \omega_{LO} = 0 \ . \tag{6.7.1.2}$$

For our model system, this can only be achieved if the renormalized exciton state that has a binding energy lower than ω_{LO}. This condition, coupled with the large Bose-Einstein factor for the LO phonon, results in a substantial phonon-driven exciton dissociation rate obtained from the supermatrix solution. This is displayed by the large shaded region in Figure 6.2. In contrast, within the 1st Born approximation, the corresponding crossing equation is given

by: $E_B + \frac{|\mathbf{k}|^2}{2m_e} + \frac{|\mathbf{k}'|^2}{2m_h} - \omega_{LO} = 0$. For the parameters of CdS can never be satisfied as the bare exciton binding energy (39 meV) is always larger than the LO phonon frequency (34 meV). Therefore, the corresponding phonon-driven dissociation within this approximation is zero at all temperatures. This is demonstrated by the fact that there is no black shaded region under the RS solution in Figure 6.2. The increase in the dissociation rate obtained from the supermatrix solution as a function of temperature is a result of the combination of the crossing equation (Eq. 6.7.1.2) being satisfied along with the large LO occupation factor.

6.8 Results for heterogeneous semiconductors

In this section, we compute the temperature dependence of the exciton binding energy and exciton dissociation rate for three different semiconductors, GaN, CdS and $BiVO_4$. To obtain accurate *ab initio* results for these materials, we first carefully converge the clamped ion, electron-screened exciton binding energies by employing the patched non-uniform Brillouin zone sampling technique [6, 245]. This is necessary to converge exciton states while using only a few thousand **k**-points in the vicinity of the lowest direct optical transition [245]. We use Wannier interpolation techniques to obtain gauge consistent electron-phonon matrix elements and clamped-ion *GW*-BSE eigenvectors within the aforementioned patch [2, 6]. For CdS and GaN, we include the first set of degenerate exciton states, whereas for $BiVO_4$ we include the lowest lying state only. These approximations are discussed and justified in Refs [2] and [6], as well as in Appendix D.6, where we provide further computational details. The full $\mathbf{D}^{ph}$ supermatrix sizes are over 300 million for GaN and CdS, and over 400 million for $BiVO_4$ before the Lanczos basis projection. In Figures 6.3 and 6.4, we plot the the exciton binding energy and the dissociation rate of the lowest excited state obtained by diagonalization of the Krylov subspace representations as a function of temperature for GaN, CdS and $BiVO_4$.

At zero temperature for GaN, we obtain a renormalization energy of -15 meV, consistent with prior work [2]. In Figure 6.3a, we see that both renormalization energies of the RS and supermatrix solutions are not strongly temperature-dependent displaying a variation of approximately 3 meV across 300K. This can be directly related to the large difference (22 meV) between the LO phonon frequency and exciton binding energy [2, 3]. However, we

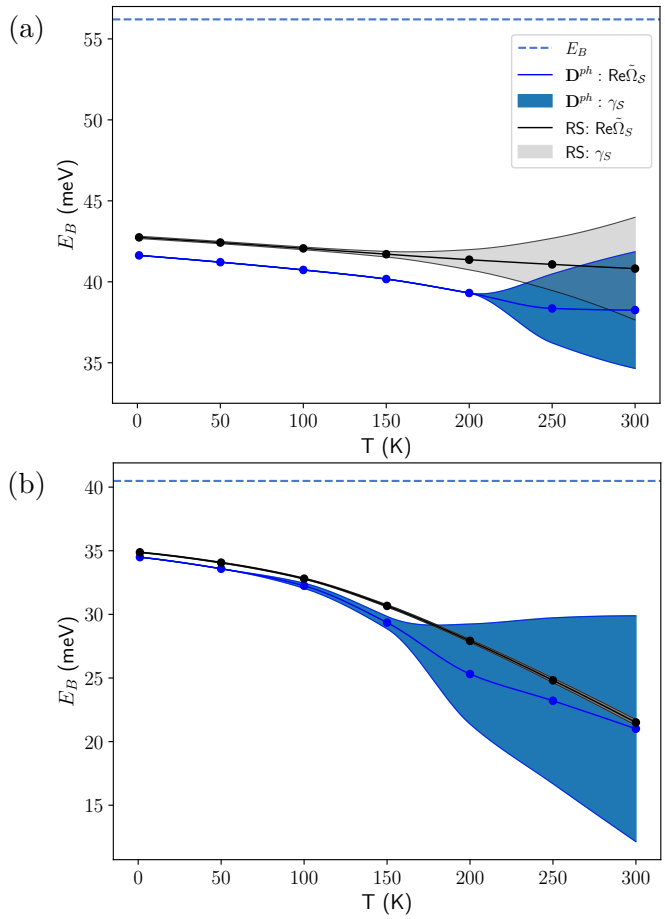

Figure 6.3: Binding energy renormalization and dissociation rates obtained from the $\mathbf{D}^{ph}$ (blue) and RS solutions (black) for (a) GaN and (b) CdS.

see a decrease in the binding energy that is more pronounced for the supermatrix solution due to its self-consistency. In addition, we also plot the phonon-driven exciton dissociation rate obtained from the first Born approximation (using a broadening of 1 meV) and the imaginary part of the supermatrix eigenvalue. At lower temperatures, the calculated dissociation rate from the full diagonalization of $\mathbf{D}^{ph}(T)$ is lower than that obtained within the first Born approximation. This is because the LO phonon frequency of GaN is already much larger than the exciton binding energy, and this difference increases with temperature, decreasing the scattering rate. Furthermore, in GaN, the lower frequency phonon modes do not contribute substantially to the screening [2, 3]. At 300K, we obtain an ultrafast dissociation lifetime of 91 femtoseconds (fs) GaN.

For CdS, at zero temperature both the supermatrix and RS energy solutions are similar, giving a renormalization energy of the exciton state of -6 meV. However, as shown in Figure 6.3b, the temperature variation of both the RS and supermatrix results is about 15 meV and much larger than that observed for GaN. This is due to the relevant coupling

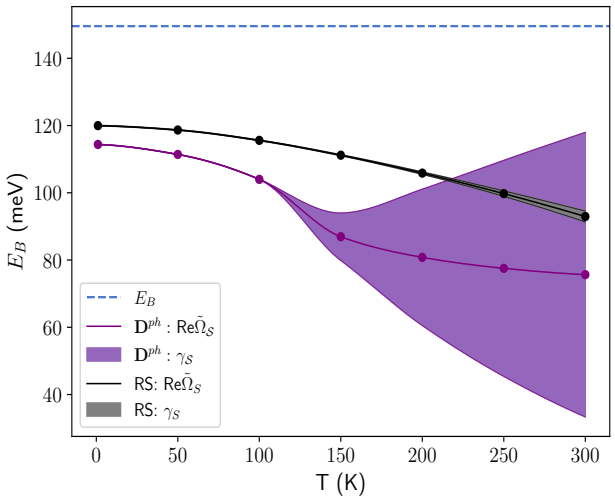

Figure 6.4: Binding energy renormalization and dissociation rates obtained from the $\mathbf{D}^{ph}$ (purple) and RS solutions (black) for $BiVO_4$.

strengths as well as energy differences given in Eq. 5.4.1.7. The LO phonon frequency and exciton binding energy of CdS are both small and similar in magnitude [2, 10]. This, coupled with the contribution of acoustic modes for the pierzoelectric material CdS, results in the substantial temperature dependence of the energy renormalization [2].

As the electron-phonon coupling is more significant in CdS, the supermatrix solution displays a more complicated temperature dependence. At higher temperatures, the substantial energy renormalizations can result in modifying the overall sign of the emission channel of the K^{ph} interaction kernel (Eq. 5.4.1.7) [10]. At temperatures higher than 100K, we also see the emergence of a strongly temperature dependent exciton dissociation rate for the supermatrix solution, contrasting with the zero scattering rate obtained within the first Born approximation [2, 3, 10]. The finite dissociative scattering rate obtained for CdS demonstrates the importance of our non-perturbative approach, since it gives qualitatively different results from the first Born approximation. At 300K, we obtain an ultrafast dissociation lifetime of 37 fs for CdS.

In Figure 6.4, we plot the results obtained for monoclinic $BiVO_4$. Clearly, we see that the effects of phonon screening on the excitons for $BiVO_4$ is significant, displaying a variation of approximately 50 meV across the temperature range. We note that this range is slightly lower than the variation range reported in Ref. [6]; we assign the slight discrepancy to the fact that partial self-consistency was used in Ref. [6]. Even at zero temperature, we obtain a binding energy change of -30 meV and -35 meV for the RS and

supermatrix solutions, respectively. This is directly the result of the significant electron-phonon coupling to 15 zone-center polar phonons and is discussed at length in Ref. [6]. We additionally find a significant temperature-dependence of the supermatrix solution as it is not simply determined by the phonon occupation factors. For the supermatrix solution, we find a substantial temperature dependence of the scattering rate, resulting in ultrafast exciton dissociation at temperatures above 100K. Similar to the exciton binding energy, we find slightly reduced scattering rates compared to Ref. [6]. This is in stark contrast to the RS results, which display a much weaker temperature dependence and a very small dissociation rate. We obtain an ultrafast phonon-driven exciton dissociation lifetime of 8 fs for $BiVO_4$ at 300K.

6.9 Conclusions

In summary, we have presented an *ab initio* approach to the frequency- and temperature-dependent quasiparticle equation for extended, periodic solids by introduction of the temperature-dependent Dyson supermatrix. We have implemented our formalism by including the phonon screening contribution within the *ab initio* BSE for real systems, demonstrating the general applicability of our method to compute fully converged non-perturbative and temperature-dependent scattering rates and energy renormalizations. With our novel approach, based on the block Lanczos algorithm, we are able to diagonalize the Dyson supermatrix while full diagonalization is highly unfeasible on any current supercomputer. The connections between our formalism and the Algebraic Diagrammatic Construction method [5, 7, 35, 36, 41] allow for an alternative theoretical and computational formulation of 'vertex corrections' and self-consistency in the context of temperature dependent electron- and exciton-phonon interactions present in periodic solids. This will provide the subject of future work that builds on the formalism presented here, hopefully leading to novel theoretical approaches for the computation of nonpertubative quasiparticle interactions and scattering rates at finite temperatures in extended periodic systems, nuclear matter and molecular systems.

7
Conclusions

In summary, this thesis presented a series of fundamental theoretical contributions to the unification and development of quantum field theory methods in many-particle physics.

In Part I, we focused on the electronic structure problem and interactions between many-fermion systems. In Chapter 2, we presented the general Green's function formalism for quantum systems governed by hermitian interactions. We presented a unified formulation centered around the Keldysh contour in order to describe systems both in and out-of-equilibrium. In this Chapter, we provided a detailed analysis on the formally exact analytic properties of the single-particle Green's function and self-energy to ensure the semi-definite property of the spectral function and causality of the theory. This naturally lead us to introduce the unified Dyson supermatrix formulation, valid for systems at zero and finite temperatures. We concluded this chapter with a detailed analysis of the two-particle Green's function and Bethe-Salpeter equation for neutral excitations. Here, we also provided an in-depth derivation and discussion outlining the differences between the Bethe-Salpeter and Dyson equations, a detail often overlooked in the literature.

In Chapter 3, we extended the hermitian theory presented in Chapter 2 to account for systems governed by an N-body non-hermitian Hamiltonian. We subsequently focused our analysis on the coupled-cluster similarity transformed Hamiltonian in order to provide a complete unification of the Green's function formalism with coupled-cluster theory. This was also inspired by the need to combine and transfer theoretical approaches between quantum chemistry, nuclear and condensed matter theory. Our analysis presented a detailed

analysis of the role that time-dependence plays in non-hermitian quantum theory, which is highly non-trivial. This was necessary not only to generate consistent non-hermitian pictures of quantum mechanics, but also in order to extend the Gell-Mann and Low theorem which is crucial for generating a diagrammatically consistent and formally exact theory. We expect that the generality of the formalism presented will also be useful in the study of other non-hermitian many-body Hamiltonians as well as open quantum systems.

We concluded Part I of this thesis with the results contained in Chapter 4. By building on the theoretical results derived in Chapters 2 and 3, here we demonstrated the emergence of the complete coupled-cluster doubles amplitude equations from the electronic self-energy by leveraging connections to the Algebraic Diagrammatic Construction method. We then proceeded to uncover the connections between many-body Green's function approaches and ionization potential/electron-affinity equation-of-motion coupled-cluster theory. Using the formal relationships uncovered, we obtained exact analytic results for the spectrum of the Hubbard dimer to contrast with other approximate schemes such as the GW approximation. As this Chapter presents significant advancements in the conceptual understanding of the relationship between the Green's function formalism and coupled-cluster theory, we expect that the formalism presented will spark new interest in the development of improved and scalable first-principles methods for ground and excited state electronic correlation in molecules and materials.

In Part II of this thesis, we focused on going beyond the Born-Oppenhiemer approximation by including the effects of the lattice dynamics on the electronic properties of infinite solids. In Chapter 5, we provided a detailed derivation of the structure of the Green's function for systems that possess a continuous spectrum. This required us to introduce the analytically continued Green's function of the second Riemann sheet, necessary in order to interpret the pole condition of the Dyson equation for continuous systems. This analysis was essential as it is not contained in the literature on electron-phonon and exciton-phonon scattering in solids. We then introduced the coupled electron-nuclear interaction Hamiltonian in the context of infinite solids, expanding the nuclear coordinates to second-order about their equilibrium positions. This naturally lead to the introduction of phonons and the phonon contribution to the screened electron-electron Coulomb interaction and

electronic self-energy that arises in the full quantum field theoretic treatment of electron-nuclear interactions (Hedin-Baym equations). Using the derived phonon contribution to the electron-electron interaction, we extended the Bethe-Salpeter equation to include the effects of harmonic lattice vibrations at finite temperatures. In the process, we provided a much needed analysis of the causal properties of the two-particle theory that also applies to the 'clamped-ion' electron-electron and exciton-polariton interactions. We provided a detailed analysis of the phonon-driven exciton dissociation scattering channel contained in the Bethe-Salpeter approach. Finally, we also provided context on effective field theory approaches based on the linear coupling between 'clamped-ion' exciton states interacting with a bath of phonons.

We conclude this thesis in Chapter 6, where we reformulated the electron-phonon contribution to the Bethe-Salpeter equation in terms of the finite temperature Dyson supermatrix. This allowed us to firmly demonstrate the connections between the effective exciton field theory presented in Chapter 5 and the Bethe-Salpeter equation. Finally, using the Dyson supermatrix formulation, we calculated the effect of including phonon screening on excitons from first principles in several heterogeneous semi-conductors of interest. Using the powerful block Lanczos algorithm we were able to diagonalize the Dyson supermatrices for these systems, a feat which is currently unfeasible on the most powerful supercomputers. We expect the formalism presented in this Chapter will lead to novel approaches for the non-perturbative calculation of energy renormalizations and scattering rates in infinite solids.

7.1 Future directions

The work presented in this thesis has uncovered several complementary and distinct future research directions. At present, there exists no unified and consistent theoretical framework whereby we can study and predict the optical properties of materials resulting from the competing interactions between correlated electron-hole pairs and explicit distortions of the lattice due to the electronic motion. The current understanding of exciton-phonon interactions consists of two related but contrasting physical pictures. The first approximation is based on the picture of an exciton that interacts with a modified, averaged potential due to the lattice vibrations. This change in potential the exciton experiences is taken to be perturbative, weakly influencing the properties of the exciton as it propagates

through the lattice. This picture was discussed extensively in Chapters 5 and 6. The second picture is based on that of an exciton-polaron [186, 223, 224]. An exciton-polaron can be thought of as a correlated electron-hole pair that is explicitly coupled to the lattice distortion accompanying its propagation through the lattice. This picture is a result of the dipole-like character of an exciton, which drags an effective polarization of the lattice along with it as it propagates through a material. Both pictures of exciton-phonon interactions are useful, corresponding to different regimes of coupling strength between the electronic and vibrational degrees of freedom of a material. As a result, they depend strongly on the characteristic properties of a specific material. However, there should exist a coherent theoretical and computational tractable framework through which both pictures arise from the same set of fundamental equations.

The central difficulty in providing a unified theoretical framework for exciton interactions is because the exciton is an emergent quasiparticle that is composed of an electron and a hole. Therefore, there is a delicate and complicated balance between the individual effects that an electron or hole experience along with their combined, correlated influence they exert on the lattice. In systems such as Lead Halide Perovskites and Transition Metal Dichalcogenides (TMDs), key optoelectronic materials used to make solar cells and photocatalysts, it has been argued that the effects due to the individual electron and individual hole that comprise an exciton are canceled by the resulting distortion of the lattice through polaronic interference effects. Therefore, it is of central importance to address these open questions by accounting for the complicated and diverse exciton interactions necessary to understand and design novel optoelectronic materials. We are currently pursuing ways to include these polaronic interference effects on the dynamics of excitons in semiconductors and insulators. This work would hopefully provide a unified theory of exciton-phonon interactions in semiconductors and insulators.

In fact, the work presented in Chapter 5 has already inspired new research directions, currently in review, on understanding phonon-mediated electron attraction in materials by extension of *ab initio* downfolding techniques to include arbitrary range electron-phonon coupling [8, 9]. Another interesting avenue for future work would be in the combination of coupled-cluster and Green's function theories for the computation of electron-phonon interactions in infinite solids [246]. This is very much an emerging field and is currently

hindered by the computational cost of coupled-cluster theory for periodic solids. However, the theoretical advances presented in this thesis can be used to develop a consistent theory of the coupled-cluster self-energy and Bethe-Salpeter kernel for the computation of excited state energies that include the interactions with harmonic lattice vibrations.

The theoretical advancements presented in Chapter 3, where we derived a consistent field theory for non-hermitian many-body interactions, will hopefully provide the foundation to explore different non-hermitian interactions such as those that emerge in the context of open quantum systems. We believe this work will also be useful in generating a fully consistent non-equilibrium Green's function theory, whereby the approach to equilibrium is also captured after a perturbation is switched off. In addition, this work will also be useful to the development of new methods in the context of the nuclear many-body problem [132, 141]. Finally, we plan to explore the analytic continuation of the Green's function and self-energy, derived in Chapter 5, when coupled to the continuum in the context of understanding the emergence of irreversibility in quantum mechanics [43, 168].

Appendices

A

Mathematical Techniques

Contents

A.1 Langreth rules

In this appendix, we give a few examples of how to calculate integrals and products of functions defined on the Keldysh contour using the Langreth rules [17, 247, 248]. In general, a function defined on the Keldysh contour is referred to as a Keldysh function and takes the general form [17]:

$$h(z,z') = h^{\infty}(z)\delta(z,z') + \theta(z,z')h^{>}(z,z') + \theta(z',z)h^{<}(z,z') \; . \tag{A.1.0.1}$$

By projecting the contour time arguments onto the different parts of the physical contour, we obtain either real-time or imaginary-time functions. This was explicitly outlined for the Green's function and self-energy in Chapter 2.

In this thesis, the main two Langreth rules we require are for contour convolutions and contour products. A typical convolution we are interested in is the two-point convolution:

$$h(z,z') = \int_\gamma d\bar{z} f(z,\bar{z}) g(\bar{z},z') \ . \tag{A.1.0.2}$$

We know that evaluation of the external z, z' time-arguments on the backward and forward branch of the real-time part of the contour gives the greater component of the Keldysh function:

$$h^>(t,t') = \int_\gamma d\bar{z} f(t_+,\bar{z}) g(\bar{z},t'_-) \tag{A.1.0.3}$$

Now, taking the contour to be simply composed of the forward and backward branches, ignoring the Matsubara strip, we have (assuming we are at equilibrium)

$$\begin{aligned} h^>(t,t') &= \int_{-\infty}^{\infty} d\bar{t}_- f(t_+,\bar{t}_-) g(\bar{t}_-,t'_-) + \int_{\infty}^{-\infty} d\bar{t}_+ f(t_+,\bar{t}_+) g(\bar{t}_+,t'_-) \\ &= \int_{-\infty}^{\infty} d\bar{t} f^>(t,\bar{t}) g^{\mathrm{T}}(\bar{t},t') + \int_{\infty}^{-\infty} d\bar{t} f^{\bar{\mathrm{T}}}(t,\bar{t}) g^>(\bar{t},t') \ . \end{aligned} \tag{A.1.0.4}$$

Now, using the relationships: $g^{\mathrm{T}} = g^> + g^{\mathrm{A}}$ and $f^{\bar{\mathrm{T}}} = f^> - f^{\mathrm{R}}$, we can rearrange this expression to get

$$h^>(t,t') = \int_{-\infty}^{\infty} d\bar{t} f^>(t,\bar{t}) g^{\mathrm{A}}(\bar{t},t') + \int_{-\infty}^{\infty} d\bar{t} f^{\mathrm{R}}(t,\bar{t}) g^>(\bar{t},t') \ . \tag{A.1.0.5}$$

By introducing the shorthand notation $f * g = \int_{-\infty}^{\infty} d\bar{t} f(t,\bar{t}) g(\bar{t},t')$, it can also be shown that the lesser component is given by

$$h^< = f^< * g^{\mathrm{A}} + f^{\mathrm{R}} * g^< \ . \tag{A.1.0.6}$$

Finally, using these two expressions, along with the identity: $h^> - h^< = h^{\mathrm{R}} - h^{\mathrm{A}}$, it is straightforward to demonstrate that

$$h^{\mathrm{R}} = f^{\mathrm{R}} * g^{\mathrm{R}} \tag{A.1.0.7a}$$

$$h^{\mathrm{A}} = f^{\mathrm{A}} * g^{\mathrm{A}} \ . \tag{A.1.0.7b}$$

These equations are important as they show that retarded/advanced convolutions do not mix different Keldysh components.

Finally, the most important Keldysh product used in this thesis is the retarded product. Suppose we have the product of two Keldysh functions

$$h(z,z') = f(z,z') g(z,z') \tag{A.1.0.8}$$

where $f^{\infty} = g^{\infty} = 0$. To find the retarded component of this expression, we note that the greater and lesser components can simply be found as $h^{\lessgtr} = f^{\lessgtr} g^{\lessgtr}$. Using these relationships, it is staightforward to demonstrate that

$$h^{\mathrm{R}}(t,t') = f^{\mathrm{R}}(t,t')g^{<}(t,t') + f^{<}(t,t')g^{\mathrm{R}}(t,t') + f^{\mathrm{R}}(t,t')g^{\mathrm{R}}(t,t') \ . \tag{A.1.0.9}$$

Upon Fourier transformation, this equation can be converted to a frequency convolution which is employed extensively throughout this thesis.

A.2 Schwinger's functional derivative technique and Hedin's equations

In the presence of a time-dependent external perturbation, the Green's function is given by

$$iG(1,2) = \frac{\left\langle \mathcal{T}_\gamma \left\{ e^{-i\int_\gamma d\bar{z} H_1(\bar{z})} \psi(1)\psi^\dagger(2) \right\} \right\rangle}{\left\langle \mathcal{T}_\gamma \left\{ e^{-i\int_\gamma d\bar{z} H_1(\bar{z})} \right\} \right\rangle} \ , \tag{A.2.0.1}$$

where $H_1(\bar{z}) = \int d\bar{\mathbf{x}} d3 \phi(\bar{1},3)\psi^\dagger(\bar{1})\psi(3)$, with $\phi(\bar{1},3) = \phi(\bar{1})\delta(\bar{1},3)$ the time-dependent local external potential that is coupled to the electronic density. We have already taken into account the time-dependence of the field operators using the Keldysh picture given in Chapter 2. Taking the functional derivative of the electronic density with respect to the external potential gives the reducible polarization propagator P^*:

$$\begin{aligned} \frac{\delta n_{\mathrm{el}}(1)}{\delta\phi(3)} = -i\Bigg(& \frac{\left\langle \mathcal{T}_\gamma \left\{ e^{-i\int_\gamma d\bar{z} H_1(\bar{z})} n(1)n(3) \right\} \right\rangle}{\left\langle \mathcal{T}_\gamma \left\{ e^{-i\int_\gamma d\bar{z} H_1(\bar{z})} \right\} \right\rangle} \\ & - \frac{\left\langle \mathcal{T}_\gamma \left\{ e^{-i\int_\gamma d\bar{z} H_1(\bar{z})} n(1) \right\} \right\rangle}{\left\langle \mathcal{T}_\gamma \left\{ e^{-i\int_\gamma d\bar{z} H_1(\bar{z})} \right\} \right\rangle} \frac{\left\langle \mathcal{T}_\gamma \left\{ e^{-i\int_\gamma d\bar{z} H_1(\bar{z})} n(3) \right\} \right\rangle}{\left\langle \mathcal{T}_\gamma \left\{ e^{-i\int_\gamma d\bar{z} H_1(\bar{z})} \right\} \right\rangle} \Bigg) \\ & = P^*(1,2) \ . \end{aligned} \tag{A.2.0.2}$$

Substituting this result into the contour equation-of-motion for the Green's function gives

$$\left(i\frac{\partial}{\partial z_1} - h(1) - v_{\mathrm{H}}(1) - \phi(1) \right) G(1,2) - i\int_\gamma d3 \ v(1,3)\frac{\delta G(1,2)}{\delta\phi(3)} = \delta(1,2) \tag{A.2.0.3}$$

Through Schwinger's functional derivative technique, we can formally close the equation-of-motion for the single-particle Green's function by introduction of the self-energy

$$\int_\gamma d3 \ \Sigma(1,3)G(3,2) = i\int_\gamma d3 \ v(1,3)\frac{\delta G(1,2)}{\delta\phi(3)} \tag{A.2.0.4}$$

Using the functional inverse of the Green's function: $\int d3\ G(1,3)G^{-1}(3,2) = \delta(1,2)$, we can write the self-energy as

$$\Sigma(1,2) = i\int_\gamma d3d4\ v(1,3)\frac{\delta G(1,4)}{\delta\phi(3)}G^{-1}(4,2) \tag{A.2.0.5}$$

From teh definition of the functional inverse, we can immediately write $\int_\gamma d4\ \frac{\delta G(1,4)}{\delta\phi(3)}G^{-1}(4,2) = -\int_\gamma d4\ G(1,4)\frac{\delta G^{-1}(4,2)}{\delta\phi(3)}$, which motivates the introduction of the reducible vertex function $\tilde{\Gamma}$:

$$\tilde{\Gamma}(1,2;3) = -\frac{\delta G^{-1}(1,2)}{\delta\phi(3)}\ . \tag{A.2.0.6}$$

The vertex function implicitly contains all the many-body interactions a single-particle experiences as it propagates through the system. Using this definition, we can isolate the functional derivative of the Green's function with respect to the external potential

$$\frac{\delta G(1,2)}{\delta\phi(3)} = \int_\gamma d4d5\ G(1,4)\tilde{\Gamma}(4,5;3)G(5,2) \tag{A.2.0.7}$$

Therefore, it is clear that

$$P^*(1,3;2,3^+) = -i\int_\gamma d4d5\ G(1,4)\tilde{\Gamma}(4,5;3)G(5,2) \tag{A.2.0.8}$$

Setting $2 \to 1^+$ we obtain the equation for the reducible polarization

$$P^*(1,2) = -i\int_\gamma d4d5\ G(1,4)\tilde{\Gamma}(4,5;2)G(5,1^+) \tag{A.2.0.9}$$

and also have

$$\Sigma(1,2) = i\int_\gamma d4d5\ v(1,4)G(1,5)\tilde{\Gamma}(5,2;4) \tag{A.2.0.10}$$

The reducible vertex can be transformed to a more fundamental quantity called the irreducible vertex. The irreducible vertex contains the dependency of inverse Green's function on the variation of the total classical potential experienced by the electrons of the system. This allows for a more effective perturbative expansion as we start from a vertex which already accounts for some of the many-body interactions (classical Hartree interaction). In theory we would like to work with the four-point vertex function in which the variation with respect to the entire potential an electron experiences is accounted for. This would take the form of

$$\Gamma^*(1,2;3,4) = -\frac{\delta G^{-1}(1,3)}{\delta J(4,2)}\ , \tag{A.2.0.11}$$

where the non-local potential is given by

$$J(4,2) = [u(4) + v_{\mathrm{H}}(4)]\,\delta(4,2) + \Sigma(4,2)\ . \tag{A.2.0.12}$$

The non-local potential already contains the self-energy and results in an irreducible vertex that is the identity. This is because this form of non-local potential makes the implicit assumption that we already know the exact electronic self-energy functional. However, it is more useful to work with the classical potential $u_{cl}(1) = \phi(1) + v_{\mathrm{H}}(1)$ from which the irreducible vertex function of Hedin's eqautions is defined as

$$\Gamma(1,2;3) = -\frac{\delta G^{-1}(1,2)}{\delta u_{cl}(3)} = \int_\gamma d4 \left(-\frac{\delta G^{-1}(1,2)}{\delta \phi(4)}\right) \frac{\delta \phi(4)}{\delta u_{cl}(3)} \tag{A.2.0.13}$$

From the total classical interaction, the inverse dielectric function can be defined as

$$\epsilon^{-1}_{\mathrm{el}}(1,2) = \frac{\delta u_{cl}(1)}{\delta \phi(2)} = \delta(1,2) + \int_\gamma d3\ v(1,3)P^*(3,2)\ . \tag{A.2.0.14}$$

The inverse electronic dielectric function can then be used to define the screened interaction W through the relation:

$$W(1,2) = \int_\gamma d3\ \epsilon^{-1}_{\mathrm{el}}(1,3)v(3,2) = v(1,2) + \int_\gamma d3d4\ v(1,3)P^*(3,4)v(4,2) \tag{A.2.0.15}$$

As the irreducible polarizability is given by the functional derivative of the density with respect to the total classical potential

$$P(1,2) = -i\frac{\delta G(1,1^+)}{\delta u_{cl}(2)}\ , \tag{A.2.0.16}$$

we can obtain the Dyson Equation for the screened interaction by the chain rule:

$$W(1,2) = v(1,2) + \int_\gamma d3d4\ v(1,3)P(3,4)W(4,2)\ . \tag{A.2.0.17}$$

Likewise using the chain rule, we can rewrite the expressions for the self-energy and polarization in terms of the irreducible vertex as

$$\Sigma(1,2) = i\int_\gamma d3d4\ W(1,4)G(1,3)\Gamma(3,2;4) \tag{A.2.0.18}$$

$$P(1,2) = -i\int_\gamma d3d4\ G(1,3)\Gamma(3,4;2)G(4,1^+) \tag{A.2.0.19}$$

Finally to derive the equation for the irreducible vertex function we can use the Dyson equation, $G^{-1}(1,2) = G_0^{-1}(1,2) - \Sigma(1,2)$, to get

$$\Gamma(1,2;3) = \delta(1,3)\delta(2,3) + \frac{\delta\Sigma(1,2)}{\delta u_{cl}(3)} \tag{A.2.0.20}$$

From the diagrammatic analysis presented in Chapter 2, we know that the self-energy is a functional of G and so we can use the chain rule

$$\Gamma(1,2;3) = \delta(1,3)\delta(2,3) + \int_\gamma d4d5 \; \frac{\delta\Sigma(1,2)}{\delta G(5,4)} \frac{\delta G(5,4)}{\delta u_{cl}(3)} \tag{A.2.0.21}$$

Identifying the BSE kernel as

$$i\frac{\delta\Sigma(1,2)}{\delta G(5,4)} = \Xi(1,4;2,5) \; , \tag{A.2.0.22}$$

we can re-write the irreducible vertex equation as

$$\Gamma(1,2;3) = \delta(1,3)\delta(2,3) - i\int_\gamma d4d5d6d7 \; \Xi(1,4;2,5)G(5,6)\Gamma(6,7;3)G(7,4) \; , \tag{A.2.0.23}$$

where we have used the relation

$$\frac{\delta G(5,4)}{\delta u_{cl}(3)} = \int_\gamma d6d7 \; G(5,6)\Gamma(6,7;3)G(7,4) \; . \tag{A.2.0.24}$$

Hedin's equations are completed with Dyson's equation for the electronic Green's function:

$$G(1,2) = G_0(1,2) + \int_\gamma d3d4 \; G_0(1,3)\Sigma(3,4)G(4,2) \; . \tag{A.2.0.25}$$

A.3 Fourier transform convention

Throughout this thesis, we use the following convention for the general Fourier transformation of an m-point correlation function:

$$\begin{aligned} &2\pi\delta(\omega_1 + \omega_2 + \cdots - \omega_3 - \omega_4 - \cdots)G^{m\text{pt}}(\omega_1, \omega_2, \cdots ; \omega_3, \omega_4, \cdots) \\ &= \int_{-\infty}^{\infty} dt_1 dt_2 \cdots dt_3 dt_4 \cdots e^{i\omega_1 t_1} e^{i\omega_2 t_2} \cdots G^{m\text{pt}}(t_1, t_2, \cdots ; t_3, t_4, \cdots) e^{-i\omega_3 t_3} e^{-i\omega_4 t_4} \cdots \end{aligned} \tag{A.3.0.1}$$

For example, the Fourier transform of the single-particle Green's function is given by

$$\begin{aligned} \int_{-\infty}^{\infty} dt_1 dt_3 e^{i\omega_1 t_1} \cdots G^{2\text{pt}}(t_1; t_3) e^{-i\omega_3 t_3} &= \int_{-\infty}^{\infty} dt_1 e^{i(\omega_1 - \omega_3)t_1} \int_{-\infty}^{\infty} d\tau e^{i\omega_3 \tau} G(\tau) \\ &= 2\pi\delta(\omega_1 - \omega_3)G(\omega_3) \end{aligned} \tag{A.3.0.2}$$

where we have used the fact that $G^{2\text{pt}}(t_1; t_3) = G^{2\text{pt}}(t_1 - t_3) = G(\tau)$, where $\tau = t_1 - t_3$. This also results in the identification that $G^{2\text{pt}}(\omega_3; \omega_3) = G(\omega_3)$. For a simple function of a single time, the Fourier transforms are defined as

$$F(\omega) = \int_{-\infty}^{\infty} d\tau e^{i\omega\tau} F(\tau) \tag{A.3.0.3a}$$

$$F(\tau) = \int_{-\infty}^{\infty} \frac{d\omega}{2\pi} e^{-i\omega\tau} F(\omega) \; . \tag{A.3.0.3b}$$

A.4 Particle-hole response function Fourier transform

At equilbrium, due to the time-independence of the Hamiltonian, the four-point response function becomes a function of three time-differences. In the particle-hole response function convention, we have $L(t_1, t_2; t_3, t_4) \equiv L(t_{13}, t_{24}; t_{23})$. Taking the general Fourier transform of this function, we can write

$$\begin{aligned}&\int_{-\infty}^{\infty} dt_1 dt_2 dt_3 dt_4 e^{i\omega_1 t_1} e^{i\omega_2 t_2} L(t_1, t_2; t_3, t_4) e^{-i\omega_3 t_3} e^{-i\omega_4 t_4} \\ &= \int_{-\infty}^{\infty} dt_1 dt_2 dt_3 dt_4 e^{i\omega_1 t_1} e^{i\omega_2 t_2} L(t_{13}, t_{24}; t_{23}) e^{-i\omega_3 t_3} e^{-i\omega_4 t_4}\end{aligned} \tag{A.4.0.1}$$

Now, using the time-differences, we can re-write this expression as

$$\begin{aligned}&\int_{-\infty}^{\infty} dt_{13} dt_{24} dt_{23} dt_4 e^{i\omega_1 t_{13}} e^{i(\omega_1+\omega_2-\omega_3)t_{24}} e^{i(\omega_3-\omega_1)t_{23}} L(t_{13}, t_{24}; t_{23}) e^{i(\omega_1+\omega_2-\omega_3-\omega_4)t_4} \\ &= 2\pi\delta(\omega_1+\omega_2-\omega_3-\omega_4) \int_{-\infty}^{\infty} dt_{13} dt_{24} dt_{23} e^{i\omega_1 t_{13}} e^{i(\omega_1+\omega_2-\omega_3)t_{24}} e^{i(\omega_3-\omega_1)t_{23}} L(t_{13}, t_{24}; t_{23})\end{aligned} \tag{A.4.0.2}$$

Using the delta function condition, we can identify $\omega_1+\omega_2-\omega_3 = \omega_4$ and re-write this expression as

$$\begin{aligned}L(\omega_1, \omega_2; \omega_3, \omega_4) &= \int_{-\infty}^{\infty} dt_{13} dt_{24} dt_{23} e^{i\omega_1 t_{13}} e^{i\omega_4 t_{24}} e^{i(\omega_2-\omega_4)t_{23}} L(t_{13}, t_{24}; t_{23}) \\ &= L(\omega_1, \omega_4, \omega_2-\omega_4)\ .\end{aligned} \tag{A.4.0.3}$$

Finally, by introduction of the Fermionic frequencies, $\omega_1 = \nu$ and $\omega_4 = \nu'$, we can introduce the Bosonic frequency, $\omega = \omega_2 - \nu'$. The reason we refer to ω as the Bosonic frequency is because, at finite temperatures, the subtraction of the two Fermionic Matsubara frequencies generates a Bosonic Matsubara frequency. This allows us to write the final expression for the particle-hole Fourier transform as

$$L(\nu, \nu', \omega) = \int_{-\infty}^{\infty} dt_{13} dt_{24} dt_{23} e^{i\nu t_{13}} e^{i\nu' t_{24}} e^{i\omega t_{23}} L(t_{13}, t_{24}; t_{23})\ . \tag{A.4.0.4}$$

Finally, by inverse transformation, we have

$$L(t_{13}, t_{24}; t_{23}) = \int_{-\infty}^{\infty} \frac{d\nu d\nu' d\omega}{(2\pi)^3} e^{-i\nu t_{13}} e^{-i\nu' t_{24}} e^{-i\omega t_{23}} L(\nu, \nu', \omega)\ . \tag{A.4.0.5}$$

By identification of the particle-hole propagator by sending $t_3 \to t_1^+$ and $t_4 \to t_2^+$, we have

$$L(t_{12}) = \int_{-\infty}^{\infty} \frac{d\omega}{2\pi} e^{-i\omega t_{12}} \left(\int_{-\infty}^{\infty} \frac{d\nu d\nu'}{(2\pi)^2} e^{i\nu\eta} e^{i\nu'\eta'} L(\nu, \nu', \omega) \right) \tag{A.4.0.6}$$

From which, we can immediately identify

$$L(\omega) = \int_{-\infty}^{\infty} \frac{d\nu d\nu'}{(2\pi)^2} e^{i\nu\eta} e^{i\nu'\eta'} L(\nu, \nu', \omega) \ . \tag{A.4.0.7}$$

Similarly, this relationship can be used to obtain the two-frequency propagator as

$$L(\nu, \omega) = \int_{-\infty}^{\infty} \frac{d\nu'}{2\pi} e^{i\nu'\eta'} L(\nu, \nu', \omega) \ . \tag{A.4.0.8}$$

A.5 Born-von-Kármán boundary conditions

In Chapters 5 and 6, we derive the effects of including electron-phonon interactions in the Bethe-Salpeter equation for infinite solids. As stated in the main body of the thesis, we employ BvK boundary conditions to describe the infinite solid [169]. We define the crystal unit cell by the primitive direct lattice vectors, $\{\mathbf{a}_1, \mathbf{a}_2, \mathbf{a}_3\}$. The pth unit cell is then indexed by the linear combination: $\mathbf{R}_p = \sum_{i=1}^{3} n_i \mathbf{a}_i$, where n_i are integers between 0 and $N_i - 1$, with N_i corresponding to the number of periodic copies along a given lattice direction. The BvK supercell then contains $N_p = \prod_i N_i$ unit cells.

The Fourier transform of the direct lattice in real space gives rise to the reciprocal lattice. The primitive reciprocal lattice vectors $\{\mathbf{b}_1, \mathbf{b}_2, \mathbf{b}_3\}$ are constructed from the primitive direct lattice vectors by the duality condition: $\mathbf{a}_i \cdot \mathbf{b}_j = 2\pi\delta_{ij}$. From the reciprocal lattice vectors, we can construct the Bloch wavevectors: $\mathbf{k} = \sum_{i=1}^{3} \frac{n_i}{N_i} \mathbf{b}_i$ which correspond to a uniform grid within a chosen unit cell of the reciprocal lattice. The uniform grid within a chosen *unit cell* of the reciprocal lattice vectors contains the same number of unit cells in the total BvK supercell: N_p. With these defintions, we arrive at the Fourier transforms

$$\sum_{\mathbf{k}} e^{i\mathbf{k}\cdot(\mathbf{R}_p - \mathbf{R}_{p'})} = N_p \delta_{pp'} \tag{A.5.0.1}$$

and

$$\sum_{p} e^{i(\mathbf{k}-\mathbf{k}')\cdot\mathbf{R}_p} = N_p \delta_{\mathbf{k}\mathbf{k}'} \ . \tag{A.5.0.2}$$

Given a vector of the reciprocal lattice $\mathbf{G} = \sum_{i=1}^{3} c_i \mathbf{b}_i$, from the duality condition, it is evident that $e^{i\mathbf{G}\cdot\mathbf{R}_p} = 1$. Therefore, any replacement of $\mathbf{k} \to \mathbf{k} + \mathbf{G}$ leaves all expressions derived in this thesis unchanged. Similarly, any shift of the direct lattice vector by another lattice vector of the BvK supercell leaves the expressions unaltered. Therefore, we are free to constrain the uniform $\mathbf{k}$-grid to consist of the set of vectors in the first Brillouin zone.

B

Proofs and Derivations for Non-Hermitian Green's Function Theory and The Coupled-Cluster Similarity Transformation

Contents

B.1 Proof of extended Gell-Mann and Low theorem

From the 'adiabatic switiching on' procedure, we have the time-evolution operator in the interaction picture as

$$\bar{U}_\eta(0,-\infty) = \mathcal{T}\left\{\exp\left(-i\int_{-\infty}^{0} dt\ \bar{H}_1(t)e^{-\eta|t|}\right)\right\} \tag{B.1.0.1}$$

If the limit

$$\lim_{\eta\to 0}\frac{\bar{U}_\eta(0,-\infty)\,|\Phi_0\rangle}{\langle\tilde{\Phi}_0|\bar{U}_\eta(0,-\infty)|\Phi_0\rangle} \equiv \frac{|\Psi_0\rangle}{\langle\tilde{\Phi}_0|\Psi_0\rangle} \tag{B.1.0.2}$$

exits then:

$$\bar{H}\frac{|\Psi_0\rangle}{\langle\tilde{\Phi}_0|\Psi_0\rangle} = E\frac{|\Psi_0\rangle}{\langle\tilde{\Phi}_0|\Psi_0\rangle} \ . \tag{B.1.0.3}$$

Therefore, the quantity $\frac{|\Psi_0\rangle}{\langle\tilde{\Phi}_0|\Psi_0\rangle}$ is an eigenstate of the full Hamiltonian, $\bar{H}$.

Proof: Consider the quantity

$$\begin{aligned}(\bar{H}_0 - E^{(0)})\,|\Psi_0(\eta)\rangle &= (\bar{H}_0 - E^{(0)})\bar{U}_\eta(0,-\infty)\,|\Phi_0\rangle \\ &= \Big[\bar{H}_0, \bar{U}_\eta(0,-\infty)\Big]\,|\Phi_0\rangle \ .\end{aligned} \tag{B.1.0.4}$$

In the biorthogonal Interaction picture, we have that

$$i\frac{\partial}{\partial t}\bar{H}_1(t) = \Big[\bar{H}_1(t), \bar{H}_0\Big] \tag{B.1.0.5}$$

Evaluating the commutators arising in Eq. B.1.0.4, we have

$$\begin{aligned}(\bar{H}_0 - E^{(0)})\,|\Psi_0(\eta)\rangle = -\sum_{n=1}^{\infty}\frac{(-i)^{n-1}}{n!}\int_{-\infty}^{0}dt_1\cdots\int_{-\infty}^{0}dt_n e^{-\eta|t_1+\ldots+t_n|} \\ \left(\sum_{i=1}^{n}\frac{\partial}{\partial t_i}\right)\mathcal{T}\left\{\bar{H}_1(t_1)\ldots\bar{H}_1(t_n)\right\}|\Phi_0\rangle\end{aligned} \tag{B.1.0.6}$$

Performing integration by parts with respect to t_1, we have

$$(\bar{H}_0 - E^{(0)})\,|\Psi_0(\eta)\rangle = -\bar{H}_1\,|\Psi_0(\eta)\rangle + i\eta g\frac{\partial}{\partial g}\,|\Psi_0(\eta)\rangle \tag{B.1.0.7}$$

where we have assumed that the interaction $\bar{H}_1$ is proportional to an arbitrary coupling constant, g, which allows us to identify [13, 24]

$$\frac{(-i)^{n-1}}{(n-1)!}g^n = ig\frac{\partial}{\partial g}\left(\frac{(-i)^n}{n!}g^n\right) \ . \tag{B.1.0.8}$$

Therefore, we have

$$(\bar{H} - E^{(0)})\,|\Psi_0(\eta)\rangle = i\eta g\frac{\partial}{\partial g}\,|\Psi_0(\eta)\rangle \tag{B.1.0.9}$$

and projecting on both sides with $\frac{\langle\tilde{\Phi}_0|}{\langle\tilde{\Phi}_0|\Psi_0(\eta)\rangle}$, we get

$$\frac{\langle\tilde{\Phi}_0|\bar{H}_1|\Psi_0(\eta)\rangle}{\langle\tilde{\Phi}_0|\Psi_0(\eta)\rangle} = i\eta g\frac{\partial}{\partial g}\Big(\log\langle\tilde{\Phi}_0|\Psi_0(\eta)\rangle\Big) = \Delta E(\eta) \ . \tag{B.1.0.10}$$

However, we also have that

$$(\bar{H} - E^{(0)})\frac{|\Psi_0(\eta)\rangle}{\langle\tilde{\Phi}_0|\Psi_0(\eta)\rangle} = \frac{i\eta g}{\langle\tilde{\Phi}_0|\Psi_0(\eta)\rangle}\frac{\partial}{\partial g}\,|\Psi_0(\eta)\rangle \tag{B.1.0.11}$$

by multiplying Eq B.1.0.9 by $\frac{1}{\langle\tilde{\Phi}_0|\Psi_0(\eta)\rangle}$. This equation can be rearranged to give

$$\left(\bar{H} - E^{(0)} - i\eta g\frac{\partial}{\partial g}\right)\frac{|\Psi_0(\eta)\rangle}{\langle\tilde{\Phi}_0|\Psi_0(\eta)\rangle} = \frac{|\Psi_0(\eta)\rangle}{\langle\tilde{\Phi}_0|\Psi_0(\eta)\rangle} \times \left(i\eta g\frac{\partial}{\partial g}\log\langle\tilde{\Phi}_0|\Psi_0(\eta)\rangle\right) \quad \text{(B.1.0.12)}$$

However, by Eq. B.1.0.10, we may rearrange the expression to give

$$\left(\bar{H} - E^{(0)} - \Delta E(\eta)\right)\frac{|\Psi_0(\eta)\rangle}{\langle\tilde{\Phi}_0|\Psi_0(\eta)\rangle} = i\eta g\frac{\partial}{\partial g}\frac{|\Psi_0(\eta)\rangle}{\langle\tilde{\Phi}_0|\Psi_0(\eta)\rangle} \quad \text{(B.1.0.13)}$$

Now, we are in a position to take the limit as $\eta \to 0$. By assumption, the right hand side is finite to all orders in perturbation theory. Therefore, the multiplication by η as $\eta \to 0$ sends the right hand side to zero. As a result, we have

$$\left(\bar{H} - E\right)\lim_{\eta\to 0}\frac{|\Psi_0(\eta)\rangle}{\langle\tilde{\Phi}_0|\Psi_0(\eta)\rangle} = 0 \quad \text{(B.1.0.14)}$$

and hence we have the extended Gell-Mann and Low theorem. By analogy, we also have

$$\left(\bar{H}^\dagger - E\right)\lim_{\eta\to 0}\frac{|\tilde{\Psi}_0(\eta)\rangle}{\langle\Phi_0|\tilde{\Psi}_0(\eta)\rangle} = 0 \quad \text{(B.1.0.15)}$$

for the left eigenstate. As a result, the ground state energy shift is given by

$$\Delta E = \frac{\langle\tilde{\Phi}_0|\bar{H}_1|\Psi_0\rangle}{\langle\tilde{\Phi}_0|\Psi_0\rangle} = \frac{\langle\Phi_0|\bar{H}_1^\dagger|\tilde{\Psi}_0\rangle}{\langle\Phi_0|\tilde{\Psi}_0\rangle}\ , \quad \text{(B.1.0.16)}$$

where $\Delta E = E - E^{(0)}$.

B.2 Normal-orderings of the similarity transformed Hamiltonian

The similarity transformed Hamiltonian is written as

$$\bar{H} = e^{-T}He^{T} = \sum_{pq}\bar{h}_{pq}a_p^\dagger a_q + \frac{1}{(2!)^2}\sum_{pq,rs}\bar{h}_{pq,rs}a_p^\dagger a_q^\dagger a_s a_r + \frac{1}{(3!)^2}\sum_{pqr,stu}\bar{h}_{pqr,stu}a_p^\dagger a_q^\dagger a_r^\dagger a_u a_t a_s + \cdots \quad \text{(B.2.0.1)}$$

Normal-ordering this Hamiltonian with respect to the reference determinant gives the expression

$$\begin{aligned}\bar{H} = \langle\Phi_0|\bar{H}|\Phi_0\rangle &+ \sum_{pq}F_{pq}\left\{a_p^\dagger a_q\right\}_0 + \frac{1}{(2!)^2}\sum_{pq,rs}\chi_{pq,rs}\left\{a_p^\dagger a_q^\dagger a_s a_r\right\}_0 \\ &+ \frac{1}{(3!)^2}\sum_{pqr,stu}\chi_{pqr,stu}\left\{a_p^\dagger a_q^\dagger a_r^\dagger a_u a_t a_s\right\}_0 + \cdots\end{aligned} \quad \text{(B.2.0.2)}$$

where the effective interaction matrix elements are given by [4]

$$F_{pq} = \bar{h}_{pq} - i\sum_{rs} \bar{h}_{pr,qs} G^0_{sr}(t-t^+) + \frac{i}{(2!)^2}\sum_{rs,tu} \bar{h}_{prs,qtu} G^{2\mathrm{ph},(0)}_{tu,rs}(t-t^+) + \cdots \tag{B.2.0.3a}$$

$$\chi_{pq,rs} = \bar{h}_{pq,rs} - i\sum_{tu} \bar{h}_{pqt,rsu} G^0_{ut}(t-t^+) + \frac{i}{(2!)^2}\sum_{tuwv} \bar{h}_{pqtu,rswv} G^{2\mathrm{ph},(0)}_{wv,tu}(t-t^+) + \cdots \tag{B.2.0.3b}$$

and so on for the three-body and higher effective interactions. Here, $-iG^0_{pq}(t-t^+) = \langle\Phi_0|a^\dagger_q a_p|\Phi_0\rangle$ and $iG^{2\mathrm{ph}(0)}_{pq,rs}(t-t^+) = \langle\Phi_0|a^\dagger_r a^\dagger_s a_q a_p|\Phi_0\rangle$ are the reference one- and two-particle reduced density matrices, respectively. The higher-order contributions are given by contracting higher-body matrix elements with reference reduced density matrices. However, we can also write the similarity transformed Hamiltonian as

$$\begin{aligned}\bar{H} = \langle\tilde{\Psi}_0|\bar{H}|\Phi_0\rangle &+ \sum_{pq}\tilde{F}_{pq}\left\{a^\dagger_p a_q\right\} + \frac{1}{(2!)^2}\sum_{pq,rs}\tilde{\Xi}_{pq,rs}\left\{a^\dagger_p a^\dagger_q a_s a_r\right\} \\ &+ \frac{1}{(3!)^2}\sum_{pqr,stu}\tilde{\chi}_{pqr,stu}\left\{a^\dagger_p a^\dagger_q a^\dagger_r a_u a_t a_s\right\} + \cdots\end{aligned} \tag{B.2.0.4}$$

where $E^{\mathrm{CC}}_0 = \langle\tilde{\Psi}_0|\bar{H}|\Phi_0\rangle = \langle\Phi_0|\bar{H}|\Phi_0\rangle$ from the coupled-cluster Lagrangian. The normal-ordered effective interactions become

$$\begin{aligned}\tilde{F}_{pq} &= \bar{h}_{pq} - i\sum_{rs}\bar{h}_{pr,qs}\tilde{G}_{sr}(t-t^+) + \frac{i}{(2!)^2}\sum_{rs,tu}\bar{h}_{prs,qtu}\tilde{G}^{2\mathrm{ph}}_{tu,rs}(t-t^+) + \cdots \\ &= F_{pq} + \sum_{ai}\chi_{pa,qi}\lambda^i_a + \frac{1}{(2!)^2}\sum_{ijab}\chi_{pab,qij}\lambda^{ij}_{ab} + \cdots\end{aligned} \tag{B.2.0.5a}$$

$$\begin{aligned}\tilde{\Xi}_{pq,rs} &= \bar{h}_{pq,rs} - i\sum_{tu}\bar{h}_{pqt,rsu}\tilde{G}_{ut}(t-t^+) + \frac{i}{(2!)^2}\sum_{tuwv}\chi_{pqtu,rswv}\tilde{G}^{2\mathrm{ph}}_{wv,tu}(t-t^+) + \cdots \\ &= \chi_{pq,rs} + \sum_{ia}\chi_{pqa,rsi}\lambda^i_a + \frac{1}{(2!)^2}\sum_{ijab}\chi_{pqab,rsij}\lambda^{ij}_{ab} + \cdots\end{aligned} \tag{B.2.0.5b}$$

and so on for the three-body and higher effective interactions. Here, $-i\tilde{G}_{pq}(t-t^+) = \langle\tilde{\Psi}_0|a^\dagger_q a_p|\Phi_0\rangle$ and $i\tilde{G}^{2\mathrm{ph}}_{pq,rs}(t-t^+) = \langle\tilde{\Psi}_0|a^\dagger_r a^\dagger_s a_q a_p|\Phi_0\rangle$ are the biorthogonal one- and two-particle reduced density matrices, respectively. The higher-order contributions are given by contracting higher-body matrix elements with biorthogonal reduced density matrices.

B.3 Relationship between the BSE kernel and the 4-point vertex function

The BSE kernel $\tilde{\Xi}$, and the 4-point vertex function $\tilde{\Lambda}^{4\text{pt}}$, are closely related. From Eq. 3.8.1.5 for the 4-point vertex function, in the real-time domain, we have

$$\begin{aligned}\tilde{G}^{4\text{pt}}_{pq,rs}(t_1,t_2;t_3,t_4) &= i\tilde{G}_{pr}(t_1,t_3)\tilde{G}_{qs}(t_2,t_4) - i\tilde{G}_{ps}(t_1,t_4)\tilde{G}_{qr}(t_2,t_3) \\ &- \sum_{tuvw}\int dtdt'dt''dt'''\tilde{G}_{pt}(t_1,t')\tilde{G}_{qu}(t_2,t'')\tilde{\Lambda}^{4\text{pt}}_{tu,vw}(t',t'';t,t''')\tilde{G}_{vr}(t,t_3)\tilde{G}_{ws}(t''',t_4)\ .\end{aligned} \tag{B.3.0.1}$$

This equation can be rewritten using the definition of the 4-point response function $\tilde{L}$ and its non-interacting counterpart $\tilde{L}_0$, as

$$\begin{aligned}\tilde{L}_{pq,rs}(t_1,t_2;t_3,t_4) &= \tilde{L}^0_{pq,rs}(t_1,t_2;t_3,t_4) \\ &+ \sum_{tuvw}\int dtdt'dt''dt'''\tilde{L}^0_{pv,rt}(t_1,t;t_3,t')\tilde{\Lambda}^{4\text{pt}}_{tu,vw}(t',t'';t,t''')\tilde{L}^0_{wq,us}(t''',t_2;t'',t_4)\ .\end{aligned} \tag{B.3.0.2}$$

Comparison of Eq. B.3.0.2 with Eq. 3.12.0.1, we see that the 4-point vertex function is the reducible BSE kernel. With this identification, we can immediately write the relationship between the BSE kernel and 4-point vertex as

$$\begin{aligned}\tilde{\Lambda}^{4\text{pt}}_{pq,rs}(t_1,t_2;t_3,t_4) &= \tilde{\Xi}_{pq,rs}(t_1,t_2;t_3,t_4) \\ &+ \sum_{tuvw}\int dtdt'dt''dt'''\tilde{\Xi}_{pv,rt}(t_1,t;t_3,t')\tilde{L}^0_{tu,vw}(t',t'';t,t''')\tilde{\Lambda}^{4\text{pt}}_{wq,us}(t''',t_2;t'',t_4)\ .\end{aligned} \tag{B.3.0.3}$$

Using this relationship, we have

$$\begin{aligned}\tilde{L} &= \tilde{L}_0 + \tilde{L}_0\tilde{\Lambda}^{4\text{pt}}\tilde{L}_0 \\ &= \tilde{L}_0 + \tilde{L}_0(\tilde{\Xi} + \tilde{\Xi}\tilde{L}_0\tilde{\Lambda}^{4\text{pt}})\tilde{L}_0 \\ &= \tilde{L}_0 + \tilde{L}_0\tilde{\Xi}\tilde{L}\end{aligned} \tag{B.3.0.4}$$

which is the Bethe-Salpeter equation (Eq. 3.12.0.1). Since the 4-point vertex is the reducible kernel of the BSE, it consists of 1PI diagrams and hence appears in the self-consistent expansion for the self-energy. As a result, the 4-point vertex can be viewed as the functional derivative of $\tilde{\Sigma}$ with respect to $\tilde{G}$: $\tilde{\Lambda}^{4\text{pt}} \sim i\frac{\delta\tilde{\Sigma}}{\delta\tilde{G}}$. The irreducible BSE kernel $\tilde{\Xi}$, consists only of 2PI diagrams as the BSE performs the geometric series summation of these terms.

B.4 Expansion of interaction-irreducible vertices

Here, we present the diagrammatic expansion of the interaction-irreducible one-body vertex. The derivation for higher-order interaction vertices is analogous. The one-body

interaction-irreducible vertex is given by

$$\tilde{F}_{pq} = \bar{h}_{pq} - i\sum_{rs}\bar{h}_{pr,qs}\tilde{G}_{sr}(t-t^+) + \frac{i}{(2!)^2}\sum_{rstu}\bar{h}_{prs,qtu}\tilde{G}^{\mathrm{2ph}}_{tu,rs}(t-t^+) + \cdots \tag{B.4.0.1}$$

Using the Dyson equation for the single-particle Green's function

$$\tilde{G}_{pq}(t-t') = G^0_{pq}(t-t') + \int dt_1 dt_2 \sum_{vw} G^0_{pv}(t-t_1)\tilde{\Sigma}_{vw}(t_1-t_2)\tilde{G}_{wq}(t_2-t') \tag{B.4.0.2}$$

and expanding the equal time two-particle Green's function as the antisymmetrized sum of the first two terms from independent-particle propagation

$$\tilde{G}^{\mathrm{2ph}}_{tu,rs}(t-t^+) \approx i\tilde{G}_{tr}(t-t^+)\tilde{G}_{us}(t-t^+) - i\tilde{G}_{ts}(t-t^+)\tilde{G}_{ur}(t-t^+), \tag{B.4.0.3}$$

we insert the Dyson equation into Eqs B.4.0.1 and B.4.0.3 to obtain

$$\begin{aligned}\tilde{F}_{pq} = F_{pq} - i\sum_{rt}\Bigg(\bar{h}_{pr,qt} - i\sum_{su}\bar{h}_{prs,qtu}G^0_{us}(t-t^+) + \frac{i}{(2!)^2}\sum_{suw\sigma}\bar{h}_{prsu,qtw\sigma}G^{\mathrm{2ph}(0)}_{w\sigma,su}(t-t^+) + ...\Bigg) \\ \times\sum_{vw}\int dt_1 dt_2 G^0_{tv}(t-t_1)\Sigma_{vw}(t_1-t_2)\tilde{G}_{wr}(t_2-t^+) + \cdots\end{aligned} \tag{B.4.0.4}$$

Now, the expression in brackets is exactly that of the effective interaction $\chi_{pr,qt}$ and so this expression simplifies to

$$\tilde{F}_{pq} = F_{pq} - i\sum_{rtvw}\chi_{pr,qt}\times\int dt_1 dt_2 G^0_{tv}(t-t_1)\tilde{\Sigma}_{vw}(t_1-t_2)\tilde{G}_{wr}(t_2-t^+) + \cdots \tag{B.4.0.5}$$

By further perturbative expansion of the higher-body Green's functions, we arrive at the expression

$$\begin{aligned}\tilde{\chi}_{pq} &= \chi_{pq} - i\sum_{rtvw}\chi_{pr,qt}\times\int dt_1 dt_2 G^0_{tv}(t-t_1)\tilde{\Sigma}_{vw}(t_1-t_2)\tilde{G}_{wr}(t_2-t^+) \\ &+ \frac{i}{(2!)^2}\sum_{\substack{rstu\\vwlo}}\chi_{prs,qtu}\times\int dt_1 dt_2 \tilde{G}_{tl}(t_1-t_2)\tilde{G}_{no}(t_1-t_2)\tilde{\Lambda}^{\mathrm{4pt}}_{lo,vw}(t_1,t_1;t_2,t_2)\tilde{G}_{vr}(t_2-t_1)\tilde{G}_{ws}(t_2-t_1) \\ &+ \cdots\end{aligned} \tag{B.4.0.6}$$

Perturbative expansion of the Green's function $\tilde{G} \approx G_0$, the self-energy $\tilde{\Sigma} \approx \tilde{\Sigma}^{\infty(0)}$ and the 4-point vertex function as $\tilde{\Lambda}^{\mathrm{4pt}(0)}_{pq,rs} \approx \chi_{pq,rs}$, allows us to write this expression diagrammatically

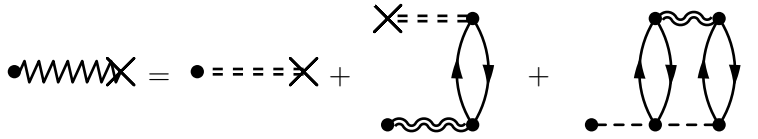

(B.4.0.7)

This is exactly the diagrammatic series presented in Section 3.8 when recovering the perturbative expansion of the coupled-cluster self-energy. The derivation for the expansion of the two-body effective interaction is entirely analogous.

B.5 Formal properties of the coupled-cluster Dyson supermatrix and self-energy

The CC quasiparticle Hamiltonian (Eq. 3.10.0.2) and CC Dyson supermatrix (Eq. 3.10.0.6) are non-hermitian but possess the same *real* spectrum. As first demonstrated in Ref. [115], a diagonalizable non-hermitian matrix possesses a *real* spectrum *if and only if* it is pseudo-hermitian with respect to a linear hermitian automorphism (metric) of the form

$$\tau = \mathbf{A}^\dagger \mathbf{A} \ . \tag{B.5.0.1}$$

This results in a biorthogonal formulation of quantum mechanics whereby the relationship between an arbitrary vector and its associated vector is given by [111]

$$\tilde{\mathbf{v}} = \tau \mathbf{v} \ . \tag{B.5.0.2}$$

This definition requires the CC Dyson supermatrix to be pseudo-hermitian:

$$(\tilde{\mathbf{D}}^{\mathrm{CC}})^\dagger = \tau \tilde{\mathbf{D}}^{\mathrm{CC}} \tau^{-1} \ . \tag{B.5.0.3}$$

It can also be shown that a diagonalizable matrix possesses a *real* spectrum *if and only if* there is a pseudo-canonical transformation that maps the matrix into a hermitian one [115]. This requires the CC and electronic Dyson supermatrices to be related by the similarity transformation

$$\mathbf{D}^{\mathrm{el}} = \mathbf{A} \tilde{\mathbf{D}}^{\mathrm{CC}} \mathbf{A}^{-1} \ , \tag{B.5.0.4}$$

such that $\mathbf{D}^{\mathrm{el}} = (\mathbf{D}^{\mathrm{el}})^\dagger$. Therefore, we can show that for an arbitrary state $\mathbf{y}$, we have

$$\mathbf{y}^\dagger \mathbf{D}^{\mathrm{el}} \mathbf{y} = \mathbf{y}^\dagger \mathbf{A} \tilde{\mathbf{D}}^{\mathrm{CC}} \mathbf{A}^{-1} \mathbf{y} \ . \tag{B.5.0.5}$$

Now, defining the arbitrary state $\mathbf{v} = \mathbf{A}^{-1}\mathbf{y}$, we can write its associated state as $\tilde{\mathbf{v}} = \mathbf{A}^\dagger \mathbf{A}(\mathbf{A}^{-1}\mathbf{y}) = \mathbf{A}^\dagger \mathbf{y}$. This results in the general relationship

$$\mathbf{y}^\dagger \mathbf{D}^{\mathrm{el}} \mathbf{y} = \tilde{\mathbf{v}}^\dagger \tilde{\mathbf{D}}^{\mathrm{CC}} \mathbf{v} \tag{B.5.0.6}$$

for any arbitrary vectors $\mathbf{y}$ and $\mathbf{v}$ related to each other by the invertible transformation $\mathbf{y} = \mathbf{A}\mathbf{v}$.

We can also provide a similar analysis for the dynamical CC quasiparticle equation. By working in the canonical basis that diagonalizes the Fock operator, we can write the frequency-dependent CC quasiparticle equation (Eq. 3.10.0.2) as

$$\tilde{\mathbf{\Sigma}}(\varepsilon)\mathbf{C} = \Delta\varepsilon\mathbf{C} \tag{B.5.0.7}$$

where $\Delta\varepsilon = \varepsilon - \epsilon$ is real and ϵ is the matrix of eigenvalues of the Fock operator. Therefore, as the eigenvalues of the non-hermitian coupled-cluster self-energy are real, the coupled-cluster self-energy must also be pseudo-hermitian. The pseudo-hermiticity of the CC self-energy is expressed with respect to the metric

$$\eta = \mathbf{B}^\dagger\mathbf{B} \ . \tag{B.5.0.8}$$

Therefore, a general state and its associated state are related via $\tilde{\mathbf{v}} = \eta\mathbf{v}$ for some general vector $\mathbf{v}$. As this is the case, we can define the pseudo-canonical transformation that takes the coupled-cluster self-energy into the hermitian electronic self-energy via

$$\mathbf{\Sigma}(\omega) = \mathbf{B}\tilde{\mathbf{\Sigma}}(\omega)\mathbf{B}^{-1} \ , \tag{B.5.0.9}$$

with $\mathbf{\Sigma}(\omega) = (\mathbf{\Sigma}(\omega))^\dagger$. Therefore, for any arbitrary state $\mathbf{x}$, we have the biorthogonal relationship

$$\mathbf{x}^\dagger\mathbf{\Sigma}(\omega)\mathbf{x} = \tilde{\mathbf{w}}^\dagger\tilde{\mathbf{\Sigma}}(\omega)\mathbf{w} \tag{B.5.0.10}$$

which holds for the general states $\mathbf{x}$ and $\mathbf{w}$ related by the invertible transformation $\mathbf{w} = \mathbf{B}^{-1}\mathbf{x}$. As a result, we immediately conclude that the coupled-cluster self-energy is biorthogonally positive semi-definite as a result of the positive semi-definite property of the electronic self-energy [40, 41, 126]. This property is summarized by the following equations for the imaginary part of the *retarded* CC self-energy

$$\mathrm{Im}\left(\tilde{\mathbf{w}}^\dagger\tilde{\mathbf{\Sigma}}(\omega)\mathbf{w}\right) \leq 0 \tag{B.5.0.11}$$

for an arbitrary state $\mathbf{w}$ and its associated state $\tilde{\mathbf{w}}$. Therefore, the CC self-energy preserves causality in the biorthogonal formalism.

The pseudo-hermitian property displayed in coupled-cluster theory can be further demonstrated by the relationship between the hermitian electronic structure Hamiltonian H, and the similarity transformed non-hermitian Hamiltonian $\bar{H}$:

$$H = e^T\bar{H}e^{-T} \ . \tag{B.5.0.12}$$

From this relationship, we find that the similarity transformed Hamiltonian is necessarily pseudo-hermitian with respect to the metric defined by

$$\tau = (e^T)^\dagger e^T \ . \tag{B.5.0.13}$$

Clearly this metric is hermitian and possesses an inverse. Therefore, coupled-cluster theory can be formulated as a biorthogonal pseudo-hermitian quantum theory with a non trivial metric defined by Eq. B.5.0.13.

B.6 Coupled-cluster ground state energy from the coupled-cluster self-energy

To show how the ground-state energy is obtained from the coupled-cluster self-energy, we use the relationship between the effective interactions given in Appendix B.2. The additional terms generated from the expectation values such as $-\frac{1}{2}\langle\tilde{\Psi}_0|\bar{W}|\Phi_0\rangle$ and so on give rise to the correct prefactors required to generate the CC amplitude equations. This can be seen by re-arranging the terms in Eq. 3.9.0.14 as

$$\begin{aligned} E_0^{\mathrm{CC}} = E_0^{\mathrm{CC}} &+ \frac{1}{2}\sum_{ia}\lambda_a^i F_{ai} + \frac{1}{2}\sum_{ka}\lambda_a^k\left(\bar{h}_{ak} + \sum_i \chi_{ai,ki} - \frac{1}{2!}\sum_{ij}\bar{h}_{aij,kij} + \cdots\right) \\ &+ \frac{1}{(2!)^3}\sum_{iklab}\lambda_{ab}^{kl}\left(\chi_{abi,kli} - \bar{h}_{abi,kli} - \sum_m \bar{h}_{abim,klim} - \cdots\right) \\ &- \frac{1}{2\cdot(3!)^2}\sum_{ijkabc}\lambda_{abc}^{ijk}\left(\bar{h}_{abc,ijk} + \sum_m \bar{h}_{abim,klim} + \cdots\right) + \cdots \end{aligned} \tag{B.6.0.1}$$

where the additional terms outside the brackets contain the four-body interaction matrices contracted with the corresponding four-body de-excitation amplitudes and so on. We can identify the terms in brackets as the effective interactions defined in Appendix B.2, $\{F_{pq}, \chi_{pq,rs}, \chi_{pqr,stu}, \cdots\}$, that arise when normal-ordering the similarity transformed Hamiltonian with respect to the reference state. To make this explicit, for the first bracketed term of Eq. B.6.0.1, we have terms of the form

$$\begin{aligned} \bar{h}_{ak} + \sum_i \chi_{ai,ki} - \frac{1}{2!}\sum_{ij}\bar{h}_{aij,kij} + \cdots &= \bar{h}_{ak} + \sum_i \bar{h}_{ai,ki} + \sum_{ij}\bar{h}_{aij,kij} + \cdots - \frac{1}{2!}\sum_{ij}\bar{h}_{aij,kij} + \cdots \\ &= \bar{h}_{ak} + \sum_i \bar{h}_{ai,ki} + \frac{1}{2!}\sum_{ij}\bar{h}_{aij,kij} + \cdots \\ &= F_{ai} \ , \end{aligned} \tag{B.6.0.2}$$

where we have used the expansion for $\chi_{ai,ki}$ given in Appendix B.2. From this analysis it is clear that the correct pre-factors required to form the CC amplitude equations are generated by subtraction of the missing higher-body expectation values that are not included in the coupled-cluster Galitskii-Migdal formula (Eq. 3.9.0.5). The second line of Eq. B.6.0.1 vanishes as the series in the brackets cancels the effective interaction, $\chi_{abi,kli}$.

B.7 Algebraic Diagrammatic Construction of the coupled-cluster self-energy

To demonstrate this, we use the Lippmann-Schwinger equation [4]

$$\Big((\omega \mp i\eta)\mathbb{1} - (\bar{\mathbf{K}}^{\lessgtr} + \bar{\mathbf{C}}^{\lessgtr})\Big)^{-1}_{LL'} = \sum_{L''}\Big((\omega \mp i\eta)\mathbb{1} - \bar{\mathbf{K}}^{\lessgtr}\Big)^{-1}_{LL''} \sum_{n=0}^{\infty}\left(\bar{\mathbf{C}}^{\lessgtr}\Big((\omega \mp i\eta)\mathbb{1} - \bar{\mathbf{K}}^{\lessgtr}\Big)^{-1}\right)^{n}_{L''L'} \tag{B.7.0.1}$$

where $L = J, A$ is a general composite index representing either forward- or backward-time ISCs. By taking the second Born approximation for this propagator [3], we have

$$\begin{aligned}\Big((\omega \mp i\eta)\mathbb{1} - (\bar{\mathbf{K}}^{\lessgtr} + \bar{\mathbf{C}}^{\lessgtr})\Big)^{-1}_{LL'} \approx{}& \Big((\omega \mp i\eta)\mathbb{1} - \bar{\mathbf{K}}^{\lessgtr}\Big)^{-1}_{LL'} \\ &+ \sum_{L''L'''}\Big((\omega \mp i\eta)\mathbb{1} - \bar{\mathbf{K}}^{\lessgtr}\Big)^{-1}_{LL''}\bar{\mathbf{C}}^{\lessgtr}_{L''L'''}\Big((\omega \mp i\eta)\mathbb{1} - \bar{\mathbf{K}}^{\lessgtr}\Big)^{-1}_{L'''L'}.\end{aligned} \tag{B.7.0.2}$$

Inserting Eq. B.7.0.2 into Eq. 3.10.2.9, using the expression for the interaction matrices in Eqs 4.2.0.2a and 4.2.0.2b, gives the series of Feynman diagrams depicted in Figure 3.3. At third-order, a self-energy Feynman diagram contains $3! = 6$ different time-orderings or Goldstone self-energy diagrams [13, 35, 41]. These are distributed equally in the form of three distinct forward-time and three distinct backward-time Goldstone self-energy diagrams, $\tilde{\Sigma}^{\mathrm{F}}(\omega)/\tilde{\Sigma}^{\mathrm{B}}(\omega)$. To illustrate these results, we take the forward-time self-energy contribution of the fifth diagram of Figure 3.3. There are three different Goldstone diagrams corresponding to the forward-time component of this diagram. The first time-ordering gives the Goldstone diagram:

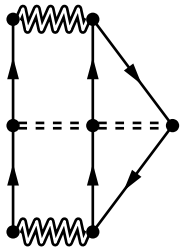

$$= \sum_{\substack{JJ'\\J''J'''}} \tilde{U}^{\mathrm{2p1h,2b}}_{p,J}\Big((\omega + i\eta)\mathbb{1} - \bar{\mathbf{K}}^{>}\Big)^{-1}_{JJ'}\bar{\mathbf{C}}^{>,\mathrm{3b}}_{J'J''}\Big((\omega + i\eta)\mathbb{1} - \bar{\mathbf{K}}^{>}\Big)^{-1}_{J''J'''}\bar{U}^{\mathrm{2p1h}}_{J''',q}\,, \tag{B.7.0.3}$$

remembering that the 2p1h ISC index, $J \equiv (i; a < b)$. From the diagram, we immediately identify the coupling matrix elements as $\tilde{U}^{\text{2p1h,2b}}_{p,J} = \tilde{\Xi}_{pi,ab}$ and $\bar{U}^{\text{2p1h}}_{J''',q} = \tilde{\Xi}_{cd,qj}$. The three-body interaction matrix element is $\bar{\mathbf{C}}^{>,\text{3b}}_{J'J''} = -\tilde{\chi}_{abj,cdi} = \tilde{\chi}_{jab,cid}$, where we use the antisymmetry of the effective interaction matrix element.

The second time-ordering gives rise to the following Goldstone diagram:

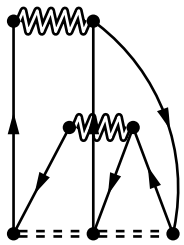

$$= \sum_{JJ'} \tilde{U}^{\text{2p1h,2b}}_{p,J} \Big((\omega + i\eta)\mathbb{1} - \bar{\mathbf{K}}^{>} \Big)^{-1}_{JJ'} \bar{U}^{\text{3b}}_{J',q} \ , \tag{B.7.0.4}$$

from which, we can immediately identify the first coupling matrix as $\tilde{U}^{\text{2p1h,2b}}_{p,J} = \tilde{\Xi}_{pi,ab}$. The second coupling matrix element contains effects resulting from the three-body interaction and is given by

$$\bar{U}^{\text{3b}}_{J,q} = \frac{1}{2} \sum_{klc} \frac{\tilde{\chi}_{abc,kli} \tilde{\Xi}_{kl,qc}}{\epsilon_k + \epsilon_l + \epsilon_i - \epsilon_a - \epsilon_b - \epsilon_c} = 0 \ . \tag{B.7.0.5}$$

This term vanishes as a result of the CC amplitude equations: $\tilde{\chi}_{abc,kli} = 0$. Therefore, the second time-ordered contribution vanishes as a result of the CC amplitude equations. The third and final time-ordered contribution to this coupled-cluster self-energy Feynman diagram is given by the Goldstone diagram:

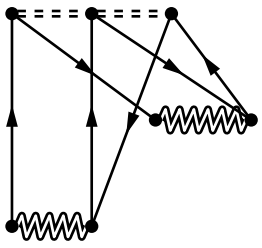

$$= \sum_{JJ'} \tilde{U}^{\text{3b}}_{p,J} \Big((\omega + i\eta)\mathbb{1} - \bar{\mathbf{K}}^{>} \Big)^{-1}_{JJ'} \bar{U}^{\text{2p1h}}_{J',q} \ . \tag{B.7.0.6}$$

The first coupling matrix element contains the three-body effective interaction and evaluates to give

$$\tilde{U}^{\text{3b}}_{p,J} = \frac{1}{2} \sum_{klc} \frac{\tilde{\chi}_{kli,abc} \tilde{\Xi}_{pc,kl}}{\epsilon_k + \epsilon_l + \epsilon_i - \epsilon_a - \epsilon_b - \epsilon_c} = 0 \ . \tag{B.7.0.7}$$

This coupling term also vanishes due to the structure of the CC similarity transformed Hamiltonian as effective interactions that have four or more lines below a vertex are zero: $\tilde{\chi}_{kli,abc} = 0$. The second coupling matrix element is identified as $\bar{U}^{\text{2p1h}}_{J',q} = \tilde{\Xi}_{ab,qi}$. Therefore, the third time-ordered contribution to the CC self-energy Feynman diagram also vanishes as a result of the CC similarity transformation.

Bringing these results together, the forward-time contribution of this third-order self-energy diagram, $\tilde{\Sigma}^{\mathrm{F,3b}}_{pq}(\omega)$, is given by

$$\tilde{\Sigma}^{\mathrm{F,3b}}_{pq}(\omega) = \sum_{\substack{JJ' \\ J''J'''}} \tilde{U}^{\mathrm{2p1h,2b}}_{p,J} \Big((\omega + i\eta)\mathbb{1} - \bar{\mathbf{K}}^{>} \Big)^{-1}_{JJ'} \bar{\mathbf{C}}^{>,\mathrm{3b}}_{J'J''} \Big((\omega + i\eta)\mathbb{1} - \bar{\mathbf{K}}^{>} \Big)^{-1}_{J''J'''} \bar{U}^{\mathrm{2p1h}}_{J''',q} \ . \tag{B.7.0.8}$$

The forward-time component of the second-order diagram, the second diagram of Figure 3.3, evaluates to

$$\tilde{\Sigma}^{\mathrm{F,2b}}_{pq}(\omega) = \sum_{JJ'} \tilde{U}^{\mathrm{2p1h,2b}}_{p,J} \Big((\omega + i\eta)\mathbb{1} - \bar{\mathbf{K}}^{>} \Big)^{-1}_{JJ'} \bar{U}^{\mathrm{2p1h}}_{J',q} \ . \tag{B.7.0.9}$$

Adding Eqs B.7.0.8 and B.7.0.9 together, we can use the spectral representation of the self-energy and the corresponding Lippmann-Schwinger equation (Eq. B.7.0.1) to perform the infinite-order summation of these two diagrams by writing

$$\tilde{\Sigma}^{\mathrm{F,2p1h(3b)}}_{pq}(\omega) = \sum_{JJ'} \tilde{U}^{\mathrm{2p1h,2b}}_{p,J} \Big((\omega + i\eta)\mathbb{1} - (\bar{\mathbf{K}}^{>} + \bar{\mathbf{C}}^{>,\mathrm{3b}}) \Big)^{-1}_{JJ'} \bar{U}^{\mathrm{2p1h}}_{J',q} \ . \tag{B.7.0.10}$$

Using the upfolded Dyson supermatrix representation, we can simply sum this self-energy contribution to infinite-order by identification of the three-body interaction matrix element: $\bar{\mathbf{C}}^{>,\mathrm{3b}}_{JJ'}$. Performing this analysis for all the forward- and backward-time interaction matrix elements defined in Eqs 3.10.2.6a and 3.10.2.6b will give the infinite-order summation of the CC self-energy diagrams depicted in Figure 3.3. The same analysis presented here can also be applied to the set of diagrams depicted in Figure 3.1 and yields the coupled-cluster Dyson supermatrix of Eq. 3.10.2.4.

C

Derivations For Exact Connection Between The Electronic Self-Energy and Coupled-Cluster Doubles Theory

Contents

C.1 Coupled-cluster doubles particle-hole-time decoupled electronic self-energy diagrams

The set of one-particle irreducible particle-hole-time decoupled self-energy diagrams that generate the exact CCD amplitude equations are shown in Figure C.1. In Figure C.1, we introduce the self-consistent notation, whereby the interaction and coupling matrices are now dependent on the solution of the CCD amplitudes. This amounts to replacing the MP2 amplitudes that are be obtained from the perturbative electronic self-energy diagrams by the full CCD amplitudes: $(t_{ij}^{ab})_{\mathrm{MP2}} \rightarrow t_{ij}^{ab}$.

Downfolding Eq. 4.3.0.4, using the modified self-consistent coupling and interaction matrices that depend on the exact CCD amplitudes (Eqs 4.3.0.10 and 4.3.0.11)

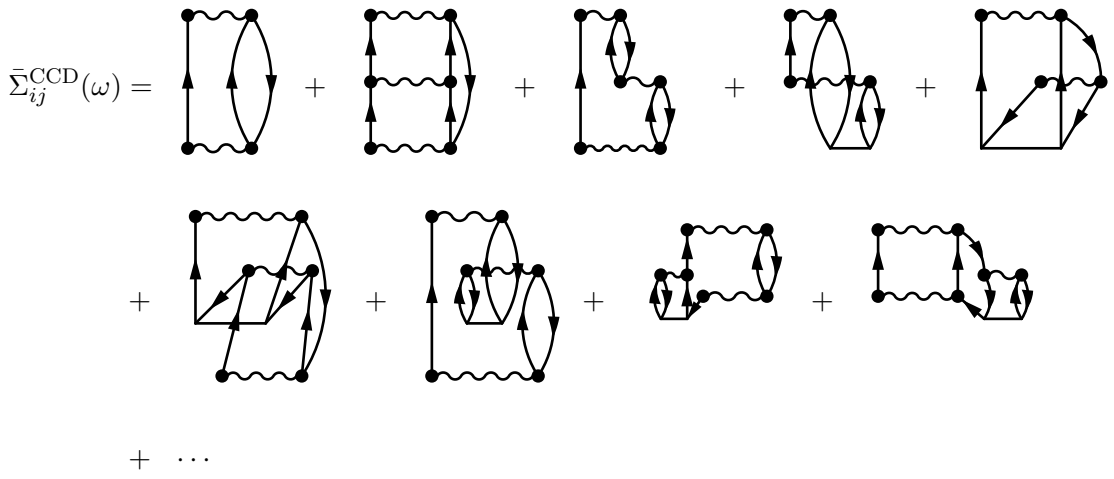

Figure C.1: The 2p1h/2h1p excitation restricted Feynman-Goldstone one-particle irreducible electronic particle-hole-time decoupled self-energy diagrams that generate the CCD amplitude equations when summed to infinite-order by the Dyson supermatrix. The final four diagrams depicted are fourth-order self-energy contributions. The solid line represents the CCD amplitude, t_{ij}^{ab}.

leads to the expression

$$\bar{\Sigma}_{ij}^{\mathrm{CCD}}(\omega) = \frac{1}{4}\sum_{\substack{kab\\lcd}} \bar{U}_{i,abk}\Big((\omega+i\eta)\mathbb{1} - (\bar{\mathbf{K}}^{>,\mathrm{2p1h}} + \bar{\mathbf{C}}^{>,\mathrm{2p1h}})\Big)^{-1}_{kab,lcd} U^{\mathrm{sc}}_{cdl,j} \ , \tag{C.1.0.1}$$

where the interaction matrix elements, $(\bar{\mathbf{K}}^{>,\mathrm{2p1h}}_{kab,jcd}+\bar{\mathbf{C}}^{>,\mathrm{2p1h}}_{kab,jcd})$, are obtained by using Eqs 4.3.0.11 to update the interaction matrices defined in Eq. 4.2.0.2a. The self-consistent coupling matrix elements, $U^{\mathrm{sc}}_{cdl,j}$, are defined in Eq. 4.3.0.10. The infinite series of self-energy diagrams contained in Eq. C.1.0.1 is presented in Figure C.1.

C.2 Coupled-cluster doubles amplitude equations from the particle-hole-time decoupled self-energy

For the virtual block of the particle-hole-time decoupled self-energy, we have the following supermatrix eigenvalue problem

$$\begin{pmatrix} \mathbf{f} & \bar{\mathbf{V}} \\ \mathbf{V}^{\dagger} & \mathbf{K}^{<,\mathrm{2h1p}} + \mathbf{C}^{<,\mathrm{2h1p}} \end{pmatrix} \begin{pmatrix} \tilde{\mathbf{X}} \\ \tilde{\mathbf{Y}} \end{pmatrix} = \begin{pmatrix} \tilde{\mathbf{X}} \\ \tilde{\mathbf{Y}} \end{pmatrix} \tilde{\mathcal{E}} \ . \tag{C.2.0.1}$$

Defining the effective doubles amplitudes as $\tilde{\mathbf{T}} = \tilde{\mathbf{Y}}\tilde{\mathbf{X}}^{-1}$ we have the extended Fock operator and self-energy Riccati equation

$$\mathbf{F}\tilde{\mathbf{X}} = \tilde{\mathbf{X}}\tilde{\mathcal{E}} \tag{C.2.0.2a}$$

$$\mathbf{V}^{\dagger} + (\mathbf{K}^{<,\mathrm{2h1p}} + \mathbf{C}^{<,\mathrm{2h1p}})\tilde{\mathbf{T}} - \tilde{\mathbf{T}}\mathbf{F} = \mathbf{0} \ , \tag{C.2.0.2b}$$

where $\mathbf{F} = \mathbf{f} + \bar{\mathbf{V}}\tilde{\mathbf{T}}$. We immediately apply the constraint of particle-hole symmetry: $\tilde{t}_{ij}^{ab} = -(t_{ij}^{ab})^*$. The corresponding extended Fock operator in the virtual space is then given by

$$\begin{aligned} F_{ab} &= \epsilon_a \delta_{ab} + \frac{1}{2} \sum_{klc} \langle ac||kl\rangle \, \tilde{t}_{kl}^{bc} \\ &= \epsilon_a \delta_{ab} - \frac{1}{2} \sum_{klc} \langle kl||bc\rangle \, t_{kl}^{ac} \ , \end{aligned} \tag{C.2.0.3}$$

where we have used the constraint of hermiticity: $F_{ab} = F_{ba}^*$. This expression is exactly that obtained from CCD theory for the extended Fock operator [4, 7]. The amplitude equations become

$$\begin{aligned} &\langle ij||ab\rangle + \frac{1}{2} \sum_{cd} \langle ab||cd\rangle \, (t_{ij}^{cd})_{\mathrm{MP2}} + \sum_{kc} \langle ka||jc\rangle \, (t_{ik}^{bc})_{\mathrm{MP2}} - \sum_{kc} \langle ak||ci\rangle \, (t_{jk}^{bc})_{\mathrm{MP2}} - \Delta_{ij}^{ab} \tilde{t}_{ij}^{ab} \\ &- \frac{1}{2} \sum_{kl} \langle ij||kl\rangle \, \tilde{t}_{kl}^{ab} + \sum_{kc} \langle jc||kb\rangle \, \tilde{t}_{ik}^{ac} - \sum_{kc} \langle ic||kb\rangle \, \tilde{t}_{jk}^{ac} - \frac{1}{2} \sum_{klcd} \tilde{t}_{kl}^{ac} \langle cd||kl\rangle \, \tilde{t}_{ij}^{bd} = 0 \ , \end{aligned} \tag{C.2.0.4}$$

which can be re-written by imposing the particle-hole symmetry constraint as

$$\begin{aligned} &\langle ab||ij\rangle + \frac{1}{2} \sum_{cd} \langle ab||cd\rangle \, (t_{ij}^{cd})_{\mathrm{MP2}} + \sum_{kc} \langle ka||jc\rangle \, (t_{ik}^{bc})_{\mathrm{MP2}} - \sum_{kc} \langle ak||ci\rangle \, (t_{jk}^{bc})_{\mathrm{MP2}} + \Delta_{ij}^{ab} t_{ij}^{ab} \\ &+ \frac{1}{2} \sum_{kl} \langle ij||kl\rangle \, t_{kl}^{ab} - \sum_{kc} \langle kb||jc\rangle \, t_{ik}^{ac} + \sum_{kc} \langle kb||ic\rangle \, t_{jk}^{ac} - \frac{1}{2} \sum_{klcd} t_{kl}^{ac} \langle kl||cd\rangle \, t_{ij}^{bd} = 0 \ . \end{aligned} \tag{C.2.0.5}$$

To generate the full CCD equations from the virtual block, we must self-consistently update the coupling and interaction matrices as follows. First, we modify the coupling matrices to be self-consistently determined from the doubles amplitude solutions:

$$V_{p,kla}^{\mathrm{sc}} = \langle pa||kl\rangle + \sum_{cm} \langle pm||kc\rangle \, t_{ml}^{ca} - \sum_{cm} \langle pm||lc\rangle \, t_{mk}^{ca} + \frac{1}{2} \sum_{cd} \langle pa||cd\rangle \, t_{kl}^{cd} \ . \tag{C.2.0.6}$$

This is analogous to the procedure carried out for the occupied block. Then we update the interaction matrices between the 2h1p states to become self-consistently dependent on the doubles amplitudes as

$$\epsilon_a \delta_{ab} \to \epsilon_a \delta_{ab} - \frac{1}{2} \sum_{ijc} \langle ij||bc\rangle \, t_{ij}^{ca} = F_{ab} \tag{C.2.0.7a}$$

$$\epsilon_i \delta_{ij} \to \epsilon_i \delta_{ij} + \frac{1}{2} \sum_{kcd} \langle ik||cd\rangle \, t_{jk}^{cd} = F_{ij} \tag{C.2.0.7b}$$

$$\langle ij||kl\rangle \to \langle ij||kl\rangle + \frac{1}{2} \sum_{cd} \langle ij||cd\rangle \, t_{kl}^{cd} = \chi_{ij,kl} \tag{C.2.0.7c}$$

$$\langle ja||bi\rangle \to \langle ja||bi\rangle + \sum_{kc} \langle jk||bc\rangle \, t_{ik}^{ac} = \chi_{ja,bi} \ . \tag{C.2.0.7d}$$

Using these quantities, we write the modified self-consistent interaction matrices as

$$\begin{aligned}(\bar{\mathbf{K}}^{<,\mathrm{2h1p}}_{ija,klb} + \bar{\mathbf{C}}^{<,\mathrm{2h1p}}_{ija,klb}) = {} & F_{ik}\delta_{ab}\delta_{jl} + F_{jl}\delta_{ab}\delta_{ik} - F_{ba}\delta_{ik}\delta_{jl} \\ & - F_{il}\delta_{ab}\delta_{jk} - F_{jk}\delta_{ab}\delta_{il} + F_{ba}\delta_{il}\delta_{jk} \\ & + \chi_{ib,al}\delta_{jk} + \chi_{jb,ak}\delta_{il} - \chi_{ij,kl}\delta_{ab} \\ & - \chi_{ib,ak}\delta_{jl} - \chi_{jb,al}\delta_{ik} \ .\end{aligned} \tag{C.2.0.8}$$

Resolving these equations in the self-energy Riccati equation (Eq. C.2.0.2b) yields the full CCD amplitude equations.

D

Dyson Supermatrix Formulation for Electron–Phonon Interactions and Computational Details

Contents

D.1 Definition of rotated coupling matrices

Here, we provide expressions for the rotated coupling matrices as a result of changing basis to the clamped-ion BSE exction basis. The matrices are given by

$$\tilde{M}^{(I)}_{v''c''\mathbf{k}''\mathbf{k}'''\nu,S'} = \sum_{c_1} g_{c''c_1\nu}(\mathbf{k}''', \mathbf{k}'' - \mathbf{k}''') A^{S'}_{v''c_1\mathbf{k}'''} \tag{D.1.0.1a}$$

$$M^{(II)}_{S,v''c''\mathbf{k}''\mathbf{k}'''\nu} = -\sum_{c_1} A^{S*}_{v''c_1\mathbf{k}'''} g_{c_1c''\nu}(\mathbf{k}'', \mathbf{k}''' - \mathbf{k}'') \tag{D.1.0.1b}$$

$$\tilde{M}^{(II)}_{v''c''\mathbf{k}''\mathbf{k}'''\nu,S'} = \sum_{v_1} g^*_{v''v_1\nu}(\mathbf{k}'', \mathbf{k}''' - \mathbf{k}'') A^{S'}_{v_1c''\mathbf{k}''} \ . \tag{D.1.0.1c}$$

The $\mathbf{\Lambda}^{(+)}$ matrix is unchanged by this basis transformation. For the model system introduced in Section 6.7, the matrix elements are given by

$$M^{(I)}_{S,\mathbf{k}''\mathbf{k}'''} = -A^{S*}_{\mathbf{k}''} g^{F*}_{\mathbf{k}''-\mathbf{k}'''} \tag{D.1.0.2a}$$

$$\tilde{M}^{(I)}_{\mathbf{k}''\mathbf{k}''',S'} = g^{F}_{\mathbf{k}''-\mathbf{k}'''} A^{S'}_{\mathbf{k}'''} \tag{D.1.0.2b}$$

$$M^{(II)}_{S,\mathbf{k}''\mathbf{k}'''} = -A^{S*}_{\mathbf{k}'''} g^{F}_{\mathbf{k}'''-\mathbf{k}''} \tag{D.1.0.2c}$$

$$\tilde{M}^{(II)}_{\mathbf{k}''\mathbf{k}''',S'} = g^{F*}_{\mathbf{k}'''-\mathbf{k}''} A^{S'}_{\mathbf{k}''} \tag{D.1.0.2d}$$

$$\Lambda^{(+)}_{\mathbf{k}\mathbf{k}',\mathbf{k}''\mathbf{k}'''} = \left(\frac{|\mathbf{k}|^2}{2m_e} + \frac{|\mathbf{k}'|^2}{2m_h} + \omega_{LO} \right) \delta_{\mathbf{k}\mathbf{k}''} \delta_{\mathbf{k}'\mathbf{k}'''} \ . \tag{D.1.0.2e}$$

D.2 Interpretation of the phonon-screened Dyson supermatrix

To demonstrate the coupling to multiparticle Green's functions contained in the K^{ph} frequency-dependent kernel, we introduce the basis of finite momentum free electron-hole pairs: $|vc\mathbf{k}\mathbf{k}'\rangle$. Remaining within the Tamm-Dancoff and quasi-boson approximations, we write the Hamiltonian consisting of independent electron-hole pairs and a bath of phonons as

$$H_0^{eh,ph} = \sum_{vc\mathbf{k}\mathbf{k}'} (\epsilon_{c\mathbf{k}} - \epsilon_{v\mathbf{k}'}) C^{\dagger}_{vc\mathbf{k}\mathbf{k}'} C_{vc\mathbf{k}\mathbf{k}'} + \sum_{\mathbf{q}\nu} \omega_{\mathbf{q}\nu} a^{\dagger}_{\mathbf{q}\nu} a_{\mathbf{q}\nu} \ . \tag{D.2.0.1}$$

Here, the operators $C^{\dagger}_{vc\mathbf{k}\mathbf{k}'}/C_{vc\mathbf{k}\mathbf{k}'}$ create/annihilate free electron-hole pairs in the state $|vc\mathbf{k}\mathbf{k}'\rangle$ and $a^{\dagger}_{\mathbf{q}\nu}/a_{\mathbf{q}\nu}$ are the creation/annihilation operators corresponding to a phonon of wavevector $\mathbf{q}$ and branch ν. It is clear that the product state of a free electron-hole pair with a phonon is an eigenstate of this Hamiltonian:

$$H_0^{eh,ph} \, |vc\mathbf{k}\mathbf{k}', n_\nu\rangle = (\epsilon_{c\mathbf{k}} - \epsilon_{v\mathbf{k}'} + \omega_{\mathbf{k}-\mathbf{k}'\nu}) \, |vc\mathbf{k}\mathbf{k}', n_\nu\rangle \ , \tag{D.2.0.2}$$

where $|vc\mathbf{k}\mathbf{k}', n_\nu\rangle = C^{\dagger}_{vc\mathbf{k}\mathbf{k}'} a^{\dagger}_{\mathbf{k}-\mathbf{k}'\nu} |\text{vac}\rangle$. In this equation we have imposed the conservation of momentum of the combined electron-hole-pair-phonon (EHPP) state such that $\mathbf{q} = \mathbf{k} - \mathbf{k}'$. Using this eigenvalue equation, we can write the interaction matrix appearing in Eqs 6.2.1.5 as

$$\begin{aligned} \Lambda^{(+)}_{vc\mathbf{k}\mathbf{k}'\nu,v'c'\mathbf{k}''\mathbf{k}'''\nu'} &= \langle vc\mathbf{k}\mathbf{k}', n_\nu | H_0^{eh,ph} | v'c'\mathbf{k}''\mathbf{k}''', n_{\nu'} \rangle \\ &= (\epsilon_{c\mathbf{k}} - \epsilon_{v\mathbf{k}'} + \omega_{\mathbf{k}-\mathbf{k}'\nu}) \delta_{vv'} \delta_{cc'} \delta_{\mathbf{k}\mathbf{k}''} \delta_{\mathbf{k}'\mathbf{k}'''} \delta_{\nu\nu'} \ . \end{aligned} \tag{D.2.0.3}$$

The resolvent of this matrix is therefore given by the retarded propagator

$$\begin{aligned} G^{eh,ph(0),R}_{vc\mathbf{k}\mathbf{k}'\nu}(\omega) &= \Big((\omega+i\eta)\mathbb{1} - H_0^{eh,ph}\Big)^{-1}_{vc\mathbf{k}\mathbf{k}'\nu,vc\mathbf{k}\mathbf{k}'\nu} \\ &= \Big((\omega+i\eta)\mathbb{1} - \mathbf{\Lambda}^{(+)}\Big)^{-1}_{vc\mathbf{k}\mathbf{k}'\nu,vc\mathbf{k}\mathbf{k}'\nu} \\ &= \frac{1}{\omega - \Delta_{c\mathbf{k},v'\mathbf{k}'} - \omega_{\mathbf{k}-\mathbf{k}'\nu} + i\eta}\ , \end{aligned} \tag{D.2.0.4}$$

which corresponds to the retarded Green's function of a non-interacting free EHPP product state [7, 142, 143]. The notation $G^{eh,ph(0),R}_{v_1c_1\mathbf{k}_1\mathbf{k}_2\nu}(\omega)$ is used to denote the diagonal elements of the EHPP Green's function. Therefore, $\mathbf{D}^{ph}$ represents the coupling of the zero momentum electron-hole pair propagator to all possible finite-momentum free EHPP propagators, with the couplings mediated by the electron-phonon vertices contained in the $\mathbf{M}^{(I)/(II)}$ and $\tilde{\mathbf{M}}^{(I)/(II)}$ matrices. Using this result, we can make this coupling structure explicit to re-write the phonon-screened BSE kernel as

$$\begin{aligned} K^{ph}_{SS'}(\omega) = &\sum_{\substack{v_1c_1\\ \mathbf{k}_1\mathbf{k}_2\\ \nu}} M^{(I)}_{S,v_1c_1\mathbf{k}_1\mathbf{k_2}\nu} G^{eh,ph(0),R}_{v_1c_1\mathbf{k}_1\mathbf{k}_2\nu}(\omega) \tilde{M}^{(I)}_{v_1c_1\mathbf{k}_1\mathbf{k}_2\nu,S'} \\ &+ \sum_{\substack{v_1c_1\\ \mathbf{k}_1\mathbf{k}_2\\ \nu}} M^{(II)}_{S,v_1c_1\mathbf{k}_1\mathbf{k_2}\nu} G^{eh,ph(0),R}_{v_1c_1\mathbf{k}_1\mathbf{k}_2\nu}(\omega) \tilde{M}^{(II)}_{v_1c_1\mathbf{k}_1\mathbf{k_2}\nu,S'}. \end{aligned} \tag{D.2.0.5}$$

This structure emphasizes that we can obtain information from the phonon-screened Dyson supermatrix that goes beyond just the 'single-particle' propagator of the theory. For example, by taking the resolvent of the supermatrix (Eq. 6.2.1.4) in the subspace of EHPP states yields the retarded correlated EHPP Green's function as (focusing only on the diagonal elements)

$$\begin{aligned} \mathcal{G}^{eh,ph,R}_{vc\mathbf{k}\mathbf{k}'\nu}(\omega) &= \Big((\omega+i\eta)\mathbb{1} - \mathbf{D}^{ph}\Big)^{-1}_{vc\mathbf{k}\mathbf{k}'\nu,vc\mathbf{k}\mathbf{k}'\nu} \\ &= \sum_{\mathcal{S}} \Big(W^{\mathcal{S},+}_{vc\mathbf{k}\mathbf{k}'\nu}\tilde{W}^{\mathcal{S},+}_{vc\mathbf{k}\mathbf{k}'\nu} + W^{\mathcal{S},-}_{vc\mathbf{k}\mathbf{k}'\nu}\tilde{W}^{\mathcal{S},-}_{vc\mathbf{k}\mathbf{k}'\nu}\Big)\frac{1}{\omega - \tilde{\Omega}_{\mathcal{S}} + i\eta}\ . \end{aligned} \tag{D.2.0.6}$$

If we take the trace of Eq. D.2.0.6 over the electron-hole pair states only ($\{vc\mathbf{k}\mathbf{k}'\}$), we obtain

$$\Pi^{R}_{\nu\nu'}(\omega) = \sum_{\mathcal{S}} \frac{1}{\omega - \tilde{\Omega}_{\mathcal{S}} + i\eta} \sum_{vc\mathbf{k}\mathbf{k}'} \Big(W^{\mathcal{S},+}_{vc\mathbf{k}\mathbf{k}'\nu}\tilde{W}^{\mathcal{S},+}_{vc\mathbf{k}\mathbf{k}'\nu'} + W^{\mathcal{S},-}_{vc\mathbf{k}\mathbf{k}'\nu}\tilde{W}^{\mathcal{S},-}_{vc\mathbf{k}\mathbf{k}'\nu'}\Big)\ . \tag{D.2.0.7}$$

This quantity can be viewed as a correlated phonon self-energy resulting from phonon-exciton interactions. These identities allow us to define the spectral function of the

correlated EHPP states as

$$\begin{aligned}\mathcal{A}^{eh,ph}(\omega) &= -\frac{1}{\pi}\text{Im tr}\mathcal{G}^{eh,ph,R}(\omega) \\ &= -\frac{1}{\pi}\text{Im}\sum_{\nu}\Pi^{R}_{\nu\nu}(\omega) \\ &= -\frac{1}{\pi}\text{Im}\sum_{\mathcal{S}}\frac{(1-Z_{\mathcal{S}})}{\omega-\tilde{\Omega}_{\mathcal{S}}+i\eta}.\end{aligned} \tag{D.2.0.8}$$

Here, we have used Eq. 6.2.1.8 to identify the renormalization factor $Z_{\mathcal{S}}$.

D.3 Fan-Migdal Dyson supermatrices

In this appendix we demonstrate how to construct the Fan-Midgal Dyson supermatrices from the dynamical Fan-Migdal electron-phonon and exciton-phonon self-energies, respectively. For the electron-phonon Fan-Migdal self-energy, we find the following expressions for the coupling and interaction matrices:

$$M^{(I)}_{n\mathbf{k},n''\mathbf{k}''\mathbf{k}_1\nu} = g^{*}_{n''n\nu}(\mathbf{k},\mathbf{k}''-\mathbf{k})\delta_{\mathbf{k}\mathbf{k}_1}\sqrt{N_B(\omega_{\mathbf{k}''-\mathbf{k}\nu})+1-f_{n''\mathbf{k}''}} \tag{D.3.0.1a}$$

$$\tilde{M}^{(I)}_{n'''\mathbf{k}'''\mathbf{k}_2\nu',n'\mathbf{k}'} = g_{n'''n'\nu'}(\mathbf{k}',\mathbf{k}'''-\mathbf{k}')\delta_{\mathbf{k}_2\mathbf{k}'}\sqrt{N_B(\omega_{\mathbf{k}'''-\mathbf{k}'\nu'})+1-f_{n'''\mathbf{k}'''}} \tag{D.3.0.1b}$$

$$N^{(I)}_{n\mathbf{k},n''\mathbf{k}''\mathbf{k}_1\nu} = g^{*}_{n''n\nu}(\mathbf{k},\mathbf{k}''-\mathbf{k})\delta_{\mathbf{k}\mathbf{k}_1}\sqrt{N_B(\omega_{\mathbf{k}''-\mathbf{k}\nu})+f_{n''\mathbf{k}''}} \tag{D.3.0.1c}$$

$$\tilde{N}^{(I)}_{n'''\mathbf{k}'''\mathbf{k}_2\nu',n'\mathbf{k}'} = g_{n'''n'\nu'}(\mathbf{k}',\mathbf{k}'''-\mathbf{k}')\delta_{\mathbf{k}_2\mathbf{k}'}\sqrt{N_B(\omega_{\mathbf{k}'''-\mathbf{k}'\nu'})+f_{n'''\mathbf{k}'''}} \tag{D.3.0.1d}$$

$$\Lambda^{(+)}_{n''\mathbf{k}''\mathbf{k}_1\nu,n'''\mathbf{k}'''\mathbf{k}_2\nu'} = (\epsilon_{n''\mathbf{k}''}+\omega_{\mathbf{k}''-\mathbf{k}_1\nu}-i\eta)\delta_{n''n'''}\delta_{\mathbf{k}''\mathbf{k}'''}\delta_{\mathbf{k}_1\mathbf{k}_2}\delta_{\nu\nu'} \tag{D.3.0.1e}$$

$$\Lambda^{(-)}_{n''\mathbf{k}''\mathbf{k}_1\nu,n'''\mathbf{k}'''\mathbf{k}_2\nu'} = (\epsilon_{n''\mathbf{k}''}-\omega_{\mathbf{k}''-\mathbf{k}_1\nu}-i\eta)\delta_{n''n'''}\delta_{\mathbf{k}''\mathbf{k}'''}\delta_{\mathbf{k}_1\mathbf{k}_2}\delta_{\nu\nu'}\ . \tag{D.3.0.1f}$$

Here, $f_{n\mathbf{k}}$ is the Fermi-Dirac distribution. The electron-phonon Fan-Migdal Dyson supermatrix is then constructed as

$$\mathbf{D}^{\text{FMd}}(T) = \begin{pmatrix} H^{\text{el}}_{n\mathbf{k},n'\mathbf{k}'} & M^{(I)}_{n\mathbf{k},J'}(T) & N^{(I)}_{n\mathbf{k},J'}(T) \\ \tilde{M}^{(I)}_{J,n'\mathbf{k}'}(T) & \mathbf{\Lambda}^{(+)}_{JJ'} & \mathbf{0} \\ \tilde{N}^{(I)}_{J',n'\mathbf{k}'}(T) & \mathbf{0} & \mathbf{\Lambda}^{(-)}_{JJ'} \end{pmatrix}, \tag{D.3.0.2}$$

where we have defined $J \equiv n\mathbf{k}\mathbf{k}'\nu$ as the composite index. Using Eqs D.3.0.1, it can easily be shown that downfolding this expression into the single-particle subspace reproduces the retarded dynamical Fan-Midgal self-energy:

$$\begin{aligned}\Sigma^{\text{FMd},R}_{n\mathbf{k},n'\mathbf{k}'}(\omega,T) =& \delta_{\mathbf{k}\mathbf{k}'}\sum_{n''\mathbf{q}\nu} g^{*}_{n''n\nu}(\mathbf{k},\mathbf{q})g_{n''n'\nu}(\mathbf{k},\mathbf{q}) \\ & \left[\frac{N_B(\omega_{\mathbf{q}\nu})+1-f_{n''\mathbf{k}+\mathbf{q}}}{\omega-\epsilon_{n''\mathbf{k}+\mathbf{q}}-\omega_{\mathbf{q}\nu}+i\eta}+\frac{N_B(\omega_{\mathbf{q}\nu})+f_{n''\mathbf{k}+\mathbf{q}}}{\omega-\epsilon_{n''\mathbf{k}+\mathbf{q}}+\omega_{\mathbf{q}\nu}+i\eta}\right].\end{aligned} \tag{D.3.0.3}$$

The same procedure can be carried out for the dynamical exciton-phonon Fan-Migdal self-energy [211]. The corresponding expressions for the coupling and interaction matrices is given by

$$M^{(I)}_{S\mathbf{Q},S''\mathbf{Q}''\mathbf{Q}_1\nu} = G^*_{S''S\nu}(\mathbf{Q},\mathbf{Q}''-\mathbf{Q})\delta_{\mathbf{Q}\mathbf{Q}_1}\sqrt{N_B(\omega_{\mathbf{Q}''-\mathbf{Q}\nu})+1} \tag{D.3.0.4a}$$

$$\tilde{M}^{(I)}_{S'''\mathbf{Q}'''\mathbf{Q}_2\nu',S'\mathbf{Q}'} = G_{S'''S'\nu'}(\mathbf{Q}',\mathbf{Q}'''-\mathbf{Q}')\delta_{\mathbf{Q}_2\mathbf{Q}'}\sqrt{N_B(\omega_{\mathbf{Q}'''-\mathbf{Q}'\nu'})+1} \tag{D.3.0.4b}$$

$$N^{(I)}_{S\mathbf{Q},S''\mathbf{Q}''\mathbf{Q}_1\nu} = G^*_{S''S\nu}(\mathbf{Q},\mathbf{Q}''-\mathbf{Q})\delta_{\mathbf{Q}\mathbf{Q}_1}\sqrt{N_B(\omega_{\mathbf{Q}''-\mathbf{Q}\nu})} \tag{D.3.0.4c}$$

$$\tilde{N}^{(I)}_{S'''\mathbf{Q}'''\mathbf{Q}_2\nu',S'\mathbf{Q}'} = G_{S'''S'\nu'}(\mathbf{Q}',\mathbf{Q}'''-\mathbf{Q}')\delta_{\mathbf{Q}_2\mathbf{Q}'}\sqrt{N_B(\omega_{\mathbf{Q}'''-\mathbf{Q}'\nu'})} \tag{D.3.0.4d}$$

$$\Lambda^{(+)}_{S''\mathbf{Q}''\mathbf{Q}_1\nu,S'''\mathbf{Q}'''\mathbf{Q}_2\nu'} = (\Omega_{S''\mathbf{Q}''}+\omega_{\mathbf{Q}''-\mathbf{Q}_1\nu}-i\eta)\delta_{S''S'''}\delta_{\mathbf{Q}''\mathbf{Q}'''}\delta_{\mathbf{Q}_1\mathbf{Q}_2}\delta_{\nu\nu'} \tag{D.3.0.4e}$$

$$\Lambda^{(-)}_{S''\mathbf{Q}''\mathbf{Q}_1\nu,S'''\mathbf{Q}'''\mathbf{Q}_2\nu'} = (\Omega_{S''\mathbf{Q}''}-\omega_{\mathbf{Q}''-\mathbf{Q}_1\nu}-i\eta)\delta_{S''S'''}\delta_{\mathbf{Q}''\mathbf{Q}'''}\delta_{\mathbf{Q}_1\mathbf{Q}_2}\delta_{\nu\nu'}\ . \tag{D.3.0.4f}$$

The result is the exction-phonon Fan-Migdal Dyson supermatrix:

$$\mathbf{D}^{\text{xct-FMd}}(T) = \begin{pmatrix} H^{\text{BSE}}_{S\mathbf{Q},S'\mathbf{Q}'} & M^{(I)}_{S\mathbf{Q},J'}(T) & N^{(I)}_{S\mathbf{Q},J'}(T) \\ \tilde{M}^{(I)}_{J,S'\mathbf{Q}'}(T) & \mathbf{\Lambda}^{(+)}_{JJ'} & \mathbf{0} \\ \tilde{N}^{(I)}_{J,S'\mathbf{Q}'}(T) & \mathbf{0} & \mathbf{\Lambda}^{(-)}_{JJ'} \end{pmatrix}, \tag{D.3.0.5}$$

where now the composite index is defined as $J \equiv S\mathbf{Q}\mathbf{Q}'\nu$. For both these self-energy approximations we have $(\mathbf{M}^{(I)})^\dagger = \tilde{\mathbf{M}}^{(I)}$ and $(\mathbf{N}^{(I)})^\dagger = \tilde{\mathbf{N}}^{(I)}$. This means both matrices can be written symbolically as

$$\mathbf{D}^{\text{FMd}}(T) = \begin{pmatrix} \mathbf{H} & \mathbf{M}_1(T) & \mathbf{N}_1(T) \\ \mathbf{M}_1^\dagger(T) & \mathbf{\Lambda}^{(+)} & \mathbf{0} \\ \mathbf{N}_1^\dagger(T) & \mathbf{0} & \mathbf{\Lambda}^{(-)} \end{pmatrix}. \tag{D.3.0.6}$$

D.4 Temperature-dependent Dyson supermatrix blocks

The temperature-dependent coupling blocks of the finite temperature Dyson supermatrix derived in Section 6.2.3 are given by:

$$M^{(I)}_{S,v''c''\mathbf{k}''\mathbf{k}'''\nu}(T) = -\sum_{v_1} A^{S*}_{v_1c''\mathbf{k}''} g^{*}_{v_1v''\nu}(\mathbf{k}''', \mathbf{k}'' - \mathbf{k}''')\sqrt{N_B(\omega_{\mathbf{k}''-\mathbf{k}'''\nu}) + 1} \tag{D.4.0.1a}$$

$$\tilde{M}^{(I)}_{v''c''\mathbf{k}''\mathbf{k}'''\nu,S'}(T) = \sum_{c_1} g_{c''c_1\nu}(\mathbf{k}''', \mathbf{k}'' - \mathbf{k}''') A^{S'}_{v''c_1\mathbf{k}'''}\sqrt{N_B(\omega_{\mathbf{k}''-\mathbf{k}'''\nu}) + 1} \tag{D.4.0.1b}$$

$$M^{(II)}_{S,v''c''\mathbf{k}''\mathbf{k}'''\nu}(T) = -\sum_{c_1} A^{S*}_{v''c_1\mathbf{k}'''} g_{c_1c''\nu}(\mathbf{k}'', \mathbf{k}''' - \mathbf{k}'')\sqrt{N_B(\omega_{\mathbf{k}'''-\mathbf{k}''\nu}) + 1} \tag{D.4.0.1c}$$

$$\tilde{M}^{(II)}_{v''c''\mathbf{k}''\mathbf{k}'''\nu,S'}(T) = \sum_{v_1} g^{*}_{v''v_1\nu}(\mathbf{k}'', \mathbf{k}''' - \mathbf{k}'') A^{S'}_{v_1c''\mathbf{k}''}\sqrt{N_B(\omega_{\mathbf{k}'''-\mathbf{k}''\nu}) + 1} \tag{D.4.0.1d}$$

$$\Lambda^{(+)}_{vc\mathbf{k}\mathbf{k}'\nu,v'c'\mathbf{k}''\mathbf{k}'''\nu'} = (\Delta_{c\mathbf{k},v\mathbf{k}'} + \omega_{\mathbf{k}-\mathbf{k}'\nu})\delta_{vv'}\delta_{cc'}\delta_{\mathbf{k}\mathbf{k}''}\delta_{\mathbf{k}'\mathbf{k}'''}\delta_{\nu\nu'}. \tag{D.4.0.1e}$$

$$N^{(I)}_{S,v''c''\mathbf{k}''\mathbf{k}'''\nu}(T) = -\sum_{v_1} A^{S*}_{v_1c''\mathbf{k}''} g^{*}_{v_1v''\nu}(\mathbf{k}''', \mathbf{k}'' - \mathbf{k}''')\sqrt{N_B(\omega_{\mathbf{k}''-\mathbf{k}'''\nu})} \tag{D.4.0.1f}$$

$$\tilde{N}^{(I)}_{v''c''\mathbf{k}''\mathbf{k}'''\nu,S'}(T) = \sum_{c_1} g_{c''c_1\nu}(\mathbf{k}''', \mathbf{k}'' - \mathbf{k}''') A^{S'}_{v''c_1\mathbf{k}'''}\sqrt{N_B(\omega_{\mathbf{k}''-\mathbf{k}'''\nu})} \tag{D.4.0.1g}$$

$$N^{(II)}_{S,v''c''\mathbf{k}''\mathbf{k}'''\nu}(T) = -\sum_{c_1} A^{S*}_{v''c_1\mathbf{k}'''} g_{c_1c''\nu}(\mathbf{k}'', \mathbf{k}''' - \mathbf{k}'')\sqrt{N_B(\omega_{\mathbf{k}'''-\mathbf{k}''\nu})} \tag{D.4.0.1h}$$

$$\tilde{N}^{(II)}_{v''c''\mathbf{k}''\mathbf{k}'''\nu,S'}(T) = \sum_{v_1} g^{*}_{v''v_1\nu}(\mathbf{k}'', \mathbf{k}''' - \mathbf{k}'') A^{S'}_{v_1c''\mathbf{k}''}\sqrt{N_B(\omega_{\mathbf{k}'''-\mathbf{k}''\nu})} \tag{D.4.0.1i}$$

$$\Lambda^{(-)}_{vc\mathbf{k}\mathbf{k}'\nu,v'c'\mathbf{k}''\mathbf{k}'''\nu'} = (\Delta_{c\mathbf{k},v\mathbf{k}'} - \omega_{\mathbf{k}-\mathbf{k}'\nu})\delta_{vv'}\delta_{cc'}\delta_{\mathbf{k}\mathbf{k}''}\delta_{\mathbf{k}'\mathbf{k}'''}\delta_{\nu\nu'}\ . \tag{D.4.0.1j}$$

By introduction of the composite index $J \equiv vc\mathbf{k}\mathbf{k}'\nu$, we can write the temperature-dependent Dyson supermatrix in terms of these matrix elements as

$$\mathbf{D}^{ph}(T) = \begin{pmatrix} \Omega_S\delta_{SS'} & M^{(I)}_{S,J'}(T) & M^{(II)}_{S,J'}(T) & N^{(I)}_{S,J'}(T) & N^{(II)}_{S,J'}(T) \\ \tilde{M}^{(I)}_{J,S'}(T) & \mathbf{\Lambda}^{(+)}_{JJ'} & \mathbf{0} & \mathbf{0} & \mathbf{0} \\ \tilde{M}^{(II)}_{J,S'}(T) & \mathbf{0} & \mathbf{\Lambda}^{(+)}_{JJ'} & \mathbf{0} & \mathbf{0} \\ \tilde{N}^{(I)}_{J,S'}(T) & \mathbf{0} & \mathbf{0} & \mathbf{\Lambda}^{(-)}_{JJ'} & \mathbf{0} \\ \tilde{N}^{(II)}_{J,S'}(T) & \mathbf{0} & \mathbf{0} & \mathbf{0} & \mathbf{\Lambda}^{(-)}_{JJ'} \end{pmatrix}. \tag{D.4.0.2}$$

D.5 Generalized Davidson algorithm

If we substantially increase the size of the Krylov subspace, or we simply want to compute a target eigenvalue of the full untruncated Dyson supermatrix, we employ the generalized Davidson algorithm [249]. The generalized Davidson algorithm is an extremely powerful iterative diagonalization method used to compute the spectrum of a general matrix about a target eigenvalue solution. It is particularly well adapted for sparse,

non-hermitian matrices. Here, we provide a brief summary but the reader is referred to Refs [131] and [249] for a more thorough account of the method. Below we simply provide an overview of the *right-sided* generalized Davidson algorithm.

Given a huge matrix, such as $\mathbf{D}^{ph}(T)$, the generalized Davidson method is centered around a subspace constructed from preconditioned residuals as opposed to the conceptually 'simpler' Krylov subspace (Eq. 6.6.0.1). The preconditioned residual space is given by

$$\mathcal{R}_n(\mathbf{D}^{ph};\mathbf{v}_1) \equiv \text{span}\{\mathbf{v}_1, \mathbf{A}^{-1}\mathbf{r}_1, \mathbf{A}^{-1}\mathbf{r}_2, \cdots, \mathbf{A}^{-1}\mathbf{r}_n\}, \tag{D.5.0.1}$$

where $\mathbf{A}^{-1} = (\mathbf{D}^{ph} - \tilde{\Omega}_{\mathcal{S}}\mathbb{1})^{-1}$ is the preconditioner, with $\tilde{\Omega}_{\mathcal{S}}$ as the target eigenvalue and $\mathbf{r}_i$ as the residual vector obtained at each iteration. The initial vector, $\mathbf{v}_1$, is usually initialized as a random vector in the full space spanned by $\mathbf{D}^{ph}$. At a given step in the iteration cycle, the subspace is obtained and expanded by solution of the reduced 'effective' eigenvalue problem

$$(\mathbf{V}_n^{\dagger}\mathbf{D}^{ph}\mathbf{V}_n)\mathbf{X}_{\mathcal{S}} = \mathbf{X}_{\mathcal{S}}\tilde{\Omega}_{\mathcal{S}} \ , \tag{D.5.0.2}$$

where $\mathbf{V}_n$ is the matrix of the orthogonalized preconditioned residual basis. Now, for each effective eigenpair, $(\tilde{\Omega}_{\mathcal{S}}, \mathbf{X}_{\mathcal{S}})$, we have a corresponding Ritz pair for the full supermatrix by projection into the full space:

$$\tilde{\mathbf{X}}_{\mathcal{S}} = \mathbf{V}_n\mathbf{X}_{\mathcal{S}} \ , \tag{D.5.0.3}$$

where $\tilde{\mathbf{X}}_{\mathcal{S}}$ is the approximate right eigenvector of the full $\mathbf{D}^{ph}$ supermatrix. The residual used to expand the pre-conditioned subspace is generated by the difference between the 'model' solution and 'exact' solution as

$$\mathbf{r}_i = \mathbf{D}^{ph}\tilde{\mathbf{X}}_{\mathcal{S}} - \tilde{\Omega}_{\mathcal{S}}\tilde{\mathbf{X}}_{\mathcal{S}} \ , \tag{D.5.0.4}$$

where $\mathbf{r}_i$ is the i-th iteration of the residual vector. From this expression, the next search direction is obtained from the correction equation obtained by solution of the linearized full eigenvalue problem

$$\begin{aligned} (\mathbf{D}^{ph} - \tilde{\Omega}_{\mathcal{S}}\mathbb{1})\mathbf{s}_i &= -\mathbf{r}_i \\ \implies \mathbf{s}_i &= -\mathbf{A}^{-1}\mathbf{r}_i \ . \end{aligned} \tag{D.5.0.5}$$

This correction vector, $\mathbf{s}_i$, is then orthogonalized with respect to the rest of the existing preconditioned subspace and the algorithm is iterated until the norm of the residual vector (Eq. D.5.0.4) is within a prespecified convergence threshold. Therefore, the iterative

generalized Davidson subspace is generated by an initial starting vector and the subsequent correction vectors constructed at each iteration until convergence is achieved. This results in an incredible reduction in the cost for diagonalization of $\mathbf{D}^{ph}$ and is particularly suited for solution of the smallest, largest or prespecified target eigenpairs. The sparse structure of the $\mathbf{D}^{ph}$ supermatrix means that the algorithm is highly efficient, making use of sparse matrix-vector multiplication speedups at each iteration.

D.6 Computational Details

System	$N_c N_v (N_{\mathbf{k}})^2 N_\nu$	$\dim(\mathbf{D}^{ph}(T))$	$\dim(\mathbf{D}^{ph}_{\mathcal{K}_r}(T))$
CdS	86,882,562	347,530,288	2,440
GaN	83,283,876	333,135,544	3,240
$BiVO_4$	109,244,304	436,977,266	3,250

Table D.1: Dimensions of the finite temperature *ab initio* Dyson supermatrices.

Our density functional theory (DFT) and density functional perturbation theory (DFPT) calculations are carried out under the Perdew-Burke-Ernzerhof (PBE) functional [250] implemented within the Quantum Espresso software package [251, 252]. For all systems, we use fully-relativistic optimized norm-conserving Vanderbilt pseudopotentials taken from Pseudo Dojo [253, 254]. We use Wannier90 [255] and EPW [256] to generate Wannier states and Wannier-Fourier interpolated electron-phonon matrix elements. We used the Berkeley*GW* software package for the *GW* and clamped-ion *GW*-BSE calculations [257]. For CdS, GaN, and $BiVO_4$, we compute the phonon dispersions on $6 \times 6 \times 6$, $6 \times 6 \times 4$, and $3 \times 3 \times 4$ grids of $\mathbf{q}$-points [2, 6].

We perform *GW* calculations within a Godby-Needs generalized plasmon pole model [258], using the DFT-PBE Kohn-Sham starting point wavefunctions, to converge the quasiparticle band gaps within 0.1 eV. The *GW* calculation parameters are: CdS (120 Ry plane wave cutoff, 750 bands, 35 Ry polarizability cutoff, $6 \times 6 \times 6$ half-shifted $\mathbf{k}$-grid), GaN (120 Ry plane wave cutoff, 750 bands, 35 Ry polarizability cutoff, $6 \times 6 \times 4$ half-shifted $\mathbf{k}$-grid), $BiVO_4$ (512 bands, 30 Ry polarizability cutoff, $3 \times 3 \times 4$ half-shifted $\mathbf{k}$-grid). For all systems, the electronic BSE kernel is computed on the same $\mathbf{k}$-grid as the *GW* eigenvalues. For CdS and

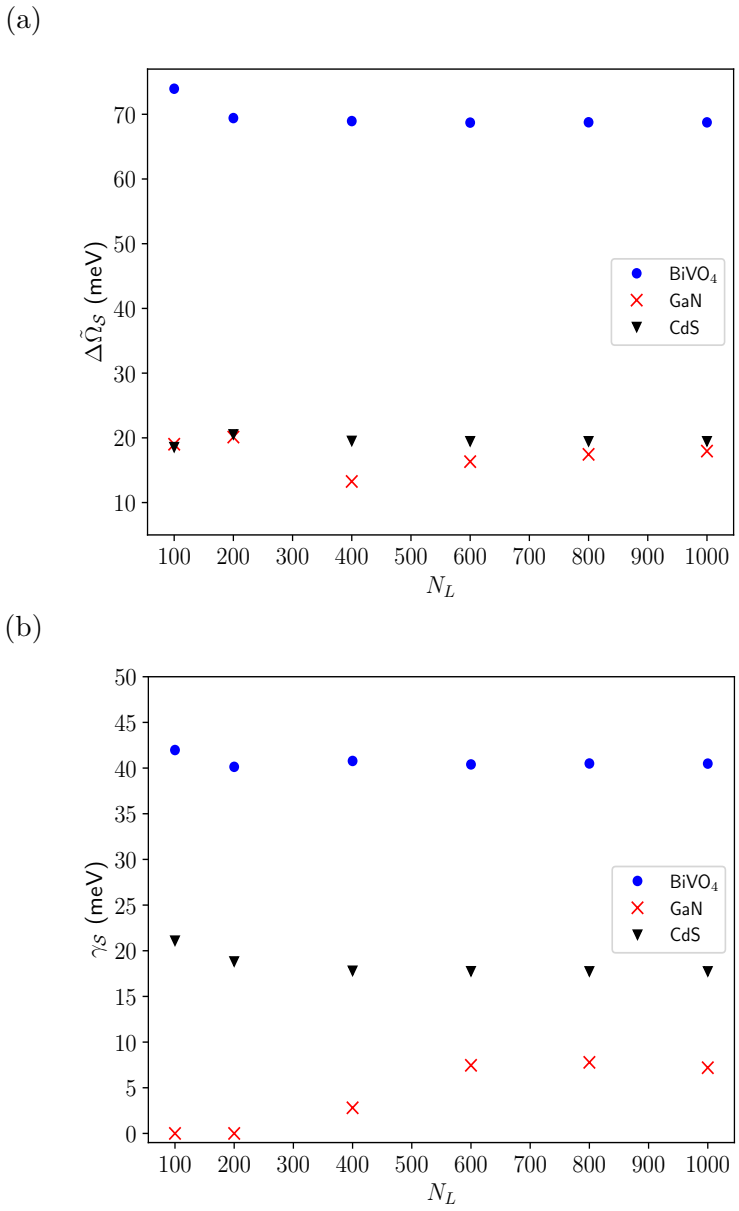

Figure D.1: Convergence of *ab initio* calculations with Krylov subspace size (N_L): CdS (300K), GaN (300K) and $BiVO_4$ (200K). (a) $\Delta\tilde{\Omega}_{\mathcal{S}}$: energy change. (b) $\gamma_{\mathcal{S}}$: dissociation rate.

GaN, we interpolate the kernel onto a fine **k**-grid using one conduction and three valence bands, whereas for $BiVO_4$ we interpolate the kernel onto two conduction and two valence bands. For CdS and GaN, we employ a Γ-centered patch, with a cutoff bound of ±0.06 (in crystal coordinates) along each direction, drawn from fine **k**-grids of $100 \times 100 \times 100$ and $100 \times 100 \times 60$, respectively [2]. For $BiVO_4$, from Ref. [6], we use the patched grid of $9 \times 9 \times 11$, drawn from a fine grid of $24 \times 24 \times 32$, both being centered about $\mathbf{k} = [1/6, -1/6, 1/8]$ in crystal coordinates. This corresponds to the medium-sized patch employed in Ref. [6]. The shift in the patch centering corresponds to the point where the lowest-lying exciton

wavefunction is centered in reciprocal space. We employ gauge consistent Wannier-Fourier interpolation to obtain the electron-phonon matrix elements computed from EPW and the clamped-ion exciton coefficients computed using Berkeley*GW* [2, 6]. The gauge consistent Wannier-Fourier interpolation and construction of the Dyson supermatrices are computed using an in-house code library. The dense patches employed in this work give rise to the full Dyson supermatrix dimensions displayed in Table D.1.

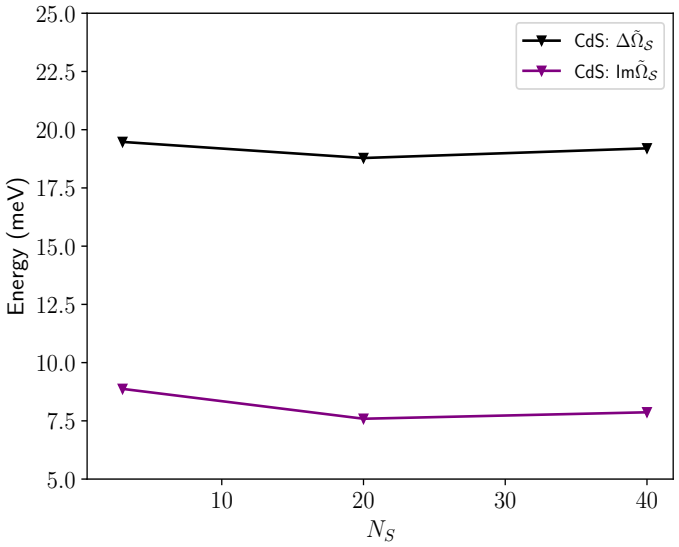

Figure D.2: CdS (T =300K, $N_L = 800$) convergence with exciton subspace size N_S: $\Delta\tilde{\Omega}_S$ (energy change) and $|\mathrm{Im}\tilde{\Omega}_S|$ (imaginary part).

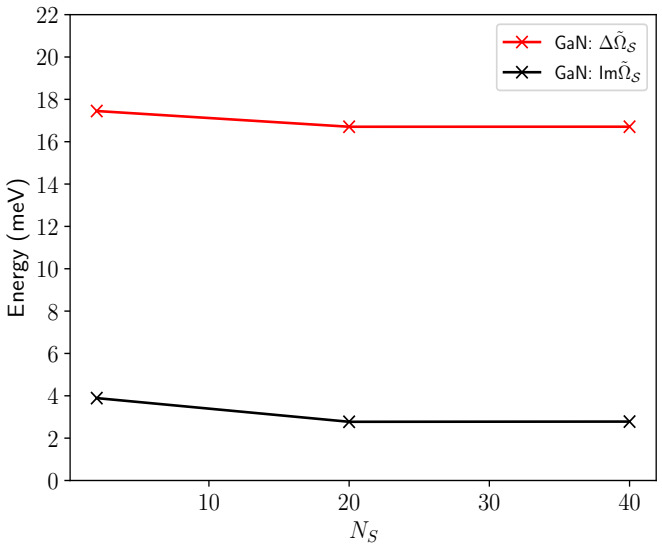

Figure D.3: GaN (T =300K, $N_L = 800$) convergence with exciton subspace size N_S: $\Delta\tilde{\Omega}_S$ (energy change) and $\mathrm{Im}\tilde{\Omega}_S$ (imaginary part).

In Figures D.1a and D.1b, we plot the convergence of the energy and scattering rate for the lowest bound state as the Krylov subspace size (N_L) increases for the three systems. For display purposes, we plot the convergence of the eigenvalue at 300K for CdS and GaN, whereas for $BiVO_4$ we plot the convergence of the eigenvalue obtained at 200K. We choose these temperatures for our convergence plots as they correspond to significantly enhanced electron-phonon coupling resulting from the temperature dependence of the wings of the $\mathbf{D}^{ph}(T)$ supermatrix [10]. For all systems, we see that convergence of both the real and imaginary parts of the lowest eigenvalue to within 0.1 meV are achieved using a Lanczos subspace spanned by $N_L = 1000$ basis vectors. However, both CdS and $BiVO_4$ display faster convergence than GaN. This is related to the fact that there is a large change in the imaginary part of the eigenvalue for GaN at 300K which arise as the increase in the size of the Lanczos subspace begins to resolve the dissociation scattering channel.

For both GaN and CdS, with $N_L = 800$ at 300K, we find the change in the real and imaginary parts of the lowest eigenvalue to be within 1 meV as the exciton subspace increases from 1 to 40. This is displayed in Figures D.2 and D.3. For $BiVO_4$, our calculations in Figure D.4, with $N_L = 800$ at 300K, demonstrate that the real and imaginary parts of the lowest renormalized exciton state are within 6 meV and 0.5 meV, respectfully as the exciton subspace increases from 1 to 50. The eigenvalue is converged at $N_S = 50$. This is in agreement with Ref [6], where our prior work demonstrated that the change in the real and imaginary parts of the lowest renormalized exciton state of $BiVO_4$ vary by less than 6 meV at 300K as the exciton subspace increases from 1 to 70. Additionally, it was also demonstrated in Ref [6] that the convergence of the exciton energy and wavefunction is achieved at $N_S = 50$, in agreement with the results presented here.

Every *ab initio* Dyson supermatrix constructed in this thesis is of the order of hundreds of millions in size. However, obtaining an exact full diagonalization of these non-hermitian matrices is unfeasible on current supercomputing systems. In addition, the relevant quasiparticle eigenvalues of interest (eigenvalues of the largest spectral weight) are so-called *interior* eigenvalues meaning that they do not exist at the extrema of the spectrum of $\mathbf{D}^{ph}(T)$. Even the massively parallelized and scalable generalized Davidson diagonalization method can fail to converge to any eigenvalues of these matrices at high temperatures. We found this to be the case for $BiVO_4$ at 300K where the iterative solver did not

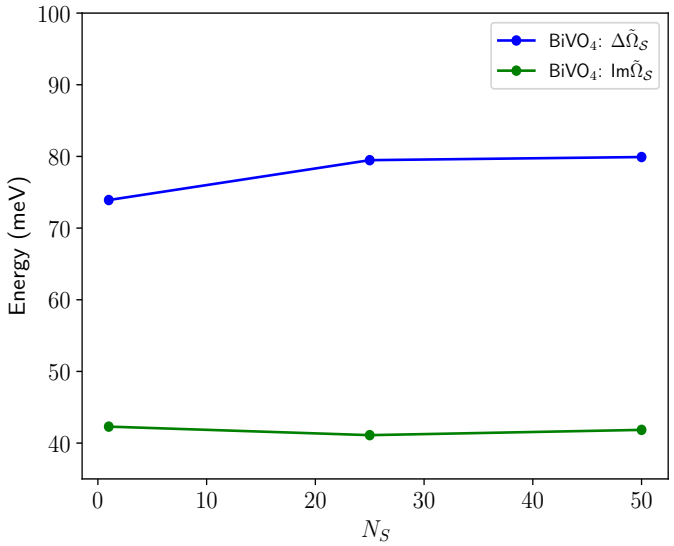

Figure D.4: $BiVO_4$ (T =300K, N_L = 800) convergence with exciton subspace size N_S: $\Delta\tilde{\Omega}_{\mathcal{S}}$ (energy change) and $|\mathrm{Im}\tilde{\Omega}_{\mathcal{S}}|$ (imaginary part).

converge to any interior eigenvalues. This is due to the fact that the pre-conditioner for the generalized Davidson method is not effective enough to converge to any complex eigenvalues for matrices of this size.

References

[1] C. J. N. Coveney and D. P. Tew, 'A regularized second-order correlation method from Green's function theory', Journal of Chemical Theory and Computation **19**, 3915 (2023).

[2] A. M. Alvertis, J. B. Haber, Z. Li, C. J. N. Coveney, S. G. Louie, M. R. Filip and J. B. Neaton, 'Phonon screening and dissociation of excitons at finite temperatures from first principles', Proceedings of the National Academy of Sciences **121**, e2403434121 (2024).

[3] C. J. N. Coveney, J. B. Haber, A. M. Alvertis, J. B. Neaton and M. R. Filip, 'Rearrangement collision theory of phonon-driven exciton dissociation', Physical Review B **110**, 054307 (2024).

[4] C. J. N. Coveney and D. P. Tew, 'Diagrammatic theory of the irreducible coupled-cluster self-energy', Physical Review B **112**, 045104 (2025).

[5] C. J. N. Coveney, 'Uncovering relationships between the electronic self-energy and coupled-cluster doubles theory', The Journal of Physical Chemistry A **129**, 8689 (2025).

[6] S. E. Gant, A. M. Alvertis, C. J. N. Coveney, J. B. Haber, M. R. Filip and J. B. Neaton, 'Ultrafast spontaneous exciton dissociation via phonon emission in $BiVO_4$', Physical Review Research **8**, 013105 (2026).

[7] C. J. N. Coveney and D. P. Tew, 'Non-hermitian Green's function theory with N-body interactions: The coupled-cluster similarity transformation', Physical Review Research **8**, 013322 (2026).

[8] N. M. Tubman, C. J. N. Coveney, C.-E. Hsu, A. Montoya-Castillo, M. R. Filip, J. B. Neaton, Z. Li, V. Vlcek and A. M. Alvertis, 'Theory of *ab initio* downfolding with arbitrary range electron-phonon coupling', Physical Review B **113**, 245144 (2026).

[9] C. J. N. Coveney, N. M. Tubman, C.-E. Hsu, A. Montoya-Castillo, M. R. Filip, J. B. Neaton, Z. Li, V. Vlcek and A. M. Alvertis, 'Phonon-mediated electron attraction in $SrTiO_3$ via the generalized Fröhlich and deformation potential mechanisms', arXiv preprint arXiv:2501.17230 (2025).

[10] C. J. N. Coveney, S. E. Gant, A. M. Alvertis, J. B. Haber, J. B. Neaton and M. R. Filip, 'Non-perturbative solutions of the finite temperature Dyson equation in periodic systems via an *ab initio* supermatrix formulation: application to the lattice screening of excitons', To be Submitted (2026).

[11] C. J. N. Coveney, S. E. Gant, A. M. Alvertis, J. B. Haber, J. B. Neaton and M. R. Filip, 'Non-perturbative finite temperature exciton-phonon scattering in heterogeneous semiconductors', To be Submitted (2026).

[12] P. A. M. Dirac, *The principles of quantum mechanics*, 27 (Oxford University Press, 1930).

[13] A. Fetter and J. D. Walecka, *Quantum theory of many particle systems* (McGraw-Hill, 1971).

[14] G. D. Mahan, *Many-particle physics* (Springer Science & Business Media, 2000).

[15] A. A. Abrikosov, L. P. Gorkov and I. E. Dzyaloshinski, *Methods of quantum field theory in statistical physics* (Courier Corporation, 1975).

[16] A. Altland and B. D. Simons, *Condensed matter field theory* (Cambridge University Press, 2010).

[17] G. Stefanucci and R. Van Leeuwen, *Nonequilibrium many-body theory of quantum systems: a modern introduction* (Cambridge University Press, 2013).

[18] M. Born and J. R. Oppenheimer, 'Zur quantentheorie der molekeln', Annalen der physik **389**, 457 (1927).

[19] P. Ring and P. Schuck, *The nuclear many-body problem* (Springer Science & Business Media, 2004).

[20] A. Carbone, A. Cipollone, C. Barbieri, A. Rios and A. Polls, 'Self-consistent Green's functions formalism with three-body interactions', Physical Review C **88**, 054326 (2013).

[21] L. V. Keldysh, in *Selected papers of leonid v keldysh* (World Scientific, 2024), pp. 47–55.

[22] J. Schwinger, 'Brownian motion of a quantum oscillator', Journal of Mathematical Physics **2**, 407 (1961).

[23] J.-M. Lihm and S. Poncé, 'Beyond-quasiparticle transport with vertex correction: self-consistent ladder formalism for electron-phonon interactions', Physical Review X **16**, 011008 (2026).

[24] M. Gell-Mann and F. E. Low, 'Quantum electrodynamics at small distances', Physical Review **95**, 1300 (1954).

[25] M. Gell-Mann and F. Low, 'Bound states in quantum field theory', Physical Review **84**, 350 (1951).

[26] R. Kubo, 'Statistical-mechanical theory of irreversible processes. i. general theory and simple applications to magnetic and conduction problems', Journal of the physical society of Japan **12**, 570 (1957).

[27] P. C. Martin and J. Schwinger, 'Theory of many-particle systems. i', Physical Review **115**, 1342 (1959).

[28] H. Ness, L. K. Dash, M. Stankovski and R. W. Godby, '*GW* approximations and vertex corrections on the Keldysh time-loop contour: application for model systems at equilibrium', Physical Review B **84**, 195114 (2011).

[29] H. Ness and L. K. Dash, 'Dynamical equations for time-ordered Green's functions: from the Keldysh time-loop contour to equilibrium at finite and zero temperature', Journal of Physics: Condensed Matter **24**, 505601 (2012).

[30] C. Barbieri and A. Carbone, 'Self-consistent green's function approaches', An Advanced Course in Computational Nuclear Physics: Bridging the Scales from Quarks to Neutron Stars, 571 (2017).

[31] R. De L. Kronig, 'On the theory of dispersion of x-rays', Journal of the Optical Society of America **12**, 547 (1926).

[32] H. K. Kramers, 'On the behavior of atoms in an electromagnetic wave field', in Skand. mat. kongress (1925), pp. 143–153.

[33] G.-C. Wick, 'The evaluation of the collision matrix', Physical Review **80**, 268 (1950).

[34] J. Goldstone, 'Derivation of the Brueckner many-body theory', Proceedings of the Royal Society of London. Series A. Mathematical and Physical Sciences **239**, 267 (1957).

[35] J. Schirmer, *Many-body methods for atoms, molecules and clusters*, Vol. 94 (Springer, 2018).

[36] F. Raimondi and C. Barbieri, 'Algebraic diagrammatic construction formalism with three-body interactions', Physical Review C **97**, 054308 (2018).

[37] V. Somà, T. Duguet and C. Barbieri, '*Ab initio* self-consistent gorkov-green's function calculations of semimagic nuclei: formalism at second order with a two-nucleon interaction', Physical Review C **84**, 064317 (2011).

[38] L. Hedin, 'New method for calculating the one-particle Green's function with application to the electron-gas problem', Physical Review **139**, A796 (1965).

[39] J. Schwinger, 'Quantum electrodynamics. I. A covariant formulation', Physical Review **74**, 1439 (1948).

[40] J. Winter, 'Study of core excitations in one-particle and one-hole nuclei by means of the six-point Green function', Nuclear Physics A **194**, 535 (1972).

[41] J. Schirmer, L. S. Cederbaum and O. Walter, 'New approach to the one-particle Green's function for finite Fermi systems', Physical Review A **28**, 1237 (1983).

[42] F. Caruso, P. Rinke, X. Ren, A. Rubio and M. Scheffler, 'Self-consistent *GW*: all-electron implementation with localized basis functions', Physical Review B **88**, 075105 (2013).

[43] I. Prigogine and T. Y. Petrosky, 'Intrinsic irreversibility in quantum theory', Physica A: Statistical Mechanics and its Applications **147**, 33 (1987).

[44] H. Feshbach and E. Lomon, 'Nucleon-nucleon scattering', Physical Review **102**, 891 (1956).

[45] H. Feshbach, 'Unified theory of nuclear reactions', Annals of Physics **5**, 357 (1958).

[46] U. Fano, 'Effects of configuration interaction on intensities and phase shifts', Physical review **124**, 1866 (1961).

[47] P.-O. Löwdin, 'Partitioning technique, perturbation theory, and rational approximations', International Journal of Quantum Chemistry **21**, 69 (1982).

[48] I. Schur, in *I. schur methods in operator theory and signal processing*, Vol. 18 (Springer, 1986), pp. 31–60.

[49] E. E. Salpeter and H. A. Bethe, 'A relativistic equation for bound-state problems', Physical Review **84**, 1232 (1951).

[50] G. Strinati, 'Application of the Green's functions method to the study of the optical properties of semiconductors', La Rivista del Nuovo Cimento (1978-1999) **11**, 1 (1988).

[51] P. Romaniello, D. Sangalli, J. A. Berger, F. Sottile, L. G. Molinari, L. Reining and G. Onida, 'Double excitations in finite systems', The Journal of Chemical Physics **130** (2009).

[52] D. Zhang, S. N. Steinmann and W. Yang, 'Dynamical second-order Bethe-Salpeter equation kernel: a method for electronic excitation beyond the adiabatic approximation', The Journal of Chemical Physics **139** (2013).

[53] D. Sangalli, P. Romaniello, G. Onida and A. Marini, 'Double excitations in correlated systems: a many–body approach', The Journal of Chemical Physics **134** (2011).

[54] E. Rebolini and J. Toulouse, 'Range-separated time-dependent density-functional theory with a frequency-dependent second-order Bethe-Salpeter correlation kernel', The Journal of Chemical Physics **144** (2016).

[55] V. Olevano, J. Toulouse and P. Schuck, 'A formally exact one-frequency-only Bethe-Salpeter-like equation: similarities and differences between GW+BSE and self-consistent RPA', The Journal of Chemical Physics **150** (2019).

[56] A. Barth and J. Schirmer, 'Theoretical core-level excitation spectra of N_2 and CO by a new polarisation propagator method', Journal of Physics B: Atomic and Molecular Physics **18**, 867 (1985).

[57] M. S. Hybertsen and S. G. Louie, 'Electron correlation in semiconductors and insulators: band gaps and quasiparticle energies', Physical Review B **34**, 5390 (1986).

[58] M. Rohlfing and S. G. Louie, 'Electron-hole excitations in semiconductors and insulators', Physical Review Letters **81**, 2312 (1998).

[59] M. Rohlfing and S. G. Louie, 'Electron-hole excitations and optical spectra from first principles', Physical Review B **62**, 4927 (2000).

[60] G. Strinati, 'Dynamical shift and broadening of core excitons in semiconductors', Physical Review Letters **49**, 1519 (1982).

[61] S. J. Bintrim and T. C. Berkelbach, 'Full-frequency dynamical Bethe–Salpeter equation without frequency and a study of double excitations', The Journal of Chemical Physics **156**, 044114 (2022).

[62] F. Aryasetiawan and O. Gunnarsson, 'The *GW* method', Reports on Progress in Physics **61**, 237 (1998).

[63] P. Romaniello, S. Guyot and L. Reining, 'The self-energy beyond *GW*: local and nonlocal vertex corrections', The Journal of Chemical Physics **131**, 154111 (2009).

[64] P. Romaniello, F. Bechstedt and L. Reining, 'Beyond the *GW* approximation: combining correlation channels', Physical Review B **85**, 155131 (2012).

[65] S. Hirata, A. E. Doran, P. J. Knowles and J. V. Ortiz, 'One-particle many-body Green's function theory: algebraic recursive definitions, linked-diagram theorem, irreducible-diagram theorem, and general-order algorithms', The Journal of Chemical Physics **147**, 044108 (2017).

[66] C. M. Bender and S. Boettcher, 'Real spectra in non-hermitian hamiltonians having PT symmetry', Physical Review Letters **80**, 5243 (1998).

[67] C. M. Bender, 'Making sense of non-hermitian hamiltonians', Reports on Progress in Physics **70**, 947 (2007).

[68] C. M. Bender and D. W. Hook, 'Pt-symmetric quantum mechanics', Reviews of Modern Physics **96**, 045002 (2024).

[69] Y. Ashida, Z. G and M. Ueda, 'Non-hermitian physics', Advances in Physics **69**, 249 (2020).

[70] V. Meden, L. Grunwald and D. M. Kennes, 'PT-symmetric, non-hermitian quantum many-body physics—a methodological perspective', Reports on Progress in Physics **86**, 124501 (2023).

[71] E. J. Bergholtz, J. C. Budich and F. K. Kunst, 'Exceptional topology of non-hermitian systems', Reviews of Modern Physics **93**, 015005 (2021).

[72] G. Barontini, R. Labouvie, F. Stubenrauch, A. Vogler, V. Guarrera and H. Ott, 'Controlling the dynamics of an open many-body quantum system with localized dissipation', Physical Review Letters **110**, 035302 (2013).

[73] N. Shibata and H. Katsura, 'Dissipative spin chain as a non-hermitian Kitaev ladder', Physical Review B **99**, 174303 (2019).

[74] G. Stefanucci, 'Kadanoff-Baym equations for interacting systems with dissipative Lindbladian dynamics', Physical Review Letters **133**, 066901 (2024).

[75] M. Šindelka, L. F. Santos and N. Moiseyev, 'Excited-state quantum phase transitions studied from a non-hermitian perspective', Physical Review A **95**, 010103 (2017).

[76] K. Wang, X. Qiu, L. Xiao, X. Zhan, Z. Bian, W. Yi and P. Xue, 'Simulating dynamic quantum phase transitions in photonic quantum walks', Physical review letters **122**, 020501 (2019).

[77] K. Wang, X. Qiu, L. Xiao, X. Zhan, Z. Bian, B. C. Sanders, W. Yi and P. Xue, 'Observation of emergent momentum–time skyrmions in parity–time-symmetric non-unitary quench dynamics', Nature communications **10**, 2293 (2019).

[78] X. Zhang, K. Hu and F. Li, 'Nonadiabatic dynamics in non-hermitian quantum systems from the quantum metric perspective', Physical Review B **112**, 224305 (2025).

[79] R. El-Ganainy, K. G. Makris, M. Khajavikhan, Z. H. Musslimani, S. Rotter and D. N. Christodoulides, 'Non-hermitian physics and PT symmetry', Nature Physics **14**, 11 (2018).

[80] M.-A. Miri and A. Alu, 'Exceptional points in optics and photonics', Science **363**, eaar7709 (2019).

[81] H. M. Hurst and B. Flebus, 'Non-hermitian physics in magnetic systems', Journal of Applied Physics **132** (2022).

[82] J. Liang, H. Zheng, F. Jin, R. Bao, K. Dini, J. Ren, Y. Liu, M. Król, E. A. Ostrovskaya, E. Estrecho, B. Zhang, T. C. H. Liew and R. Su, 'Twist-induced non-hermitian topology of exciton–polaritons', Nature Physics, 1 (2025).

[83] Q. Liang, D. Xie, Z. Dong, H. Li, H. Li, B. Gadway, W. Yi and B. Yan, 'Dynamic signatures of non-hermitian skin effect and topology in ultracold atoms', Physical Review Letters **129**, 070401 (2022).

[84] E. Zhao, Z. Wang, C. He, T. F. J. Poon, K. K. Pak, Y.-J. Liu, P. Ren, X.-J. Liu and G.-B. Jo, 'Two-dimensional non-hermitian skin effect in an ultracold Fermi gas', Nature **637**, 565 (2025).

[85] I. Shavitt and R. J. Bartlett, *Many-body methods in chemistry and physics: mbpt and coupled-cluster theory* (Cambridge University Press, 2009).

[86] T. Helgaker, P. Jorgensen and J. Olsen, *Molecular electronic-structure theory* (John Wiley & Sons, 2013).

[87] M. Nooijen and J. G. Snijders, 'Coupled-cluster approach to the single-particle Green's function', International Journal of Quantum Chemistry **44**, 55 (1992).

[88] M. Nooijen and J. G. Snijders, 'Coupled-cluster Green's function method: working equations and applications', International Journal of Quantum Chemistry **48**, 15 (1993).

[89] B. Peng and K. Kowalski, 'Coupled-cluster Green's function: analysis of properties originating in the exponential parametrization of the ground-state wave function', Physical Review A **94**, 062512 (2016).

[90] B. Peng and K. Kowalski, 'Green's function coupled-cluster approach: simulating photoelectron spectra for realistic molecular systems', Journal of Chemical Theory and Computation **14**, 4335 (2018).

[91] A. Shee and D. Zgid, 'Coupled-cluster as an impurity solver for Green's function embedding methods', Journal of Chemical Theory and Computation **15**, 6010 (2019).

[92] B. Peng, N. P. Bauman, S. Gulania and K. Kowalski, in *Annual reports in computational chemistry*, Vol. 17 (Elsevier, 2021), pp. 23–53.

[93] A. Shee, C.-N. Yeh and D. Zgid, 'Exploring coupled-cluster Green's function as a method for treating system and environment in Green's function embedding methods', Journal of Chemical Theory and Computation **18**, 664 (2022).

[94] O. J. Backhouse and G. H. Booth, 'Constructing "full-frequency" spectra via moment constraints for coupled-cluster Green's functions', Journal of Chemical Theory and Computation **18**, 6622 (2022).

[95] R. Quintero-Monsebaiz, E. Monino, A. Marie and P.-F. Loos, 'Connections between many-body perturbation and coupled-cluster theories', The Journal of Chemical Physics **157**, 231102 (2022).

[96] E. Monino and P.-F. Loos, 'Connections and performances of Green's function methods for charged and neutral excitations', The Journal of Chemical Physics **159** (2023).

[97] J. Tölle and G. K.-L. Chan, 'Exact relationships between the *GW* approximation and equation-of-motion coupled-cluster theories through the quasi-boson formalism', The Journal of Chemical Physics **158** (2023).

[98] V. Rishi, A. Perera and R. J. Bartlett, 'A route to improving RPA excitation energies through its connection to equation-of-motion coupled-cluster theory', The Journal of Chemical Physics **153**, 234101 (2020).

[99] M. F. Lange and T. C. Berkelbach, 'On the relation between equation-of-motion coupled-cluster theory and the *GW* approximation', Journal of Chemical Theory and Computation **14**, 4224 (2018).

[100] G. E. Scuseria, T. M. Henderson and D. C. Sorensen, 'The ground state correlation energy of the random phase approximation from a ring coupled cluster doubles approach', The Journal of Chemical Physics **129**, 231101 (2008).

[101] J. Tolle, 'Fully analytic G_0W_0 nuclear gradients', The Journal of Physical Chemistry Letters **16**, 3672 (2025).

[102] J. Tolle, M.-P. Kitsaras and P.-F. Loos, 'Fully analytic nuclear gradients for the Bethe–Salpeter equation', The Journal of Physical Chemistry Letters **16**, 11134 (2025).

[103] J. J. Phillips and D. Zgid, 'Communication: the description of strong correlation within self-consistent Green's function second-order perturbation theory', The Journal of Chemical Physics **140**, 241101 (2014).

[104] D. Neuhauser, R. Baer and D. Zgid, 'Stochastic self-consistent second-order Green's function method for correlation energies of large electronic systems', Journal of Chemical Theory and Computation **13**, 5396 (2017).

[105] A. A. Kananenka, A. R. Welden, T. N. Lan, E. Gull and D. Zgid, 'Efficient temperature-dependent Green's function methods for realistic systems: using cubic spline interpolation to approximate Matsubara Green's functions', Journal of Chemical Theory and Computation **12**, 2250 (2016).

[106] L. Reining, 'The *GW* approximation: content, successes and limitations', Wiley Interdisciplinary Reviews: Computational Molecular Science **8**, e1344 (2018).

[107] O. J. Backhouse and G. H. Booth, 'Efficient excitations and spectra within a perturbative renormalization approach', Journal of Chemical Theory and Computation **16**, 6294 (2020).

[108] O. J. Backhouse, M. Nusspickel and G. H. Booth, 'Wave function perspective and efficient truncation of renormalized second-order perturbation theory', Journal of Chemical Theory and Computation **16**, 1090 (2020).

[109] P. Pokhilko, S. Iskakov, C.-N. Yeh and D. Zgid, 'Evaluation of two-particle properties within finite-temperature self-consistent one-particle Green's function methods: theory and application to *GW* and GF2', The Journal of Chemical Physics **155**, 024119 (2021).

[110] C. J. C. Scott, O. J. Backhouse and G. H. Booth, 'A moment-conserving reformulation of *GW* theory', The Journal of Chemical Physics **158** (2023).

[111] D. C. Brody, 'Biorthogonal quantum mechanics', Journal of Physics A: Mathematical and Theoretical **47**, 035305 (2013).

[112] J. Southall, D. Hodgson, R. Purdy and A. Beige, 'Comparing hermitian and non-hermitian quantum electrodynamics', Symmetry **14**, 1816 (2022).

[113] D. C. Brody, 'Consistency of PT-symmetric quantum mechanics', Journal of Physics A: Mathematical and Theoretical **49**, 10LT03 (2016).

[114] W. Pauli, 'On Dirac's new method of field quantization', Reviews of Modern Physics **15**, 175 (1943).

[115] A. Mostafazadeh, 'Pseudo-hermiticity versus PT-symmetry III: equivalence of pseudo-hermiticity and the presence of antilinear symmetries', Journal of Mathematical Physics **43**, 3944 (2002).

[116] C. M. Bender, D. C. Brody and H. F. Jones, 'Complex extension of quantum mechanics', Physical Review Letters **89**, 270401 (2002).

[117] Y.-G. Miao and Z.-M. Xu, 'Investigation of non-hermitian Hamiltonians in the Heisenberg picture', Physics Letters A **380**, 1805 (2016).

[118] R. A. Chiles and C. E. Dykstra, 'An electron pair operator approach to coupled-cluster wave functions. Application to He_2, Be_2, and Mg_2 and comparison with CEPA methods', The Journal of Chemical Physics **74**, 4544 (1981).

[119] N. C. Handy, J. A. Pople, M. Head-Gordon, K. Raghavachari and G. W. Trucks, 'Size-consistent Brueckner theory limited to double substitutions', Chemical Physics Letters **164**, 185 (1989).

[120] D. P. Tew, 'Explicitly correlated coupled-cluster theory with Brueckner orbitals', The Journal of Chemical Physics **145** (2016).

[121] Y. Takasu, T. Yagami, Y. Ashida, R. Hamazaki, Y. Kuno and Y. Takahashi, 'PT-symmetric non-hermitian quantum many-body system using ultracold atoms in an optical lattice with controlled dissipation', Progress of Theoretical and Experimental Physics **2020**, 12A110 (2020).

[122] J. Gauss and J. F. Stanton, 'Coupled-cluster calculations of nuclear magnetic resonance chemical shifts', The Journal of Chemical Physics **103**, 3561 (1995).

[123] S. Hirata, I. Grabowski, J. V. Ortiz and R. J. Bartlett, 'Nonconvergence of the Feynman-Dyson diagrammatic perturbation expansion of propagators', Physical Review A **109**, 052220 (2024).

[124] C. Møller and M. S. Plesset, 'Note on an approximation treatment for many-electron systems', Physical Review **46**, 618 (1934).

[125] R. D. Mattuck and A. Theumann, 'Expressing the decoupled equations of motion for the Green's function as a partial sum of feynman diagrams', Advances in Physics **20**, 721 (1971).

[126] F. Bruneval, A. Förster and Y. Pavlyukh, 'GW+ 2SOSEX self-energy made positive semidefinite', Journal of Chemical Theory and Computation **21**, 10223 (2025).

[127] M. Nooijen and R. J. Bartlett, 'Equation-of-motion coupled-cluster method for electron attachment', The Journal of Chemical Physics **102**, 3629 (1995).

[128] S. Hirata, M. Nooijen and R. J. Bartlett, 'High-order determinantal equation-of-motion coupled-cluster calculations for electronic excited states', Chemical Physics Letters **326**, 255 (2000).

[129] S. Hirata, M. Nooijen and R. J. Bartlett, 'High-order determinantal equation-of-motion coupled-cluster calculations for ionized and electron-attached states', Chemical Physics Letters **328**, 459 (2000).

[130] C. Barbieri, T. Duguet and V. Somà, 'Gorkov algebraic diagrammatic construction formalism at third order', Physical Review C **105**, 044330 (2022).

[131] H.-G. Weikert, H.-D. Meyer, L. S. Cederbaum and F. Tarantelli, 'Block lanczos and many-body theory: application to the one-particle green's function', The Journal of chemical physics **104**, 7122 (1996).

[132] F. Marino, W. G. Jiang and S. J. Novario, 'Diagrammatic ab initio methods for infinite nuclear matter with modern chiral interactions', Physical Review C **110**, 054322 (2024).

[133] V. Soma, C. Barbieri and T. Duguet, '*Ab initio* self-consistent gorkov-green's function calculations of semi-magic nuclei: numerical implementation at second order with a two-nucleon interaction', Physical Review C **89**, 024323 (2014).

[134] S. J. Bintrim and T. C. Berkelbach, 'Full-frequency *GW* without frequency', The Journal of Chemical Physics **154**, 041101 (2021).

[135] M. Nooijen and R. J. Bartlett, 'Similarity transformed equation-of-motion coupled-cluster theory: details, examples, and comparisons', The Journal of Chemical Physics **107**, 6812 (1997).

[136] J. F. Stanton and J. Gauss, 'A simple scheme for the direct calculation of ionization potentials with coupled-cluster theory that exploits established excitation energy methods', The Journal of Chemical Physics **111**, 8785 (1999).

[137] M. Musiał, S. A. Kucharski and R. J. Bartlett, 'Equation-of-motion coupled-cluster method with full inclusion of the connected triple excitations for ionized states: IP-EOM-CCSDT', The Journal of Chemical Physics **118**, 1128 (2003).

[138] E. Opoku, F. Pawłowski and J. V. Ortiz, 'A new generation of non-diagonal, renormalized self-energies for calculation of electron removal energies', The Journal of Chemical Physics **159**, 124109 (2023).

[139] E. Opoku, F. Pawłowski and J. V. Ortiz, 'New-generation electron-propagator methods for calculations of electron affinities and ionization energies: tests on organic photovoltaic molecules', Journal of Chemical Theory and Computation **20**, 290 (2023).

[140] E. Opoku, F. Pawłowski and J. V. Ortiz, 'New-generation electron-propagator methods for molecular electron-binding energies', The Journal of Physical Chemistry A **128**, 1399 (2024).

[141] F. Marino, C. Barbieri and G. Colò, 'Gorkov algebraic diagrammatic construction for infinite nuclear matter', arXiv preprint arXiv:2601.03763 (2026).

[142] G. Riva, P. Romaniello and A. J. Berger, 'Multichannel Dyson equation: coupling many-body Green's functions', Physical Review Letters **131**, 216401 (2023).

[143] G. Riva, P. Romaniello and J. A. Berger, 'Derivation and analysis of the multichannel Dyson equation', Physical Review B **110**, 115140 (2024).

[144] T. C. Berkelbach, 'Communication: random-phase approximation excitation energies from approximate equation-of-motion coupled-cluster doubles', The Journal of Chemical Physics **149**, 041103 (2018).

[145] G. E. Scuseria, T. M. Henderson and I. W. Bulik, 'Particle-particle and quasiparticle random phase approximations: connections to coupled-cluster theory', The Journal of Chemical Physics **139**, 104113 (2013).

[146] A. Marie, P. Romaniello, X. Blase and P.-F. Loos, 'Anomalous propagators and the particle–particle channel: bethe–salpeter equation', The Journal of Chemical Physics **162** (2025).

[147] A. Köhn and A. Tajti, 'Can coupled-cluster theory treat conical intersections?', The Journal of Chemical Physics **127** (2007).

[148] E. F. Kjønstad and H. Koch, 'Resolving the notorious case of conical intersections for coupled cluster dynamics', The Journal of Physical Chemistry Letters **8**, 4801 (2017).

[149] N. C. Handy, 'Energies and expectation values for be by the transcorrelated method', The Journal of Chemical Physics **51**, 3205 (1969).

[150] S. Tsuneyuki, 'Transcorrelated method: another possible way towards electronic structure calculation of solids', Progress of Theoretical Physics Supplement **176**, 134 (2008).

[151] S. McArdle and D. P. Tew, 'Improving the accuracy of quantum computational chemistry using the transcorrelated method', arXiv preprint arXiv:2006.11181 (2020).

[152] N. Lee and A. J. W. Thom, 'Studies on the transcorrelated method', Journal of Chemical Theory and Computation **19**, 5743 (2023).

[153] E. Opoku, F. Pawłowski and J. V. Ortiz, 'A new generation of diagonal self-energies for the calculation of electron removal energies', The Journal of Chemical Physics **155**, 204107 (2021).

[154] J. Ortiz, 'Dyson-orbital concepts for description of electrons in molecules', The Journal of Chemical Physics **153**, 070902 (2020).

[155] G. E. Scuseria, 'On the connections between Brueckner–coupled-cluster, density-dependent Hartree–Fock, and Density Functional Theory', International Journal of Quantum Chemistry **55**, 165 (1995).

[156] S. Hirata, 'Higher-order equation-of-motion coupled-cluster methods', The Journal of Chemical Physics **121**, 51 (2004).

[157] J. Hubbard, 'Electron correlations in narrow energy bands III: an improved solution', Proceedings of the Royal Society of London. Series A. Mathematical and Physical Sciences **281**, 401 (1964).

[158] G. Lani, P. Romaniello and L. Reining, 'Approximations for many-body Green's functions: insights from the fundamental equations', New Journal of Physics **14**, 013056 (2012).

[159] R. M. Martin, L. Reining and D. M. Ceperley, *Interacting electrons* (Cambridge University Press, 2016).

[160] G. Riva, T. Fischer, S. Paggi, J. A. Berger and P. Romaniello, 'Multichannel Dyson equations for even-and odd-order Green's functions: Application to double excitations', Physical Review B **111**, 195133 (2025).

[161] A. Ammar, A. Marie, M. Rodríguez-Mayorga, H. G. A. Burton and P.-F. Loos, 'Can *GW* handle multireference systems?', The Journal of Chemical Physics **160**, 114101 (2024).

[162] A. M. Alvertis, J. B. Haber, Z. Li, C. J. N. Coveney, S. G. Louie, M. R. Filip and J. B. Neaton, 'Phonon screening and dissociation of excitons at finite temperatures from first principles', Proceedings of the National Academy of Sciences **121**, e2403434121 (2024) 10.1073/pnas.2403434121.

[163] M. Reed and B. Simon, *III: Scattering theory*, Vol. 3 (Elsevier, 1979).

[164] Y. Toyozawa, 'Theory of Line-Shapes of the Exciton Absorption Bands', Progress of Theoretical Physics **20**, 53 (1958) 10.1143/PTP.20.53.

[165] Y. Toyozawa, 'Interband effect of lattice vibrations in the exciton absorption spectra', Journal of Physics and Chemistry of Solids **25**, 59 (1964) 10.1016/0022-3697(64)90162-3.

[166] C. G. Bollini, O. Civitarese, A. L. De Paoli and M. C. Rocca, 'Gamow states as continuous linear functionals over analytical test functions', Journal of Mathematical Physics **37**, 4235 (1996).

[167] O. Civitarese and M. Gadella, 'Physical and mathematical aspects of Gamow states', Physics Reports **396**, 41 (2004).

[168] I. E. Antoniou and I. Prigogine, 'Intrinsic irreversibility and integrability of dynamics', Physica A: Statistical Mechanics and its Applications **192**, 443 (1993).

[169] F. Giustino, 'Electron-phonon interactions from first principles', Reviews of Modern Physics **89**, 015003 (2017).

[170] P. B. Allen and V. Heine, 'Theory of the temperature dependence of electronic band structures', Journal of Physics C: Solid State Physics **9**, 2305 (1976).

[171] P. B. Allen and M. Cardona, 'Theory of the temperature dependence of the direct gap of germanium', Physical Review B **23**, 1495 (1981).

[172] F. Giustino, S. G. Louie and M. L. Cohen, 'Electron-phonon renormalization of the direct band gap of diamond', Physical Review Letters **105**, 265501 (2010).

[173] C. Faber, J. L. Janssen, M. Côté, E. Runge and X. Blase, 'Electron-phonon coupling in the C_{60} fullerene within the many-body GW approach', Physical Review B **84**, 155104 (2011).

[174] S. Poncé, J.-M. Lihm and C.-H. Park, 'Verification and validation of zero-point electron-phonon renormalization of the bandgap, mass enhancement, and spectral functions', npj Computational Materials **11**, 117 (2025).

[175] A. Marini, 'Ab initio finite-temperature excitons', Physical Review Letters **101**, 106405 (2008).

[176] X. Gonze and C. Lee, 'Dynamical matrices, born effective charges, dielectric permittivity tensors, and interatomic force constants from density-functional perturbation theory', Physical Review B **55**, 10355 (1997).

[177] G. Baym, 'Field-theoretic approach to the properties of the solid state', Annals of Physics **14**, 10.1006/aphy.2000.6009 (1961) 10.1006/aphy.2000.6009.

[178] E. G. Maksimov, 'A self-consistent description of the electron-phonon system in metals and the problem of lattice stability', Zh. Eksp. Teor. Fiz **69**, 2236 (1975).

[179] J. Lafuente-Bartolome, C. Lian, W. H. Sio, I. G. Gurtubay, A. Eiguren and F. Giustino, 'Ab initio self-consistent many-body theory of polarons at all couplings', Physical Review B **106**, 075119 (2022).

[180] J. Lafuente-Bartolome, C. Lian, W. H. Sio, I. G. Gurtubay, A. Eiguren and F. Giustino, 'Unified approach to polarons and phonon-induced band structure renormalization', Physical Review Letters **129**, 076402 (2022).

[181] J. Pollmann and H. Büttner, 'Effective Hamiltonians and bindings energies of Wannier excitons in polar semiconductors', Physical Review B **16**, 4480 (1977).

[182] J. B. Haber, 'Exciton-phonon interactions in complex materials', PhD thesis (University of California, Berkeley, 2022).

[183] W. H. Sio, C. Verdi, S. Poncé and F. Giustino, 'Ab initio theory of polarons: formalism and applications', Physical Review B **99**, 235139 (2019).

[184] W. H. Sio, C. Verdi, S. Poncé and F. Giustino, 'Polarons from first principles, without supercells', Physical Review Letters **122**, 246403 (2019).

[185] W. H. Sio and F. Giustino, 'Polarons in two-dimensional atomic crystals', Nature Physics **19**, 629 (2023).

[186] Z. Dai, J. Lafuente-Bartolome and F. Giustino, 'Polarons from first principles', arXiv preprint arXiv:2512.06176 (2025).

[187] N. V. Prokof'ev and B. V. Svistunov, 'Polaron problem by diagrammatic quantum monte carlo', Physical Review Letters **81**, 2514 (1998).

[188] A. S. Mishchenko, N. V. Prokof'Ev, A. Sakamoto and B. V. Svistunov, 'Diagrammatic quantum Monte Carlo study of the Fröhlich polaron', Physical Review B **62**, 6317 (2000).

[189] T. Hahn, S. Klimin, J. Tempere, J. T. Devreese and C. Franchini, 'Diagrammatic Monte Carlo study of Fröhlich polaron dispersion in two and three dimensions', Physical Review B **97**, 134305 (2018).

[190] L. X. Benedict, E. L. Shirley and R. B. Bohn, 'Theory of optical absorption in diamond, Si, Ge, and GaAs', Physical Review B **57**, R9385 (1998).

[191] H. Shi, R. Yan, S. Bertolazzi, J. Brivio, B. Gao, A. Kis, D. Jena, H. G. Xing and L. Huang, 'Exciton dynamics in suspended monolayer and few-layer MoS_2 2d crystals', ACS nano **7**, 1072 (2013).

[192] L. M. Herz, 'How lattice dynamics moderate the electronic properties of metal-halide perovskites', The Journal of Physical Chemistry Letters **9**, 6853 (2018).

[193] M. Bokdam, T. Sander, A. Stroppa, S. Picozzi, D. D. Sarma, C. Franchini and G. Kresse, 'Role of polar phonons in the photoexcited state of metal halide perovskites', Scientific Reports **6**, 1 (2016).

[194] N. S. Ginsberg and W. A. Tisdale, 'Spatially resolved photogenerated exciton and charge transport in emerging semiconductors', Annual Review of Physical Chemistry **71**, 1 (2020).

[195] G. Grancini, M. Maiuri, D. Fazzi, A. Petrozza, H.-J. Egelhaaf, D. Brida, G. Cerullo and G. Lanzani, 'Hot exciton dissociation in polymer solar cells', Nature Materials **12**, 29 (2013).

[196] O. P. Dimitriev, 'Dynamics of excitons in conjugated molecules and organic semiconductor systems', Chemical Reviews **122**, 8487 (2022).

[197] F. Bechstedt and J. Furthmüller, 'Influence of screening dynamics on excitons in Ga_2O_3 polymorphs', Applied Physics Letters **114**, 6 (2019) 10.1063/1.5084324.

[198] A. Schleife, M. D. Neumann, N. Esser, Z. Galazka, A. Gottwald, J. Nixdorf, R. Goldhahn and M. Feneberg, 'Optical properties of In_2O_3 from experiment and first-principles theory: influence of lattice screening', New Journal of Physics **20**, 053016 (2018).

[199] R. Perea-Causín, S. Brem and E. Malic, 'Phonon-assisted exciton dissociation in transition metal dichalcogenides', Nanoscale **13**, 1884 (2021).

[200] Y. Park and D. T. Limmer, 'Renormalization of excitonic properties by polar phonons', The Journal of Chemical Physics **157**, 10.1063/5.0100738 (2022) 10.1063/5.0100738.

[201] S. G. Motti, M. Kober-Czerny, M. Righetto, P. Holzhey, J. Smith, H. Kraus, H. J. Snaith, M. B. Johnston and L. M. Herz, 'Exciton formation dynamics and band-like free charge-carrier transport in 2d metal halide perovskite semiconductors', Advanced Functional Materials, 2300363 (2023).

[202] J. B. Haber, D. Y. Qiu, F. H. da Jornada and J. B. Neaton, 'Maximally localized exciton Wannier functions for solids', Physical Review B **108**, 125118 (2023).

[203] C. D. Spataru, 'Electronic and optical gap renormalization in carbon nanotubes near a metallic surface', Physical Review B **88**, 125412 (2013).

[204] C. D. Spataru and F. Léonard, 'Many-body effects on the electronic and optical properties of strained semiconducting carbon nanotubes', Physical Review B **88**, 045404 (2013).

[205] M. R. Filip, J. B. Haber and J. B. Neaton, 'Phonon screening of excitons in semiconductors: halide perovskites and beyond', Physical Review Letters **127**, 067401 (2021).

[206] A. Champagne, J. B. Haber, S. Pokawanvit, D. Y. Qiu, S. Biswas, H. A. Atwater, F. H. da Jornada and J. B. Neaton, 'Quasiparticle and optical properties of carrier-doped monolayer mote2 from first principles', Nano Letters **23**, 4274 (2023).

[207] A. Champagne, M. Camarasa-Gómez, F. Ricci, L. Kronik and J. B. Neaton, 'Strongly bound excitons and anisotropic linear absorption in monolayer graphullerene', Nano Letters **24**, 7033 (2024).

[208] Z. N. Mauri, C. J. Ciccarino, J. B. Haber, D. Y. Qiu and F. H. da Jornada, 'Exciton-polaritons and exciton localization from a first-principles interacting Green's function formalism', arXiv preprint arXiv:2503.13613 (2025).

[209] S. D. Mahanti and C. M. Varma, 'Effective electron-hole interactions in polar semiconductors', Physical Review B **6**, 2209 (1972).

[210] S. Sunakawa, 'On the theory of rearrangement collisions', Progress of Theoretical Physics **24**, 963 (1960).

[211] G. Antonius and S. G. Louie, 'Theory of exciton-phonon coupling', Physical Review B **105**, 085111 (2022).

[212] H.-Y. Chen, D. Sangalli and M. Bernardi, 'Exciton-phonon interaction and relaxation times from first principles', Physical Review Letters **125**, 107401 (2020).

[213] P. Cudazzo, 'First-principles description of the exciton-phonon interaction: a cumulant approach', Physical Review B **102**, 045136 (2020).

[214] Y.-H. Chan, J. B. Haber, M. H. Naik, J. B. Neaton, D. Y. Qiu, F. H. da Jornada and S. G. Louie, 'Exciton lifetime and optical linewidth profile via exciton-phonon interactions: theory and first-principles calculations for monolayer MoS_2', arXiv preprint arXiv:2212.08451 (2022).

[215] J. Tölle and G. K.-L. Chan, 'Exact relationships between the *GW* approximation and equation-of-motion coupled-cluster theories through the quasi-boson formalism', The Journal of Chemical Physics **158** (2023).

[216] T. Chiarotti, A. Ferretti and N. Marzari, 'Energies and spectra of solids from the algorithmic inversion of dynamical hubbard functionals', Physical Review Research **6**, L032023 (2024).

[217] A. Marini, R. Del Sole and G. Onida, 'First-principles calculation of the plasmon resonance and of the reflectance spectrum of silver in the gw approximation', Physical Review B **66**, 115101 (2002).

[218] P. Cudazzo, M. Gatti, F. Roth, B. Mahns, M. Knupfer and A. Rubio, 'Plasmon dispersion in molecular solids: picene and potassium-doped picene', Physical Review B—Condensed Matter and Materials Physics **84**, 155118 (2011).

[219] M. Szyniszewski, E. Mostaani, N. D. Drummond and V. Fal'Ko, 'Binding energies of trions and biexcitons in two-dimensional semiconductors from diffusion quantum monte carlo calculations', Physical Review B **95**, 081301 (2017).

[220] K. Xie, X. Li and T. Cao, 'Theory and ab initio calculation of optically excited states—recent advances in 2d materials', Advanced Materials **33**, 1904306 (2021).

[221] S. Poncé, E. R. Margine, C. Verdi and F. Giustino, 'EPW: electron–phonon coupling, transport and superconducting properties using maximally localized Wannier functions', Computer Physics Communications **209**, 116 (2016).

[222] J. S. Zhou, M. Gatti, J. J. Kas, J. J. Rehr and L. Reining, 'Cumulant Green's function calculations of plasmon satellites in bulk sodium: influence of screening and the crystal environment', Physical Review B **97**, 035137 (2018).

[223] Z. Dai, C. Lian, J. Lafuente-Bartolome and F. Giustino, 'Excitonic polarons and self-trapped excitons from first-principles exciton-phonon couplings', Physical Review Letters **132**, 036902 (2024).

[224] Z. Dai, C. Lian, J. Lafuente-Bartolome and F. Giustino, 'Theory of excitonic polarons: from models to first-principles calculations', Physical Review B **109**, 045202 (2024).

[225] Y. Bai, Y. Wang and S. Meng, 'Ab initio self-trapped excitons', Physical Review Letters **133**, 046903 (2024).

[226] W. Lee, A. M. Alvertis, Z. Li, S. G. Louie, M. R. Filip, J. B. Neaton and E. Kioupakis, 'Phonon screening of excitons in atomically thin semiconductors', Physical Review Letters **133**, 206901 (2024).

[227] V. M. Galitskii and A. B. Migdal, 'Application of quantum field theory methods to the many-body problem', Sov. Phys. JETP **7**, 18 (1958).

[228] J. P. Nery, P. B. Allen, G. Antonius, L. Reining, A. Miglio and X. Gonze, 'Quasiparticles and phonon satellites in spectral functions of semiconductors and insulators: cumulants applied to the full first-principles theory and the fröhlich polaron', Physical Review B **97**, 115145 (2018).

[229] A. Marini, S. Poncé and X. Gonze, 'Many-body perturbation theory approach to the electron-phonon interaction with density-functional theory as a starting point', Physical Review B **91**, 224310 (2015).

[230] L. Chaput, A. Togo and I. Tanaka, 'Finite-displacement computation of the electron-phonon interaction within the projector augmented-wave method', Physical Review B **100**, 174304 (2019).

[231] G. Brunin, H. P. C. Miranda, M. Giantomassi, M. Royo, M. Stengel, M. J. Verstraete, X. Gonze, G.-M. Rignanese and G. Hautier, 'Phonon-limited electron mobility in Si, GaAs, and GaP with exact treatment of dynamical quadrupoles', Physical Review B **102**, 094308 (2020).

[232] I.-T. Lu, J.-J. Zhou and M. Bernardi, 'Efficient ab initio calculations of electron-defect scattering and defect-limited carrier mobility', Physical Review Materials **3**, 033804 (2019).

[233] F. Da Pieve, S. Di Matteo, D. Sébilleau, R. Gunnella, G. Stefani and C. R. Natoli, 'Angular correlation between photoelectrons and Auger electrons within scattering theory', Physical Review A **75**, 052704 (2007).

[234] K. B. Le, A. Esquembre-Kučukalić, H.-Y. Chen, I. Maliyov, Y. Luo, J.-J. Zhou, D. Sangalli, A. Molina-Sánchez and M. Bernardi, 'Magnon-phonon interactions from first principles', Physical Review B **112**, L180403 (2025).

[235] J.-M. Lihm, S. Poncé and C.-H. Park, 'Self-consistent electron lifetimes for electron-phonon scattering', Physical Review B **110**, L121106 (2024).

[236] J.-M. Lihm and S. Poncé, 'Nonperturbative self-consistent electron-phonon spectral functions and transport', Physical Review Letters **134**, 186401 (2025).

[237] Y.-H. Chan, J. B. Haber, M. H. Naik, J. B. Neaton, D. Y. Qiu, F. H. da Jornada and S. G. Louie, 'Exciton lifetime and optical line width profile via exciton–phonon interactions: theory and first-principles calculations for monolayer MoS_2', Nano Letters **23**, 3971 (2023).

[238] C. Lanczos, 'Solution of systems of linear equations by minimized iterations', J. Res. Nat. Bur. Standards **49**, 33 (1952).

[239] C. Lanczos, 'Iterative solution of large-scale linear systems', Journal of the Society for Industrial and Applied Mathematics **6**, 91 (1958).

[240] B. N. Parlett, *The symmetric eigenvalue problem* (SIAM, 1998).

[241] J. K. Cullum and R. A. Willoughby, *Lanczos algorithms for large symmetric eigenvalue computations: vol. i: theory* (SIAM, 2002).

[242] V. Hernandez, J. Roman, A. Tomas and V. Vidal, 'Lanczos methods in slepc', Polytechnic University of Valencia, Province of Valencia (2006).

[243] G. H. Wannier, 'The structure of electronic excitation levels in insulating crystals', Physical Review **52**, 191 (1937) 10.1103/PhysRev.52.191.

[244] H. Fröhlich, 'Electrons in lattice fields', Advances in Physics **3**, 325 (1954) 10.1080/00018735400101213.

[245] A. M. Alvertis, A. Champagne, M. Del Ben, F. H. da Jornada, D. Y. Qiu, M. R. Filip and J. B. Neaton, 'Importance of nonuniform Brillouin zone sampling for ab initio Bethe-Salpeter equation calculations of exciton binding energies in crystalline solids', Physical Review B **108**, 235117 (2023) 10.1103/PhysRevB.108.235117.

[246] A. F. White, Y. Gao, A. J. Minnich and G. K.-L. Chan, 'A coupled cluster framework for electrons and phonons', The Journal of Chemical Physics **153** (2020).

[247] D. C. Langreth, in *Linear and nonlinear electron transport in solids* (Springer, 1976), pp. 3–32.

[248] L. Kantorovich, 'Generalized Langreth rules', Physical Review B **101**, 165408 (2020).

[249] E. R. Davidson, in *Methods in computational molecular physics* (Springer, 1983), pp. 95–113.

[250] J. P. Perdew, K. Burke and M. Ernzerhof, 'Generalized Gradient Approximation Made Simple', Physical Review Letters **77**, 3865 (1996).

[251] P. Giannozzi, S. Baroni, N. Bonini, M. Calandra, R. Car, C. Cavazzoni, D. Ceresoli, G. L. Chiarotti, M. Cococcioni, I. Dabo, A. Dal Corso, S. Fabris, G. Fratesi, S. de Gironcoli, R. Gebauer, U. Gerstmann, C. Gougoussis, A. Kokalj, M. Lazzeri, L. Martin-Samos, N. Marzari, F. Mauri, R. Mazzarello, S. Paolini, A. Pasquarello, L. Paulatto, C. Sbraccia, S. Scandolo, G. Sclauzero, A. P. Seitsonen, A. Smogunov, P. Umari and R. M. Wentzcovitch, 'QUANTUM ESPRESSO: a modular and open-source software project for quantum simulations of materials', Journal of Physics: Condensed Matter **21**, 395502 (2009).

[252] P. Giannozzi, O. Andreussi, T. Brumme, O. Bunau, M. Buongiorno Nardelli, M. Calandra, R. Car, C. Cavazzoni, D. Ceresoli, M. Cococcioni, N. Colonna, I. Carnimeo, A. Dal Corso, S. de Gironcoli, P. Delugas, R. A. DiStasio, A. Ferretti, A. Floris, G. Fratesi, G. Fugallo, R. Gebauer, U. Gerstmann, F. Giustino, T. Gorni, J. Jia, M. Kawamura, H.-Y. Ko, A. Kokalj, E. Küçükbenli, M. Lazzeri, M. Marsili, N. Marzari, F. Mauri, N. L. Nguyen, H.-V. Nguyen, A. Otero-de-la-Roza, L. Paulatto, S. Poncé, D. Rocca, R. Sabatini, B. Santra, M. Schlipf, A. P. Seitsonen, A. Smogunov, I. Timrov, T. Thonhauser, P. Umari, N. Vast, X. Wu and S. Baroni, 'Advanced capabilities for materials modelling with Quantum ESPRESSO', J. Phys.: Condens. Matter **29**, 465901 (2017) 10.1088/1361-648X/aa8f79.

[253] D. R. Hamann, 'Optimized norm-conserving Vanderbilt pseudopotentials', Physical Review B - Condensed Matter and Materials Physics **88**, 1 (2013) 10.1103/PhysRevB.88.085117.

[254] M. J. van Setten, M. Giantomassi, E. Bousquet, M. J. Verstraete, D. R. Hamann, X. Gonze and G. M. Rignanese, 'The PSEUDODOJO: Training and grading a 85 element optimized norm-conserving pseudopotential table', Computer Physics Communications **226**, 39 (2018) 10.1016/j.cpc.2018.01.012.

[255] G. Pizzi, V. Vitale, R. Arita, S. Blügel, F. Freimuth, G. Géranton, M. Gibertini, D. Gresch, C. Johnson, T. Koretsune, J. Ibanez-Azpiroz, H. Lee, J. M. Lihm, D. Marchand, A. Marrazzo, Y. Mokrousov, J. I. Mustafa, Y. Nohara, Y. Nomura, L. Paulatto, S. Poncé, T. Ponweiser, J. Qiao, F. Thöle, S. S. Tsirkin, M. Wierzbowska, N. Marzari, D. Vanderbilt, I. Souza, A. A. Mostofi and J. R. Yates, 'Wannier90 as a community code: New features and applications', Journal of Physics Condensed Matter **32**, 10.1088/1361-648X/ab51ff (2020) 10.1088/1361-648X/ab51ff.

[256] H. Lee, S. Poncé, K. Bushick, S. Hajinazar, J. Lafuente-Bartolome, J. Leveillee, C. Lian, J.-M. Lihm, F. Macheda, H. Mori, H. Paudyal, W. H. Sio, S. Tiwari, M. Zacharias, X. Zhang, N. Bonini, E. Kioupakis, E. R. Margine and F. Giustino, 'Electron–phonon physics from first principles using the EPW code', npj Computational Materials **9**, 156 (2023) 10.1038/s41524-023-01107-3.

[257] J. Deslippe, G. Samsonidze, D. A. Strubbe, M. Jain, M. L. Cohen and S. G. Louie, 'BerkeleyGW: A massively parallel computer package for the calculation of the quasiparticle and optical properties of materials and nanostructures', Computer Physics Communications **183**, 1269 (2012) 10.1016/j.cpc.2011.12.006.

[258] R. W. Godby and R. J. Needs, 'Metal-insulator transition in Kohn-Sham theory and quasiparticle theory', Phys. Rev. Lett. **62**, 1169 (1989) 10.1103/PhysRevLett.62.1169.